Magnetohydrodynamic simulations of the interaction between a magnetized young star and its accretion disc.

Nicolas Bessolaz

GRENOBLE I UNIVERSITY
JOSEPH-FOURIER

PhD joint with

EINDHOVEN UNIVERSITY OF TECHNOLOGY

DISSERTATION
by

Nicolas BESSOLAZ

to obtain the degrees of

DOCTOR OF THE JOSEPH-FOURIER UNIVERSITY

and

DOCTOR OF THE EINDHOVEN UNIVERSITY OF TECHNOLOGY

Specialty : ASTROPHYSICS – PHYSICS & DILUTE MEDIA

Magnetohydrodynamic simulations of the interaction between a magnetized young star and its accretion disc

---

Thesis defense on May 29th 2008
with the following dissertation committee

Mrs.	Marina ROMANOVA	Referee
Mrs.	Silvia ALENCAR	Referee
Mr.	Jean-Louis MONIN	Chairperson
Mr.	Jonathan FERREIRA	Supervisor at LAOG
Mr.	Niek LOPES CARDOZO	Supervisor at the FOM institute
Mr.	Rony KEPPENS	co-Supervisor at CPA
Mr.	Jean-François DONATI	Examinator
Mr.	Richard van de SANDEN	Examinator

PhD thesis prepared within the SHERPAS and FOST teams at the Laboratory of AstrOphysics of Grenoble (France), the Center for Plasma Astrophysics team in Leuven (Belgium) and the Plasma Physics group at the FOM institute Rijnhuizen (The Netherlands).

Nicolas BESSOLAZ

star-disc interaction, stellar formation, accretion discs, numerical methods, MHD.

PhD thesis — Grenoble I University (Joseph-Fourier) and Technische Universiteit Eindhoven (TUE)

— May 2008 —

ABSTRACT :

Nowadays, observation of slow rotators (3-8 days period) in star forming regions is still puzzling for accepted theoretical models, since efficient physical processes have to be considered to extract angular momentum brought by circumstellar matter accreting onto these stars, which moreover are still in a contraction phase. The interaction of the stellar magnetic field with its surrounding accretion disc is often presented as a possible explanation for this issue. In this thesis, we first present the state of the art of the star-disc interaction problem highlighting both the observations, theory and previous simulations which support it. Then, we model this interaction between a dipolar stellar magnetic field and a consistent accretion disc model including dissipative effects and we carry out simulations using the Versatile Advection Code (VAC) which solves the equations of magnetohydrodynamics.

The first goal of this thesis is to re-examine the conditions required to steadily deviate an accretion flow from a circumstellar disc into a magnetospheric accretion column onto a slow rotating young forming star. A new analytical and predictive criterion on the truncation of discs by the dipolar stellar field is derived stressing the importance of the disc thermal pressure. The physics of accretion columns is explained in detail. We confirm the numerical results of Romanova et al. (2002, ApJ, 578, 420) and find accretion funnels for stellar dipole fields as low as 140 G in the low accretion rate limit of $10^{-9}M_{\odot}yr^{-1}$. With our present numerical setup with no proper disc magnetic field, we found no evidence of winds, neither disc driven nor X-winds, and the star is only spun up by its interaction with the disc in this slow rotation range.

The second goal of this thesis is to test the robustness of magnetospheric accretion by doing a parameter space study varying the stellar magnetic field and rotation rate, and the amount of dissipation within the disc. Accretion columns are always present when the inner parts of the disc rotates quicker than the star, with oscillations of the truncation radius in presence of disc viscosity. The stellar accretion rate diminishes when the stellar magnetic field strength or rotation rate increases, which reduces the angular momentum brought onto the star. However, a disc-locking state is not clearly found, but stellar winds can be another possibility to efficiently extract angular momentum. This is already seen in our simulations even though we do not control here the mass loading into the stellar corona.

RESUME :

L'observation de rotateurs lents dans les régions de formation d'étoiles reste encore aujourd'hui une énigme puisque les mécanismes physiques sous-jacents permettant d'expliquer une extraction efficace du moment cinétique apporté par l'accrétion de matière autour de ces étoiles, qui sont de plus toujours en phase de contraction, ne sont pas clairement identifiés. L'interaction du champ magnétique de ces étoiles avec le disque d'accrétion en rotation autour d'elles est souvent présentée comme la solution pour ce problème. Dans cette thèse, je dresse d'abord le panorama d'ensemble qui justifie ce paradigme d'interaction étoile/disque tant du point de vue observationnel que théorique. Ensuite, je modélise cette interaction en prenant en compte le champ magnétique stellaire considéré ici comme dipolaire et un disque d'accrétion en incluant les effets dissipatifs dans ce dernier. J'effectue alors des simulations

numériques en utilisant le code VAC (Versatile Advection Code) qui résout les équations de la magnétohydrodynamique.

Le premier objectif de cette thèse est de ré-examiner les conditions nécessaires pour détourner de manière permanente l'écoulement d'accrétion du disque dans une colonne d'accrétion, dans le cas d'une étoile jeune tournant lentement. Un nouveau critère analytique et prédictif est obtenu pour trouver la position de troncation du disque par la magnétosphère de l'étoile considérée dipolaire et je montre l'importance du gradient de pression thermique dans le disque. La physique des colonnes d'accrétion est expliquée en détail. On confirme les résultats numériques de Romanova et al. (2002, ApJ, 578, 420) en trouvant des colonnes d'accrétion pour des champs magnétiques stellaires ayant une composante dipolaire aussi faible que 140 G dans le cas limite de faible taux d'accrétion sur l'étoile autour de $10^{-9} M_{\odot}$ par an. Avec le choix de notre configuration initiale sans champ magnétique propre dans le disque, je ne trouve pas véritablement de vent de matière, qu'il soit étendu dans le disque ou concentré autour de la troncation du disque comme décrit par le modèle de vent X, et l'étoile est toujours accélérée par l'interaction avec son disque dans le cas où on a un rotateur lent.

Le deuxième but de cette thèse est de tester la robustesse de l'accrétion magnétosphérique en faisant une étude de l'espace des paramètres où on fait varier le champ magnétique et la vitesse de rotation de l'étoile ainsi que l'importance des effets dissipatifs dans le disque. Les colonnes d'accrétion sont toujours présentes quand les parties internes du disque tournent plus vite que l'étoile avec des oscillations du rayon de troncation du disque en présence de viscosité. Le taux d'accrétion sur l'étoile diminue quand le champ magnétique stellaire ou sa vitesse de rotation augmente, ce qui réduit l'apport de moment cinétique à la surface de l'étoile. Pourtant, je ne trouve pas clairement une configuration où la rotation de l'étoile est fixée à une faible valeur par la présence du disque et la présence de vents stellaires semble être une autre possibilité d'extraire efficacement du moment cinétique comme c'est déjà entrevu dans mes simulations même si je ne contrôle pas ici le taux de perte de masse dans le vent.

Acknowledgements

It is now time to thank all the people who support me in the last years to achieve this thesis.

First of all, I would like to thank my supervisors. Rony Keppens brought me all his expertise in numerical simulations, above all at the beginning of the thesis guiding me in this complex field where I was nearly a beginner, but also then letting me do my own experience trusting me. I would like to thank him for the fruitful discussions we had about my simulation results but also for his pragmatic view which helps me to advance when I was too cautious and I had doubts about my work. Jonathan Ferreira, although not being used to numerical experimentations, took time to discuss about the simulations and I would like to thank him for his wide background in Physics which has been a source of inspiration for my own research. Jérôme Bouvier and Catherine Dougados allow me to obtain the best observational background of these versatile YSO.

But also this thesis enables me to work in different European institutes which was very wealthy. I will always remember my office in the Rijhnuizen castle surrounded by a very beautiful park with a lot of hens and ducks, the Leuven city very animated during nights with very tasty beers. I was also very glad to share the second floor of LAOG with many other students who put a very pleasant atmosphere. I would like to thank the Nicolas' team, Tim, Benoît, Rémy and Philippe but also the persons in the same position like me i.e. Myriam, Geoffroy, Oscar and Guillaume. I would like to specially thank Claudio for his friendship and collaboration to make comparison of our work with the PLUTO code. It was really helpful to get confidence in simulations for this difficult numerical work but also to identify their limits due to the different numerical schemes used. Finally, I would like to thank my parents and my sisters for encouraging me and helping me to overpass difficulties in the last months to finally write this thesis and also all people I do not cite here but I met during these years.

Contents

List of Figures

Introduction

In this thesis, I am interested in studying one of the main steps in the stellar formation process within the low mass range ($M_* < 1.5 M_\odot$) corresponding to T-Tauri stars (TTS). Classical T-Tauri stars (CTTS) are magnetically active, show evidence for circumstellar accretion discs, and can have mean photospheric magnetic field magnitudes around 2kG (e.g. Johns-Krull et al. 1999). Such a strong stellar field is enough to disrupt the inner accretion disc, provided that one really measures the large scale magnetic field and not only local strong multipolar components from starspots. However, this does not seem to be the case since recent polarimetric measurements (Valenti & Johns-Krull 2004) indicate a weak dipolar component lower than 200 G. Moreover, observations show evidence for non direct accretion. Inverse P-Cygni profiles with strong redshift absorption wings are indicative of polar accretion near free-fall velocities along magnetospheric field lines from the inner disc edge (Edwards et al. 1994; Bouvier et al. 1999, 2003). The main goal of this thesis is to give the best physical understanding of the formation and properties of this magnetospheric accretion, starting from a consistent modelling of the accretion flow, by including the magnetic interaction within the Magnetohydrodynamics (MHD) framework.

Although the magnetic field structure of these stars is probably complex (Gregory et al. 2006), dynamical models of star-disc interaction usually assume an aligned dipole field, to simplify the analytical work. Under this assumption, stellar field lines threading the Keplerian disc below the co-rotation radius $r_{\rm co} = (GM_*/\Omega_*^2)^{1/3}$, where Ω_* is the stellar angular velocity, would lead to a spin up of the star, whereas those beyond $r_{\rm co}$ to a spin down. The radial extent of angular momentum exchange between the star and the disc is then determined by (1) the disc truncation radius $r_{\rm t}$, where the magnetic dipole diverts the radially accreting flow to funnel flows; and (2) an outer radius $r_{\rm out}$ beyond which no more stellar field lines are connected to the disc. In this framework, a star-disc interaction occurring on a large radial extension (as proposed by Ghosh & Lamb 1979; Cameron & Campbell 1993; Armitage & Clarke 1996), may lead to a disc-locking situation where the star remains at a slow rotation rate, despite accretion. On the other hand, it has been argued that this scenario is unlikely, since the stellar field lines would be opened up by differential rotation until severing this causal link (Aly & Kuijpers 1990; Lovelace et al. 1995; Matt & Pudritz 2005,for a recent discussion on that issue). The outcome of this latter scenario would be a star-disc interaction limited to a small radial extension around the disc truncation radius. Many theoretical models then assume that the disc inner edge should be close to the co-rotation radius (Königl 1991; Shu et al. 1994) for the sake of angular momentum equilibrium.

In Chapter 1, we present the astrophysical context by drawing an overview of the observational constraints underlying the star-disc paradigm. Next, we explain the different theoretical ideas which try to understand the magnetospheric accretion and the efficient

extraction of angular momentum via this large scale magnetic interaction, but also linked ejections phenomena.

In Chapter 2, we present the numerical techniques based on finite volume schemes we used in the next chapters to carry out MHD simulations of this star-disc system with the VAC code and then discuss previous numerical works.

In Chapter 3, we detail our numerical modelling of the system including a disc both viscous and resistive, a splitting strategy for the magnetic field to accurately calculate the magnetic stresses and relevant boundary conditions to correctly treat the stellar surface.

In Chapter 4, we revisit the physical conditions to form accretion funnels in the slow stellar rotation range and derive a new analytical criterion to find the disc truncation radius based on our accretion physics understanding. We verify this prediction by performing simulations with a weak dipole field and find accretion columns with accretion rate compatible with weak accretors.

In Chapter 5, we carry out a parameter space study of the star-disc system by varying different star/disc characteristics such as the stellar magnetic field strenght B_*, the stellar rotation rate Ω_* and the dissipative properties of the disc described by both diffusivity η and viscosity ν. We particularly study their influence on the formation of funnel flows and the resulting stellar accretion rate. We also try to find configurations with extended magnetosphere in order to really test the possibility of a disc-locking state.

Introduction

Pendant cette thèse, je me suis intéressé à étudier une des étapes importantes de la formation stellaire correspondant à la phase des étoiles T Tauri pour les étoiles de faible masse ($M_* < 2M_\odot$). Les étoiles T-Tauri classiques (CTTS) présentent une activité magnétique avec des champs à leur surface atteignant en moyenne 2 kG (voir par exemple les travaux de Johns-Krull et al. 1999) ainsi que des preuves de l'existence de disques d'accretion autour d'elles. Cet intense champ magnétique est suffisant pour détruire le disque d'accrétion dans ses régions internes, à condition que le champ mesuré soit un champ à grande échelle et pas uniquement le champ local avec des composantes multipolaires concentrées dans les taches sombres magnétiques qu'on observe comme sur notre soleil. Cependant, cela ne semble pas être le cas puisque de récentes observations en polarimétrie (Valenti & Johns-Krull 2004) indique une composante dipolaire plus faible que 200 G. En outre, les observations montrent des preuves d'accrétion non directe sur l'étoile. Les profils P-Cygni inverses avec une forte absorption décalée vers le rouge sont des indices montrant que l'accrétion est détournée vers les pôles magnétiques de l'étoile à partir du bord interne du disque le long des lignes de champ magnétique et que les vitesses atteintes à la surface de l'étoile sont proches de la vitesse de chute libre (Edwards et al. 1994; Bouvier et al. 1999, 2003). L'objectif principal de ce travail est de fournir une compréhension la plus détaillée possible de la formation et des propriétés de cette accrétion magnétosphèrique à partir d'une modélisation cohérente de l'écoulement d'accrétion en incluant l'effet de l'interaction magnétique dans le cadre de la théorie de la Magnéto-HydroDynamique (MHD).

Bien que la topologie du champ magnétique de ces étoiles soit probablement complexe (Gregory et al. 2006), les modèles théoriques décrivant la dynamique de l'interaction entre l'étoile et son disque considèrent généralement un champ magnétique dipolaire aligné avec l'axe de rotation de l'étoile permettant de simplifier les calculs analytiques. Avec cette hypothèse, les lignes de champ magnétique stellaires traversant le disque Képlérien en deçà du rayon de corotation défini comme $r_{\rm co} = (GM_*/\Omega_*^2)^{1/3}$, où Ω_* est la vitesse angulaire de l'étoile, tendent à accélérer l'étoile tandis que celles connectées au delà de $r_{\rm co}$ participent à son freinage. L'extension radiale de la région où il y a un échange de moment cinétique entre l'étoile et le disque est ainsi déterminée par : (1) la position du rayon de troncation du disque $r_{\rm t}$, où le champ magnétique dipolaire dévie l'écoulement radial d'accrétion et donne une nappe d'accrétion convergeant vers les pôles de l'étoile ; et (2) le rayon extérieur $r_{\rm out}$ à partir duquel les lignes de champ magnétique de l'étoile ne sont plus connectées au disque. Dans ce cadre, une interaction entre l'étoile et le disque sur une large extension radiale, (comme proposée dans les modèles de Ghosh & Lamb 1979; Cameron & Campbell 1993; Armitage & Clarke 1996), peut amener à une configuration de "disc-locking" où l'étoile maintient une vitesse de rotation constante malgré l'accrétion de masse en continu. Cependant, ce scénario est improbable puisque les lignes de champ stellaires seront plus ou moins rapidement ouvertes par la rotation différentielle jusqu'à limiter très significativement le lien causal entre l'étoile et son disque (Aly & Kuijpers 1990; Lovelace et al. 1995; Matt & Pudritz 2005,pour une discussion récente de cet aspect). Le résultat de ce dernier scénario serait alors une interaction entre l'étoile et son disque limitée à proximité du rayon de troncation du disque. Beaucoup de modèles théoriques supposent alors que le rayon interne du

disque devrait être proche du rayon de corotation (Königl 1991; Shu et al. 1994) pour satisfaire une situation d'équilibre en ce qui concerne le moment cinétique de l'étoile.

Dans le chapitre 1, je présente le contexte astrophysique en dressant un tour d'horizon des contraintes observationnelles mettant en évidence le paradigme de l'interaction disque/étoile. Ensuite, je discute les différentes idées théoriques qui essayent d'expliquer l'accrétion magnétosphérique et l'efficacité de l'extraction du moment cinétique associée à une interaction magnétique à grande échelle entre l'étoile et son disque, mais aussi par l'intermédiaire des phénomènes d'éjection.

Au chapitre 2, je présente tout d'abord les techniques numériques basées sur les schémas à volumes finis que nous utilisons par la suite pour effectuer des simulations MHD de l'interaction disque/étoile avec le code VAC, et dans une deuxième partie, je discute des travaux numériques antérieurs réalisés à ce sujet.

Au chapitre 3, je détaille notre modélisation numérique du système incluant un disque à la fois visqueux et résistif, le traitement spécifique du champ magnétique où on ne calcule que les écarts à la configuration dipolaire initiale ce qui permet une meilleure évaluation numérique des forces magnétiques en jeu, ainsi que les conditions aux limites adéquates pour traiter correctement la surface de l'étoile.

Au chapitre 4, je revisite les conditions physiques conduisant à la formation de colonnes d'accrétion pour une étoile tournant lentement et je dérive un nouveau critère analytique pour déterminer la position du rayon de troncation du disque basé sur la compréhension de la physique de l'accrétion. Je vérifie cette prédiction en effectuant des simulations avec un champ magnétique dipolaire faible et je trouve des colonnes d'accrétion compatibles avec des taux d'accrétion plutôt faibles pour les CTTS.

Au chapitre 5, j'effectue une étude de l'espace des paramètres du système composé par le disque et l'étoile en variant plusieurs de ses caractéristiques comme le champ magnétique stellaire B_*, la vitesse de rotation de l'étoile Ω_* et les propriétés dissipatives du disque décrites à la fois par sa diffusivité η et sa viscosité ν. J'étudie en particulier leur influence sur la formation des colonnes d'accrétion et le taux d'accrétion résultant à la surface de l'étoile. Nous essayons aussi d'obtenir des configurations avec une magnétosphère de l'étoile étendue pour tester vraiment la possibilité d'avoir un état où la rotation de l'étoile est maintenue à une valeur constante par la présence du disque par l'intermédiaire de l'interaction magnétique, ce qui pourrait expliquer comment ces étoiles jeunes âgées de quelques millions d'années peuvent se débarrasser de leur moment cinétique pour tendre ensuite vers des rotateurs très lents comme notre soleil.

1

Astrophysical context

Chapter content

1. Observational overview for T-Tauri stars

In this part, we will sum up the main properties of T Tauri stars obtained from half a century of ever more accurate observations underlying the star-disc interaction paradigm. We particularly concentrate on knowledge of large rotation periods, magnetic field constraints and evidences of truncated discs and the spectral features indicating magnetospheric accretion.

§ 1. Basic properties

T Tauri stars are low-mass stars ($M \sim 0.3 - 1.5 M_\odot$) with an age of a few million years which are still in gravitational contraction, describing an Hayashi (1966) nearly vertical track towards the main sequence in the Hertzsprung-Russel diagram. This corresponds to a step where the protostellar core has reached a nearly hydrostatic equilibrium and maintains an effective temperature around 4000 K as long as convective transport is dominant (negligible radiative core). Their radius goes from 4 $R_\odot$ for the youngest stars of one million years old till solar radii for the most old ones near the ZAMS. The presence of a strong lithium absorption line (EW [1] >

[1] Equivalent Width

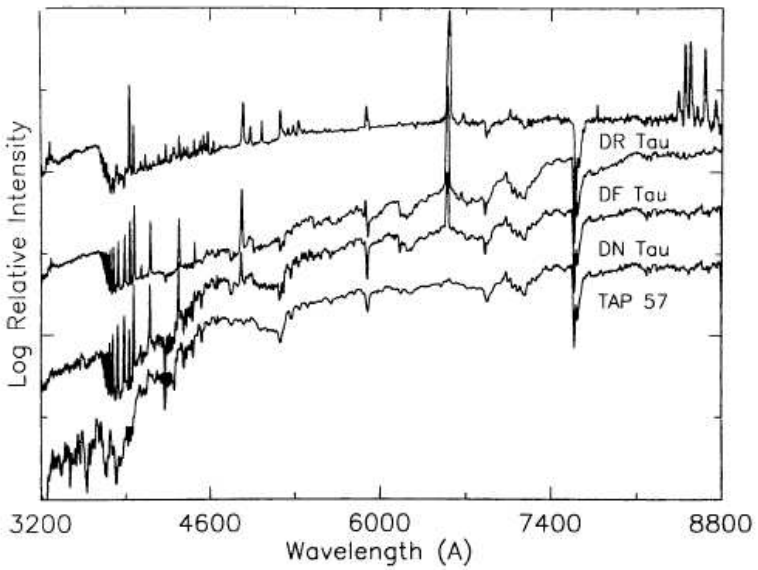

Figure 1. Optical spectra for late spectral type K T-Tauri stars with an increasing level of emission lines and veiling from the bottom to the top. The star TAP57 is classified as a WTTS (from Bertout 1989). One clearly distinguishes the H_α line at 6563 Å and also the UV excess below 4000 Å.

0.25 Å) stresses their youth and shows that the hydrogen fusion has still not begun. Actually, they shine thanks to their gravitational contraction.

T Tauri stars are primarily irregular variable stars with an amplitude in the visible band up to 3 magnitudes (Bertout 1989). They are linked to nebulae which are more or less dark (Jones & Herbig 1979), which entails strong absorption $A_V \sim 1 - 50$ in magnitudes of the visible range. The nearest star formation regions are the Taurus-Auriga (with the prototype star T Tau) and Ophiucus clouds at 150 pc, and then the Lupus one at 190 pc. The first systematic study and classification of these stars was done in 1945 by Joy who noticed strong emission lines which dominate the classical stellar absorption spectrum (see Fig. 1) and particularly the Balmer lines such as H_α, and CaII H and K lines like in the solar chromosphere even if T Tauri stars are cold stars. Actually, the emission line intensity is often 10 times larger than the continuum. One distinguishes two kinds of T Tauri stars, viewed with respect to the importance of the H_α emission line : Classical T Tauri star (CTTS) with EW > 10 Å and Weak T Tauri stars (WTTS) with EW < 10 Å. In CTTS, the photospheric lines are shallow (and in extreme cases nearly absent), with respect to other stars with the same effective temperature (Basri 1990, Hartigan et al. 1990). This veiling continuum is often understood as emission coming from the inner parts of the accretion flow reaching the stellar surface as accretion shocks which hide the photospheric spectrum. The resulting hot spots have effective temperature around 6000K (see e.g. MN Lupi in Strassmeier et al. 2005). The variability of the line profiles is a characteristic of CTTS and the timescales go from few hours till years (Johns & Basri 1995, Alencar & Basri 2000).

Star formation is the result of gravitational collapse of molecular clouds. Since these clouds have some angular momentum initially, one expects that the collapse has not a spherical symmetry but gives birth to a disc perpendicular to the rotation axis. In the star formation process, TTS are considered as class II sources (Adams et al. 1987, Andre et al. 1993) since a lot of circumstellar matter has already condensed into such a disc, enabling us to observe these

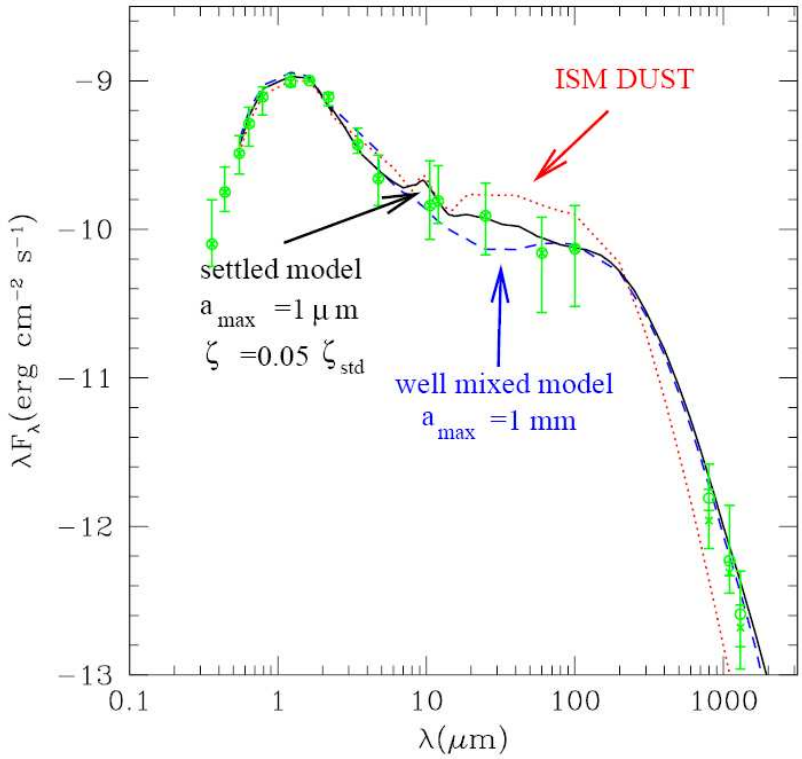

Figure 2. SED of disc models for different properties of the dust component (the size distribution follows $n(r) \propto r^{-3.5}$) : well-mixed ISM dust (dotted line), well mixed grains with $r_{max} = 1$ mm (dashed line) and dust settling from $r_{max} = 1$ μm at the disc surface to $r_{max} = 1$ mm at the disc midplane (solid line). Data points represent the median observed SED of CTTS in Taurus obtained with the IR spatial telescope Spitzer and corresponds to the following stellar parameters : $M_* = 0.5 M_\odot$, $R_* = 2 R_\odot$ and a mean accretion rate of $10^{-8} \mathrm{M}_\odot.\mathrm{yr}^{-1}$. One can distinguish the stellar component below 2 μm and the silicate band at 10 μm. One clearly sees that spectra favour a settlement of dust in the disc midplane (from d'Alessio et al.2003).

sources not only in radio and IR wavelengths like class I sources but also in the optical range. The mid IR excess observed in Spectral Energy Distribution (SED) (at wavelengths $\lambda < 10 \mu m$) is often fitted by a circumstellar thin Keplerian disc, assumed optically thick including both viscosity and passive effects (reprocessing of the stellar radiation field) whereas the optical-near IR part corresponds to the stellar blackbody corrected for absorption effects (Bertout et al. 1988). Many T-Tauri stars present also flat spectra in the far IR range which can be understood by a flaring of the disc in the outer parts enhancing reprocessing (Kenyon & Hartmann 1987) or by a flatter temperature distribution due to extra heating sources at larger scales (Adams, Lada & Shu 1988). Recently, self-consistent models by Chiang & Goldreich (1997), Dullemond et al. (2002) and D'Alessio (2003) have been developed to predict SED with greater details including both gas and dust with a radiative transfer using relevant dust opacities crucial for the temperature range around T Tauri stars. They particularly obtain the silicate band at 10 μm. A settling of dust in the disc midplane is also taken into account which reproduces well the mid-IR spectra (see Fig. 2).

An UV excess is also present (see Fig. 1). Explained in first models by an optically thick isothermal boundary layer [2] radiating half of the accretion power (Bouvier et al. 1986, Bertout et al. 1988), this is interpreted nowadays as accretion shocks onto the star (see the example of DF Tau in Bertout et al. (1988) with modulation in the U band modeled by a hot spot with temperature around 6500-9100 K).

§ 2. Disc accretion rates and clues for inner disc holes

Until recently, only indirect evidences for such discs were known. For instance, to explain the IR excess with the emission of dust, one can not assume a spherical envelope, otherwise the absorption would be too strong compared to the observations (Myers et al. 1987). The lack of redshifted forbidden lines is another clue of the presence of a screen around the star hiding a part of a wind (Appenzeller et al. 1984, Edwards et al. 1987). Detection of polarization in IR is also indicative of light scattering on non isotropic dust grains structures (Menard & Bastien 1992). Thanks to the development of high angular resolution techniques (for instance in millimetric interferometry with IRAM and VLA; see e.g. Sargent & Beckwith 1987, Dutrey et al. 1996) and the HST in the last decade, we can now resolve the accretion disc at the a.u. scale in the edge-on objects such as HH30 (Burrows et al. 1996), HK Tau B (O'Dell & Wen 1994) or proplyds in the Orion nebula (McCaughrean & O'Dell 1996, Smith et al. 2005).

Otherwise, the strongest indirect evidence for accretion in CTTS is the detection of redshifted absorption in upper Balmer and permitted metallic lines at velocities of up to several hundred km.s^{-1}, with large optical and UV excesses (Edwards et al. 1994, and references therein). These large infall velocities are compatible with free fall material coming from several stellar radii away supporting the idea of truncated discs. Analysis of IR excess and colors from models including such a hole between the star and the disc compared to full extended discs reaching the stellar surface gives a truncation radius $r_t \sim 2-6R_* = 0.4-0.8r_{\rm co}$ (Kenyon, Yi & Hartmann 1996, Meyer et al. 1997) where $r_{\rm co}$ denotes the corotation radius. The difficulty in such studies is the correct dereddening of broadband photometry measurements. This truncation radius is well below the dust sublimation radius (Eisner et al. 2005, Akeson et al. 2005) probed in near-IR interferometry which is $r_{sub} \sim 8-20R_*$ and which corresponds to a temperature around 1400 K where one can no longer have solid dust grains. Recently, CO fundamental ro-vibrational lines at 4.6 μm are used to probe the inner gas (Najita, Carr & Mathieu (2003) and see also the review of Protostars and Planets V by Najita et al. (2007)) with temperature between 2000 and 4000 K and densities greater than 10^{10}cm^{-3}. By interpreting the wings of these symmetric double peaked lines as the maximum Keplerian speed of the disc, they derived $r_t \sim 2-5R_* \sim 0.5-1r_{\rm co}$ (see Fig. 3) similar to previous estimates from IR excess. However, the assumption of Keplerian motion is questionable since we expect the disc rotation to be modified by the stellar magnetosphere.

Energy balance calculations and measurements of line emission give typical accretion rates for TTS of 10^{-7} to 10^{-9}M$_\odot$.yr^{-1} (Gullbring et al 1998, Lamzin et al. 2001 and see table 38 in Chap. 4). Estimates of accretion rates are done mainly from the veiling hot UV-optical continuum emission because the IR part of the spectrum is often modified by reprocessing. It is necessary to differentiate accretion shock emission from the intrinsic photospheric one above all in the

[2] Boundary layer models can not explain for instance inverse P Cygni profiles, the presence of hot spots deduced from photometry studies and the low rotation rate of CTTS.

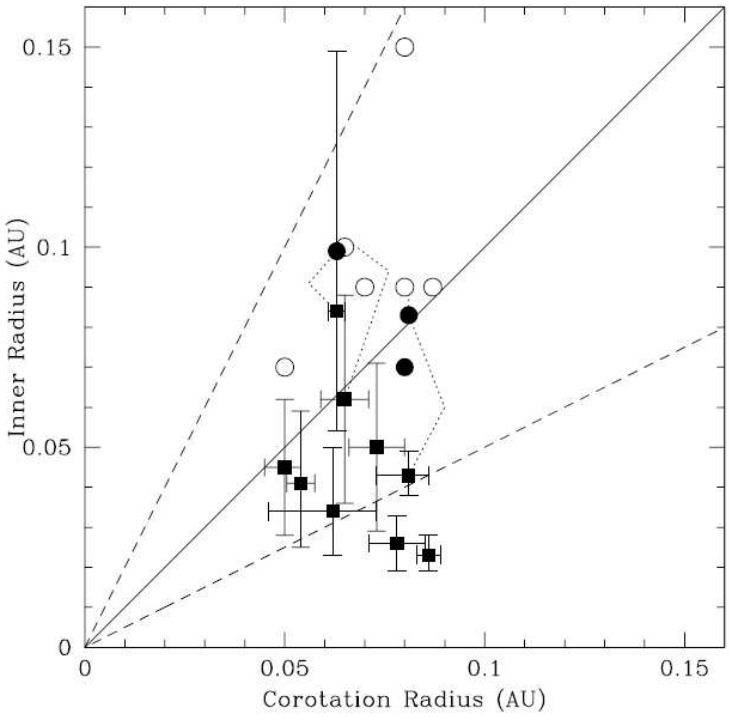

Figure 3. Gaseous inner disc radii for TTS from CO fundamental emission (filled squares) compared with corotation radii for the same sources. Also shown are dust inner radii from near-infrared interferometry (filled circles; Akeson et al., 2005a,b) or spectral energy distributions (open circles; Muzerolle et al., 2003). The solid and dashed lines indicate an inner radius equal to, twice, and 1/2 the corotation radius. The points for the three stars with measured inner radii for both the gas and dust are connected by dotted lines (from Najita et al. 2005).

case of low accretion rate, which gives discrepancies often of one order of magnitude between different studies because of different chosen interstellar absorption coefficients. Actually, WTTS were often chosen as template stars to assess the veiling (e.g. in Hartigan et al. 1995) but they can undergo also reddening which gives different A_V estimates for different color excess such as E(V-R) [3] and E(B-V) due to for instance the presence of cool spots. That is why recent studies (Gullbring et al. 1998) use dwarfs of same spectral type and gravity surface for deducing veiling. The accretion luminosity is derived from the energy equation assuming magnetospheric accretion with a free-fall speed profile starting from the disc inner edge and finally producing shocks close to the stellar surface (Calvet & Gullbring 1998) :

$$L_{acc} \simeq \frac{GM_*\dot{M}}{R_*}(1 - \frac{R_*}{r_t}) \tag{2.1}$$

The sources of uncertainties in calculating L_{acc} are the bolometric correction (since L_{acc} is deduced from a flux excess in a limited range of wavelengths), the orientation of accretion columns with respect to the line of sight which modify the filling factor, the stellar mass and radius deduced from the stellar luminosity and effective temperature, and the disc truncation radius position. Gullbring et al. (1998) deduced also a direct calibration law between the U band magnitude and

[3] By definition, E(V-R)= $(V-R)_{object} - (V-R)_{template} = \frac{A_V}{R_{V-R}} + log(\frac{1+r_V}{1+r_R})$ where R_{V-R} is given by the interstellar extinction law and r_V is the veiling in band V.

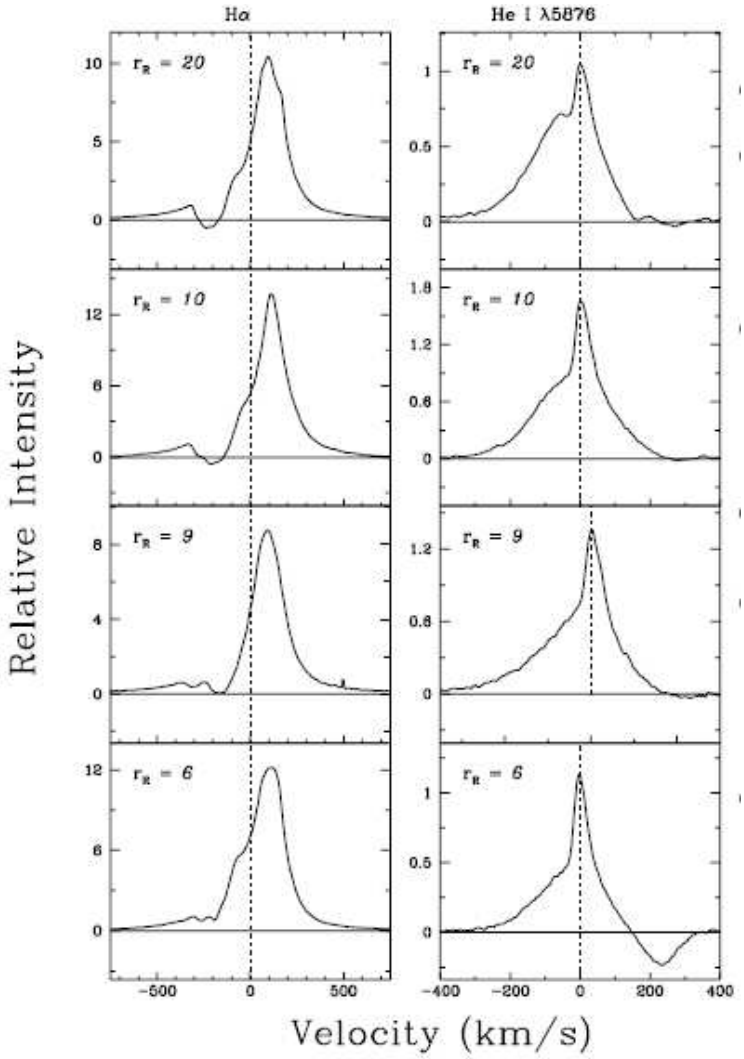

Figure 4. Different H_α and HeI lines for DR tau ordered by the magnitude of the veiling in the R band r_R (from Beristain et al. 1998). For high veiling, we can see P Cygni profiles for H_α lines indicative of an ejection process and Inverse P Cygni profile for HeI lines for low veiling which probe accretion phenomena. Negative velocities measured in the stellar rest frame correspond to blueshifted motions.

the accretion rates making it possible to derive accretion rates for a larger sample of T Tauri stars where there are no good spectroscopy data.

§ 3. Spectral features

Let us now have a look to the specific spectrum of TTS in order to better understand the physical conditions encountered around these stars. At low spectral resolution, strong emission lines are visible such as the Balmer lines H_α,H_β,H_γ, NaD, HeI, CaII and FeII (Alencar & Basri 2000). We focus on this emission part of the spectrum. The presence of strong Balmer emission lines is particularly noteworthy [4] since it is usually linked to higher mass stars of class Be,Ae.

[4] T Tauri stars have F-M spectral class where one expects neutral or ionized metal lines which dominate.

Using high spectral resolution, most of the lines have complex structure with more than one component and present high time variability. The broad component ($FWHM \sim 200\text{km.s}^{-1}$) of the lines are almost symmetric and centrally peaked (with respect to the stellar rest frame), and asymmetric narrow absorption components are present in Balmer and NaD lines. These different parts of a line have a different origin. The broad part is characteristic of an ionized medium with high orbital velocities around the star because of Doppler broadening. Edwards et al. (1994) show blueward asymmetric [5] emission lines due to disc shadowing effects and inverse P Cygni profiles (see Fig. 4), where the redshift absorption reaches several hundreds of $km.s^{-1}$. This strong infall is explained by accretion of material diverted from the disc midplane along the stellar magnetosphere acting as a nozzle which falls at free-fall speed and forms what is called an accretion column (or funnel flow). This redshift absorption is above all prominent in H_β and H_γ lines since H_α lines are quickly thermalized with increasing accretion rates and thus the emission is almost produced in the continuum. There is also an inclination effect with edge-on objects which show stronger redshift absorption than small inclination ones. The trend to see centrally peaked lines comes also from the fact that the main emitting volume in an accretion funnel flow has low velocity since it is perpendicular to the line of sight. Models of free-fall inflow through a dipolar field by Hartmann & Calvet (1994) and Muzerolle et al. (1998) reproduce such behaviour. Absorption with very little velocity with respect to the peak can be interpreted as material being loaded onto the magnetospheric field lines at the base of the accretion column. Modelization of the funnel flow emission including the treatment of the shock (Calvet & Gullbring 1998) permits also to put a constraint on the filling factor covered by the accretion columns which is always around or less than a few percent, in agreement with constraints from amplitude of variability and color changes seen in photometric studies (see e.g. Bouvier et al. 1999).

P Cygni profiles observed are directly interpreted as wind components. Blueshifted absorption seen in Balmer and NaD lines and generally narrow are coming from an ejected flow at $50-100\text{km.s}^{-1}$ absorbing cold photons from the star. A strong correlation between CaII, MgII and H_α lines is observed supporting an accretion flow origin for these lines and not a wind (Calvet et al. 1985, Bouvier 1987). Forbidden lines ([NII] 6584 Å, [SII] 6716,6731 Å) are also observed (Hartigan, Edwards & Ghandour 1995) which probe directly outflows. [OI] 6300 Å is present in all CTTS which have also important veiling and this line is absent in WTTS. This clearly indicates a correlation between accretion and ejection processes in CTTS (Cabrit et al. 1990, Corcoran & Ray 1998). A closer view to these forbidden lines shows also different components. A high velocity component is understood as a stellar jet whereas a low velocity component is linked to denser regions often spatially extended and is interpreted as a disc wind. For high accretors, a hot helium wind is observed with the HeI 10830 Å in near IR (Edwards et al. 2006, Kwan & Edwards 2007). In this case, blueshifted absorption extends up to 400km.s^{-1} and is a good indication of stellar winds.

Synoptic studies of some CTTS such as AA Tau (Bouvier et al. 1999, 2003, 2007) seen nearly edge-on or TW Hya (Alencar & Batalha 2002) instead pole-on, show periodic changes in the lines shape over a rotation timescale (see Fig. 5) and even quicker on timescales of few hours like in RU Lup (Stempels & Piskunov 2002). Time delay of about 1 day between flux variations of different

[5] To avoid confusion with lines only shifted, the symmetry of the two wings of the line is checked (see fig10 in Alencar & Basri 2000).

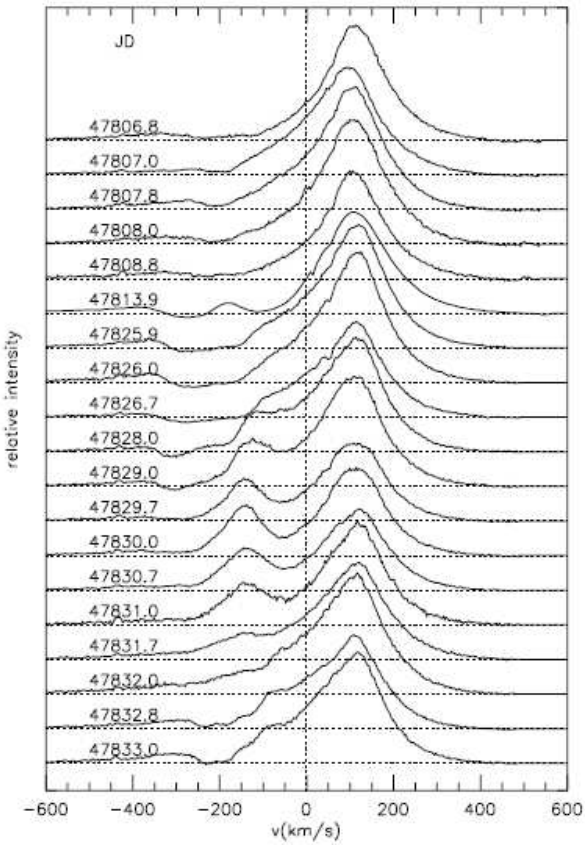

Figure 5. Evolution of an H_α line profile on a stellar period timescale with a modification of the blueshifted part. Julian time is given for each line (from Alencar et al. 2000).

lines forming at different altitudes from H_α till HeI are observed in AA Tau and compatible with a free fall motion of a bullet of matter along the magnetospheric field lines. Correlation between blueshifted and redshifted absorption components of the H_α line is also observed in AA Tau (see Fig. 6) which can be explained by a cycle of accretion and ejection due to the inflation of the magnetosphere.

§ 4. The issue of the slow rotation

One of the striking facts in low mass star formation regions is the observation of slow rotators ($P_* \sim 3-8$ days, Vogel & Kuhi 1981, Bouvier et al. 1995) like Classical T-Tauri Stars (CTTS) although they are pre-main sequence stars still in a contracting stage and while they are accreting rotating mass from their environment. This dynamic evolution seems to be controlled by the presence of a disc (see fig. 7) for most of these stars with $M_* > 0.3M_\odot$ since similar young stars without disc signature such as Weak-line T Tauri Stars are fast rotators (periods shorter by a factor 2-4, see e.g. Bouvier et al. 1993,1995, Kundurthy et al. 2006).

In the last two decades, a lot of wide field optical surveys were done making it possible to measure rotation periods of TTS in many open clusters such as the Orion one (ONC), NGC2264 and IC348 (e.g. Bouvier et al. 1995, Herbst et al. 2002, Lamm et al. 2005, Littlefair et al. 2005, Cieza & Baliber 2007). CTTS are generally slow rotators with periods longer that 2 days (for

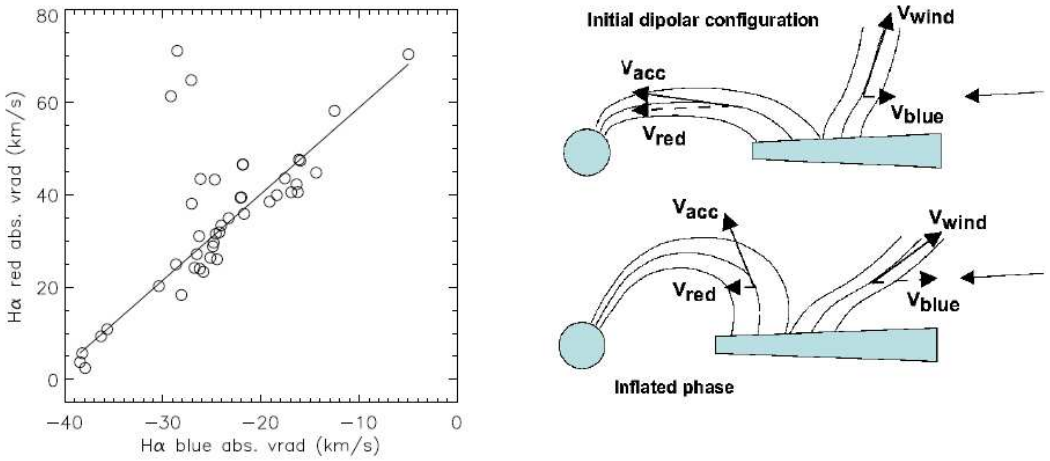

Figure 6. Correlation between the blueshifted and redshifted absorption components of the H_α line in AA Tau (from Bouvier et al. 2003). This can be explained by the expansion of the magnetosphere which increases the blueshifted velocities along the line of sight while the accretion is reduced.

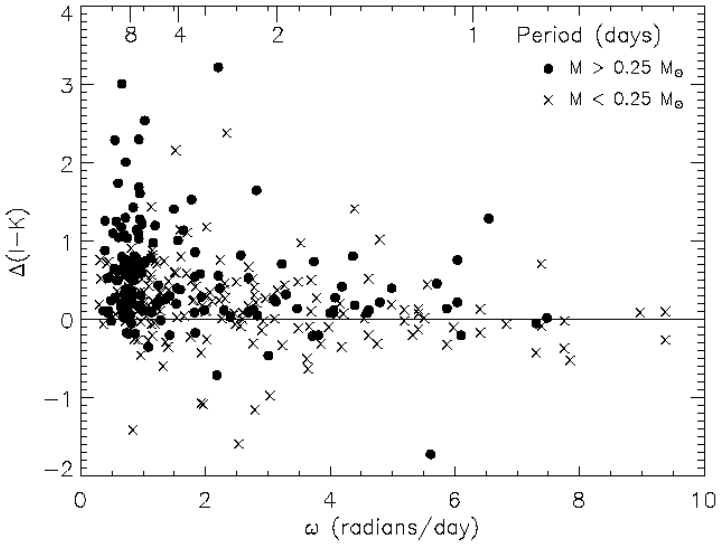

Figure 7. Infrared excess emission measured by I-K as function of the stellar angular velocity ω (or periods). One clearly observes a concentration of slow rotators with significant infrared excess for not too low mass stars (M>0.25 $M_\odot$) (from Herbst & al. 2002).

$0.3M_\odot < M < 1.25M_\odot$) corresponding to equatorial velocities around 15km.s^{-1} (Edwards et al. 1993). The period range is between 2 days (maximum for G2 stars) and inferior to 12 days (maximum for K7-M0 stars). Thus, we do not have very slow rotators like the Sun. For stellar mass range greater than 0.3 $M_\odot$, the period distribution is clearly bimodal with peaks near 2 days for WTTS and 8 days for CTTS in the ONC and near 1 and 4 days in the two times older NGC2264 (see Fig. 8). This spinning-up in the older cluster can be explained by the stellar contraction. However, Stassun et al. (1999,2001) or Rebull (2001) did not find clear clues for this bimodal distribution and correlation between slow rotators and evidences for the presence of accretion discs, contrary to observations from Bouvier et al. (1993) and more recently Cieza &

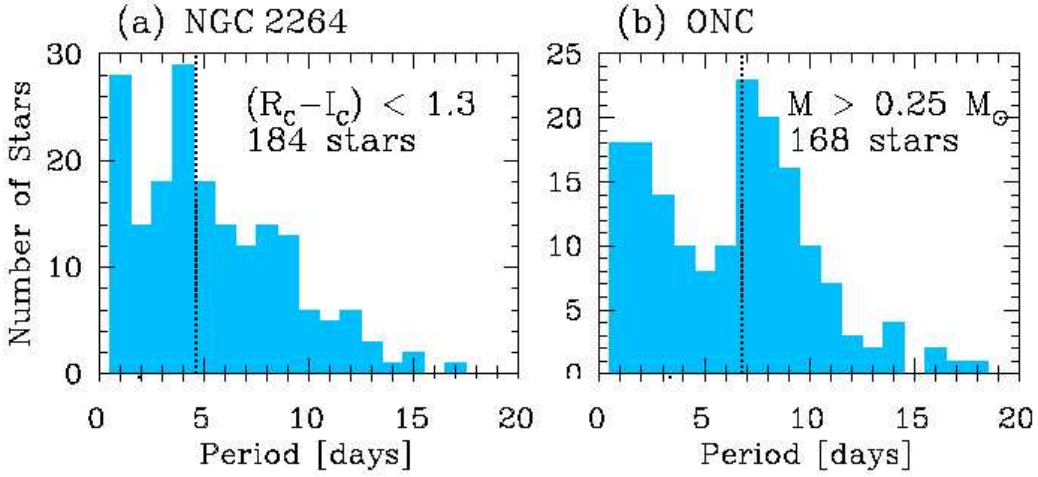

Figure 8. Rotation periods distribution function in NGC 2261 (a) and the Orion Nebula Cluster (b) for the stellar mass range $M_* \sim 0.25 - 1.2 M_\odot$ (from Herbst et al. 2007).

Baliber (2007). Herbst et al. (2002) explain the discrepancy about the rotation period distribution by the fact that the sample in the Orion nebula taken in Stassun et al. (1999,2001) has a large mass range including very low mass stars ($M < 0.25 M_\odot$) which are always fast rotators with a peaked period distribution around 2 days, perhaps because of the shorter disc lifetime around these stars. However, a systematic link between slow rotators and the presence of discs is still debating in the literature mainly due to difficulties to find enough reliable proxies for detecting correctly such discs via global criteria such as IR excess.

There are different techniques to deduce projected rotational velocities on the line of sight $v_{rot}.sin(i)$ as discussed in Bouvier et al. (1986). The classical one is to use cross correlation of rotational broadened lines from the absorption photospheric spectrum [6]. The rotation value is obtained by dividing the Fourier Transform (FT) of a mean broadened line by the FT of a line from a stellar template with the same spectral type and a very low rotation. The sources of uncertainties in a decreasing order of importance are : the amount of veiling, differential rotation effects, magnetic effects ... A more indirect technique is to use the light curves obtained in broad band photometry (Bouvier et al. 1993,1995, Stassun et al. 1999). In this case, one avoids the uncertainties on the inclination effect and the stellar radius estimate, but it is not 100 % reliable because the modulation of the flux depends on the source position producing this variability with respect to the stellar surface. This can be caused by stellar activity (spots remaining during several periods) but also by the warped inner edge of the accretion disc where accreted matter is lifted up. In the latter case, we have to hope it is localized near corotation otherwise we do not correctly assess the rotation. To assess the reliability of this method, the correlation between the rotational velocity measured and the FWHM of a photospheric line such as Li(6700 Å) can be checked.

[6] The quicker the star rotation is, the larger the FWHM of the line is and the lower the intensity of its maximum is for energy conservation reasons.

To give some order of magnitude, we calculate the period of a T Tauri star of 0.8 $M_\odot$ and 2 $R_\odot$ at 10% of the breakup speed ($k = \frac{\Omega_*}{\Omega_K} = 0.1$) with Ω_* for the stellar angular velocity :

$$P_* = 3.7 \left(\frac{k}{0.1}\right)^{-1} \left(\frac{M_*}{0.8M_\odot}\right)^{-\frac{1}{2}} \left(\frac{R_*}{2R_\odot}\right)^{\frac{3}{2}} \text{days} \tag{4.2}$$

To have a 8 or 10 days period corresponding to the distribution peak of CTTS, the same star has to rotate respectively at 4.6% or 3.7 % of the breakup speed [7]. Thus, efficient physical processes are needed to provide enough angular momentum losses. This is what is called the angular momentum problem since the specific angular momentum of molecular cloud cores is 5 orders of magnitude higher than low mass stars on the ZAMS (e.g. Bodenheimer 1995). Theoretical models try to include disc and stellar winds but also a large scale interaction between the star and the disc to solve this issue. But to do a long term evolution study from pre-main sequence stars till main sequence stars, it is really important also to take into account the changes of internal structure of these stars during their contraction (e.g. the appearance of a radiative core which modifies the stellar moment of inertia) as demonstrated in Keppens, Mac Gregor & Charbonneau (1995) who study the effects on the stellar period distribution function of different dynamo laws (B_* proportional to Ω_* or saturated) and different core/convective coupling time in the case of stellar wind bringing away angular momentum from the star. They particularly found the necessity of including a fraction of 'disc-locking' systems lasting $\sim 10Myr$ in the initial period distribution to explain further evolution towards solar type ages with a majority of very slow rotators. Bouvier et al. (1997) also found this necessity by assuming solid rotation at a constant rate for a disc lifetime distribution initially, next purely stellar contraction and then a classical solar type wind braking from the ZAMS. Star-disc interaction needs to extract around a third of the stellar angular momentum per Myr to explain the further evolution along the main sequence (Bouvier 2007). Chapter 5 of this thesis will tackle this issue by looking at the possibility to have such a disc-locking state.

§ 5. Stellar Magnetic field constraints

Magnetic field measurements on stars are really difficult. They are done using the Zeeman effect which gives a splitting of a spectral line λ_0 (in Å) into several components shifted in wavelength by $\Delta\lambda$ due to the presence of a magnetic field of strength B (in G) : $\Delta\lambda = 4.67 \times 10^{-13}\lambda_0^2 g_B B$ where g_B is the Landé factor providing the sensitivity of the considered line with respect to the magnetic field. The shifted components σ are circularly polarized with opposite directions and the central one is linearly polarized. Zeeman broadening measurements are done above all in the IR to overpass Doppler broadening effects because it grows with λ^2. The most common line used is the Ti I at 2.2 μm. It is necessary to well assess temperature and rotation to disentangle magnetic effects from classical ones using insensitive lines such as CO at 2.35 μm. This technique is sensitive to the distribution of the magnetic field strength but not to its topology. To probe the magnetic topology, we need to measure circular polarization for individual spectral lines and thus use very high resolution spectra ($\frac{\lambda}{\Delta\lambda} > 50000$) obtained by spectropolarimeters such as ESPADON at CFHT or Narval at the Pic du Midi. In this high

[7] Note the strong dependence on the stellar radius. If we have a younger star with $R_* = 3R_\odot$, an 8 day period star corresponds to 8.5 % of the breakup speed.

resolution technique, circular polarization signatures from different regions of the photosphere seen in absorption do not cancel (because they have different Doppler shifts resolved in spectrum due to the stellar rotation) and can be detected by accumulating signal of different magnetically sensitive lines with a least squares deconvolution. By following the evolution of polarization over a stellar period, it is possible to reconstruct the topology of the magnetic field at the stellar surface (Donati et al. 2007).

There are direct proofs of kG fields (Basri, Marcy & Valenti 1992, Guenther et al. 1999, Johns-Krull & Valenti 2000) with mean photospheric field between 1 and 3 kG (see Fig. 9). Thus, TTS are strongly magnetized much more that the Sun since they have lower surface gravity by typically an order of magnitude.

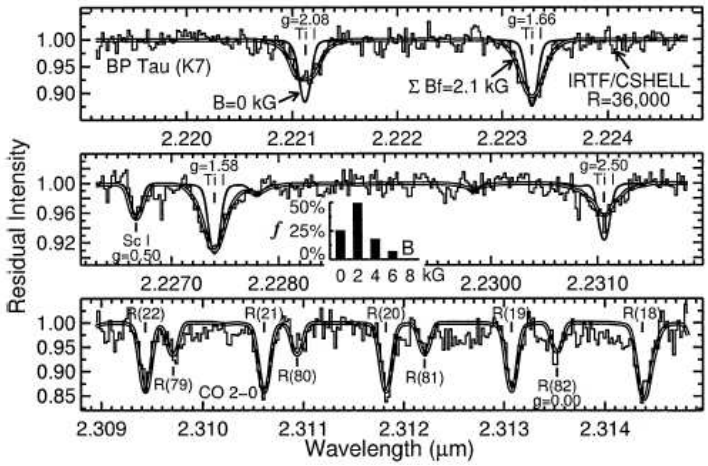

Figure 9. Spectrum of BP Tau (histogram) with a fitted magnetic model (double line) taking into account a distribution of magnetic field strength reaching 6 kG with different filling factors and with a mean field of 2kG covering half of the stellar surface (from Valenti & Johns-Krull 2004). One can notice that a non magnetic model (single line) does not explain the broadening of Ti I lines but agrees for CO lines.

However, polarization from photospheric lines in these stars is really weak since we still have almost an upper limit around 200G (Johns-Krull & Valenti 2001, Smirnov et al. 2003,2004, Valenti & Johns-Krull 2004). Actually, we measure magnetic field around 1-3 kG in the spots at the Sun surface but these regions correspond to closed field lines with no net longitudinal component with respect to the line of sight, which thus do not contribute to net polarization for spatially unresolved observations of other stars. The large scale solar magnetic field is as low as 4 G ! In CTTS, significant net circular polarization is detected only in emission lines near the accretion shock in HeI and CaII IR triplet lines since magnetic field lines with the same polarity are isolated in an accretion column. Magnetic field strength for the longitudinal component within the funnel flow is found to be similar to the mean magnetic field strength (Valenti & Johns-Krull 2004). However, elsewhere on the stellar photosphere, circular polarization due to large scale magnetic field measured in photospheric absorption lines such as FeI are very low giving a magnetic field often lower than 200 G (see Fig. 38 in Chap. 4). This contradiction could be explained in different ways. First, the magnetic stellar surface is really complex and not dipolar with some strong unipolar field tubes going from the stellar surface and connecting to the disc inner edge. Otherwise, one could have amplification of magnetic field in the shock where

the HeI line is formed (all current studies consider shocks in the hydrodynamic case within the funnel flow) or we could have an high obliquity between the magnetic field axis and the rotation axis which would be in favour of intrinsic dipolar kG fields since many stars are seen rather pole-on (Smirnov et al. 2005).

Thus, the current trend is to consider only weak large scale structure magnetic field and a much more complex structure including multipolar components at smaller scales as the extrapolations of magnetograms done by Gregory et al. (2006) using force-free approximation suggest (see Fig. 10). For instance, Safier (1998) already criticized magnetospheric accretion models for not including the effects of a realistic stellar corona such as a stellar wind which would blow open most of the closed field beyond $\sim 3R_*$. Very recently using spectro-polarimetric data from ESPADONS, Donati et al. (2007a,b) tune down this trend by finding a strong dipolar component of 1.2 kG around BP Tau still fully convected and a lower dipolar component of 350 G around V2129 Oph which is more evolved with the presence of a radiative core. But a larger sample of stars is needed to draw a firm conclusion on the magnetic field topology around CTTS.

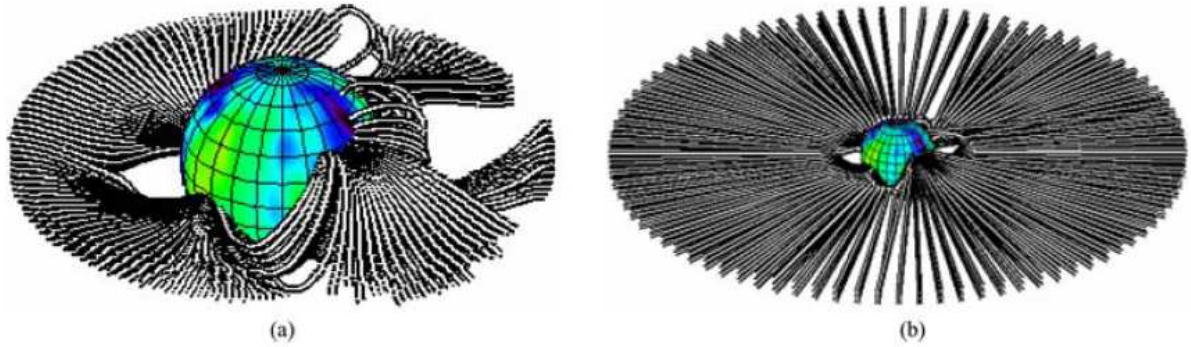

Figure 10. Magnetic field lines extrapolation for a CTTS that resembles LQ Hya (a) or AB Dor (b) (from Gregory et al. 2006).

X-ray flux levels about thousand times the solar one (Montmerle et al. 1993, Feigelson & Montmerle 1999) indicate very intense coronal activity. Correlation with the stellar angular velocity of this activity (Damiani & Micela 1995, Stelzer & Neuhäuser 2001) stresses also a highly time dependent magnetosphere and supports a dynamo origin, although these stars are fully convective. Particularly, accreting T Tauri stars have lower X-ray emission. Recently, high resolution X ray spectra obtained with the space telescopes Chandra and XMM-Newton show that the accretion shocks produce soft X rays (Günther et al. 2007).

2. Theoretical background of the star-disc interaction

Previously, we have emphasized the observational constraints characterizing the accretion process around T Tauri stars. Now, we present the theoretical framework to take them into account by firstly explicit the basic components of the magnetic interaction theory between a central object and a surrounding accretion flow considering a large scale interaction zone. Then, we describe constraints allowing steady-state funnel flows corresponding to solutions to the Bernoulli equation. Next, we tackle the influence of disc conductivity on the star/disc

connectivity and the resulting angular momentum balance achieved. Finally, we present alternative ways to solve the angular momentum issue by having powerful stellar jets or Reconnection X winds (ReX).

§ 6. The global picture of an extended star-disc interaction

The magnetic interaction between an accretion flow and a central object was first studied in the context of accreting neutron stars (Ghosh & Lamb 1978, Scharlemann 1978). Actually, some accreting X-ray sources such as Her X-1 or Cen X-3 show spinning-down episodes, in addition to their secular spin-up that one can not explain without taking into account the stellar magnetic field.

First, one can wonder which topology for the magnetic field to take into account in models. This ultimately relates to the fundamental origin of the magnetic field in astrophysical objects. Nearly all the analytical studies assume a dipolar stellar magnetic field aligned with the stellar rotation axis (perpendicular to the disc midplane). The main reason is the simplification in the calculations but we can argue that we are interested in large scale magnetic interaction and that all the multipolar components decrease quicker than the dipolar one. Ghosh & Lamb (1979), Goodson et al. (1999), Matt & Pudritz (2004) consider such a magnetic topology with no proper disc magnetic field. The initial penetration of the stellar field inside the disc is also not tackled in models. Ghosh & Lamb claim it can be the result of diffusive instabilities but without further quantification, the resulting magnetic field is prescribed to remain dipolar. Otherwise, Rekowski & Brandenburg (2004) consider a dynamo origin for the disc magnetic field but a fossil origin can also be argued coming from the advection of the magnetic flux from the primordial molecular cloud (Hirose et al. 1997, Miller & Stone 1997) or from the opening of the stellar magnetosphere as claimed by Shu et al. (1994). Safier (1998) points out the need for an inherent time dependent magnetosphere coupled with a complex topology and concludes that consistent models explaining the low rotation periods are far from achieved.

Let us now have a look to the magnetic star-disc connection itself. Analytical models consider a force-free atmosphere above the disc corotating with the star. The differential rotation along a field line connecting the star to the disc then builds a toroidal magnetic field B_ϕ within the disc which can not increase too much because of the ever growing current sheet built up in the equatorial plane causing eventually reconnection. The physics of reconnection is still partially understood since the Sweet-Parker and Petshek models are not able to quantify correctly important quantities such as the dissipation of energy or the reconnection rate which vanish when the resistivity tends towards zero. Recent progress considering sub MHD scale processes imply decoupling between electrons and ions described by the Whistler dynamics and show that efficient and fast reconnection is possible (Shay et al. 2001). Analytical estimates consider a critical pitch angle $\gamma_c = \frac{B_\phi}{B_z}$ close to unity beyond which reconnection appears above the disc (see the numerical work of Udzensky et al. (2002) and references therein). In the outer parts of the disc in the case of no proper disc magnetic field and thus no possible ejection, one can consider an unmagnetized standard accretion disc since the stellar magnetic field decreases very quickly with the radial distance and becomes negligible beyond r_S. When one approaches the central object, the magnetic stresses become more important and finish by dominating the accretion flow.

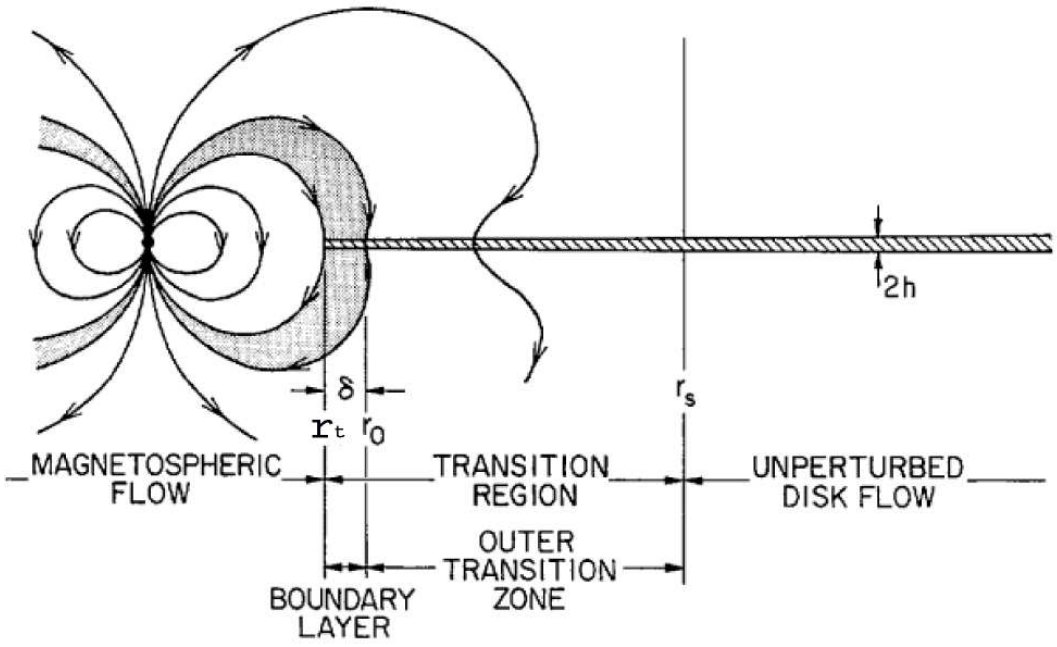

Figure 11. Schematic picture of the Ghosh & Lamb model (adapted from Ghosh & Lamb 1978).

Usually, one defines the Alfvén radius r_A in case of spherical accretion as the radius where the total (ram+thermal) matter pressure is balanced by the magnetic pressure of the central object (Elsner & Lamb 1977). This balance derives from the Bernoulli invariant where we suppose a force-free magnetic field with $B_\phi \ll B_p$ and $v_\phi \ll v_p$.

$$\frac{B^2}{8\pi} = \frac{1}{2}\rho v_R^2, \tag{6.3}$$

where $4\pi R^2 \rho v_R = \dot{M}$. Thus, $B^2 = \frac{\dot{M}}{R^2} v_R$. The minimum Alfvén radius is obtained for free-fall speeds $v_R = \sqrt{\frac{2GM}{R}}$. By assuming a dipole field $B = B_*(\frac{R_*}{R})^3$, we finally have :

$$r_A = B_*^{\frac{4}{7}} \dot{M}^{-\frac{2}{7}} (2GM_*)^{-\frac{1}{7}} R_*^{\frac{12}{7}}. \tag{6.4}$$

In physical units, one obtains :

$$\frac{r_A}{R_*} = 7.2 (\frac{B_*}{1000G})^{\frac{4}{7}} (\frac{\dot{M}}{10^{-8} M_\odot yr^{-1}})^{-\frac{2}{7}} (\frac{M_*}{0.8 M_\odot})^{-\frac{1}{7}} (\frac{R_*}{2R_\odot})^{\frac{5}{7}} \tag{6.5}$$

But in accretion discs, the ram pressure is much greater for the same accretion rate because of the concentration of mass within a small solid angle around the star except if one really considers accretion at sonic speed (since an accretion disc is rotationally supported). We will discuss that point in chapter 4 of this thesis.

Ghosh & Lamb (1978,1979) study this transition region by assuming the slippage of the magnetic field lines through reconnection with $\gamma_c = 1$. Thus, one has a large scale interaction between r_A and r_S (see Fig. 11). The vertical mass loading onto magnetospheric field lines is prescribed and scaled by the local sound speed and follows an ad-hoc parabolic function which cancels outside r_0 and is equal to unity at r_t. They assume an hydrostatic vertical equilibrium neglecting magnetic pressure effects and the mass outflow. They consider that the

disc temperature at the transition is dominated by the ohmic heating. By solving numerically the radial momentum equation with the above constraints and neglecting viscosity, they found a boundary layer at $r_t = 0.41 r_A$ with a width $\delta \sim 0.03 r_A$. This corresponds to a change from Keplerian motion to corotation with the star. Inside the magnetosphere, the magnetic field is weakly distorted since the magnetic energy increases towards the star as r^{-6} much quicker that the matter energy as $r^{-\frac{5}{2}}$.

Finally, one can calculate the resulting magnetic torques acting on the star due to this large star-disc connection between r_t and r_S. An important radius is the co-rotation radius $r_{\rm co} = (GM_*/\Omega_*^2)^{1/3}$ where Ω_* is the stellar angular velocity, which corresponds to a position where the disc material rotates at the same speed as the star. The stellar field lines threading the Keplerian disc below the co-rotation radius would lead to a spin up of the star, whereas those beyond $r_{\rm co}$ to a spin down. For slow rotators ($r_t << r_{\rm co}$), we will have a global spin up. For sufficiently fast rotators ($\Omega_* > 0.4\Omega_A$ from Ghosh & Lamb 1979) corresponding to a truncation radius close to the corotation one ($r_t/r_{\rm co} > 0.54$), one can obtain a global spin down. For a given stellar rotation rate, one can have alternative periods of spinning-up and spinning-down due to the accretion rate variation. Beyond $r_{\rm co}$, one needs a dominant turbulent torque to have a consistent accretion flow till the disc inner edge since the magnetic torque tends to accelerate disc material in that case but Bardou & Heyvaerts (1996) argue that this leads to diffusion of the magnetic flux outwards. Otherwise, Aly & Kuipers (1990) propose that the excess of angular momentum coming from the star could be transported outwards by extended shock waves which are formed by the acceleration of matter by the magnetic torque beyond and not too near $r_{\rm co}$, in the case of negligible viscous stress.

§ 7. Variability of the disc truncation radius

Many authors argue that the disc truncation happens when the magnetic field overpasses the gravitational energy which demands a strong field to stop the accretion playing the role of a physical wall, typically greater than kilo Gauss as already deduced above from the Ghosh & Lamb model. We will focus on this topic in chapter 4 of this thesis and will demonstrate that equipartition between the thermal pressure and the magnetic one is sufficient and can be achieved for relevant stellar magnetic field strength $B_* \sim 140G$ and accretion rate $\dot{M} \sim 10^{-9} M_\odot yr^{-1}$ in the context of CTTS.

But, generally these analytical considerations are not sufficient to identify precisely the truncation radius at any time because it undergoes some variations owing to the accretion flow (see the effect of viscosity in Chap. 5) or some instability which can develop at this transition between the magnetosphere and the accretion disc. We will focus here on some possible instabilities. There is the interchange (also known as Kruskal Schwarzschild) instability which is the magnetic equivalent of the hydrodynamic Rayleigh Taylor one (Baan 1977,1979). Actually the denser accretion disc tends to diffuse due to gravity through the lighter magnetosphere but there are the stabilizing magnetic tension and buoyancy which counteract. Accumulation of mass happens in the disc midplane till the instability is triggered and a large blob of matter accretes directly onto the star. This instability is efficient only well below corotation. Recent 3D simulations by Kulkarni & Romanova (2007) show such a kind of instability at the disc inner edge (see chapter 2). When the effective gravity becomes weaker near the corotation, there

are possible ballooning mode interchange driven for instance by an inward pressure gradient (Spruit & Taam 1993). There is also Kelvin-Helmholtz instability since material inside the magnetosphere corotates with the star contrary to accretion flow at sub-Keplerian speeds. Most of these instabilities can only be studied in extremely high resolution 3D simulations and this is beyond the scope of this thesis. Hence, we will mostly assume rather stationary conditions for the truncation radius in the following.

§ 8. The physics of stationary funnel flows

One of the most striking points of the star-disc interaction is the formation of accretion columns or accretion curtains in the axisymmetry framework. A necessary condition to have such a non equatorial accretion is to disrupt the accretion disc beyond the stellar radius as discussed previously. Then, one can understand magnetospheric accretion in ideal MHD as an accumulation of matter at this disc inner edge since matter can not cross the magnetic surface which finishes by pouring along magnetic field lines when the effective gravity points inwards.

Without taking into account the process of the mass loading onto the closed magnetic field lines (the accretion physics is considered as a boundary condition), Ostriker & Shu (1995), Li & Wilson (1999) and Koldoba & al (2002) study the constraints given by the Bernoulli equation to have a steady state solution of a funnel flow in ideal MHD conditions. The equations for the funnel flows are :

$$\nabla \cdot (\rho \mathbf{v}) = 0\,, \tag{8.6}$$

$$\nabla \cdot (\rho \mathbf{v}\mathbf{v} - \mathbf{B}\mathbf{B} + P_{tot}\mathbf{I}) = 0\,, \tag{8.7}$$

$$\nabla \times (\mathbf{v}\mathbf{B} - \mathbf{B}\mathbf{v}) = 0\,. \tag{8.8}$$

One assumes a barotropic equation of state $P = P(\rho)$. By splitting the poloidal and toroidal components, we write :

$$\mathbf{v} = \mathbf{v}_p + \Omega r \mathbf{e}_\phi\,, \tag{8.9}$$

$$\mathbf{B} = \mathbf{B}_p + B_\phi \mathbf{e}_\phi\,, \tag{8.10}$$

$$\tag{8.11}$$

By integrating equations 8.6-8.8 along a magnetic field line as it is done in MHD wind theory, one obtains $\mathbf{v}_p \times \mathbf{B}_p = 0$ and one has the 4 classical MHD invariants :

$$\kappa = \frac{\rho V_p}{B_p}\,, \tag{8.12}$$

$$\Omega_* = \Omega - \frac{\kappa}{\rho r} B_\phi\,, \tag{8.13}$$

$$\lambda = \Omega r^2 - r\frac{B_\phi}{\kappa}\,, \tag{8.14}$$

$$E = \frac{1}{2}(v_p^2 + r^2(\Omega - \Omega_*)^2) + \int \frac{dP}{\rho} - \frac{GM}{r} - \frac{1}{2}\Omega_* r^2\,, \tag{8.15}$$

$$\tag{8.16}$$

κ is the mass loading rate per magnetic flux unit, Ω_* can be interpreted as the rotation rate of a magnetic surface and corresponds to a frame where the electric field is cancelled. It usually corresponds to the stellar rotation rate. λ is the specific angular momentum in the funnel per magnetic flux unit and E is the Bernoulli equation corresponding to the fluid energy per unit of mass which is calculated in the frame which corotates with the curtain.

The magnetic shear within the funnel flow is thus given by combining the invariants κ and Ω_* :

$$\frac{B_\phi}{B_p} = \frac{\Omega r}{v_p}\frac{(\Omega - \Omega_*)}{\Omega} \tag{8.17}$$

It depends on both the ratio of toroidal to poloidal velocities and the relative angular velocity shear. Thus, large poloidal velocities tend to reduce the magnetic torque on the star but the flow velocity is imposed by the disc accretion physics. The same trend is achieved if the accreted matter within the funnel flow tends to corotate with the star which depends on the stellar boundary conditions. Contrary to classical models such as the Ghosh & Lamb (1978) or Matt & Pudritz (2005) ones where a force-free corotating magnetosphere with the star is considered, the magnetic torque is not localized at the disc/corona interface but is distributed along the magnetic field line allowing a differential rotation between the disc surface and stellar boundary conditions. Thus, one has a strong relation between the disc accretion rate, the magnetospheric accretion and magnetic torques due to ideal MHD equations and finally a possible different angular momentum balance from classical models considering separately accretion and magnetic torques.

By combining the invariants Ω_* and λ, one deduces the expressions for Ω and B_ϕ for a steady state depending only on boundary conditions via the chosen values for λ, κ and Ω_* :

$$\Omega = \frac{\Omega_* + \lambda r^2 \frac{v_p}{B_p}}{1 - M_{a,p}^2}\,, \tag{8.18}$$

$$\lambda\kappa = \Omega r^2 \kappa - r B_\phi\,, \tag{8.19}$$

$$B_\phi = \frac{1}{r}\frac{\lambda + 4\pi\kappa\Omega_* r^2}{1 - M_{a,p}^2}, \tag{8.20}$$

$$E = \frac{1}{2}(v_p^2 + r^2(\Omega - \Omega_*)^2) + \int \frac{dP}{\rho} - \frac{GM}{R} - \frac{1}{2}\Omega_*^2 r^2\,, \tag{8.21}$$

where $M_{a,p}^2 = \frac{4\pi\kappa^2}{\rho}$ is the square of the poloidal Alfvén Mach number.

Next, one can express the Bernoulli equation as function of ρ and R along a field line from 8.21 :

$$E = \frac{1}{2\rho^2}\kappa^2(B_p^2 + B_\phi^2) + \int \frac{dP}{\rho} - \frac{GM}{R} - \frac{1}{2}\Omega_*^2 r^2. \tag{8.22}$$

With this expression, one clearly sees the magnetic energy term. Along a pure dipolar magnetic field, one has $R = R_0 sin^2\theta$ and $B_p = \frac{\mu}{R^3}\sqrt{4 - 3sin^2\theta}$ thus :

$$E = \frac{1}{2\rho^2 R^6}\kappa^2\mu^2(4 - 3\frac{R}{R_0}) + \frac{1}{2\rho^2}\kappa^2 B_\phi^2 + \int \frac{dP}{\rho} - \frac{GM}{R} - \frac{1}{2}\Omega_*^2\frac{R^3}{R_0}. \tag{8.23}$$

One can first have a look to the effective potential $V_{eff} = -\frac{GM}{R} - \frac{1}{2}\Omega_*^2 r^2$ to find which dipolar field lines allow direct magnetospheric accretion by considering two cases : (1) a rigid rotating funnel flow corotating at the stellar speed and (2) a differentially rotating funnel flow going smoothly from Keplerian rotation for the footpoint anchored into the disc to the stellar rotation

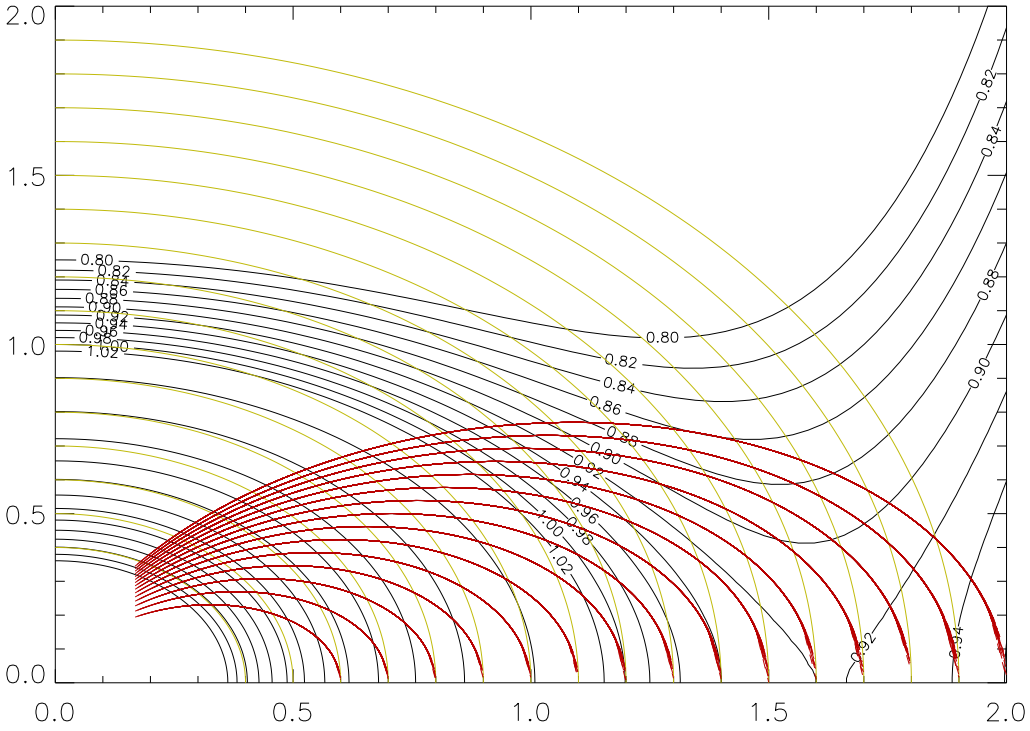

Figure 12. Equipotential lines (black lines) in the (r,z) plane for the effective gravity in the case of a rigid rotation of the magnetosphere. The values represent the opposite of the effective potential. We identify the corotation at 1.6. The red lines corresponds to magnetic field lines for a pure dipolar field and the brown lines represents circles. Along a given field line, accretion is possible if the opposite of the effective gravity keeps increasing from the equatorial plane towards the star. We find that polar accretion is possible only for $r \leq 1.4$ corresponding to $r_t < 0.875 r_{\rm co}$.

due to a non negligible magnetic torque within the funnel ($B_\phi \neq 0$). In this study, one obtains an upper constraint on the truncation radius defined as the position where polar accretion is allowed till the stellar surface by the effective potential. In case (1), we find that magnetospheric accretion is allowed for $r_t < 0.875 r_{\rm co}$ (see Fig. 12). In case (2), for a disc Keplerian velocity two times greater than the stellar one (considering a smooth rotational function linking these boundary conditions along a dipolar field line), we find $r_t < 0.69 r_{\rm co}$ (see Fig. 13).

Now, one considers the complete Bernoulli invariant. Li & Wilson (1999) assume that the funnel is isothermal such that $\int \frac{dP}{\rho} = c_s^2 \ln \frac{\rho}{\rho_d}$. They looked for solutions where disc material can reach the star through accretion curtains and which satisfy the Bernoulli equation. They assume a non zero B_ϕ such that the magnetic torque extracts the total angular momentum of the disc matter as in Ostriker & Shu (1995) corresponding to $\lambda = 0$ i.e. $B_\phi = \frac{4\pi\kappa\Omega_* r}{1-M_{a,p}^2}$. The Bernoulli equation written in adimensional units is thus :

$$E' = A(u^2 - 2\ln(u) + 2ln(\frac{B_p}{B_{p,d}}) + 2\ln(M_{s,d})) + \frac{1}{2}C^2 r'^2 \frac{2M_{a,p}^2 - 1}{(1-M_{a,p}^2)^2} - \frac{1}{R'}, \qquad (8.24)$$

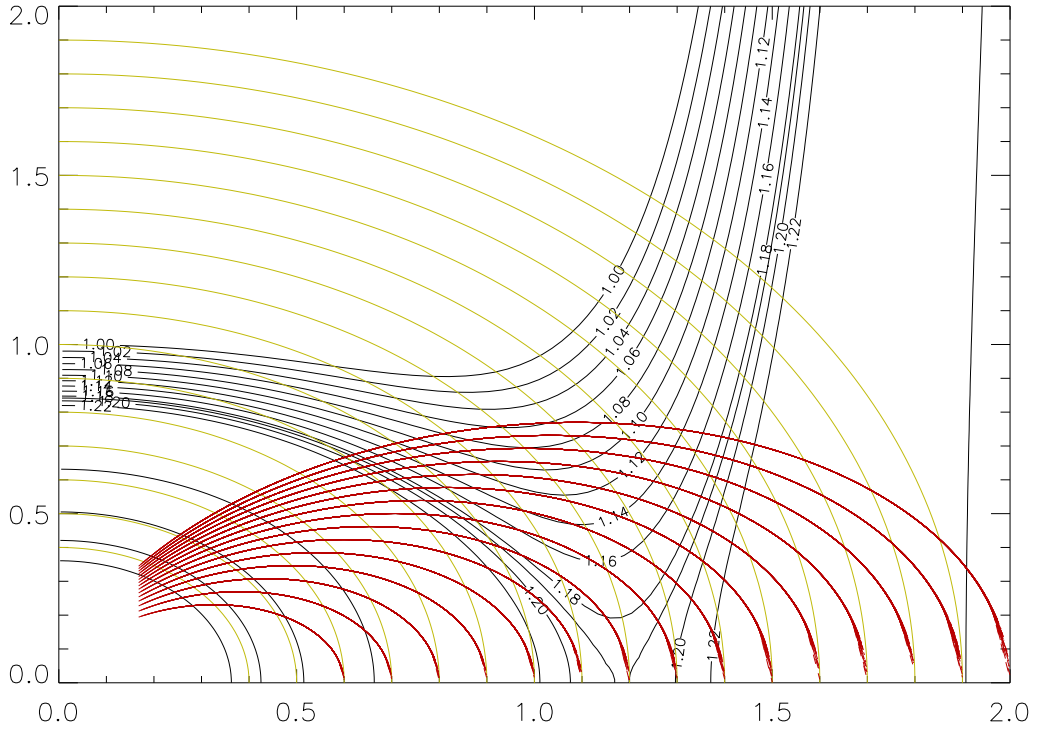

Figure 13. Equipotential lines (black lines) for the effective gravity V_{eff} in the case of differentially rotating magnetic field lines with the same legend as in Fig. 12. The polar accretion is possible here only for $r \leq 1.1$ corresponding to $r_t < 0.69 r_{\rm co}$.

where $E' = \frac{E}{v_{K,d}^2}$, $r' = \frac{r}{r_d}$, $R' = \frac{R}{r_d}$, $u = \frac{v_p}{c_s}$, $A = \frac{1}{2}(\frac{c_s}{v_{K,d}})^2$, $C = (\frac{\Omega_*}{\Omega_{K,d}})^2 = (\frac{r_t}{r_{co}})^3$. If one considers a very sub-Alfvénic flow ($M_{a,p} \sim 0$), the Bernoulli equation is equivalent to the case of a rigid rotating curtain at the stellar rate. We study again the topology of the Bernoulli equation like in their paper by drawing isocontours of E′ in the (u,s_d) plane where $s_d = 1 - R'$ is the complement to the spherical radius along a dipolar field line as function of the disc temperature characterized by A and the position of the field line footpoint r_t with respect to the corotation caracterized by C.

Solutions with pure poloidal dipole field are possible only well below the corotation radius ($r_t < 0.84 r_{\rm co}$ or $\Omega_* < 0.77 \Omega_{K,d}$ i.e. $C \leq 0.6$; see Fig. 14) and with a sufficient thermal pressure at the disc boundary condition characterized by the disc aspect ratio $c_s/v_{Kd} > 0.04$ i.e. $A > 10^{-3}$ in order to have sufficient negative effective gravity to reach the sonic critical point in the funnel before the stellar surface.

Actually, solutions with magnetospheric accretion nearer to the corotation implies initial velocities at the funnel base highly supersonic (see Fig. 15) which is in contradiction with rotationally supported accretion flows. However, one can tune down a bit the constraint on C since one considers here ideal MHD conditions till the disc midplane while accretion within the disc is described by resistive MHD where accretion is not constrained to be parallel to the field. Thus, the transition is at several disc scale height. Besides, the scale height at the truncation of

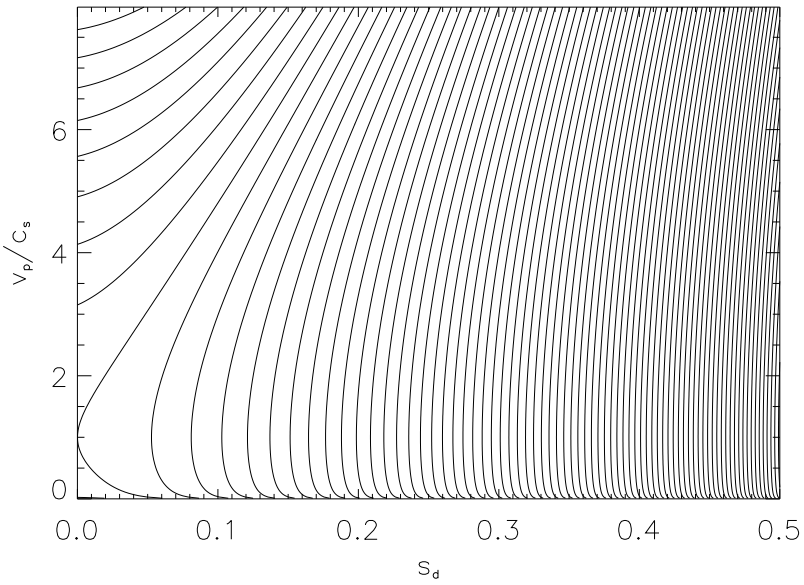

Figure 14. Contour of the normalized Bernoulli integral E' for a disc with an aspect ratio 0.054 ($A = 1.5 \times 10^{-3}$) and a magnetic field line anchored below the corotation ($C = 0.6$) as function of the Mach sonic number and the distance along the funnel flow in units of $s_d = 1 - R'$. The disc midplane corresponds to $s_d = 0$ and the stellar surface is on the right side. The sonic point corresponds to the saddle point which is localized at the disc midplane. We find solutions for initial sonic speeds.

the disc is expected to be bigger than the one chosen for the initial unmodified disc due to the compression of matter at this inner edge. One draws again the isocontours of E' by modifying the horizontal scale now in units of the disc scale height h which corresponds to do a zoom in previous plots such as Fig. 14. One can find transonic solutions with initial speeds near sonic but subsonic speeds till $C \sim 0.7$ which reach the sonic point localized at 2h (see Fig. 16).

However, in any case, this condition on C entails a distorted poloidal dipolar field by accretion at the base of the funnel which prevents the mass loading even for small distortion as low as $\frac{B_r}{B_z} \sim 0.01$ due to magnetic compression. Actually, from the energetics requirements, this produces a potential sink in the Bernoulli equation. We observed such a poloidal field deformation in our simulations shown in Chapter 4 but one has the compression of the disc matter at the truncation radius which enhances the thermal pressure and makes it possible to form accretion funnels. This effect is not considered in the Li & Wilson paper. Thus, to find steady-state accretion columns, they consider another levitation force to have magnetospheric accretion such as the gradient of B_ϕ. This is relevant in the case of near-Alfvénic flow ($M_{a,p}^2 \leq 1$) and they found solutions for initial Mach number within the disc around 0.1 and $0.22 < M_{a,p}^2 < 0.7$ by considering the case $r_t = r_{\rm co}$ to still use a pure poloidal dipolar field. Thus, the Bernoulli equation gives a constraint on the possible $M_{a,p}$. But they do not consider the effect of large B_ϕ on the accretion process which particularly has the trend to produce non stationary solutions due to opening of the magnetic field.

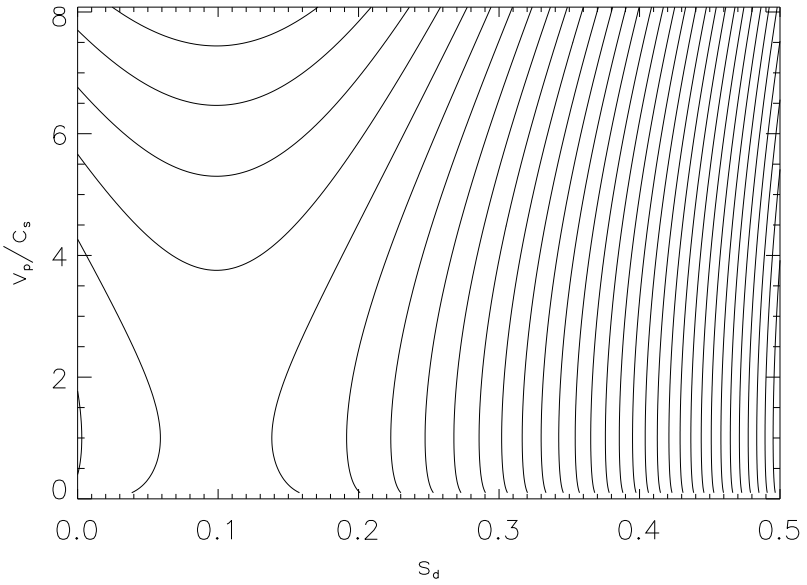

Figure 15. Contour of the Bernoulli integral for a disc with an aspect ratio 0.054 ($A = 1.5 \times 10^{-3}$) and a magnetic field line anchored at corotation ($C = 1$). We now find solutions only for initial supersonic speeds with a sonic Mach number higher than 5.

Koldoba & al. (2002) consider a polytropic equation of state with a constant entropy within the funnel flow. They analyse the critical sonic point in the Bernoulli invariant. They also consider a sub-Alfvénic flow such that $\frac{B_\phi}{B_p} \ll 1$ and find conditions to have transonic flows. They obtain this is possible only for a limited radial range around the corotation radius. For instance, for a thin disc with a disc aspect ratio $\epsilon = 0.1$ and $\gamma = \frac{5}{3}$, they find $0.873\, r_{\rm co} < r < 0.971 r_{\rm co}$. The lower limit is due to the constraint on the sonic point to be outside the disc. The upper limit is caused by the necessity to have enough disc thermal pressure to accelerate matter at the funnel base in order to reach the sonic point before the stellar surface. The hotter the disc is, the further this latter limit is. It is even possible to have transonic funnel flows a bit beyond corotation for $c_{sd} > 0.08 v_K(r_{co})$. But for $r > 1.25 r_{co}$, only transient accretion flows are possible.

One can remark that the energy reservoir in the isothermal regime is lower than the adiabatic regime $\int \frac{dP}{\rho} = \frac{c_{s,d}^2}{\gamma - 1} \left(\frac{\rho}{\rho_d}\right)^{\gamma - 1}$ and that is why it is necessary to have truncation radius well below corotation to have possible funnel flow in this case. The simulations done in chapter 4 are done in the adiabatic regime but without neglecting the toroidal field and we found in this case transonic funnel flows.

For observers, it is important to know the velocity field within an accretion column to deduce spectral line shapes which then can be compared with high resolution spectra showing complex emission lines structure. Hartmann et al. (1994) and Muzerolle et al. (1998) made such calculations to reproduce spectral features for force-free dipole field but they always use a free-fall velocity law and a constant mass loading invariant κ within the funnel without taking into account critical points. The temperature distribution is empirical taking into account a volumetric heating term and nearly constant in the main part of the funnel flow. The seminal

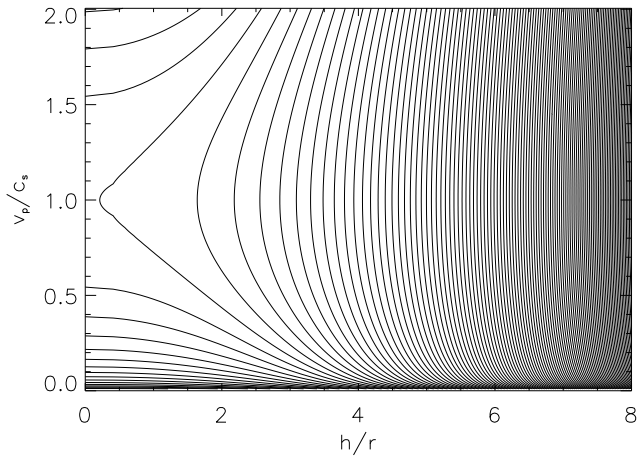

(A)

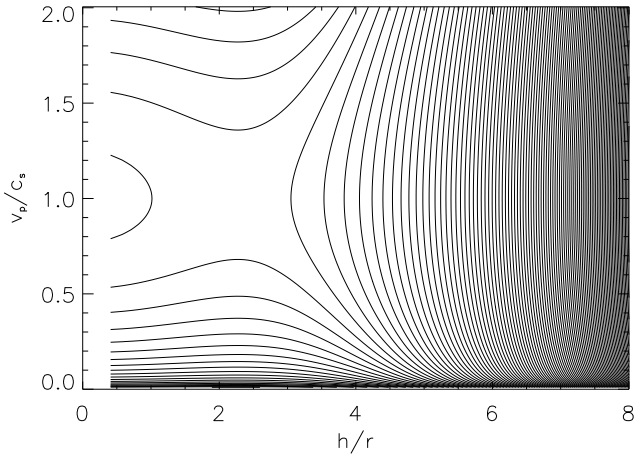

(B)

Figure 16. Isocontours of E' with the same disc aspect ratio ($A = 1.5 \times 10^{-3}$) as previously zooming in near the sonic saddle point for (A) C=0.6 (same case as Fig. 14) and (B) C=0.7 using a different scale in units of h for the position along a magnetic field line.

work of Martin (1996) studied the stationary temperature distribution along purely dipolar magnetic lines by solving the equation of internal energy including heating and cooling terms and prescribing the dynamics (density and velocity field like previously). He considers coolants such as Bremstralhung, MgII and CaII lines and heating processes such as photoionization and ambipolar diffusion. He found that the dominant term is the adiabatic heating term in the first part of the accretion column whereas MgII and CaII lines play an important role of thermal regulation near the star limiting the temperature up to 6500 K for $\dot{M} = 10^{-7} M_{\odot}.yr^{-1}$ and up to 8000 K for $\dot{M} = 10^{-8} M_{\odot}.yr^{-1}$. However, Muzerolle et al. (1998) do not reproduce correctly observed lines profiles using this temperature distribution and probably inclusion of magnetic field effect is necessary to have consistent calculations.

§ 9. The importance of the disc diffusivity for the stellar rotational evolution

The dissipative disc properties are central to correctly estimate global torques depending on the toroidal field magnitude and magnetic flux distribution. van Ballegooijen (1994), Udzensky et al. (2002) study the existence of stationary large scale magnetic interaction between the central object and the disc. They study the effect of diffusivity and initial magnetic topology on the effective connectivity by calculating force-free fields for different pitch angles. van Ballegooijen (1994) assume small disc resistivity such that periodic reconnection events appear in the magnetosphere due to the expansion of the poloidal field like in Aly & Kuipers (1990) but here with a large scale magnetic field. Lovelace et al. (1995) consider also a very highly conductive disc (diffusivity comparable or less than the viscosity) but still neglect the possible radial diffusion of the magnetic field and show that the build up of toroidal magnetic field entails the expansion of the poloidal magnetic field into the corona if the plasma is sufficiently light and cold. This leads to the opening of the magnetic field lines similar to the coronal mass ejection process in the context of solar physics (Aly 1981,1984, Low 2001). The expansion of a loop connecting the star to the disc drives material which finally gives a convergent flow near the rotation axis and a divergent one outwards. One can then reach a state with three different regions : an open stellar field, a closed magnetosphere and an open disc field if the reconnection rate is absent or sufficiently slow (for instance because of a high velocity wind along the opened field lines, greater than the contraction Alfvén speed linked to reconnection as proposed by Uzdensky 2004). Numerical calculations done by Uzdensky show a critical pitch angle $\gamma_c \sim 1$ from which the poloidal magnetic field is opening.

Haeyvaerts & Bardou (1996) consider also the inflation of the poloidal magnetic field but with disc diffusivity sufficiently high ($Rm \sim 1$) to make the radial diffusion of the magnetic field important. One can obtain in this case an expansion of the magnetic field radially within the disc. This is due to the build of toroidal field by differential rotation, leading to a change in the distribution of the disc magnetic flux which increases outwards and can finally be expelled from the disc except if there is a proper disc magnetic field to stop this diffusion.

Matt & Pudritz (2004,2005) formulate a general steady-state model to calculate the global torque on the accreting star by including this opening effect of the magnetic field topology characterized by the critical pitch angle γ_c and giving rise to a restricted star-disc connection from r_t till r_{out} contrary to the Armitage & Clarke (1996) calculations and previous models therein (where $r_{out} \sim \infty$). They consider a steady thin accretion disc with a constant accretion rate $\dot{M}_a$ in time and space (neglecting a possible disc wind). This disc is resistive (η_m), truncated at r_t and with $\beta >> 1$. The corona above the disc is assumed force-free ($\beta << 1$) and similar to a perfect conductor. In order to have a long term star-disc connection for a given magnetic field line, the toroidal diffusion velocity v_d must be equal to the drift velocity between the Keplerian speed and the equatorial stellar speed $v_K(r) - v_*$ at the footpoint anchored in the disc. One can estimate v_d by writing the induction equation for B_z (neglecting the radial diffusion of it). One has $v_d = \gamma_c p v_K$ where $p = \frac{B_r|_h}{B_z}$. The stationary state gives $\gamma_c p = (\frac{r}{r_{\rm co}})^{\frac{3}{2}} - 1$ from which one deduces $r_{out} = (1 + \gamma_c p)^{\frac{2}{3}} r_{\rm co}$. If one considers a viscous disc using an α prescription for it (see Chap. 3 for more details), one has $p = \frac{\alpha}{Pr_m}\frac{h}{r} << 1$ where $Pr_m = \frac{\nu}{\eta_m}$ is the turbulent magnetic Prandtl number. One expects typically $p \sim 10^{-2}$ for reasonable parameters such as $\alpha \sim 0.1$ and $\epsilon \sim 0.1$.

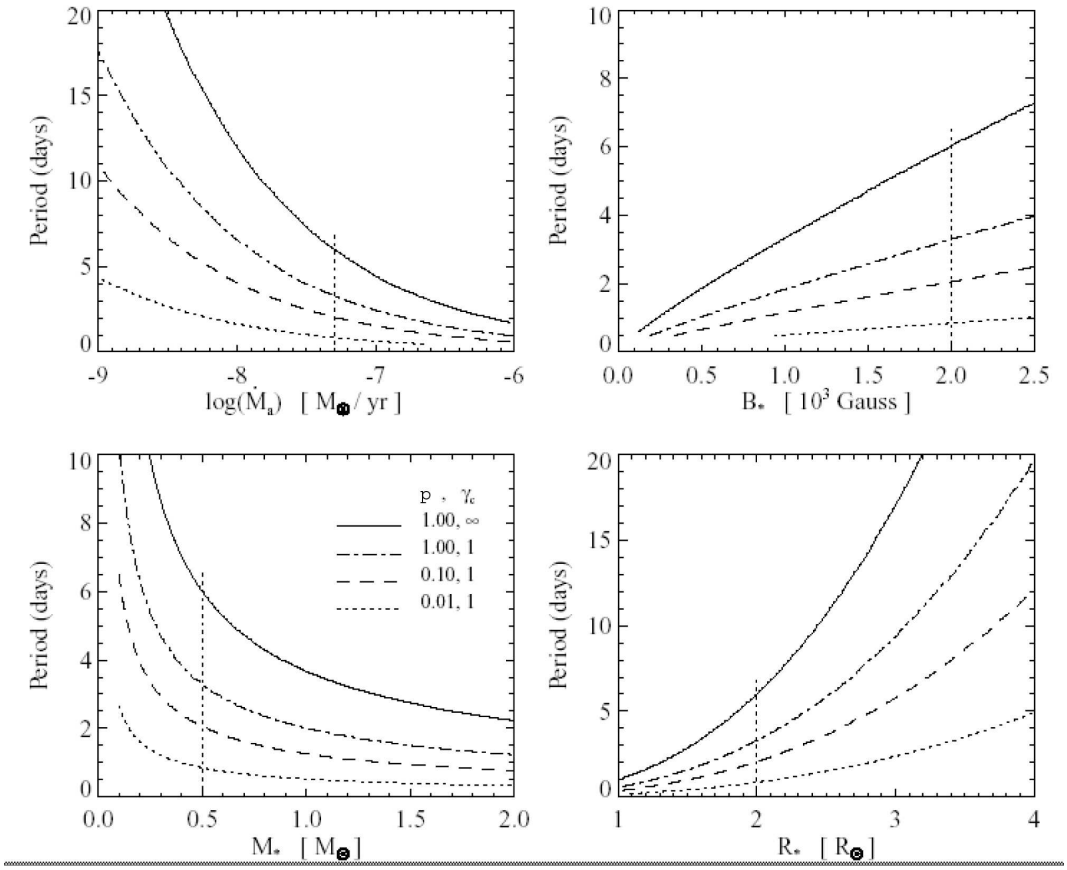

Figure 17. Equilibrium rotation period as a function of $\dot{M}_a$,B_*,M_* and R_* (from Matt & Pudritz 2005). The solid line corresponds to a global closed magnetosphere (with $\gamma_c \sim \infty$ and $p = 1$) whereas the other cases consider a partial opening of the magnetic field taking $\gamma_c = 1$ and different values for the diffusion parameter $p = 0.01(\text{dotted lines}), 0.1(\text{dashed lines})$ and $1\ (\text{dash} - \text{dotted lines})$.

The global magnetic torque on the star due to the large scale connection between the star and the disc is then given by :

$$\tau_m = \int_{r_t}^{r_{out}} r^2 B_\phi B_z dr = \int_{r_t}^{r_{out}(\gamma_c,p)} \gamma_c \frac{\mu^2}{r^4} dr, \tag{9.25}$$

where one neglects the deformation of the dipolar field by the accretion flow ($B_z = \frac{\mu}{r^3}$) and possible reconnection re-establishing some connection during short periods. One can notice that the more twisted the magnetic field line is, the stronger the torque is and that the accretion will increase the magnetic flux distribution near the disc inner edge. The global accretion torque is expressed as $\tau_a = \dot{M}_a \sqrt{GM_* r_t}$. Matt & Pudritz (2004) neglect here the effect of the stellar magnetic field on the disc which tends to corotate with the star at the truncation radius. The star equilibrium state called usually "disc-locking state" is obtained when $\tau_m + \tau_a = 0$. They found that the truncation radius needs to be at corotation for relevant values $p\gamma_c < 1$ unlike extended magnetosphere models like Cameron & Campbell (1993) which gives $r_t/r_{\text{co}} \sim 0.915$. They conclude that no efficient disc-locking state compatible with observations is possible when the partial opening of the magnetosphere is included (see Fig. 17) even though considering kG fields. Moreover, if we use observational constraints on large scale magnetic field around 200 G

(Johns-Krull et al. 1999), one finds an equilibrium period as low as 1 day even without taking into account the opening of the stellar magnetic field. This is not compatible with observations of slow rotators whose period is rather one order of magnitude greater. Thus, one can conclude from these analytical models that the star disc interaction is not sufficient to explain slow stellar rotation rates and one needs other efficient physical mechanisms to extract the stellar angular momentum. However, one also has to tune down these conclusions since the accretion torque is crudely assessed and probably reduced in reality. Recently, Dai & Li (2006) and Kluzniak & Rappaport (2007) obtain a more realistic accretion torque with a disc rotation profile reaching corotation within the magnetosphere cavity using a 1D steady state viscous disc model but prescribing different toroidal field laws.

§ 10. Ejection processes to solve the angular momentum issue?

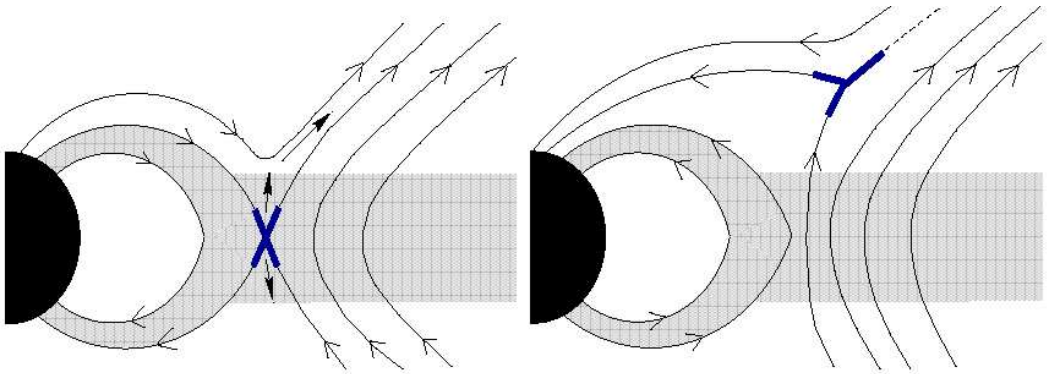

Figure 18. Magnetic configuration of the star-disc system including a proper disc magnetic field (from Ferreira, Dougados & Cabrit 2006). Left : Parallel configuration with an MHD X point. Right : Anti-parallel configuration.

To extract efficiently the angular momentum within the disc before it reaches the star, one can consider an extra disc magnetic field. The evolution of the stellar rotation rate can be given by this general expression neglecting the star-disc global magnetic torque :

$$I_* \frac{d}{dt}(\Omega_*) = -\Omega_* \frac{d}{dt}(I_*) - 2\dot{M}_e \Omega_* \lambda r_{\rm in}^2 + \dot{M}_a \left(\sqrt{G M_* r_t} - k^2 \Omega_* R_*^2 \right) \tag{10.26}$$

where $I_* = k^2 M_* R_*^2$ is the stellar moment of inertia considered as a spherical solid body with $k^2 = \frac{1}{5}$ for a fully convective star and $\lambda = \frac{r_A}{r_{in}}$ is the magnetic lever arm of a possible outflow whose inner footpoint is localized at r_{in}.

The different terms on the right hand side are torques respectively due to the contraction of the star, the ejection term due to a disc or stellar wind with a characteristic ejection rate $\dot{M}_e$, and the third term is the advection of the angular momentum brought by matter from a Keplerian accretion disc. R_* and M_* time evolution are deduced by assuming the contraction of the star along an Hayashi track starting from the break-up speed :

$$4\pi R_*^2 T_*^4 \sigma = \frac{d}{dt}\left(\frac{3GM_*^2}{7R_*}\right). \tag{10.27}$$

The expression (10.26) is a generalization of the works of Matt & Pudritz (2005) which neglects the contraction term, and Ferreira & al. (2000) which constrains the accretion rate to maintain the X point at corotation.

One can rewrite Eq. (10.26) as

$$\frac{1}{\Omega_*}\frac{d}{dt}(\Omega_*) = -\frac{1}{I_*}\frac{d}{dt}(I_*) - 2\frac{\dot{M}_e}{I_*}\lambda r_{\rm in}^2 + \frac{\dot{M}_a}{I_*}R_*^2((\frac{r_t}{R_*})^{\frac{1}{2}} - k^2), \tag{10.28}$$

by dividing expression (10.26) by the stellar angular momentum to assess the different timescales of each process. One has the Kelvin-Helmholtz contraction timescale :

$$\tau_{KH} = \frac{3GM_*^2}{27\pi R_*^3 T_*^4 \sigma} = 1.2\times 10^6 (\frac{M_*}{0.4M_\odot})^2 (\frac{R_*}{2R_\odot})^{-3} (\frac{T_*}{4000K})^{-4}\text{years}, \tag{10.29}$$

the magnetic braking timescale due to ejection :

$$\tau_m = \frac{k^2}{\lambda}\frac{M_*}{\dot{M}_e}(\frac{R_*}{r_{in}})^2 = 8\times 10^5 (\frac{k^2}{0.2})(\frac{\lambda}{100})^{-1}(\frac{M_*}{0.4M_\odot})(\frac{\dot{M}_e}{10^{-9}M_\odot yr^{-1}})^{-1}(\frac{R_*}{r_{in}})^2\text{years} \tag{10.30}$$

and the accretion timescale :

$$\tau_a = k^2\frac{M_*}{\dot{M}_a}(\frac{r_t}{R_*})^{-\frac{1}{2}} = 8\times 10^6 (\frac{k^2}{0.2})(\frac{M_*}{0.4M_\odot})(\frac{\dot{M}_a}{10^{-8}M_\odot yr^{-1}})^{-1}(\frac{r_t}{R_*})^{-\frac{1}{2}}\text{years}. \tag{10.31}$$

One obtains for relevant parameters of CTTS chosen above $\tau_m < \tau_{KH} < \tau_a$ showing that ejection can be efficient enough to maintain a slow rotation rate.

There are two main magnetic configurations depending on the orientation of the disc magnetic field with respect to the stellar magnetic moment (see Fig. 18). In the anti-parallel configuration, one will have a closed dipolar magnetosphere near the star where polar accretion along the magnetic field lines can happen. This magnetosphere is stretched outwards when one enters the disc region and a disc wind topology exists in the outer parts of the disc. This disc wind can have a stellar origin from the opening of the magnetosphere like in the Shu (1994) model (see below). The disc field makes it possible to extract angular momentum from the disc by a MHD non relativistic magnetocentrifugal jet if physical conditions are met (equipartition field, high disc diffusivity, see Ferreira & Pelletier 1995). But to extract angular momentum from the star as the latter section stresses, it seems to be necessary to have a proper stellar wind in this configuration. Matt & Pudritz (2005) propose such a powerfull stellar wind ($\frac{\dot{M}_e}{\dot{M}_a} \sim 0.1$) which needs to have a wide opening angle with magnetic lever arm around 200 i.e. $r_A \sim 14R_*$ to have sufficient angular momentum loss in the aim to have an equilibrium state and counteract the low stellar rotation rate and low magnetic field strength. However, the large mass loss rate of about 10 % of the accretion rate can not be explained by magneto-centrifugal effects due to the weak field and low rotation rate. Already, disc wind theory for Keplerian discs give an upper limit around 1 % for cold winds (Ferreira 1997) and at best 10-20 % by including heating at the disc surface (Casse & Ferreira 2000, Ferreira et al. 2006). Thus, it demands an efficient heating at the base of the wind which can not be explained by thermal pressure because too high temperatures are needed ($T > 10^6 K$) and this is in contradiction with constraints on HeI emission lines formation around $T \sim 10^4 K$ (Edwards et al. 2006). Recent simulations in ideal MHD of hot coronal winds by Matt & Pudritz (2007) confirm this by producing too high X ray emission. Models (see e.g. Strafella et al. 1998 for Herbig winds) thus assume less dissipative acceleration processes such as turbulent Alfvén wave pressure (DeCampli 1981). Actually, the large scale magnetic field

anchored in the convective zone of the star can be easily pinched and thus generate such Alfvén waves.

Shu et al. (1994) propose a specific kind of disc wind, the so-called "X-wind" to brake the star. They consider a viscous and low resistive accretion disc truncated near corotation $r_{\rm co}$ with a small penetration of the stellar magnetic field inside the disc. This small disc diffusivity is sufficient to avoid the expansion of the magnetic field as the magnetic flux is trapped near the corotation radius and thus the differential rotation is reduced. They impose a high mass ejection efficiency in the X wind ($\frac{\dot{M}_X}{\dot{M}_a} \sim \frac{1}{3}$) which is concentrated at the disc inner edge slightly beyond $r_{\rm co}$ and has a spherical Alfvén surface but this strong assumption is not self consistently verified as they do not treat the underlying disc. Particularly, they consider force-free field enforcing matter entering the magnetosphere to corotate with the star but the great bending of magnetic field lines near the X point can restrict the high mass loading assumed. Moreover, we already mention that disc wind theory limits drastically the mass loading with an upper limit around 10-20 % (Casse & Ferreira 2000) for warm solutions from sub-Keplerian discs even if magnetic flux is spatially extended in that case. Angular momentum extraction from the star is possible in this model because the X wind has the property to extract all the disc angular momentum by assumption as they impose $\lambda = 0$. Thus, stellar angular momentum can be transferred from the funnel to the disc inner edge near the X point. Consistent MHD simulations including this disc structure still need to test this configuration.

In the parallel configuration, the disc magnetic field is parallel to the stellar magnetic moment[8], and one has a real MHD X point where the magnetic field cancels in the disc midplane. At this reconnection point, the accreted matter is lifted upwards by the Lorentz force. Some matter is accreted inside the closed magnetosphere whereas the other is ejected. Contrary to disc wind models, the ejection efficiency could be much higher since the Lorentz force actually lifts up matter in this configuration but this ejection is really time dependent depending on the reconnection rate. Matter is then dragged outwards and accelerated away along the newly reconnected field lines. Since these lines are now anchored to the star, this can lead to an efficient braking as shown in Ferreira et al. (2000). But the whole ReX wind model depends on the physics of reconnection which is still not fully understood. Particularly, to carry out simulations of this configuration, it seems to be necessary to include the Hall term in the MHD equations and to use AMR techniques to catch the relevant physics well below the MHD scale as already discussed before.

By focusing on the angular momentum evolution of a protostar on long timescales, one can take an average state in time with a mean ejection rate $\dot{M}_X = f\dot{M}_a$ linked to the inner disc accretion rate $\dot{M}_a$ and Ferreira et al. (2000) solves Eq. (10.28) with the accretion term constrained to maintain the X point at the corotation radius. The initial stellar magnetic field has the following expression $B_* = B_{*,0}(\frac{R_*}{r})^n$ to take into account deviations from pure dipole fields. This field is equal to the opened disc wind at the X point and needs to be in equipartition with thermal pressure to have ejection and thus its strength is directly linked to the inner disc accretion rate. As soon as the magnetospheric field undergoes some reconnection with the disc field, and if there is no dynamo creating new stellar closed magnetic field, the disc accretion

[8]The stellar magnetic field could be originated in this case from the trapping of some flux in the protostellar core from the collapse of the molecular cloud. However, this fossil origin is not supported by the fully convective behaviour of a young star.

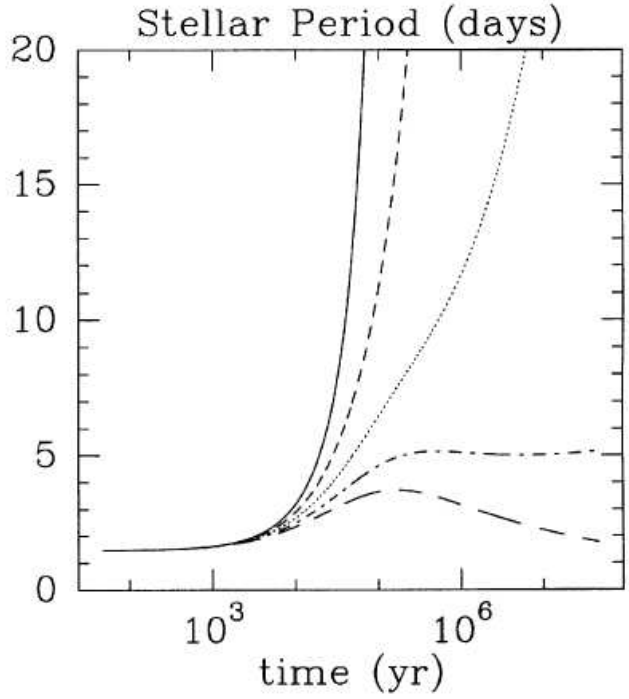

Figure 19. Stellar period evolution for an initial condition with f=0.1, $\lambda = 3$, $R_{*,0} = 4R_\odot$, $M_{*,0} = 0.4M_\odot$,$\dot{M}_{a,0} = 10^{-5}M_\odot yr^{-1}$, $T_* = 3000K$ and different initial stellar magnetic field index n=1 (solid),n=3.41 (dashed), n= 3.87 (dotted), n=4.4 (dash-dotted) and n=5 (long-dashed) with no stellar dynamo (from Ferreira et al. 2000)

has to adapt to remain the X point near the corotation on long timescales. By prescribing the decrease law of the magnetospheric flux, Ferreira et al. (2000) finds that the ReX wind model is able to explain efficient braking towards a tenth of the breakup for a timescale around 10^5 years (see Fig. 19) and n=3-4 (see Fig. 19). But this model is more reliable for class 0 objects since one considers initially high accretion rate $M_{a,0} = 10^{-5}M_\odot yr^{-1}$ and thus powerful ejection events. It is also questionable to assume a steady ejection whereas reconnection events are really time dependent. Moreover, the final stellar field due to the stellar contraction reaches high values of several kG starting from 200 G. Finally, the high efficiency of stellar braking is probably a bias of not imposing a minimum accretion torque consistent with observations since in this model, the accretion rate steeply drops below $10^{-8}M_\odot yr^{-1}$ after 1 Myr. Further investigations including explicitly this accretion term is necessary to conclude for class II objects such as T Tauri stars.

2

Numerical MHD

Chapter content

In this chapter, we focus on presenting the methodology used in the numerical tool to study the star-disc interaction. This is the only way to take into account the coupling between the stellar magnetic field and the accretion disc because of a complex geometry and strong gradients of magnetic field, density and dissipative effects such as diffusivity and viscosity between disc and magnetosphere. Then, we sum up the previous numerical work done in this field in the last decades.

1. Numerical methods

Equations in physics are usually written as a set of Partial Differential Equations (PDE) such as the Maxwell equations to describe the electromagnetic field or the hydrodynamic equations to describe the flow of a fluid. There are few analytical solutions for these systems, usually making crude simplifications. Numerical methods translate this continuous description into a finite set of discrete values by discretizing the PDE onto a grid of points which can be evolved in time by a relevant algorithm. In this part, we will present how finite volume methods work since we will use them to carry out simulations of star-disc interaction. To have more information, we advice the books of Toro (1999) and LeVeque (2003). We finally present the VAC code with the main numerical scheme used in this thesis, and specify the computational grid chosen and the typical computational time used for our simulations.

§ 11. Finite volume discretization

The physical problem is expressed in terms of conservation laws, which are equivalent (for continuous and differentiable quantities) to the integral form of the PDE. Contrary to finite difference methods where one directly discretizes the differential operators of the PDE, integral approximation is used. This integral form has the advantage to take into account both continuous and discontinuous solutions and ensure the conservation of physical properties such as mass, momentum or energy, which are called conservative variables. For instance, the conservation of mass which is written $\partial_t \rho + \nabla \cdot (\rho \mathbf{v}) = 0$ is integrated over a control volume V : $\partial_t \int_V \rho dV = \int_V \nabla \cdot (\rho \mathbf{v}) dV$. Then, the right hand side of this equation is transformed by using the Green-Ostrogradsky theorem :

$$\partial_t \int_V \rho dV = \int_S \rho \mathbf{v}.d\mathbf{S} \tag{11.32}$$

Thus, the variation in time of the averaged density over a control volume is equal to the balance between flux of matter entering the volume across the closed surface $d\mathbf{S}$ and flux of matter escaping from it. One assumes here that there is no source and sink terms which could respectively create mass or make it disappear. Because the flux entering a given volume is identical to that leaving the adjacent volume, these methods are conservative by construction. To solve numerically this kind of equation, the conservative variables are discretized onto a structured static grid (eulerian approach) and the cell centers quantities are interpreted like the averaged values of these variables over each cell. For sake of simplicity, the 1D version of (11.32) integrated between two adjacent time steps n and n+1 separated by Δt for a grid point i can be written as :

$$\rho_i^{n+1} - \rho_i^n = \frac{1}{\Delta x} \int_{t^n}^{t^{n+1}} \int_{x_{i-\frac{1}{2}}}^{x_{i+\frac{1}{2}}} \frac{\partial \rho v}{\partial x} dx dt = \frac{\Delta t}{\Delta x} (F(x_{i+\frac{1}{2}}) - F(x_{i-\frac{1}{2}})) \tag{11.33}$$

where $\rho_i^n = \frac{1}{\Delta x}\int_{x_{i-\frac{1}{2}}}^{x^{i+\frac{1}{2}}} \rho(x,t_n)dx$,

$F_{i+\frac{1}{2}} = F(x_{i+\frac{1}{2}}) = \frac{1}{\Delta t}\int_{t^n}^{t^{n+1}} f(\rho(x_{i+\frac{1}{2}},t))dt$ where f is the flux of density i.e. ρv.

The fluxes are computed at each cell interface but one only follows the variable values at the centers of each cell and thus some interpolations are necessary as we will see further. The key to have good numerical schemes is to give accurate values for the numerical fluxes $F_{i+\frac{1}{2}}$ and $F_{i-\frac{1}{2}}$ at the cell edges $x_{i-\frac{1}{2}}$ and $x_{i+\frac{1}{2}}$ (which are averaged in time) of the chosen grid in order to advance in time the values of the conservative variables averaged over the control volume, while having a stable and consistent numerical scheme.

Let me define these two latter terms. A scheme is consistent when the local errors with respect to the exact solutions vanish when the spatial and temporal resolution goes towards infinity. We also define the order of a scheme to quantify its accuracy. This can be found by replacing the discrete values in the scheme by a Taylor expansion of a sufficient smooth solution in Δx and Δt. For instance, $\rho_{i+1}^{n+1} = \rho((i+1)\Delta x,(n+1)\Delta t) = \rho(i\Delta x,n\Delta t) + (\Delta x)\partial_x\rho|_{x=i\Delta x} + (\Delta t)\partial_t\rho|_{t=i\Delta t} + O(\Delta x^2) + O(\Delta t^2)$. A scheme is stable if truncation errors introduced by the discretization and errors due to round-off noise at machine precision remain bounded during the time evolution. The Lax theorem ensures that a consistent and stable numerical scheme converges. This is proved only for linear systems. In practice, we can compute the numerical solution for different grid resolution and check for instance that the global error $\Sigma_i(u_i - u_i^C)$ computed over all the grid points u_i (for a given resolution with respect to the coarse resolution u_i^C) converges when the grid is refined (see e.g. Stone et al. 1992).

The discretization of the integral form of the other differential operators is given by

$$\int_V \nabla P dV = \Sigma_i \tilde{P} d\mathbf{S}_i, \tag{11.34}$$

$$\int_V \nabla \times \mathbf{B} dV = \Sigma_i d\mathbf{S}_i \times \tilde{\mathbf{B}}_i, \tag{11.35}$$

where $d\mathbf{S}_i$ represents the normal surface value at each interface of a cell and $\tilde{P}$ and $\tilde{\mathbf{B}}$ the average values at the cell interfaces, as computed from the neighbouring cell center values.

§ 12. The CFL condition

The aim is to compute the solution for the largest local time step possible in order to save computational time and make a study for long term evolution. The physical restriction is to control the propagation of information brought by waves or advected with the fluid. If one considers the maximum speed of propagation $c_{\max}$ and a typical width Δx of a cell, we can only take $\Delta t < \frac{\Delta x}{c_{\max}}$ in an explicit scheme otherwise we will have a situation corresponding to unphysical speeds and numerical instabilities will develop. This is called the Courant-Friedrich-Lewy condition. One can make a von-Neumann analysis to find the stability domain of a linear scheme by taking a solution written as $\rho_i^n = A^n exp(jBi\Delta x)$ where $j^2 = -1$. When the ratio $|\frac{A^{n+1}}{A^n}|$ is greater than one, we get an unconditionally unstable scheme. For instance, the conservation of mass discretized using an upwind formula for the time derivative $\partial_t|_i\rho = (\rho_i^{n+1} - \rho_i^n)/\Delta t$ and a centered formula for the spatial derivative $\partial_x|_i\rho = (\rho_{i+1}^n - \rho_{i-1}^n)/(2\Delta x)$ gives an unstable scheme since $\frac{A^{n+1}}{A^n} = 1 - v\frac{\Delta t}{\Delta x}sin(i\Delta x)$ such that $||\frac{A^{n+1}}{A^n}|| > 1$. A way of ensuring a second order

accurate scheme in space while obtaining stability for it is to replace in the time derivative ρ^n by $(\rho^n_{i-1} + \rho^n_{i+1})/2$. This is called the Lax scheme.

In our simulations, this restriction on the time step is a main difficulty because the limiting time step is located near the star due to the overwhelming stellar magnetic field which increases as r^{-3} for a dipole. However, one needs to have the maximum resolution at this location since for instance we want to compute correctly the magnetic stresses. Thus, we have typical simulations with several millions of time steps, which is not ideal because of the accumulation of truncation errors. An idea would be to use implicit schemes but we need to have enough accuracy in the calculations of magnetic stress such that we can not choose an arbitrary larger time step as stability theory claims. Besides, an implicit scheme is time consuming since at each time step one has to solve a non linear system of equations whose number is proportional to the number of grid points. A possibility would be to use an hybrid explicit/implicit technique linked to Adaptive Mesh Refinement like in the BATSRUS code (e.g. Tóth et al. 2003) for space weather simulations but we can only meaningfully use an implicit scheme in the region where the disc and star are not connected. For instance, the time step in our simulations is limited by the magnetosphere cavity and we could use implicit treatment in this region but not within the funnel flow.

In the case of resistive (or viscous) MHD, there is an additional constraint coming from the diffusion timescale $\Delta t < \frac{(\Delta x)^2}{\eta}$ where η is the resistivity (or dynamic viscosity). The grid resolution and the magnitude of the resistivity (or dynamic viscosity) determine whether this constraint or the CFL condition is more restrictive.

§ 13. The choice of the numerical flux

§ 13.1. *Methodology*

There are two main approaches to choose the expression of the numerical fluxes :

- upwind methods using explicitly the wave propagation information, based on (approximate) Riemann solvers.
- centered or symmetric methods without using the characteristics of the equations.

The upwind methods are more accurate since they take into account some mathematical properties of the equations. One of the famous upwind methods is the Godunov method. The numerical flux is computed from solutions of classical Riemann problems [9] at each cell interface assuming that the solution is piecewise-constant within each cell. One should use the exact solution of the self-similar Riemann Problem in x/t and then simply evaluate the flux at centre assuming it is constant during Δt : $F_{i+\frac{1}{2}} = f(\rho(x_i, 0))$ where f is the flux of the conservative variable ρ.

[9] The Riemann problem is a particular initial value problem where we have a discontinuity with two constant states at each side of a cell.

§ 13.2. *The case of the scalar advection equation*

For instance, one can look for the solution of the Riemann problem for the scalar advection equation $\partial_t \rho + v\partial_x \rho = 0$ where v is a constant. The initial condition is

$$\rho_0 = \begin{cases} \rho_L & if\ x < 0, \\ \rho_R & if\ x > 0. \end{cases} \tag{13.36}$$

By using the change of variables $u = x - vt$, one has $\partial_u \rho = 0$. Thus, one deduces

$$\rho(x,t) = \rho_0(x - vt) = \begin{cases} \rho_L & if\ x/t < v, \\ \rho_R & if\ x/t > v. \end{cases} \tag{13.37}$$

One has the propagation of the initial discontinuity at the speed v. The propagation of information is along the characteristic curve $\frac{dx}{dt} = v$ which is a straight line in this simplest case. The numerical flux in this case is :

$$F_{i+\frac{1}{2}} = F_{i+\frac{1}{2}}(\rho_{xi}) = \begin{cases} \rho_L v & if\ v > 0, \\ \rho_R v & if\ v < 0. \end{cases} \tag{13.38}$$

§ 13.3. *Riemann solvers for linear hyperbolic systems*

In general, a system of conservation laws for a set of conservative variables U_i will be described by a set of hyperbolic equations characterized by a flux function F such that

$$\partial_t U_i + \partial_{x_j} F_j(U_i) = 0. \tag{13.39}$$

One can rewrite this system in a similar form as the advection equation :

$$\partial_t U_i + A(U)\partial_{x_j} U_i = 0, \tag{13.40}$$

where $A(U) = \partial_{U_j} F_j(U_i)$ is the Jacobian matrix of F.

Let us assume that A is constant, so that F=AU is linear in the unknowns. If A can be put in a diagonal form namely $\Lambda = (\lambda_i) = R^{-1}AR$ in a specific vector basis R (the system is then called strictly hyperbolic), one will have

$$\partial_t W_i + \lambda_i \partial_{x_j} W_i = 0, \tag{13.41}$$

where $W_i = R^{-1}U_i$ are called characteristic variables, since for a constant matrix A one will have propagation of the initial value of W_i at speed λ_i along the characteristics $dx_i/dt = \lambda_i$. One has a system of decoupled scalar advection equations with speeds λ_i which can be understood as propagation of different waves (see Fig. 20). The general solution is then obtained by decomposing the initial values onto the right eigenvectors R :

$$U_i = \Sigma_i W_{0,i}(x - \lambda_i t) R_i. \tag{13.42}$$

Finally, the numerical flux is given by :

$$F_{i+\frac{1}{2}} = A U_{i+\frac{1}{2}}(0). \tag{13.43}$$

In other words, each discontinuity in the initial data travels at its characteristic speed given by the eigenvalues of A while the jump values for the variables across the discontinuities are proportional to the right eigenvectors of A.

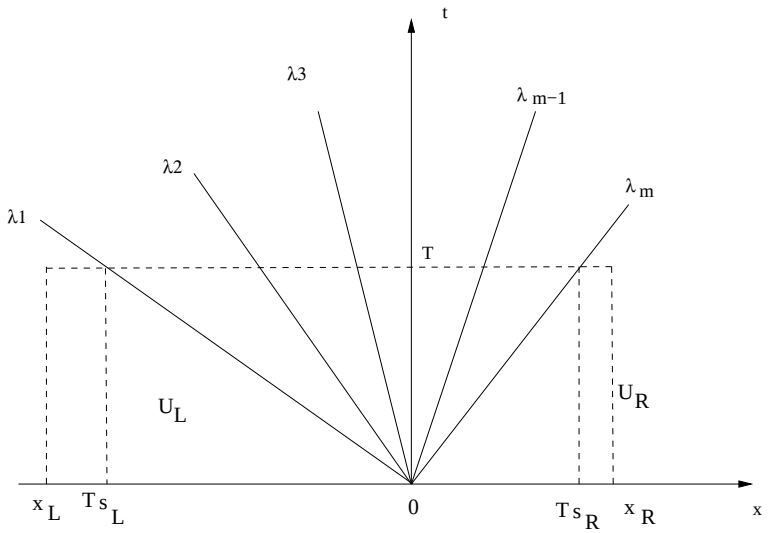

Figure 20. General solution of the Riemann problem in the (x,t) plane. At the cell interface located at x=0, we represent the propagation of the different wave characteristics of the system considered. The information transported by the fastest waves reaches distances equal to $s_R T$ and $s_L T$ at the end of the time step T which is lower than the cell width $[x_L, x_R]$ due to the CFL condition.

In general and already for the Euler equations, one has non linear equations with complex characteristic curves which can cross each other since the different possible waves depend on the sound speed and the fluid speed which are local quantities depending on the solution, which is equivalent to non constant λ_i. Thus one can have development of discontinuities from a continuous initial condition and one needs to check that the propagation speed of each new discontinuity is consistent with the possible set of waves described by the equations and not a numerical effect due to a bad discretization of the equations. This relates to the Lax condition $\lambda(U_R) < s < \lambda(U_L)$ where s is the speed of a possible discontinuity. Conservative schemes can handle this important fact.

The general solution of the Riemann Problem for the 1-D Euler equation consists in one wave (shock or rarefaction) travelling to the right, a second wave (shock or rarefaction) moving to the left and a contact discontinuity [10] between them. The respective characteristics speeds are v+c, v and v-c where v is the fluid speed and c is the sound speed. In MHD, the general solution for this 1D Riemann Problem includes an entropy wave with velocity v, a pair of Alfvén waves $v \pm v_A$ where $v_A = B/\sqrt{\rho}$ and four magnetosonic waves with characteristic speeds $v \pm v_{SM}$ and $v \pm v_{FM}$ where $v_{FM,SM} = \frac{1}{2}({c_s}^2 + {v_A}^2 \pm \sqrt{({c_s}^2 + {v_A}^2)^2 - 4{c_s}^2{v_A}^2})$.

§ 13.4. *Approximate Riemann solvers for non linear equations*

We discuss here the simplest and most common approximate Riemann solver namely the Roe (1981) solver initially designed for the Euler equation and then extended in MHD (Brio & Wu 1988, Ryu et al. 1995, Cargo & Gallice 1997). The idea is to linearize the flux function and then evaluate it in an average state $\tilde{U}$ between left and right values. In practice, we take an arithmetic average of the primitive variables $U_{LR} = (U_R + U_L)/2$ for the MHD equations and then evaluate the Jacobian matrix of the flux function at this point : $A = \tilde{A}(U_R, U_L)$ and deduce the average

[10] jump in density and temperature with continuity for pressure and normal component of velocity

eigenvalues $\tilde{\lambda}_i(U_R, U_L)$ and eigenvectors $\tilde{R}_i$. The matrix has to be consistent with the exact Jacobian of the system and obey the Rankine-Hugoniot relation $F(U_R) - F(U_L) = \tilde{A}(U_R - U_L)$. Finally, one projects the initial condition value onto $\tilde{R}_i$ to find $\tilde{U}_{i+\frac{1}{2}}(0)$.

$$\tilde{U}_{i+\frac{1}{2}}(0) = U_L + \Sigma_{\tilde{\lambda}_i<0}\alpha_i\tilde{R}_i = U_R - \Sigma_{\tilde{\lambda}_i>0}\alpha_i\tilde{R}_i \tag{13.44}$$

where $\alpha_i = \tilde{L}_i \cdot (U_R - U_L)$ are jump values for the variables across the discontinuities and $\tilde{L}_i$ is the left eigenvectors of $\tilde{A}$. The numerical flux can not be deduced from the obvious relation $F_{i+\frac{1}{2}} = \tilde{A}\tilde{U}_{i+\frac{1}{2}}(0)$ since for instance if one has supersonic flows going from the left in the hydrodynamic case, using expression from Eq. 13.44 gives contribution from U_R in the intercell flux due to the average state depending on both U_R and U_L. This is wrong as it does not respect the upwind property which stresses that the intercell flux can only depend on the left value in this case. The correct numerical flux is :

$$F_{i+\frac{1}{2}} = F_L + \Sigma_{\tilde{\lambda}_i<0}\alpha_i\tilde{\lambda}_i\tilde{R}_i, \tag{13.45}$$

where $F_L = AU_L$ or more generally by doing an arithmetic average :

$$F_{i+\frac{1}{2}} = \frac{1}{2}(F_R + F_L) - \frac{1}{2}\Sigma_i\alpha_i|\tilde{\lambda}_i|\tilde{R}_i. \tag{13.46}$$

There are also other approximate Riemann solvers which do not take into account the full set of waves present in the exact solution of the Riemann problem :

- The HLL solver (Harten Lax van Leer 1983) which takes into account only the lowest and largest wave speed.
- The HLLC solver (Toro, Spruce & Spears 1994) which includes also the contact discontinuity with respect to the HLL one.
- The Lax-Friedrichs solver (Rusanov 1961) which considers only the fastest wave.

These latter incomplete Riemann solvers are often used in practice because they are robust for complex physical problems and efficient from the computational time point of view since one does not need a decomposition of the numerical solution onto the eigenvectors at each cell interface.

Let us show now how to find the expression for the intercell flux in the HLL scheme. In this case, one considers only an intermediate state U_* between the initial values (U_R, U_L) at each side of the considered interface separated by two waves propagating respectively leftwards and rightwards with the maximum speeds s_L and s_R allowed by the equations of the considered system. The initial condition is :

$$U = \begin{cases} U_L & if\ s_L > 0, \\ U_* & if\ s_L \leq 0 \leq s_R, \\ U_R & if\ s_R < 0. \end{cases} \tag{13.47}$$

The Rankine-Hugoniot relations across the two possible discontinuities give : $F_* - F_L = s_L(U_* - U_L)$ and $F_R - F_* = s_R(U_R - U_*)$ where $F_L = F(U_L)$. By solving this system of two equations with the two unknowns (U_*, F_*), the intercell flux is given by

$$F_{i+\frac{1}{2}} = \begin{cases} F_L & if\ s_L > 0, \\ F_* & if\ s_L \leq 0 \leq s_R, \\ F_R & if\ s_R < 0, \end{cases} \tag{13.48}$$

where $F_* = \frac{s_R F_L - s_L F_R + s_R s_L (U_R - U_L)}{s_R - s_L}$.

§ 14. Variables reconstruction, slope limiters and high resolution schemes

To increase the spatial resolution of a scheme, it is necessary to do extrapolation of the variables over the width of a cell. However, it is crucial not to introduce spurious oscillations due to extrapolations from the two sides of a cell edge in a region of sharp gradients. Thus, the slope of the extrapolated variable at a cell interface is chosen by comparing values of the two adjacent slopes a_1 and a_2 computed from the neighbouring cells in a given direction and is set to zero when one has opposite slopes and to a limited slope defined for each type of limiter otherwise. This is called the reconstruction process. This allows the solution to keep monotonicity and thus ensures the Total Variation Diminishing property of a scheme, i.e. that the numerical total variation $TV = \Sigma_i |U_{i+1} - U_i|$ keeps decreasing with time. One can also remark that for a linear extrapolation, the average of a variable over the cell size is still consistent with its definition in the finite volume meaning. One can consider a higher order extrapolation of variables like a parabolic reconstruction of variables used in the PPM (Piece-wise Parabolic Method) method of Collela & Woodward which is third order accurate.

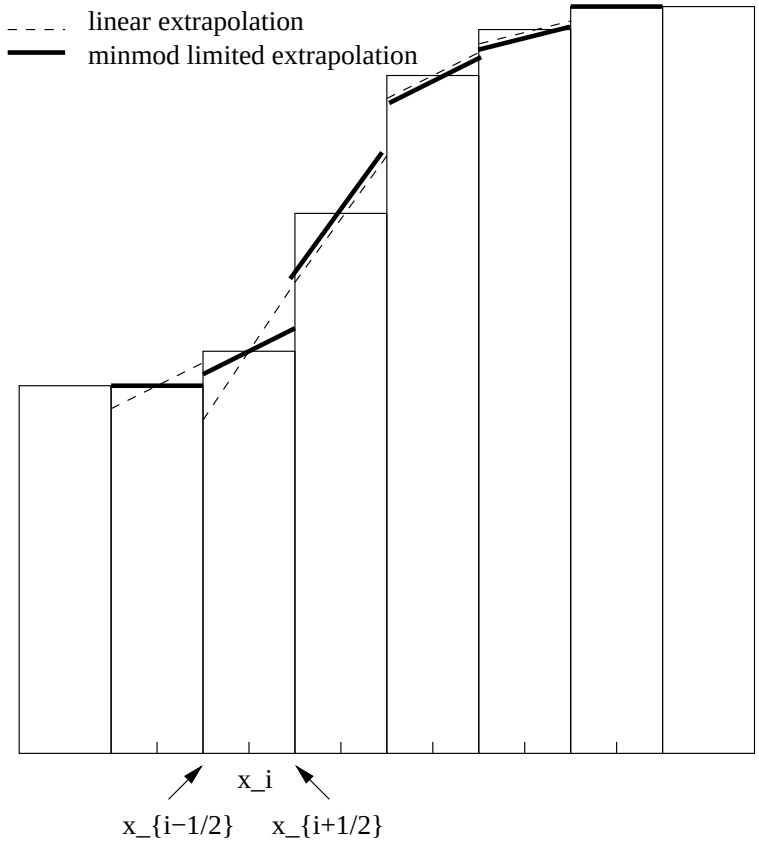

Figure 21. Spatial reconstruction of variables with slope limiters.

One describes now the most common slope limiters in decreasing order of numerical diffusion :

- minmod=sign(a_1) max(0,min($|a_1|$,sign(a_1).a_2))
- woodward=minmod($2\Delta U_{j-\frac{1}{2}}, 2\Delta U_{j+\frac{1}{2}}, \frac{1}{2}(U_{j-\frac{1}{2}} + U_{j+\frac{1}{2}})$)
- van leer=$2\frac{max(a_1 \times a_2, 0)}{a_1+a_2+10^{-12}}$

where $\Delta U_{j-\frac{1}{2}} = U_j - U_{j-1}$. Fig. 21 shows an example of reconstruction in 1D using a minmod limiter. Actually, the limitation on slopes is equivalent to have some artificial viscosity introduced in classical finite difference schemes to avoid spurious oscillations (known as the Gibbs phenomenon) in presence of steep gradients.

The monotonous property of such schemes impose at most first order accuracy (Godunov theorem) when discontinuities like shocks are present. Finally, the reconstruction on conservative variables or even better on primitive variables (to better control thermal pressure like in our problem) before applying the Riemann solver on the edge values u_R and u_L gives higher accuracy in the evaluation of the intercell fluxes.

§ 15. The issue of positivity

Most of the MHD numerical schemes such as the Roe one do not generally ensure the positivity property which corresponds to the physical characteristic of variables such as pressure and density (Einfeldt et al. 1991) to be positive. This is particularly critical for highly magnetized media which can lead to negative pressure since the total density energy is dominated by the magnetic energy. Thus one generally imposes a lower limit for pressure when its computation from the total density energy give such unphysical values due to truncation errors. The HLL scheme, and even better less diffusive HLLC, can handle such a positivity property by a correct choice of the fastest speeds.

§ 16. Methods for multidimensional systems

All numerical schemes discussed so far are developed in one dimension since the Riemann problem is solved in 1D for the propagation of waves normal to the grid interface in each direction. To generalize them for multidimensional purposes, one can use the Strang operator splitting which uses one dimensional methods for each coordinate direction. For a 2-D problem, the general system is separated into 1-D problems with a source term S :

$$\partial_t U + \partial_x F_x = S/2, \tag{16.49}$$

$$\partial_t U + \partial_y F_y = S/2. \tag{16.50}$$

By defining solution operators for each direction L_x and L_y, one has $U^{n+1} = L_x L_y U^n$ or $U^{n+1} = L_y L_x U^n$ but these splitting schemes are first order accurate in time. To have second order accuracy, one has to interchange the order of operators such that $U^{n+2} = L_x L_y L_y L_x U^n$. However, this splitting method favours some directions for the propagation of waves and can lead to numerical instabilities (Quirk 1994) when shockwaves are formed obliquely across the grid. For instance, quantities such as $\frac{\partial B_y}{\partial y}$ involved in the induction equation in MHD are ignored in 1D numerical schemes.

Another approach is the unsplit finite volume technique where all the flux contributions are taken into account in a single step, but this is an area of ongoing research in the context of shock-capturing numerical algorithms for MHD (Mignone et al. 2005, Gardiner & Stone 2005).

§ 17. Discretization in axisymmetry

When a physical system owns a cylindrical symmetry like for a simplified model of an accretion disc (neglecting possible non axisymmetric perturbations), all the variables with respect to the ϕ direction are invariants and the equations simplify.

However, one has to be careful to the discretization of the integral terms in finite volume methods, particularly the radial component of gradient operators and toroidal components of tensors since surface edges normal to the phi component are misaligned by $\Delta\phi$ and thus give a radial contribution. Actually, the fluxes in the toroidal direction are null by definition of axisymmetry but one has to consider projection of these toroidal fluxes components in the mean radial direction $\mathbf{e_r}$ of a cell. For instance, let us consider the integral of the radial gradient of pressure P over the control volume of a cell V_j :

$$\int_{V_j} \nabla_r P dV = \int_S P d\mathbf{S} \cdot \mathbf{e}_r = \frac{1}{2}(P_{i+1} + P_i) d\mathbf{S}_{r,i+1} - \frac{1}{2}(P_{i-1} + P_i) d\mathbf{S}_{r,i-1} - P_{j+1} d\mathbf{S}_{\Phi,j+1} \Delta\frac{\Phi}{2} - P_j d\mathbf{S}_{\Phi,j-1} \Delta\frac{\Phi}{2}. \tag{17.51}$$

Finally, as $V_j = r\Delta\Phi d\mathbf{S}_\Phi$ and $P_j = P_{j+1}$ one has :

$$\int_{V_j} \nabla_r P dV = \Sigma_i \tilde{P} d\mathbf{S}_{r,i} - V\frac{P_j}{r}, \tag{17.52}$$

and similarly, one finds that

$$\int_{V_j} (\nabla \times \mathbf{B})_\phi dV = \Sigma_i (d\mathbf{S}_i \times \tilde{\mathbf{B}}_i)_\phi - V\frac{B_z}{r}, \tag{17.53}$$

where $\tilde{P}$, $\tilde{\mathbf{B}}_i$ are averaged values obtained from the neighbouring cells and P_j, B_z are cell-centered values. Thus, these geometrical terms introduce source terms in the equations.

§ 18. The ideal MHD equations

The usual ideal MHD equations written in conservative form are :

$$\frac{\partial \rho}{\partial t} + \nabla \cdot (\rho \mathbf{v}) = 0, \tag{18.54}$$

$$\frac{\partial \rho \mathbf{v}}{\partial t} + \nabla \cdot (\rho \mathbf{v}\mathbf{v} - \mathbf{B}\mathbf{B}) + \nabla(\frac{B^2}{2} + P) = 0, \tag{18.55}$$

$$\frac{\partial \mathbf{B}}{\partial t} + \nabla \cdot (\mathbf{v}\mathbf{B} - \mathbf{B}\mathbf{v}) = 0, \tag{18.56}$$

$$\frac{\partial E}{\partial t} + \nabla \cdot ((E + \frac{B^2}{2} + P)\mathbf{v} - \mathbf{B}(\mathbf{B} \cdot \mathbf{v})) = 0, \tag{18.57}$$

where ρ is the plasma density, $\mathbf{v}$ the total velocity, $\mathbf{B}$ the magnetic field, P the thermal pressure and

$$E = \frac{P}{\gamma - 1} + \rho\frac{\mathbf{v}^2}{2} + \frac{\mathbf{B}^2}{2}, \tag{18.58}$$

is the total density energy of the fluid. One can introduce P_{tot} for the total pressure, the sum of the thermal pressure P and the magnetic pressure:

$$P_{tot} = P + \frac{\mathbf{B}\cdot\mathbf{B}}{2}. \tag{18.59}$$

To close the system, one considers here that the equation of state is that of a perfect gas, in which case $P = (\gamma - 1)\epsilon$ where ϵ is the internal energy of the fluid.

The flux function for the first component is written in cylindrical coordinates as :

$$\mathbf{F_r} = \begin{pmatrix} \rho v_r \\ \rho v_r^2 + P_{tot} - B_r^2 \\ \rho v_r v_\phi - B_r B_\phi \\ \rho v_r v_z - B_r B_z \\ 0 \\ v_r B_\phi - B_r v_\phi \\ v_r B_z - B_r v_z \\ (E + P_{tot})v_r - B_r(B_r v_r + B_\phi v_\phi + B_z v_z) \end{pmatrix}. \tag{18.60}$$

One also has contribution to the flux from geometrical source terms due to axisymmetry as demonstrated in the last paragraph which is written as :

$$\mathbf{S} = \begin{pmatrix} 0 \\ (\rho v_\phi^2 + P_{tot} - B_\phi^2)/r \\ (-\rho v_\phi v_r + B_\phi B_r)/r \\ 0 \\ 0 \\ (v_r B_\phi - B_r v_\phi)/r \\ 0 \\ 0 \end{pmatrix}. \tag{18.61}$$

One can remark for instance the contribution due to the centrifugal force.

In general, one has to take into account physical dissipation terms which are not always expressed like a conservative term such as resistivity. They are typically treated like source terms. One also has to consider the divergence free constraint of the magnetic field $\nabla\cdot\mathbf{B} = 0$ which means that there are no magnetic monopoles.

§ 19. Numerical techniques to ensure the divergence-free property of the magnetic field

The standard shock-capturing discretization methods do not ensure $\nabla\cdot\mathbf{B} = 0$ in multi-dimensional MHD because the discrete divergence of the discrete curl operator is not exactly zero in general. There are three main methods to deal with this problem, well discussed in Tóth (2000) and presented below. One also finds codes which evolve directly the vector potential defined as $\mathbf{B} = \nabla\times\mathbf{A}$ which requires to write special numerical schemes where second order derivatives are computed and thus the order of accuracy is reduced by one.

§ 19.1. *Powell source terms and diffusion*

This method keeps the terms involving $\nabla \cdot \mathbf{B}$ in the equation since they are not numerically equal to zero and appear like source terms :

$$\frac{\partial \rho \mathbf{v}}{\partial t} + \nabla \cdot (\rho \mathbf{v}\mathbf{v} - \mathbf{B}\mathbf{B}) + \nabla(\frac{B^2}{2} + P) = -(\nabla \cdot \mathbf{B})\mathbf{B}, \tag{19.62}$$

$$\frac{\partial \mathbf{B}}{\partial t} + \nabla \cdot (\mathbf{v}\mathbf{B} - \mathbf{B}\mathbf{v}) = -(\nabla \cdot \mathbf{B})\mathbf{v}, \tag{19.63}$$

$$\frac{\partial E}{\partial t} + \nabla \cdot ((E + \frac{B^2}{2} + P)\mathbf{v} - \mathbf{B}(\mathbf{B} \cdot \mathbf{v})) = -(\nabla \cdot \mathbf{B})\mathbf{B} \cdot \mathbf{v}, \tag{19.64}$$

The term in the momentum equation implies a magnetic force parallel to the magnetic field, the term in the induction equation describes the advection of monopoles with the flow.

The MHD equations written like this are no longer conservative but these source terms remain of the order of the truncation errors and Powell et al. (1999) have shown that these terms can stabilize TVD numerical schemes. Moreover, these terms help to increase robustness of methods with simplified Riemann solvers like TVDLF (Tóth & Odstril 1996). The drawback is that the jump conditions across shocks can be incorrect.

This method is sufficient if $|\nabla \cdot \mathbf{B}|$ remains small with respect to other dynamical terms during the time evolution, typically inferior to one percent. An improvement is to add a diffusion term in the induction equation to avoid accumulation of monopoles at the boundaries of the computational domain because of accretion for instance.

§ 19.2. *Projection scheme*

This method is a cleaning technique after each time step when the numerical scheme is completed. It was initially proposed by Brackbill & Barnes (1980) and consists in projecting the magnetic field $\mathbf{B}$ onto a vectorial subspace where the magnetic field $\mathbf{B}'$ is divergence free. We can find a scalar potential Φ such that $\mathbf{B} = \mathbf{B}' + \nabla\Phi$ which physically does not modify the Lorentz force. This is equivalent to solve the Poisson equation : $\Delta^2\Phi = \nabla \cdot \mathbf{B}$. One can prove that this new magnetic field corresponds to the smallest correction which removes the unphysical part of the numerical solution. This elliptic equation can be solved by using an iterative solver and by calculating the laplacian using the same discretized differential operators as calculating $\nabla \cdot \mathbf{B}$. This calculation is a bit CPU time consuming till 30 % of the total computational time. One also have to choose correctly the boundary conditions for Φ in accord with the boundary conditions for $\mathbf{B}$.

This correction will imply a modification of the magnetic energy and as the total energy density is conserved since it is generally a conservative variable of a scheme, it will entail a modification of the thermal pressure. For magnetically dominated region, one often prefers to ensure thermal pressure conservation to avoid appearance of negative pressure. Thus, we will modify the total energy density as $e^{n+1} = e^n + (\nabla\Phi)^2/2 - \nabla\Phi \cdot \mathbf{B}$.

§ 19.3. *Constrained transport method*

This method is based on a physical interpretation of the induction equation. By taking the divergence of this latter equation, we obtain that the divergence of the magnetic field remains

constant during the time evolution. Thus, it is sufficient to have initially a solution with a divergence free field to ensure this property at further times. The common technique is to use a staggered grid where the magnetic field is not calculated at the cell centers but at the cell edges. The induction equation translates the circulation of the electromotive force along a cell interface. Numerically, one estimates $\mathbf{v} \times \mathbf{B}$ at the cell corners and then using a finite difference discretization for a cartesian grid, one has :

$$B_x^{n+1}{}_{i+\frac{1}{2},j} = B^n_{x\,i+\frac{1}{2},j} + \Delta t \frac{(\mathbf{v}\times\mathbf{B})_{i+\frac{1}{2},j+\frac{1}{2}} - (\mathbf{v}\times\mathbf{B})_{i+\frac{1}{2},j-\frac{1}{2}}}{\Delta y}, \tag{19.65}$$

and similar updates for the other components. Then, the divergence at time n+1 is :

$$(\nabla \cdot B^{n+1})_{i,j} = \frac{B^n_{x\,i+\frac{1}{2},j} - B^n_{x\,i-\frac{1}{2},j}}{\Delta x} + \frac{B^n_{y\,i,j+\frac{1}{2}} - B^n_{y\,i,j-\frac{1}{2}}}{\Delta y}, \tag{19.66}$$

and from Eq. 19.65, we can remark the perfect cancellation of the electromotive force terms and thus that the divergence of B does not change. Thus, the accuracy reached by this method is the round off errors of computers. It is useful to realize that numerically the divergence free property will be satisfied for a particular discretization and consistent boundary conditions. In finite volume methods, we have to use interpolation in time and space to calculate $\mathbf{v} \times \mathbf{B}$ terms at the cell corners from the cell centers values.

§ 20. Boundary conditions

The resolution of equations in physics is always equivalent to solve what one calls an initial value and boundary value problem i.e. besides having modelized the physical system by some equations and choosing an initial condition for it, one has to specify conditions on variables at the boundaries in time or/and space. There are different kind of boundary conditions : Dirichlet boundary conditions when one puts values on variables themselves, Neumann boundary conditions when one specifies values for the derivatives of these variables. In numerical work, this is translated by imposing boundary conditions at the edges of the simulation box on conservative variables or primitive ones to better control for instance the thermal pressure. To prescribe boundary conditions, an extra layer of cells around the computational domain called ghost cells is added where the variable values are updated at each time step. The width of this ghost cell layer depends on the stencil of the scheme directly linked to the order of accuracy of the discretized differential operators. It is usually equal to two cells as many numerical schemes are second order accurate. It is very important to correctly define these boundary conditions in order not to have bias in the numerical results. For instance, one often chooses what is called outflow boundary conditions which corresponds to Dirichlet boundary conditions where values in the ghost cells are just a copy of values at the edges of the computational domain for easiness purposes. Although such a choice can be justified for supersonic flows in hydrodynamic simulations since characteristics are directed out of the computational domain, in other cases, it could destroy the initial equilibrium since it cancels the pressure force for instance. The general way of implementing consistent boundary conditions is to control that only those waves whose characteristics are directed outwards.

2. The VAC code

For simulations presented in this thesis, we use the Versatile Advection Code (VAC). This code was initiated by Gábor Tóth at the Astronomical Institute at Utrecht from November 8 1994. The project was done in a collaboration with the FOM Institute for Plasma Physics, the Mathematics department at Utrecht and the CWI at Amsterdam. In particular, Rony Keppens (FOM), Mikhail Botchev (Mathematics Dept.), and Auke van der Ploeg (CWI) contributed significantly to the development since 1996. The code has been extensively tested (Tóth & Odstril 1996) on standard numerical tests for hydrodynamics and MHD modules. Now, a MPI version of this code exists and very recently an hybrid block-AMR (Adaptive Mesh Refinement) version (van der Holst & Keppens 2007), also in spherical coordinates is released allowing in the near future to carry out very high resolution simulation of the star-disc interaction problem presented in this thesis.

§ 21. Description of the code

For a detailed presentation of the code, we advice the reader to see an introductory level course given by Tóth called "Computational magnetohydrodynamics" in Porto in 1998. This code is written using finite volume methods making it possible to treat correctly discontinuous solutions of a physical problem like propagation of shocks. Flux limiters are used to avoid spurious oscillations that would otherwise occur near shocks which represent discontinuities in the solution domain. They ensure the Total Variation Diminishing (TVD) characteristic of a scheme.

There are different equation modules implemented in VAC : the simple transport equation, the Euler equations for compressible hydrodynamics with adiabatic or full energy equation and the resistive MHD equations with isothermal or full energy equation. We can add extra source terms by writing a subroutine in the vacusr module. The code is written in Fortran90 using the Loop Annotation SYntax (LASY) developed by Tóth (1997) making it possible to write subroutines using a dimension independent notation. A perl script preprocessor is executed to choose the physics module, the dimension of the problem, the numerical methods to compile, the grid size and the name of the vacusr file where the initial, extra source terms and boundary conditions are set up for the problem considered.

There are a series of predefined boundary conditions such as 'fixed' (where we impose the variable value), 'cont' (copy of the variable value just inside the computational box corresponding to Neumann condition), 'grad1' (extrapolation of variables using the initial gradient), 'symm' and 'asymm' for taking into account the symmetry or asymmetry of the variables when one has an axis of symmetry such as the stellar rotation axis or the disc equatorial plane. For instance, the toroidal magnetic field cancels within the disc midplane for a simulation done in axisymmetry and thus one uses the 'asymm' boundary condition for this component whereas the radial and vertical components of the magnetic field are symmetric at this same location. For our purpose, we use complex boundary conditions specially to treat the stellar surface which we code up in the subroutine 'specialboundary'. We will describe our boundary conditions in chapter 3.

§ 22. TVD Lax Friedrichs scheme

In this thesis, we will present results of star-disc interaction simulations using the TVDLF scheme which is second order accurate in time and space.

We explicit the different steps of the scheme as implemented in VAC. From the centered cell values w_{CT} of the grid, one calculates the values at the edges, both for a left value w_{LC} and a right one w_{RC} using the upwind subroutine. This routine makes a linear extrapolation from cell center to cell edge, using a slope estimate from the two adjacent cells. This is done with different slopes limiters defined in the subroutine dwlimiter, in order to ensure the TVD property of the scheme. Thus, the scheme has a stencil of 5 cells.

We solve the equations using cylindrical coordinates. However, the geometry of our problem including the star is spherical. Thus, we use a generalized grid where the grid centers (r, z) follow circles.

Thus, we need to do a change of coordinate frame to be in the local frame linked to the cell normal directions using the rotatew subroutine in vacgrid.gencoord.t in order to calculate correctly the flux balance for each cell. Next, we calculate the velocity components at each cell edge for each side v_{LC} and v_{RC} (using getv in vacphys0.t) to estimate the transport fluxes $v_{LC} * w_{LC}$ and $v_{RC} * w_{RC}$. Then, the flux components f_{LC} and f_{RC} excluding the transport terms are added using the subroutine getflux in vacphys.mhd0.t. We go back to the cylindrical frame with the subroutine addflux rotate. The Lax-Friedrich scheme corresponds to an approximate Riemann solver taking into account only the fastest characteristic speed. Thus, we add to the calculated flux the following term $-\frac{1}{2}c_{max}(w_{RC} - w_{LC})$ which corresponds to a dissipative term stabilizing the scheme. The update of the conservative variables is done using the subroutine addflux which is written in the case of cartesian coordinates :

$$w_{i,new} = w_{i,new} - qdt\frac{(f_{i+\frac{1}{2}} - f_{i-\frac{1}{2}})}{dx_{idim}} \tag{22.67}$$

One finally adds the source terms such as gravity, viscosity or resistivity using the subroutine addsource2 and the geometrical corrections due to curvature terms for non-cartesian grids using the addgeometry subroutine. These latter terms are added in an unsplit way, i.e. we do not separate them according to the direction considered.

We use a Hancock predictor during the half time step to make the spatial reconstruction on variables at each cell edge using time centered values at $\frac{\Delta t}{2}$ for the variables. This makes it possible to better control numerical diffusion and makes the overall scheme second order accurate in space and time for smooth solutions.

§ 23. Practical details of our simulations

§ 23.1. *Resolution and grid*

In order to correctly treat the physics of accretion within the disc and near the stellar surface, it is necessary to have the best spatial resolution. Actually, it is really important to have enough resolution within the disc to well assess the different torques or to have a good approximation of the pressure gradient which play a main role to establish accretion columns as we will see in chapter 4. The best option would be to use an AMR strategy but the code in the spherical

coordinates was not avalaible at the beginning of this work. That is why we use a static radial stretched spherical grid to enhance the resolution at the inner edge of the simulation box (see Fig. 22). The stretch ratio is around 30 i.e. that the cell width at the inner edge is thirty times smaller than the cell width at the outer edge. Thus, we have a better resolution than Romanova et al. (2002) within the disc and funnel flow by a factor 2 since we used a smaller radial range for the physical domain focusing on the disc inner parts and we double the resolution in θ. We define a grid with near isotropic cells to avoid local anisotropic numerical diffusion such that we have 100 uniform cells in the orthoradial direction and 180 points in the radial direction. We can also notice that the radial numerical diffusion is really reduced in the inner parts of such a grid.

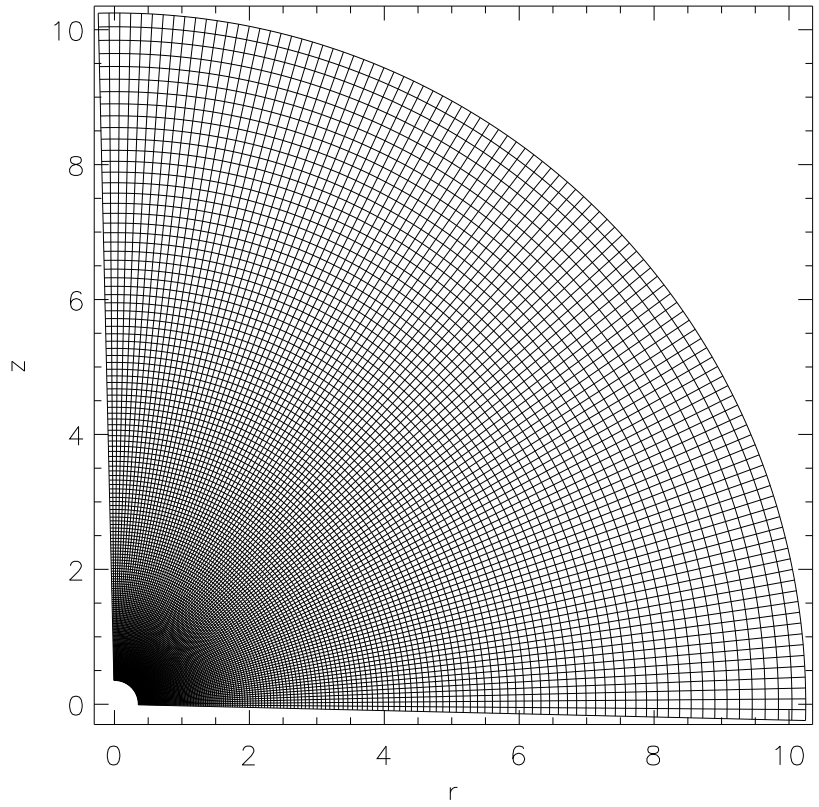

Figure 22. Typical grid used in simulations including the ghost cells layer. The resolution is 174×104 in the radial and orthoradial directions respectively. The intersections in this plot correspond to the cell centers. We can notice the symmetry of the rows at each side of the axis and the equator.

§ 23.2. *Computational time considerations*

To carry out simulations presented in the next chapters, we use local computational resources from the Grenoble observatory (SCCI) with the Icare cluster and from the Leuven cluster (VIC). Typically, we have nodes of quadri-processors Opteron at 2.4 GHz. Simulations done for this thesis are mainly jobs launching on one node and lasting between one week and one month. For instance, simulations in the propeller regime ($B_* = 476G$) take 6 days using autoparallelization

onto 4 processors to do 16 rotation periods at the disc inner edge. Simulations with weaker stellar fields ($B_* = 141G$) last one week to do 63 rotation periods at the disc inner edge using also 4 processors. This corresponds to nearly four months of physical time.

3. Review of previous numerical simulations of star-disc interaction

Before presenting in the next chapter our own modelling of the star-disc interaction problem, we now present an overview of the numerical work done in the last decade, highlighting the different approaches and results found. First, we briefly present long term evolution of the star-disc interaction by including the disc only as a boundary condition and then discuss 2.5 D and 3D simulation results of the full system solving the disc physics.

§ 24. Long term evolution without resolving the disc structure

These simulations are focused on the outflow formation. Fendt & Camenzind (1996) study the collimation of an initially dipolar field into a jet due to the differential rotation using a finite element code to calculate initially a force-free configuration. They consider a dipolar magnetosphere with two initial conditions for the magnetic flux within the disc localized at the edge of the simulation box : a disc wind type mainly focused at the disc inner edge or a constant flux corresponding to a stellar field expelled from the disc. The simulations done in axisymmetry with the ZEUS-3D code (Stone & Norman 1992) last several thousands of keplerian periods at the disc inner edge. The resolution is typically 250×250 for a computational box till 40 R_*. They consider the disc as a boundary condition by prescribing the mass inflow into the corona in hydrostatic equilibrium. They solve the ideal MHD equations considering a polytropic law with $\gamma = 5/3$. They choose an initially numerically force-free distorted dipole field in order to be consistent with the inflow boundary condition in the disc which requires inclined enough magnetic field line to support the launching of a disc wind as described by the Blandford & Payne (1982) criterion. The stellar magnetic field is in equipartition with the disc thermal pressure at the disc truncation radius. They find that the initial magnetic field topology is destroyed by an expanding bubble of hot and low density gas towards the axis. This is due to the winding up of the poloidal magnetic field by the differential rotation with a positive toroidal field for the magnetic field lines anchored within the disc and a negative toroidal field for the stellar magnetic field lines.

A disc wind is formed in the inner parts of the disc with injection velocity around $0.001 v_{K,i}$ and terminal velocities reaching around half of the Keplerian speed. Actually, poloidal magnetic acceleration has no effect since the flow is initially super-Alfvénic and this is a centrifugal acceleration. For a rotating star, they find a transient high speed collimated flow towards the axis similar to Goodson et al. (1997). But the feed-back from the disc is not considered here. Fendt & Elstner (2000) go further with this work by prescribing a stellar wind with a constant velocity initially sub-Alfvénic. The disc truncation radius is now located at the corotation radius. The resulting opening angle of the stellar wind is between 30° and 55° depending on the mass loading ratio between the disc and the stellar wind. These two regions are separated by a neutral line with low density where numerical reconnection happens several times during the

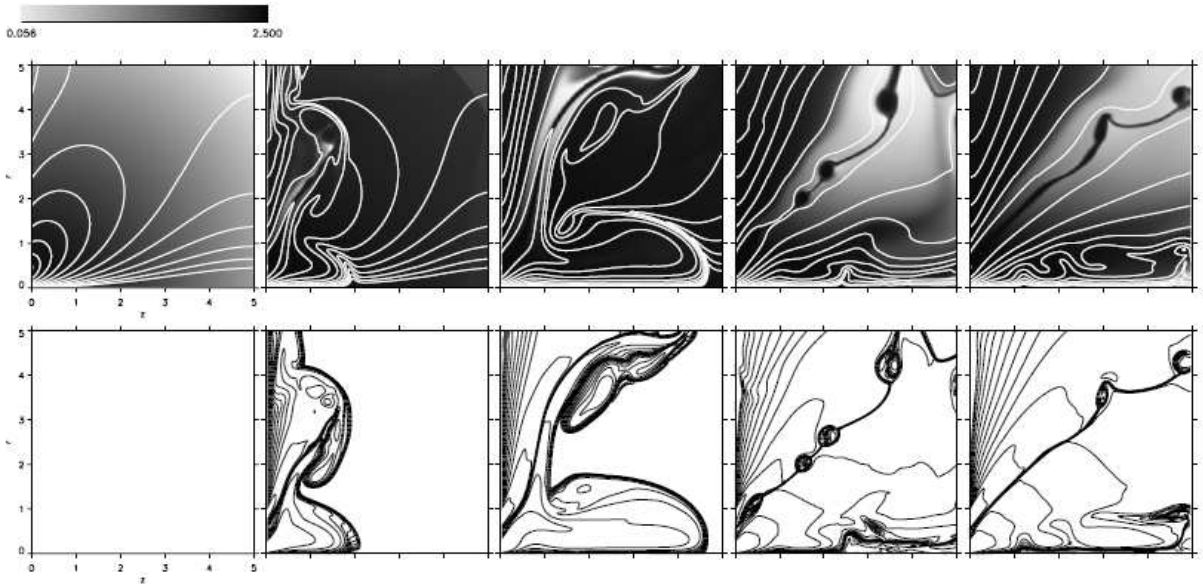

Figure 23. Series of snapshots at t=0,10,20,80,160 $\Omega_K^{-1}(r=1)$ showing the density distribution and the poloidal magnetic field lines (above) and the contours of the toroidal magnetic field (below) for a stellar outflow rate twice lower than the disc one (from Fendt & Elsner 2000). The accretion disc midplane is the vertical axis and the normalized spatial unit corresponds to 2 R_*. From an initially distorted dipolar field, the magnetic field for the stationary state corresponds to a nearly spherical topology. One can remark the formation of several plasmoids in the current sheet oriented at 45° with respect to the disc midplane and also knots within the axial jet.

simulation. Second, a transient axial jet is formed corresponding to the acceleration of the initial coronal material by the expansion of the poloidal field with high velocity around 0.2-0.3 $v_{K,i}$. The opening of the magnetosphere here do not lead to the formation of an X wind as claimed by Shu et al. (1994).

A stationary state is reached after 400 keplerian rotations at the disc inner edge with a spherical outflow topology with two components and no collimation (see Fig. 23). The non collimation of the stellar flow could be due to the lack of a sufficient poloidal current which usually collimates a jet by the hoop stress because one has two opposite electric systems separated by the neutral line. A proper disc magnetic field could support this collimation. No dipolar accretion is observed for different reasons : the initial topology of the distorted magnetic field lines and the position of the truncation radius located at the corotation radius. But the main reason is due to the non treatment of the disc accretion physics as we will explain in chapter 4.

Yelenina et al (2006) study the magnetic field topology dependence as function of the disc diffusivity treating also the disc as a boundary condition in the case of the propeller regime ($r_t > r_{\rm co}$). They consider a radial stretched spherical grid and implement a special boundary condition to take into account consistently the surface disc resistivity by imposing the magnetic flux time evolution and the velocity field using the Ohm's law. They start from a pure dipole magnetic field with $B_* = 300G$ and a differentially rotating magnetosphere and find periodical ejections of plasmoids (corresponding to 10 Keplerian rotations at the disc inner edge) because of the opening of the poloidal magnetic field. The periodicity increases with the disc resistivity since the build up of the toroidal field is less efficient. Moreover, the plasmoid ejection occurs further out from the star in this latter case as the poloidal field is no longer frozen and one has a

magnetic flux diffusion outwards as described by Heyvaerts & Bardou (1996) but disc accretion is not incorporated here.

§ 25. 2.5 D simulations with the dynamical evolution of the disc

Although treating the disc as a boundary condition is interesting in order to reach quickly a stationary state for ejection, it is unavoidable to include the disc structure in the computational domain to correctly describe this complex system. Actually, the accretion physics needs to be resolved to understand the mechanism of disc truncation and polar accretion, and to understand the transfer of angular momentum between the disc and the star via the magnetic field. The drawback of simulations which resolve the disc is to overpass the first numerical transients due to the chosen initial condition in order to be able to draw firm conclusions.

§ 25.1. *Truncation of discs and formation of accretion columns*

Miller & Stone (1997) carried out resistive MHD simulations with the Zeus code using a uniform spherical grid with $(N_R, N_\theta) = (100, 50)$ extended up to 4 stellar radii for a few Keplerian stellar periods. They consider a thin cold and resistive disc embedded in a low density isothermal magnetosphere with a contrast of density of 100. The magnitude of the resistivity is too small ($\alpha_m \approx 0.001 - 0.1$ and uniform within the disc) to avoid strong advection of the poloidal magnetic field with the accretion. Then, this unfavored field topology prevents matter from being lifted up along the magnetospheric field. This effect is increased for a rotating star. Thus matter accumulates at the inner edge and the ram pressure dominates at a certain moment because of efficient angular momentum extraction within the disc due to the channel flow solution of the Magneto Rotational Instability (MRI). As a result, even for strong stellar field ($B_* = 1kG$) at equipartition initially with the disc thermal pressure, they find equatorial accretion (see Fig. 24). They also consider configurations where a parallel disc magnetic field is in equipartition with the stellar field at the disc inner edge giving rise to an X point in the disc midplane. In those cases as also in Hirose et al. (1997), they found polar accretion, since there is no more magnetic tension effects preventing matter from being lifted up.

Kuker et al. (2003) study the star-disc interaction including an α type viscosity ($\dot{M} \sim 10^{-7} M_\odot.yr^{-1}$) and diffusivity within the disc. They also take into account radiative energy transport by a flux-limited diffusion approximation in order to have a stable accretion disc for long term evolution. Their domain starts at 1.7 R_*. They consider a solar mass star with $R_* = 3R_\odot$ and $P_* = 5.6$ days. They find a disruption of the disc only for strong stellar magnetic field $B_* > 1 - 10$kG. Actually, for $B_* = 100$G, the truncation radius defined by equipartition between thermal pressure and magnetic pressure is below the inner edge of the computational domain as shown in chapter 4. Thus, they have too weak field ($\frac{B^2}{\rho v_\Phi^2} \approx 10^{-4}$) with respect to the accretion rate to avoid direct accretion from happening. For $B_* = 10$kG, one has a truncated disc at $R = 10R_*$ beyond the corotation radius with no accretion columns observed. With the radiation transport switched on, the truncated radius is closer to the star at $8R_*$ and one has a cooler corona with $T \sim 5000$K.

Contrary to the previous studies, Romanova et al. (2002) start from an equilibrium solution with a differentially rotating corona at the same speed as the disc using a larger scale domain. This is extended up to 1.47 a.u. but with the same resolution at the stellar surface as Miller

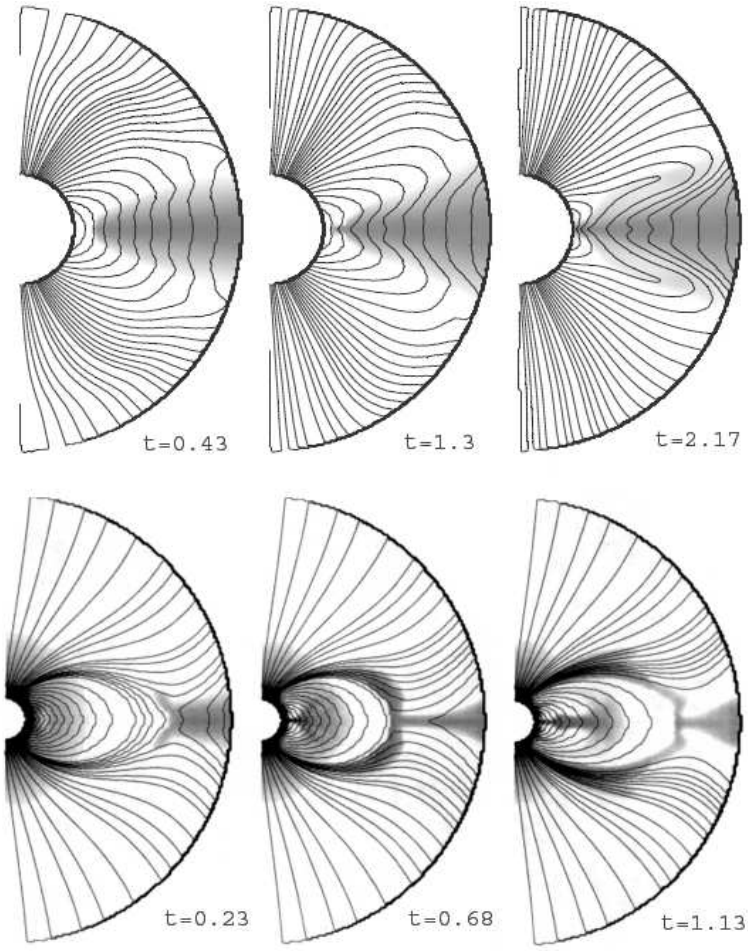

Figure 24. Two types of simulation with different magnetic initial configuration with the resulting accretion process used in Miller & Stone (1997). Above : A pure dipolar field (even strong) gives direct equatorial accretion due to efficient angular momentum extraction within the disc by the MRI well visible with the kink on the magnetic field lines in the disc. Below : A disc magnetic field is added with the same polarity as the stellar magnetic moment which gives rise to an X point allowing polar accretion. Time unit corresponds to the Keplerian period at the stellar surface.

& Stone (1997) thanks to a radial stretched spherical grid ($(N_R, N_\theta) = (150, 51)$). Moreover, they use a Roe type solver written directly with the vector potential field $\mathbf{A}$ ($\mathbf{B} = \nabla \times \mathbf{A}$). For the first time, one observes the formation of accretion columns for purely stellar dipolar field without additional disc field. The initial condition includes a disc with an α type viscosity, but it is not initially a standard accretion disc since density increases outwards with a pressure gradient directed inwards, slightly super-keplerian as we can see on hydrodynamic simulations with $\alpha = 0$. The accretion is larger at the disc surface with respect to the disc midplane like we will show in chapter 3. This explains the evolution of the magnetic topology, since because of lack of disc diffusivity, all the magnetic flux is driven inwards, particularly in the case where the disc inner edge starts initially from the corotation and $r_t << r_{\rm co}$. Thus, the initial solution is really disturbed since we have finally radial magnetic field lines (with a star-disc connection focused on the disc inner edge) within the disc (see Fig. 25a) and the accretion rate is always increasing because of the accumulation of the magnetic flux. The simulation is thus stopped since the truncation radius goes inwards and lasts 50 rotation periods at the disc inner edge.

The truncation radius is determined initially by the equipartition between the magnetic pressure and the disc kinetic pressure and is well below the corotation. It disappears for $B_* < 200G$ and typical accretion rate onto the star around $8.10^{-8} M_\odot.yr^{-1}$, and one has direct equatorial accretion. The stellar period is 9 days. The structure of the funnel flow itself is studied. Within the accretion column, they found sub-Alfvénic but supersonic flows ($v_p/v_A < 0.1$ and $m_s \sim 4$) and sub-keplerian rotation with small twisting of the poloidal magnetic field ($B_\phi/B_p < 0.3$). The force responsible for the lifting-up of matter is the thermal pressure and then gravity causes acceleration of matter till near free-fall speed. The magnetic force has no dynamic effect contrary to the Li & Wilson (1999) predictions.

§ 25.2. *Time evolution of the magnetic topology and angular momentum balance*

Romanova et al. (2002) observe an opening of the magnetic field lines because of differential rotation at large distance but not near the star because of relatively high coronal density which prevents the opening to occur. The spinning-down of the star is mainly due to the twist of the opened field lines connected to the star, similar to a magnetic tower effect. Thus, there is a numerical bias since the corona has a heavy density which amplifies the braking torque. Since the disc structure is highly perturbed and fairly thick, one can wonder if the funnel flow formation and its evolution in time in relation with the global angular momentum balance is influenced by this specific initial disc structure and resulting magnetic flux distribution. We will discuss this point in chapters 4 and 5.

Long et al. (2005) use the same initial condition as Romanova et al. (2002) to study the existence of a disc-locking state i.e. a given configuration with $B_*, \Omega_*, \dot{M}$ where the angular momentum brought by accretion and the magnetic torque within the funnel is exactly balanced by magnetic braking torques in order to have a star which is locked at a constant rotation rate. The angular momentum due to accretion is always negligible with respect to one stored by the magnetic field. Thus, they find a solution where the global magnetic torque is nul on average at the stellar surface over 200 rotation periods at the disc inner edge. This corresponds to $r_{\rm co} \sim 5R_*$ i.e. $P_* \sim 4.5$ days for $B_* = 2kG$ and $\dot{M} \sim 2.2 \times 10^{-8} M_\odot.yr^{-1}$. The truncation radius is then $r_t \sim 3.6 - 3.9R_*$. For a stronger field $B_* = 10kG$ and a coarser grid $(N_R, N_\theta) = (91, 31)$, they find a different locked state with $R_{co} \sim 9.2R_*$ i.e. $P_* \sim 10.4$ days and $r_t \sim 6.2R_*$ for $\dot{M} \sim 3.6 \times 10^{-8} M_\odot.yr^{-1}$. In all cases, they find $r_t/r_{co} \sim 0.67 - 0.78$. Outside this locked state when $r_t/r_{co} < 0.67$, the spin-up of the star is reduced when the stellar magnetic field increases or viscosity decreases. But there is still the same bias than previously with a perturbed magnetic structure due to ideal MHD conditions with a closed magnetosphere just at the disc inner edge (see Fig. 25a). With this restricted closed magnetosphere, the braking of the star, which counteracts the accelerating magnetic torque within the funnel, comes from the opened field lines anchored within the star and is not properly a "disc-locking" state in the Ghosh & Lamb (1979) sense but instead a kind of stellar wind as proposed by Matt & Pudritz (2005). The significant braking obtained here is due to the choice of the initial condition with a corona not magnetically dominated and the result is model dependent. The case with stronger stellar field $B_* = 10kG$ and lower coronal density shows that the braking by the magnetic tower is really reduced and negligible and the dominant braking torque comes from the stretched radial field lines connected to the star which are partly embedded within the disc. A striking fact is that the change of sign for the angular momentum transport is below r_{co} as if the star spins quicker

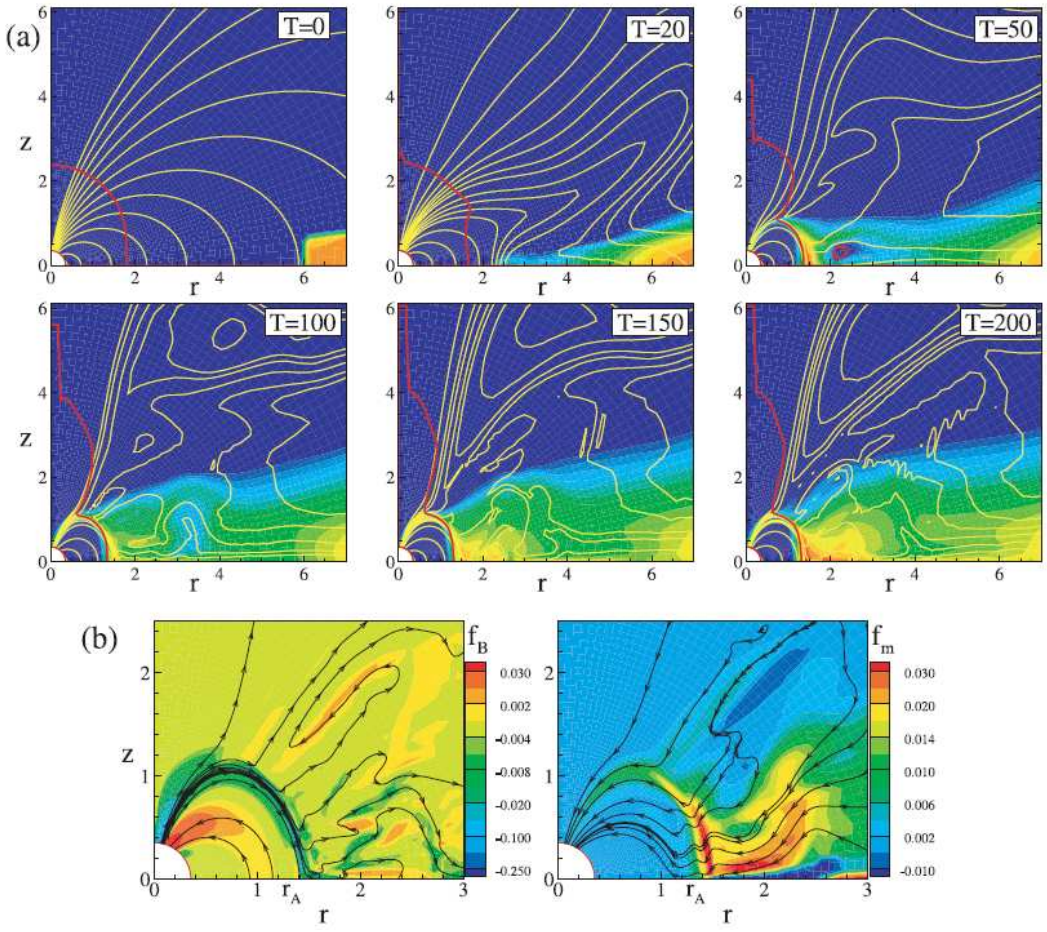

Figure 25. a- Time evolution of an ideal MHD simulation with the setup defined in Romanova et al. (2002) including a viscous disc ($\alpha_\nu = 0.02$) and $R_{\rm co} = 1.7$ (from Long et al. 2005). b-Angular momentum fluxes brought by matter f_m and by the magnetic field f_B. The reversal of sign of the angular momentum flux transported by the magnetic field is well below the corotation at $r \sim 1.2$.

than initially prescribed in the boundary conditions (see Fig. 25b). This probably underlines the difficulty to correctly compute the magnetic stresses using a simple outflow boundary condition for B_ϕ.

Another more general remark is that even though simulations found a star with a locked rotation rate, extrapolation of simulations results on longer timescales have to include the spin up of the star due to contraction (see Chapter 1 and e.g. Bouvier et al. 2007) and thus it is still necessary to find a more efficient way to extract angular momentum, for instance by X winds or reconnection X-winds as discussed in Chapter 1. In other words, to really have a disc-locking state, it is necessary to have a global magnetic braking in simulations to balance the contraction process on longer timescales and not only a global torque nul on average on dynamical timescales.

The initial condition of Kuker et al. (2003) entails the opening of the magnetic field in the outer parts ($R > 8R_*$) with ejection at 45° at an efficiency around 10 %. Actually, the outflow boundary conditions near the star causes a Bondi type accretion with accumulation of matter around the star and vertical compression of the magnetosphere. The disc resistivity is not

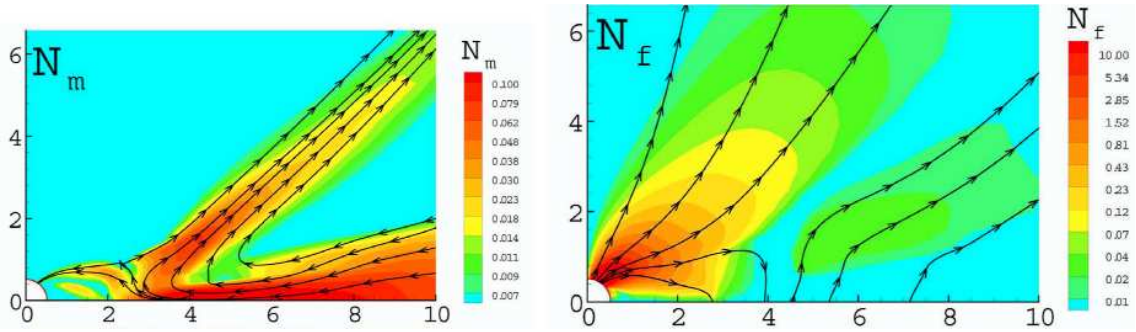

Figure 26. Angular momentum fluxes brought by matter N_m and by the magnetic field N_f in the propeller regime (from Romanova et al. (2005)).

sufficient to prevent the poloidal field from opening and finally, the disc and the star are no longer connected. Thus, stellar braking can only come from the opened field lines connected to the star, but the accretion torque still dominates and the star is therefore spun up.

§ 25.3. *Ejection processes resulting from the star-disc interaction*

Romanova et al. (2004a,2005), Ustyugova et al. (2006) investigate the case of the propeller regime where the corotation radius is smaller than the truncation radius ($r_{co} < r_t$). The star rotates between 58 % and 82% of the breakup speed. The simulations last 2000 stellar rotation periods but the resolution is lower than previously (only 30 points for the angular direction). Now, a sub-Keplerian accretion disc with both viscosity and resistivity is used with typically $\alpha_m = \alpha_v = 0.2$ prescription as defined in chapter 3. The simulation lasts 2500 stellar rotation periods which is really huge and lets us see many oscillations of the disc truncation radius with periodic opening of the magnetosphere and linked ejections. The period of oscillations increases with the stellar magnetic moment and rotation rate. There are both a vertical expansion of the magnetosphere with a magnetic tower configuration and a radial expansion of it. Then, there are two kinds of configurations according to the amount of disc dissipation at the disc inner edge. In the case of weak disc dissipation ($\alpha_v = \alpha_m \sim 0.02$) like in Romanova et al. (2004), the magnetosphere does not rotate rigidly and tends to the disc Keplerian speed at r_t. Thus, there is no strong centrifugal outflow as we can expect for a solid rotation of the magnetosphere . An elongated transient funnel flow can therefore be formed by accumulation of mass at the disc inner edge due to viscosity and matter is stacked near the magnetic tower till the ram pressure is sufficient to produce reconnection and entails episodic accretion onto the closed magnetosphere. In the case of higher disc dissipation ($\alpha_m = \alpha_v = 0.2$), disc material diffuses in an easier way through the magnetosphere and can acquire angular momentum from the super-Keplerian rigid rotation and then is expelled in outflows by the centrifugal force.

Angular momentum is extracted from the star both by the magnetic tower wind and by the ejection along the neutral line (see Fig. 26). The rate of spin down increases as the accretion rate increases, which is really different from the non propeller regime. A parameter space study shows that strong outflows reaching escape velocities are only found for sufficiently high viscous disc with $\alpha_v > 0.1$. Ejection happens mainly along the magnetic neutral line and thus is centrifugally and thermally driven. As the viscous heating seems to be permitted contrary to our simulations in chapter 5, it could enhance thermal pressure at the disc surface. Besides, higher

viscosity provides a further penetration into the magnetosphere and thus a greater centrifugal support for outflows. The ejection efficiency also increases with the stellar magnetic strength and rotation rate. But too high disc diffusivity restricts it since the angular momentum transfer between the disc material and the magnetospheric field is reduced in that case.

Hayashi et al. (1996) start from an unstable initial condition with a non rotating star and corona which maximizes the magnetic torques. They have a non viscous and non resistive Keplerian disc but include an anomalous resistivity when the current exceeds a fixed initial threshold (they impose the reconnection rate by this way). They only study (because of too short computational time, lower than a keplerian period) the expansion of the poloidal magnetic field predicted by Lovelace et al. (1995) and the ejection of a first low density plasmoid at small scale (< 0.1 au) but with high resolution $(N_R, N_\theta) = (300X360)$.

Goodson et al. (1999) go on with this study on a larger scale (till 26 a.u. to study the outflow formation) with high resolution ($0.1R_\odot$) near the star and longer term evolution (130 days). They take into account a rotating ($P_* = 1.8$days) solar mass star with $R_* = 1.5R_\odot$ and $B_* = 500G$. They consider a viscous ($\alpha_\nu \sim 0.2(r/1a.u.)^{-1.5}$ or $\dot{M} = 10^{-7}M_\odot.yr^{-1}$ close to the star) and highly conductive disc truncated at $8.5R_\odot$ (uniform conductivity) beyond the corotation $r_{\rm co} = 6.3R_\odot$ corresponding to a propeller regime. The disc is rather thick ($h/r \sim 0.3$). They observe periodic cycles of accretion-ejection lasting 25 days linked to reconnection events because of huge viscosities within the disc ($\nu \sim 5.10^{16}$cm^{2}s^{-1} at $10R_\odot$ ten times greater than resistivity) and diffusivity in the corona enhancing reconnection events. A two-component outflow is formed from the inflation of the magnetic field and is sustained through reconnection events and the condition that there is accretion between reconnections to feed the jet i.e. one needs to be below corotation. The plasmoids separate the internal collimated jet from the disc wind component. Contrary to a steady state model like Ghosh & Lamb (1979), angular momentum is extracted from the disc beyond the corotation thanks to the disc wind. There is a global braking torque on the star due to the stellar jet with an average spinning down time of $2.5.10^5$ yr consistent with observations of jets lifetime (Reipurth, Bally & Devine 1997). This torque is well reduced at each reconnection event. Increasing the resistivity gives shorter cycles and smaller truncation radius. Hayashi et al. (1996) and Goodson et al. (1999) use a thin corona with a rapid drop in density as R^{-4} which enhances the opening of the magnetic field lines because of high Alfvén speeds decreasing slowly as r^{-1} as discussed in Romanova et al. (2002).

von Rekowski & Brandenburg (2004) consider also a proper disc magnetic field including dynamo effects within the disc in the anti-parallel direction with respect to the stellar field. They found that MHD outflows can be formed in this configuration and accretion is really unsteady but periodic as in Goodson et al. (1999). Angular momentum exchange is really complex with some part of the star which can be spun up whereas other parts can undergo braking. von Rekowski & Brandenburg (2006) including also a stellar dynamo with complex multipolar components show that high stellar magnetic fields can be reached till 750G. In this case, accretion occurs mainly at low latitudes and is no longer quasi periodic. But the main drawback of their simulation is that they do not ensure the mass conservation (a density threshold is fixed) in the disc and thus accretion processes are not correctly controlled.

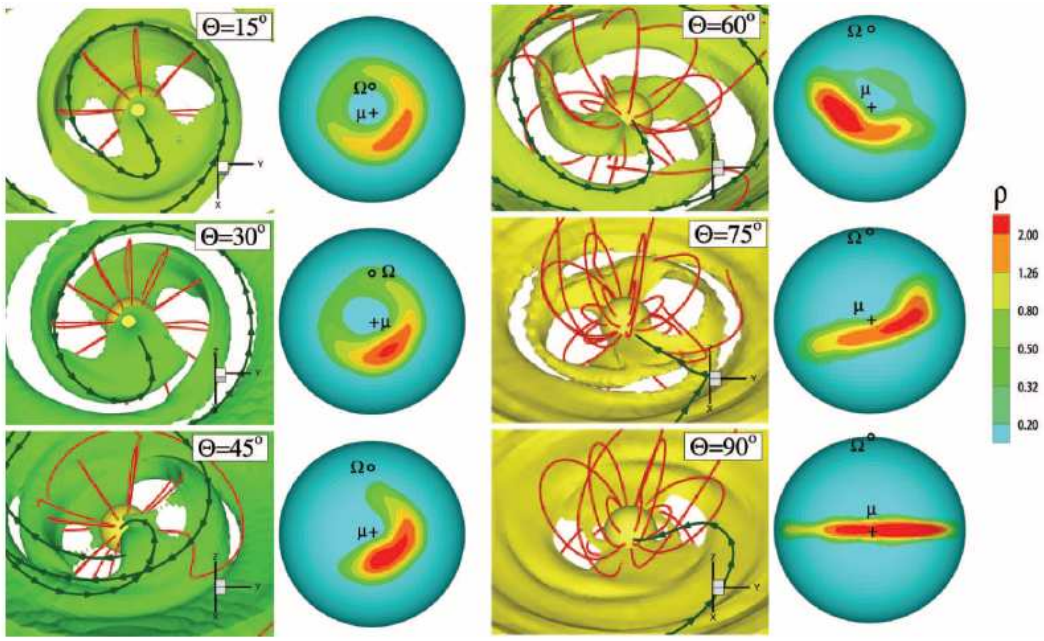

Figure 27. Topology of the funnel flow accretion as function of misalignment angle θ and the corresponding hot spot position at the stellar surface. Simulation from Romanova et al. (2004b).

§ 26. 3D simulations

3D simulations have been recently performed by the group of Romanova (Romanova et al. 2003, 2004b, Romanova et al. 2006) for a tilted dipole and more complex stellar field with multipolar components (Long et al. 2007). These simulations open the possibility to really compare theory versus observations thanks to the introduction of inclined magnetic field with respect to the stellar rotation axis which makes it possible to introduce some variability as one really observes (Bouvier et al. 2003,2006). Synthetic spectra from these simulations can be extracted (Kurosawa et al. 2006, 2008) which provides a theoretical background to interpret complex features in high resolution spectra.

§ 26.1. *Accretion columns and hot spots*

3D simulations by the Romanova group use a special ideal MHD code solving the equations in the stellar rotating frame and a splitting strategy for the magnetic field. A specific "cubed-sphere" grid developed by Koldoba et al. (2002b) is defined corresponding to nearly the same spatial extension as in 2D (extended up to $45R_*$) with a resolution of $(N_R, N_\theta, N_\phi) = (70, 58, 119)$. Disc viscosity initially ignored in these simulations has been incorporated in Romanova et al. (2004b) and Long et al. (2007) but no mass feeding at the outer edge is allowed which is not crucial for the timescales around ten rotation periods at the disc inner edge reached till now.

For small misalignment angles of the magnetic axis with respect to the rotation one ($\theta < 30°$), Romanova et al. (2003) observes two streams of accretion reaching the stellar surface at high latitude. At higher misalignment angles ($30° < \theta < 60°$), the accretion splits into four streams (see Fig. 27). At even larger ones, one has mainly direct accretion onto the magnetic poles. One obtains similar accretion truncation radii as in 2D for small misalignment ($\theta < 30°$) but the disc

is warped, specially in the direction of the remote magnetic pole. The magnetospheric accretion shape depends on the density since large densities give narrow streams while lower ones give much wider accretion flows.

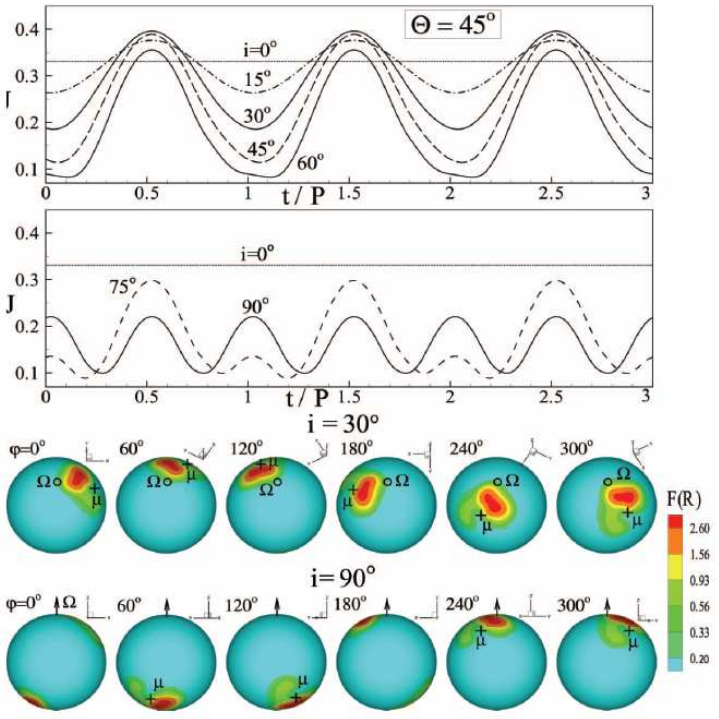

Figure 28. Light curves as function of the inclination angle for a configuration with a misalignment angle $\theta = 45°$. Bottom : the energy flux distribution in the hot spots are shown at the stellar surface for different phases of a rotation period. Simulation from Romanova et al. (2004b).

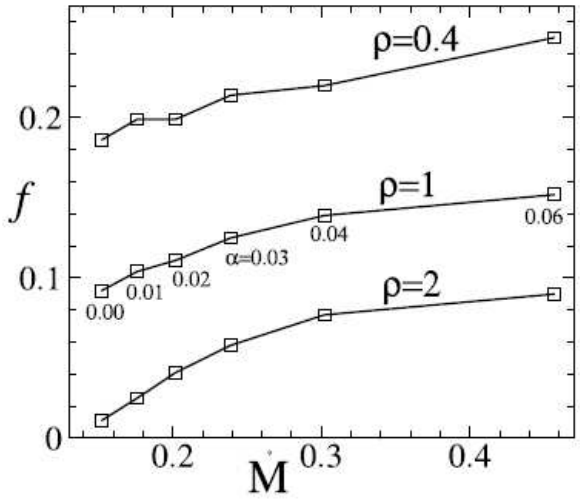

Figure 29. Fraction of the star f covered by hot spots as function of accretion rate $\dot{M}$ and density levels ρ in the hot spots. The reference values are $\dot{M}_0 = 1.9 \times 10^{-7} \mathrm{M}_\odot \mathrm{yr}^{-1}$ and $\rho_0 = 4.9 \times 10^{-12} \mathrm{gcm}^{-3}$. Simulation from Romanova et al. (2004b).

The different position and shapes of the hot spots due to these different geometries (see Fig. 28) give rise to a wide range of variabilities for instance in the deduced light curves. Finally, the filling factor due to hot spots is found to increase with the disc accretion rate and the disc density (see Fig. 29). These filling factors are consistent with observations (see chapter 1).

In the case of pure quadrupolar field inclined with respect to the rotation axis, the accretion flow arrives at the magnetic equator belt but is not axisymmetric. In the case of a mixed and similar magnitude dipole/quadrupole magnetic components inclined with respect to the rotation axis, the accretion flow is more complex with still accretion within the magnetic belt but this latter has moved towards the lower magnetized pole due to the quadrupolar component. In high inclined configurations, matter can also accrete towards the magnetic poles. Otherwise, the hot spots are more brighter with a dominant dipole field since matter is accreted further out along the magnetosphere.

§ 26.2. *Other sources of variability such as the Rayleigh-Taylor instability*

For small inclination angle ($\theta < 30°$) and including some disc viscosity in 3D simulations, Kulkarni & Romanova (2007) observe direct accretion onto the stellar equator with thin tongues of matter which cross the closed magnetosphere in dynamical timescale (see Fig. 30). Near the star, matter follows the magnetic field lines forming "miniature funnel-like flows". Accretion of matter within a tongue conserves its angular momentum contrary to material within the funnel flow. The number of tongues varies between 2 and 7 and is highly time dependent introducing high variability with no clear periodicity in the light curves. This instability is triggered for sufficient amount of viscosity ($\alpha > 0.04$) which brings much matter at the disc inner edge and thus enhances its accumulation. This behaviour is a characteristic of magnetic Rayleigh-Taylor instability.

For higher inclination, the instability is no longer present because funnel flow formation is energetically more favorable.

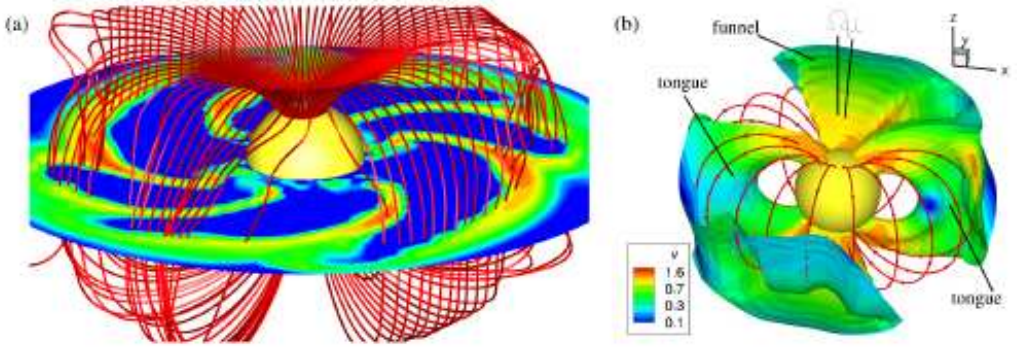

Figure 30. (a) Density distribution in the equatorial plane showing penetration of tongues of matter through magnetosphere in the presence of disc viscosity with $\alpha_m = 0.1$. (b) Contours of the velocity profile within the funnel flows and tongues for a constant density surface (from Kulkarni & Romanova 2007).

3

MHD model of the star-disc system

Chapter content

In this chapter, after having checked the relevance of using MHD for describing our problem, we explicit how we modelize the accretion disc including both viscosity and diffusivity. Next, we present how we treat the star-disc interaction by imposing specific boundary conditions at the inner edge of the simulation box to mimic the stellar magnetosphere. We further assume axisymmetry and use a splitting strategy for the magnetic field to ensure accurate magnetic force calculations.

1. The validity of MHD in this context

The MHD formalism treats the global interplay between a conductive fluid and the embedded electromagnetic field. The validity of the fluid approach needs enough particle density at the Debye scale and a negligible velocity drift between the species (e.g. ions and their orbiting electrons) which constitute the plasma, making it possible to consider the plasma as a single

fluid. It is also necessary to have a sufficient ionization rate to have a coupling with magnetic fields.

In a thin Keplerian accretion disc, vertical hydrostatic equilibrium gives a thermal pressure equal to $P = \rho\Omega_K^2 h^2$ from which one can deduce the midplane temperature distribution $T \sim \frac{m_i}{k_B}\Omega_K^2 h^2 = 10^6 \frac{M_*}{M_\odot}\frac{r}{0.1\text{a.u.}}\epsilon^2 K$ where $\epsilon = \frac{h}{r}$. For $\epsilon = 0.05$, one has T=2500 K at r=0.1 a.u. which is well above the dust sublimation temperature and this indicates that the inner parts of discs are dominated by gas. Then, one can deduce the mean plasma density n by assuming a constant accretion rate and typical radial velocities around the sound speed since the inner part of the disc is controlled by the magnetic field (see chapter 4) hence : $\dot{M} = 4\pi r n m_H^+ c_s h$ where $c_s = \Omega_K h$ and thus :

$$n = \frac{\dot{M}}{4\pi m_H^+ \sqrt{GM_*}\epsilon^2} r^{-\frac{3}{2}} = 1.14 \times 10^{19} \frac{\dot{M}}{10^{-7} M_\odot yr^{-1}} (\frac{M_*}{M_\odot})^{-\frac{1}{2}} (\frac{\epsilon}{0.05})^{-2} (\frac{r}{0.1 a.u.})^{-\frac{3}{2}} m^{-3}. \quad (26.68)$$

The ratio between the Debye length $\lambda_D = \sqrt{\frac{\epsilon_0 k_B T}{ne^2}}$ characterizing the range of the Coulomb electrostatic interaction in the plasma and the scale height of the disc h at r=0.1 a.u. is then equal to $\frac{\lambda_D}{h} = 9.8 \times 10^{-7}/hm = 1.3 \times 10^{-15}$. Thus, the plasma is globally neutral. Moreover, one has $n\lambda_D^3 \gg 1$ which validates the fluid approach.

One can now estimate the drift velocity $|u_e - u_i|$ between ions and electrons from the typical current density J_0 throughout the plasma and compare it with the typical Alfvén velocity v_A :

$$\frac{|u_e - u_i|}{v_A} = \frac{J_0}{n_e q_e v_A} = \frac{B_0}{n_e q_e \mu_0 h v_A} = \frac{r_0}{h}, \quad (26.69)$$

where $r_0 = \frac{c}{\omega_p}$ is the ion Larmor radius and $\omega_P = \sqrt{\frac{ne^2}{m_e \epsilon_0}}$ is the plasma frequency. Typically, $r_0 = 1.6 \times 10^{-3} m$ and thus, the drift is totally negligible and the MHD model which is a one fluid treatment is sufficient.

If one now considers the physical property of a stellar magnetosphere, for a mean density of $n_e = 10^7 m^{-3}$ and $T \sim 10^6 K$, one finds $\lambda_D \sim 20m$ which is still small with respect to the stellar radius. Hence, the use of a continuous fluid model even in this dilute medium is still appropriate.

2. The accretion disc model

Accretion discs around YSO have typically a broad radial range extended from a few stellar radii till several hundreds a.u. (see millimetric observations of CO molecular lines e.g. by Dutrey at al. 1996). The stellar magnetic field decreases quickly with distance and since we want to study the magnetic influence of the star onto the circumstellar disc, we focus on the inner parts of the disc below 1 au, which also allows us not to waste computational time.

§ 27. Design of an equilibrium initial condition

The atmosphere around the accretion disc is called here 'corona'. In reality, there is a sharp transition between the accretion disc and the surrounding medium, but it is necessary not to have too low density for computational reasons. Thus, we define a low density corona with enough density contrast with respect to the disc (typically > 100) which is in pressure equilibrium with the disc. This implies for an isothermal equation of state a hot corona ($T \sim 10^6 K$). We can

argue that this corona is heated by the radiation field of the interstellar medium and(or) the star, or by reconnection events in the magnetosphere. But it is a mere bias imposed by simulations forbidding direct use of them for computing radiative transfer.

The idea is to find a solution for a disc in equilibrium with the atmosphere. In order to limit the numerical transient because of the strong stellar field near the stellar surface, one needs to truncate the disc before it reaches the stellar surface. To ensure pressure equilibrium with the corona at the disc inner edge, there are different strategies. One can adjust the corona pressure while ensuring enough density contrast between disc and corona. One always choose a disc pressure decreasing like $r^{\frac{-5}{2}}$ compatible with stationary Keplerian accretion disc models and temperature law decreasing outwards like r^{-1} which gives a constant opening angle for the disc. The first initial condition we construct takes into account an isothermal corona. In that case, one can always find a truncation radius but the density towards the star increases too quickly and it becomes difficult to follow correctly the accreting material onto the star (see e.g. Bessolaz et al. 2006). The advantage of high densities at the stellar surface is to limit the drop of the time step in computations. Thus, we finally choose an adiabatic corona with the same polytropic index as the disc but in this case, we can not ensure pressure equilibrium at the inner edge since disc and corona pressures have the same dependency on r. However, the deformation of the dipolar field quickly balances the jump in pressure due to truncation. In these solutions, one imposes a non rotating corona which implies an initial shear at the disc-corona transition. We detail this initial condition in chapter 4 and use it for the simulations presented in chapters 4 and 5.

The interesting method of Romanova et al. (2002) is to find a corona which rotates at the same speed as the disc in order to avoid transients and at the star speed below the truncation radius by balancing the centrifugal force, pressure and gravity assuming an isothermal equation of state. However, this gives a disc structure where the density increases outwards, a pressure gradient directed inwards which demands a slightly super-Keplerian rotation and a constant sound speed within it. This results in large accretion rate considering α type viscosity even in the disc midplane as shown in this chapter. Moreover, the disc is pretty thick which could be a bias making easier polar accretion and we will discuss this in chapters 4 and 5.

We find it is possible to construct a solution where one can prescribe a differential rotation along magnetic field lines to avoid the initial shear while conserving a standard model for the accretion disc. We impose that a magnetic field line rooted inside the disc rotates with the same Keplerian speed as the footpoint. Initially, we consider a purely dipole field. Each dipolar magnetic field line is described by $R = R_0 sin^2\theta$ in spherical coordinates and hence $r = r_0 sin^3\theta$ in cylindrical coordinates where r_0 identifies the magnetic field line whose footpoint is at r_0 in the disc midplane. The rotation law within the disc at r_0 is then prescribed to be $v_d = \sqrt{\frac{GM_*}{r_0^3}}$. By replacing r_0 by the equation of a dipolar magnetic field line, one obtains the rotation law throughout the domain : $v_d = \sqrt{\frac{GM_* r^8}{R^9}}$ using $sin\theta = \frac{r}{R}$. We then make a correction on density in order to balance gravitational and centrifugal forces perpendicular to the magnetic surfaces. Below the disc truncation radius, the corona turns either with the stellar angular velocity or with a smoother profile till the stellar rotation profile. We do not present simulations using this last setup in this thesis.

§ 28. Temperature in simulations

In our work, we do not solve radiative transfer equilibrium to find the temperature distribution. We just assume that any heating source term within the disc like viscous or ohmic ones are directly radiated by removing the appropriate terms in the equations as discussed further in this chapter. Thus, we treat our disc as an optically thin medium by assuming a cooling term function exactly balancing the heating. This is the crudest but simplest way to avoid disc thermal instabilities to develop in long term simulations because of accumulation of heating. Actually, one expects that for the temperature and density distributions considered, one has an optically thick medium where it is crucial to choose the correct opacity regime. The weak point is that we hope that the dynamical behaviour is not too dependent on the radiative processes which is not obvious but commonly accepted as a first step towards more realistic simulations.

To interpret observations, models assume an optically thick medium which radiates the viscous energy release like a blackbody at each distance and gives a typical effective temperature distribution $T(r) \propto r^{-\frac{3}{4}}$. To reproduce the flat SED in mid-IR observed in T Tauri disc, one needs to take into account the stellar radiation field which heats a flared disc surface and dominates in the outer parts of the disc. All the observational data refers to surface temperature because of the medium opacity. The vertical hydrostatic equilibrium and the disc thickness imposes the midplane temperature which is the only quantity we control in our model. For computational reasons, we can not choose a too small aspect ratio. We fix $\epsilon = 0.1$ which gives an equatorial temperature at the disc inner edge a bit hot, namely $10^4 K$.

§ 29. The issue of the viscous torque

It is really important to have a correct description of an accretion flow within the disc far from the magnetized central object in order to treat in a next step the interaction with it. Besides, it is necessary to have accretion in the propeller configuration where the magnetic field has a dynamical effect beyond the corotation radius, accelerating matter.

Astrophysical accretion discs are powered by the release of gravitational potential energy as gas spirals down onto the central object. The dynamics and evolution of accretion discs depend upon how angular momentum is transported outwards from one fluid element to another. In astrophysical fluids orbiting around objects such as stars or compact objects, we indirectly detect accretion flow from continuum emitting spectra in IR for YSO, in X rays for X-ray binaries. We deduce from this radiation estimates for accretion rates which are enormous with respect to what is expected from classical molecular viscosity calculated from local properties of the plasma. The Reynolds number inferred from observations reaches $Re \sim 10^{15}$ which shows an unavoidable turbulent origin for this efficient transport. However, many theoretical studies have tried to understand which physical processes can trigger this turbulence with not yet a complete understanding. We sum up here the main results. Firstly, people have tried to use local hydrodynamic processes. The main point is that Keplerian flows are linearly stable with respect to rotation (Rayleigh criterion : $\frac{d}{dr}((\Omega r^2)^2) > 0$). Convection instability triggered by the energy release in the midplane gives transport of the angular momentum in the wrong direction (inwards) with too small efficiency ($\alpha \approx 10^{-4}$, Stone & Balbus 1996). Recently, Lesur & Longaretti (2005) using shearing box simulations have shown that non linear hydrodynamic instability can

only reach at best $\alpha \approx 10^{-5}$. In the case the plasma is sufficiently conducting, the presence of a weak magnetic field ($\beta \geq 1$) rapidly generates magnetohydrodynamical turbulence via a linear instability (Velikhov 1959, Balbus & Hawley 1991). Different α values were obtained for this MRI instability from 10^{-3} till 0.2 depending on the field topology. The largest values are obtained with a net flux of the poloidal magnetic field whereas the lowest are found with purely toroidal field (King et al. 2007). Although the MRI instability seems to saturate near equipartition, stability studies in the cylindrical limit (variable profiles depending only on radial coordinates) also show overstability in this parameter range when there is a dominating toroidal field ($\frac{B_\phi}{B_p} = 10$, see Blokland et al. 2005). Recently, Lesur & Longaretti (2007) shows a correlation between the transport efficiency and the magnetic Prandtl number Pm (defined from the microscopic viscosity and resistivity values explicitly introduced in their simulations) and reach $\alpha \sim 1$ for $Pr_m \sim 10$.

In any case, all these numerical studies locally calculate the α parameter from second order perturbations of the velocity flow $< \delta v_p . \delta v_\phi >$ and the magnetic field $< \delta B_p . \delta B_\phi >$ but it still lacks consistent parametric models to include the turbulence behaviour into global simulations. That is why global simulations of astrophysical objects still need to use a pragmatic approach to take into account dissipative physical processes like viscosity or resistivity by including ad hoc macroscopic parameters while ensuring to diminish the erratic influence of numerical dissipation. For instance, to include astrophysical magnitude of viscosity, one assumes that the hydrodynamic stress tensor description is still valid and one prescribes an eddy viscosity $\nu = \alpha c_s h$ (Shakura & Sunyaev 1973) where α gives the magnitude of viscosity, c_s is the local disc sound speed and h is the disc scale height. This eddy viscosity scales the size of the turbulent motion with respect to its maximum extent within the disc and to its non supersonic velocity (otherwise, there is strong dissipation through shocks). This definition is equivalent to the initial Shakura-Sunyaev (1973) prescription $\tau_{r\phi} = -\alpha P$ in the case of negligible radiative pressure compared to the thermal one which is always the case for YSO.

§ 30. On the α disc prescription in cylindrical coordinates

The hydrodynamic viscous stress tensor for a newtonian fluid (i.e. the shear stress is proportional to the velocity gradients) with no bulk viscosity is written (cf Landau & Lifchitz 1971) :

$$\tau_{ij} = \rho\nu(\partial_i V_j + \partial_j V_i - \frac{2}{3}\delta_{ij}\partial_k V_k) \tag{30.70}$$

where $\partial_i = \frac{\partial}{\partial X_i}$ is the covariant derivative with respect to the X_i coordinate. One considers a cylindrical coordinate system (r,ϕ,z) and axisymmetry around the rotation axis z. One particularly has $\frac{\partial v_i}{\partial \phi} = 0$ but the covariant derivative $\partial_\phi v_r = -v_\phi$ is not zero since the vector basis in cylindrical coordinates has not fixed coordinates. The dominant part of the viscous tensor in thin accretion discs ($\frac{h}{r} << 1$) is $\tau_{r\phi}$ which corresponds to the transfer of radial angular momentum due to the angular velocity shear. We have : $\tau_{r\phi} = \rho\nu(\frac{1}{r}\frac{\partial v_r}{\partial \phi} - \frac{v_\phi}{r} + \frac{\partial v_\phi}{\partial r}) = \rho\nu r\frac{\partial}{\partial r}\Omega$. Stationary accretion imposes the radial stratification of density : $\rho = \rho_0(\frac{r}{r_0})^{-\frac{3}{2}}$ for a constant aspect ratio $\epsilon = \frac{h}{r}$. Thus, for stationary Keplerian accretion discs assuming Shakura-Sunyaev α prescription, one deduces : $div(\tau_{r\phi}) = \frac{-3}{2r^2}\frac{d}{dr}(\rho\nu r^2\Omega) > 0$ since $\rho\nu \propto r^{-1}$. Therefore, one obtains an accelerating torque in the disc midplane in contradiction with the viscous dissipative nature

of this torque. Different disc scale height $h \propto r^{\delta}$ with $\delta > 0$ leads to the same conclusion. But if one integrates vertically the equations to have characteristics of the mean flow, one recovers coherency like in the works of Shakura & Sunyaev (1973) or Lynden-Bell & Pringle (1974) : $\int_0^h div(\tau_{r\phi})dz = \frac{-3}{2r^2}\frac{\partial}{\partial r}(\frac{\dot{M}_a}{4\pi Re}r^2\Omega) = \frac{-3}{4r}\frac{\dot{M}_a}{\pi Re}\Omega < 0$ because $\dot{M}_a \approx 4\pi r h \rho u_r \approx 4\pi\rho h \nu Re$. The reason for this discrepancy comes from the constraint of assuming constant accretion rate in 1D models.

From a general point of view, one can write the conservation equation of angular momentum to deduce the radial velocity in the equatorial plane by using the general α prescription $\tau_{r\phi} = -\alpha P$:

$$\rho\frac{u_r}{r}\frac{d(\Omega r^2)}{dr} = \frac{1}{r^2}\frac{d(r^2\alpha P)}{dr}. \tag{30.71}$$

One then deduces :

$$u_r = -\frac{2\alpha P}{\rho\Omega_K r}\left(\frac{\partial lnP}{\partial lnr} + 2\right) = -2\alpha\epsilon c_s\left(\frac{\partial lnP}{\partial lnr} + 2\right), \tag{30.72}$$

by considering an isothermal disc $P = \rho c_s^2$. Thus, for standard accretion discs with $\frac{\partial lnP}{\partial lnr} = -\frac{5}{2}$, one always has outflow in the midplane but for 1D models, this constraint becomes $u_r = -2\alpha\epsilon c_s\left(\frac{\partial lnP}{\partial lnr} + 3\right)$ obtaining inflow in the midplane with $m_s = -\frac{u_r}{c_s} = \alpha\epsilon$.

One can notice that in spherical coordinates, one always has a viscous negative viscous torque $div(\tau_{r\phi}) = \frac{-1}{2R^3}\frac{\partial}{\partial R}(\rho\nu R^3\Omega sin(\theta)) < 0$ due to the different expression of the divergence operator. Thus, this caveat shows that one has to be cautious when combining the standard disc profiles with the partial viscous torque expression using the α prescription. However, we will see that one can recover coherency to describe 2D accretion flow in cylindrical coordinates by considering other components in the stress tensor.

Some numerical works show this phenomenon of backflow in the equatorial plane (Urpin 1984, Rosczyska & al. 1994, Kley & Lin 1992). An interesting point is that for high viscosity values and taking into account other components of the viscous stress tensor, one can obtain a global accretion flow throughout the disc because this enables a sufficient coupling between the radial and vertical transfer of angular momentum via the $\tau_{z\phi}$ components thanks to vertical angular velocity shear and sufficiently steep vertical viscosity profiles. For instance, Kley & Lin (1992) find such a possibility by using $\alpha > 0.1$ for an isothermal equation of state but they also take into account radiation energy transport with power-law Kramers opacities which slightly modifies the critical viscosity value. Otherwise, Kluzniak & Kita (2000) find $\alpha > 0.7$ for a polytropic equation of state.

§ 31. The viscous accretion disc in Romanova et al. (2002)

As an example, we revisit the initial condition used in Romanova et al. (2002), from the point of view of the α prescription chosen and its implied accretion rate. We do the same analysis as the latter paragraph with the alpha prescription for the kinematic viscosity $\nu = \alpha T_d/\Omega_K$ where $T_d = T_{d0}v_{K0}$ and $T_{d0} = 0.01$. One finds the following expression for the radial velocity within the disc considering the initial density (see Fig. 31), pressure and toroidal velocity profiles

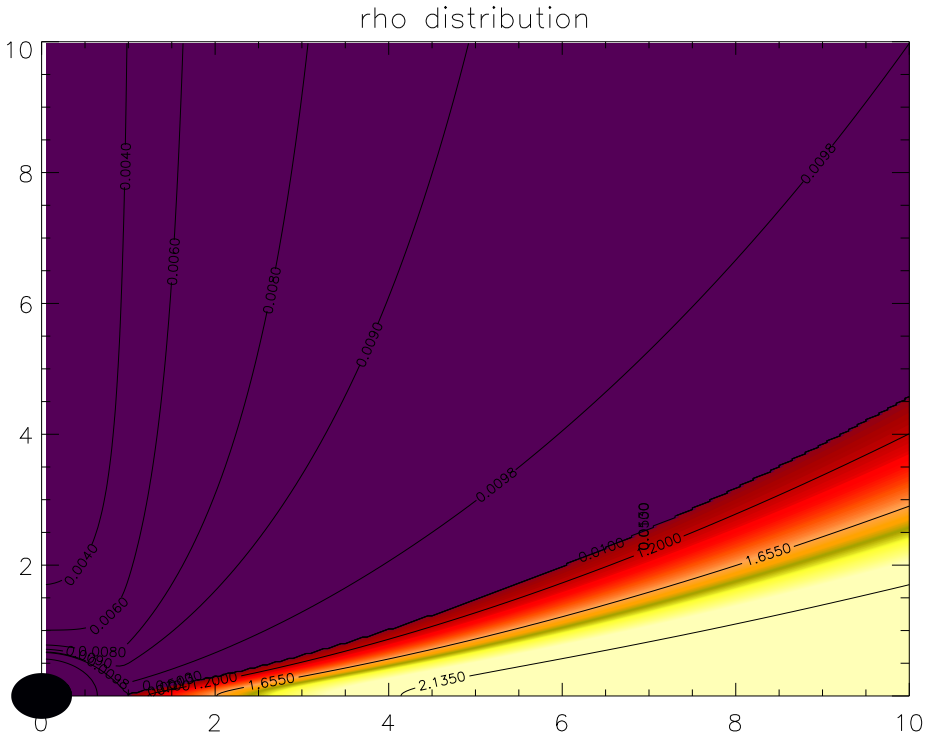

Figure 31. Density distribution in normalized units corresponding to the initial condition defined in Romanova et al. 2002 with a truncation radius at r=1.

($\Omega = k_c \frac{GM}{r^3}$ where $k_c = 1.01$) used in Romanova et al. (2002) :

$$u_r = -\frac{6\nu}{r} + \frac{3\nu}{rT_{d0}} \left(\frac{r^3}{(r^2+z^2)^{\frac{3}{2}}} - k_c \right) \tag{31.73}$$

Thus, one has a great inflow velocity in the disc midplane $u_r = -\frac{9\nu}{r}$ coherent with a disc pressure gradient directed inwards for this initial condition. Moreover, the radial velocity increases in the upper parts of the disc (see Fig. 32).

Although this disc solution is not self-similar, one can have an idea of the disc accretion rate by using the classical expression $\dot{M} = -4\pi r \int \rho u_r dz$. One obtains in this case a huge accretion rate when one goes outwards (see Fig. 33). Note that this shows that our simple analytical estimate does not give a stationary model. In simulations, there is a reconstruction of the disc structure from the initial condition towards a much common viscous accretion disc. It is necessary to take into account the vertical component of the stress tensor to construct such an analytical model. However, one already recovers the order of magnitude given by Romanova et al. (2002) with $\dot{M}_a \sim 0.05$ for $\alpha = 0.01$ at the disc inner edge corresponding to $\dot{M}_a \sim 1.4 \times 10^{-8} M_\odot yr^{-1}$ which is really high for such an α value.

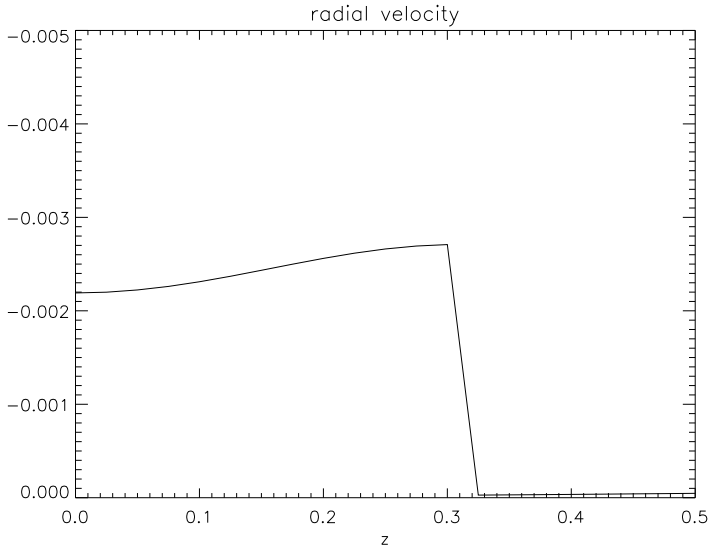

Figure 32. Vertical profile of the radial velocity for $\alpha = 0.01$ at r=2 from Eq. (31.73). One has strong inflow throughout the disc. The sonic Mach number is really big reaching $m_s = 0.02$ in the disc midplane with respect to standard disc model where one expects $m_s = \alpha\epsilon \sim 0.001$.

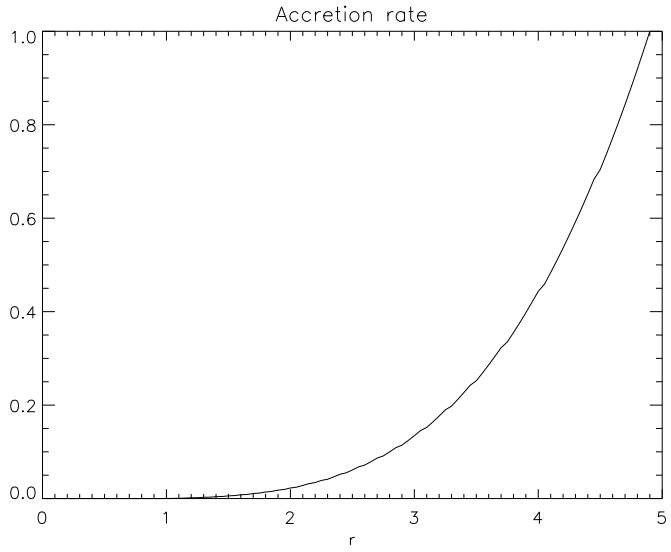

Figure 33. Accretion rate deduced from Fig. 32 using the initial condition of Romanova et al. (2002) in normalized units for $\alpha = 0.01$.

§ 32. Viscous hydrodynamic simulations

One presents now simulations incorporating viscosity within a purely hydrodynamic disc in order to illustrate our previous statements after having explained how viscosity is treated in the VAC code.

§ 32.1. *Implementation of α type viscosity in VAC*

The viscous hydrodynamics equations in conservative form are :

$$\frac{\partial \rho}{\partial t} + \nabla \cdot (\rho \mathbf{v}_p) = 0, \tag{32.74}$$

$$\frac{\partial \rho \mathbf{v}}{\partial t} + \nabla \cdot (\rho \mathbf{v}\mathbf{v}) = \nabla \cdot (\tau), \tag{32.75}$$

$$\frac{\partial E}{\partial t} + \nabla \cdot ((E + P)\mathbf{v}) = \nabla \cdot (v \cdot \tau). \tag{32.76}$$

where the expressions for the viscous stress is given by Eq. 30.70. The two terms involving τ are treated in VAC as source terms.

The goal is to maintain a mean accretion motion throughout the disc. To avoid convective instability, it is necessary to cancel the viscous heating which dominates in the disc midplane where density is maximum. The energy equation written above in conservative form involving τ contains both transport terms of viscous energy and local dissipation of viscous energy which increases the disc temperature. In order to cancel the viscous heating, we can either substract the heating term which writes $\rho \nu_v \tau_{i,j} \partial_j(\tau_{i,j})$ or replace the conservative term by only the transport part written $v \cdot \nabla \cdot (\tau)$. We choose this latter approach in our simulations.

§ 32.2. *The backflow mechanism*

The simulations are done here for an isothermal disc model, $\alpha_v = 0.4$ and $\epsilon = 0.15$ to have a good resolution within the disc (between 40 and 80 points in the vertical direction). The density and pressure distributions for the disc assuming vertical hydrostatic equilibrium are given by :

$$\rho = \rho_0 \left(\frac{r}{R_0}\right)^{-\frac{3}{2}} \exp\left(-\frac{z^2}{2h^2}\right), \tag{32.77}$$

$$P = \rho_0 \frac{GM_*}{R_0} \epsilon^2 \left(\frac{r}{R_0}\right)^{-\frac{5}{2}} \exp\left(-\frac{z^2}{2h^2}\right). \tag{32.78}$$

The disc is in sub-Keplerian rotation :

$$\Omega = \Omega_{\rm K} \left(1 - \frac{5}{4}\epsilon^2 - \frac{1}{4}\frac{z^2}{r^2}\right). \tag{32.79}$$

The atmosphere of the disc is in hydrostatic equilibrium (non rotating) and in pressure equilibrium (for all r) at the disc surface :

$$\rho = \rho_{c0} \left(\frac{R}{R_0}\right)^{-\frac{3}{2}}, \tag{32.80}$$

$$P = \rho_{c0} \frac{2}{5} \frac{GM_*}{R_0} \left(\frac{R}{R_0}\right)^{-\frac{5}{2}}. \tag{32.81}$$

The density contrast between corona and disc is : $\frac{\rho_{c0}}{\rho_{d0}} \approx \epsilon^2 \exp(-\frac{1}{2}) \sim 100$. The prescription for the dynamic viscosity is written as $\eta_v = \rho \nu_v = \rho \alpha_v \frac{c_s^2|_{z=0}}{\Omega_K} exp(-8x^4)$. Thus, the viscosity drops on a vertical disc scale height. We use a vertical profile to extrapolate the sound speed from the disc midplane since we have a hot corona over it, which otherwise would give rise to viscosity. One initially considers no poloidal velocity and let viscosity build the accretion flow.

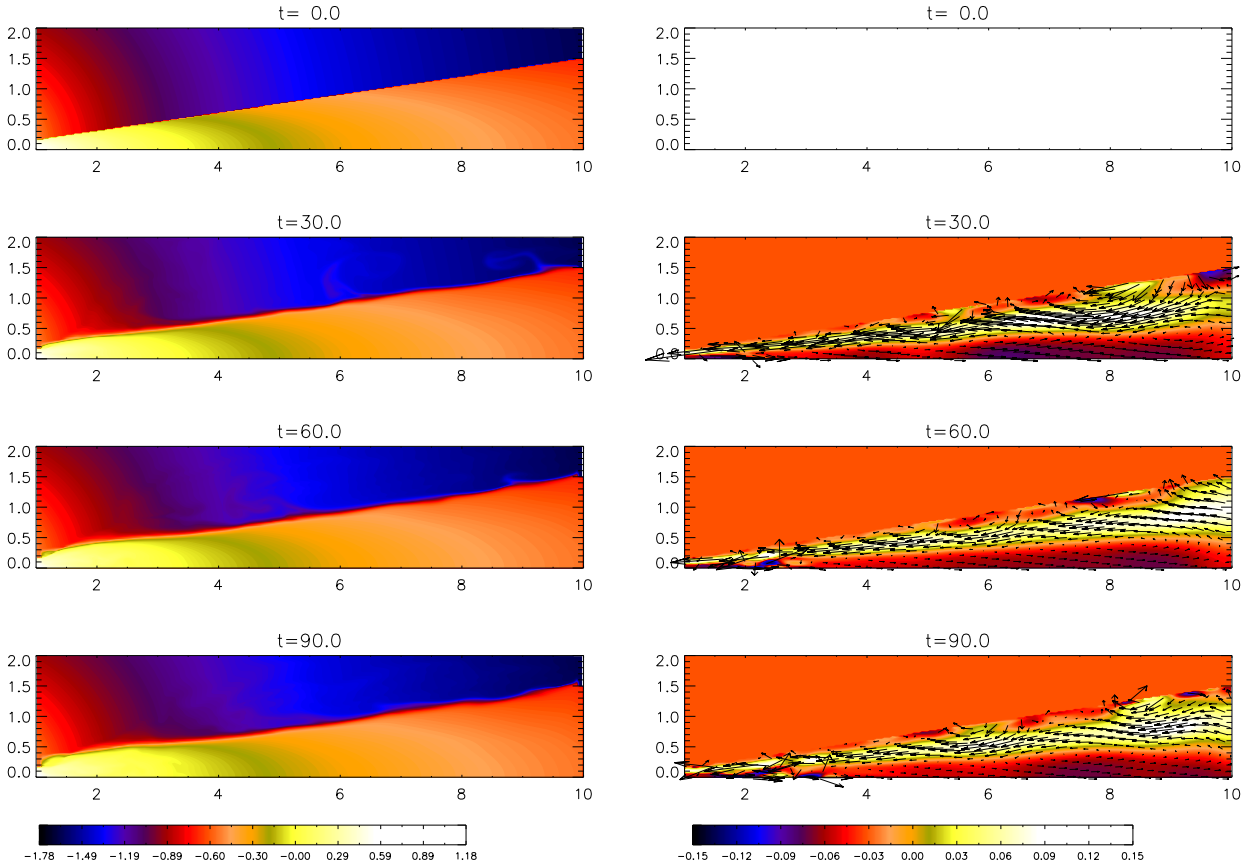

Figure 34. Viscous simulation with $\alpha_v = 0.4$ and taking into account only $\tau_{r\phi}$. Left panels shows the density distribution in log scale for different times given in periods at r=1 and right panels shows the distribution of sonic Mach numbers within the disc. We see outflow in the disc midplane.

We first include only the a priori dominant $\tau_{r\phi}$ viscous component. One makes a simulation with $\alpha_v = 0.4$. One takes outflow conditions for the poloidal velocity components and fix the other variables at the inner and outer disc edge to retain the initial vertical equilibrium similar to Kley & Lin (1992). Otherwise, symmetric and asymmetric boundary conditions are used for the disc midplane in order to simulate only the upper part of the accretion disc. We use a uniform cylindrical grid with $(N_r, N_z) = (200, 100)$ corresponding to a radial range [0,10] and a vertical one [0,2] including the whole upper disc. We used the TVD MUSCL scheme to solve the viscous hydrodynamics equations. This scheme is a Roe type Riemann solver and uses limiters on characteristic variables.

The simulation (see Fig. 34) shows the development of flow within the disc due to viscous torques. The viscous timescale is given by $\tau_v = r^2/\nu_v = \frac{1}{\alpha_v \epsilon^2}\Omega_K^{-1}$ and the simulations presented here last 10 τ_v at the disc inner edge. One can see strong accretion in the upper parts of the disc (reaching $m_s = 0.1$) but outflow ($m_s = -0.03 - 0.05$) near the disc midplane as discussed in the last paragraph with a value consistent with Eq. (30.72). However, we have globally an accretion rate within the disc (see Fig. 35). We integrate vertically the sonic Mach number and

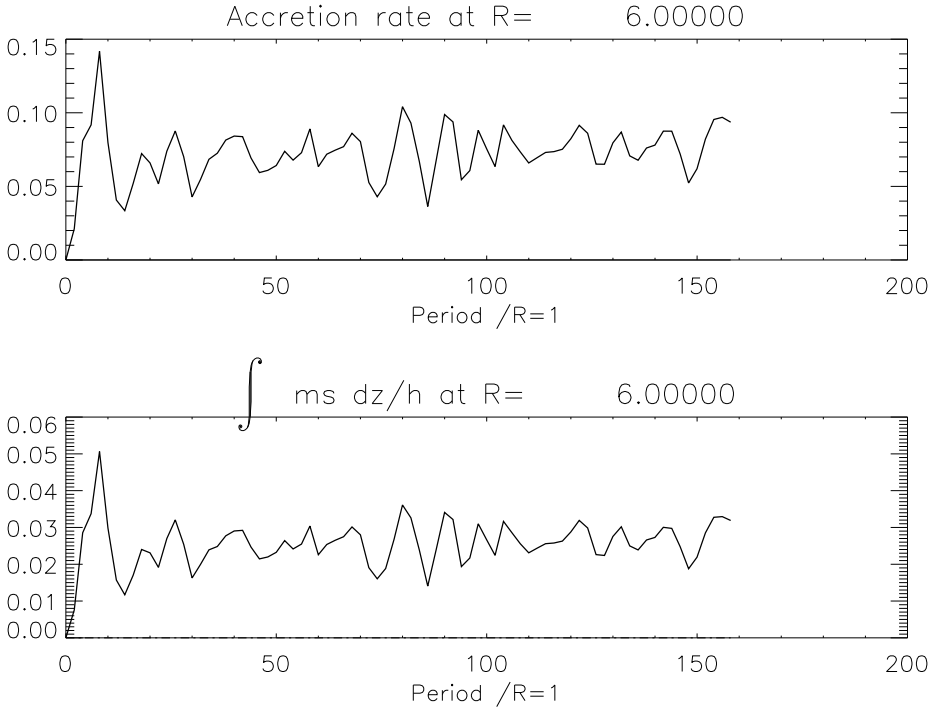

Figure 35. Top- Evolution in time of the accretion rate for $\alpha_v = 0.4$ and taking into account only $\tau_{r\phi}$. Bottom- Evolution in time of the vertically averaged sonic Mach number.

find $\tilde{m}_s = 0.025$ (see Fig. 35) which is smaller than the expected $m_s = 0.06$ for the vertically averaged accretion disc model. Otherwise, one observes some disturbance at the disc surface due to the non rotating corona which disturbs also the disc inner parts at longer timescales.

§ 32.3. *Towards a coherent picture of an accretion disc*

We include here all the components of the viscous stress tensor. In this case, we observe accretion throughout the disc even in the disc midplane (see Fig. 36) with the same accretion rate as previously and the same mean sonic Mach number. Thus, one has a consistent inflow of matter within the disc but the accretion speed remains smaller than the 1D accretion models which will give smaller accretion rates.

§ 33. The diffusivity within magnetized accretion discs

In order to enable accretion of matter throughout a magnetized disc, it is necessary to take into account a diffusion effect. Actually, ideal MHD conditions will give advection of the poloidal magnetic field due to viscous accretion which causes accumulation of magnetic flux towards the star and also maximize the build of toroidal magnetic field within the disc, giving rise to unsteady configurations. The diffusion is done by introducing in the induction equation a decrease of the electric field due to dissipation of currents, characterized by a resistivity parameter ν_m, and in the energy equation the ohmic dissipation ηJ^2 where $\eta = \frac{\nu_m}{\mu_0}$ is the disc diffusivity.

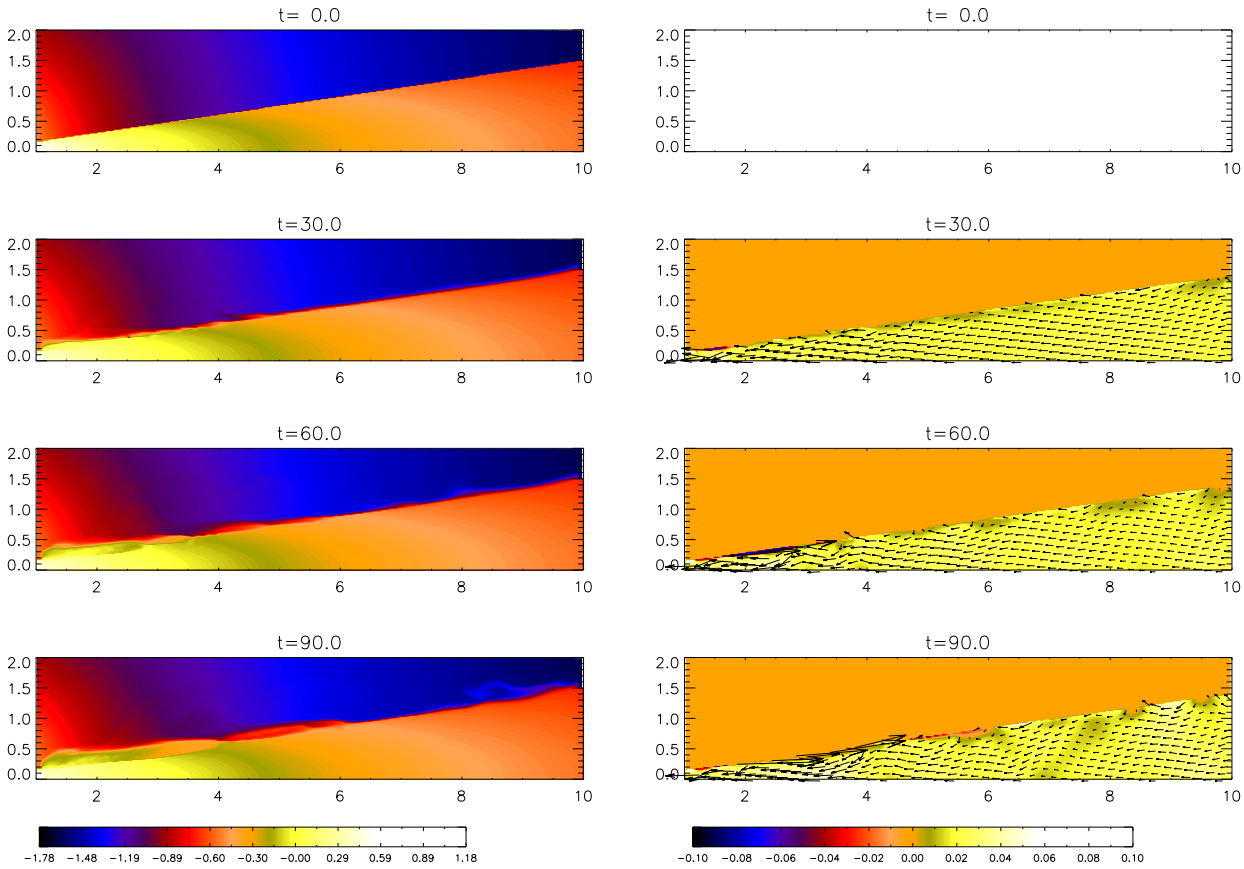

Figure 36. Viscous simulation with $\alpha_\nu = 0.4$ and taking into account the complete viscous stress. Left panels shows the density distribution in log scale and right panels shows the distribution of sonic Mach numbers within the disc. We have no longer back flow in the disc midplane.

$$\frac{\partial \mathbf{B}}{\partial t} + \nabla \cdot (\mathbf{vB} - \mathbf{Bv}) = \nabla \times (\eta(\nabla \times \mathbf{B})). \tag{33.82}$$

One can notice that for a uniform resistivity and no macroscopic motion, we find a standard diffusion equation for the magnetic field. Otherwise, the magnitude of radial diffusion of matter through purely vertical magnetic field in steady-state is directly controlled by η as $u_r = -\frac{\eta}{B^2}\frac{dP_{mag}}{dr}$. For the same reason as viscosity, we use an α prescription to quantify this resistivity. It is a zero order approximation for describing turbulence at smaller scales (unresolved by the numerics) which gives birth at macroscopic scale to a diffusion of plasma across the magnetic field lines. The relevant speed here is the Alfvén speed and thus one could write : $\nu_\mathrm{m} = \alpha_\mathrm{m} v_A h$. There are different drawbacks with this expression. First, contrary to viscosity, density does not appear explicitly here to cancel resistivity outside the disc. Besides, it is worse, since the Alfvén speed which is proportional to the inverse of density, increases above it. Thus, it is necessary to impose a vertical decreasing profile of resistivity after calculating the speed at the disc midplane. One takes different profiles in this thesis. One chooses a profile with a steep decrease over a vertical

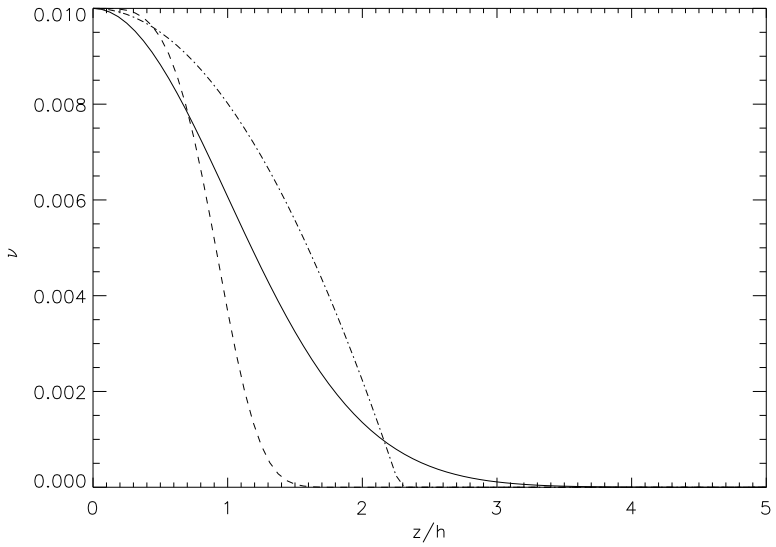

Figure 37. Different vertical diffusivity profiles as defined in the text : $f_1(x)$ (dashed), $f_2(x)$ (solid) and $f_3(x)$ (dashed-dotted).

scale height $f_1(x) = exp(-x^4)$ where $x = \frac{z}{h}$ which gives a weak resistive upper disc layer which can be explained by the high ionization rate caused by the stellar radiation field. Otherwise, one chooses a profile which follows the disc pressure and density vertical distributions namely $f_2(x) = exp(-\frac{x^2}{2})$ for an isothermal disc and $f_3(x) = \frac{2}{5\epsilon^2}\left(\frac{R_0}{\sqrt{r^2+z^2}} - \left(1 - \frac{5}{2}\epsilon^2\right)\frac{R_0}{r}\right)$ for an adiabatic disc (see Fig. 37) consistent with a vertical hydrostatic equilibrium. $f_1(x)$ will be used in chapter 4 and $f_3(x)$ in chapter 5.

Besides, we are interested in studying the interaction of the disc with a stellar field. Thus, the Alfvén speed decreases very quickly radially outwards and will give significant resistivity only at the disc inner edge. Theory of full-developed turbulence claim that the origin of turbulence within discs does not distinguish between viscosity and resistivity (corresponding to effective magnetic Prandtl number equal to unity) and thus one expects that MRI is the main trigger for it. As MRI saturates for $\beta \sim 1$ where we expect to have the truncation of the disc, we decide to take the sound speed for the characteristic speed and cut off the resistivity profile when $\beta \sim 1$. Finally, we assume :

$$\nu_{\rm m} = \alpha_{\rm m} c_s|_{z=0} h f(x). \tag{33.83}$$

One still needs a vertical prescription f(x) since we always have a hot corona. Finally, the heating coming from the compression of matter near the truncation radius enhances resistivity with the expression above which is not physically relevant for the same reason of quenching the MRI. Thus, we extrapolate the resistivity in this inner parts, when it becomes to increase going inwards, by using a standard profile proportional to the square root of the radial distance. The same extrapolation is done for kinematic viscosity since in this region, the Keplerian profile is well modified by the magnetic field (see chapter 4) reaching a maximum and then diminishing which corresponds then to a wrong transport of angular momentum by viscosity, also unrealistic since turbulence in this region has to be quenched.

In the VAC code, the resistive module treats the disc diffusivity as source terms. However, in the high diffusivity range ($\alpha_m \sim 1$), we noticed the development of an unphysical negative constant toroidal field at each radius within the disc which increases with time and finishes to destroy the radial disc equilibrium. Thus, we decided to write a new implementation of the diffusivity by adding a new term directly in the flux function to increase the accuracy. Actually, with this method, the resistive part is computed at the cell edge like the advection part in the induction equation and at the same time contrary to the treatment with source terms. Axisymmetry allows us to find a second order tensor whose the divergence corresponds exactly to the resistive terms in the induction equation : $\tau_{i,j} = \epsilon_{i,j,k}\eta J_k$ where J_k is the component of the current density. This new implementation solves the previous issue and simulations with this high disc dissipation effect are presented in the next chapters.

3. The stellar magnetosphere

§ 34. Design of boundary conditions

One needs for our problem to put some relevant boundary conditions to mimic the presence of a central object. However, we do not plan to simulate the star itself because it is a real complex job and it is not reliable for global simulations because of too large computational CPU time for instance to resolve the merging of matter and the linked shocks created by the accretion flow. We also neglect the backreaction of the transfer of mass and angular momentum onto the stellar rotation rate. This is because the timescales probed in simulations are always inferior to decades, which is really small with respect to the stellar braking timescale around 10^5 yr. Thus, we are interested in studying the magnetic coupling between the star and the disc so we have to prescribe the magnetic field near the star surface. For sake of simplicity, one considers that the stellar magnetic field is constant in time and one uses a classical dipolar expression parametrized by the stellar magnetic moment μ which is written in cylindrical coordinates (r,z) as :

$$\begin{cases} B_r(r,z) = \frac{3\mu r z}{(r^2+z^2)^{\frac{5}{2}}}, \\ B_z(r,z) = \frac{3\mu z^2}{(r^2+z^2)^{\frac{5}{2}}} - \frac{\mu}{(r^2+z^2)^{\frac{3}{2}}}. \end{cases} \tag{34.84}$$

Obviously, the first effect of the presence of the star is its gravity which attracts the surrounding matter and gives an accretion disc after the preliminary collapse in the early stages of stellar formation. This term is added in the VAC code as a source term. We study here only the inner parts of the accretion disc (below 1 a.u.) and as we consider initially a thin one, we can neglect disc selfgravity.

Then, we assume that the stellar corona is a perfect conductor medium i.e. without resistivity. Using also the axisymmetry and stationarity, the Ohm's law $\mathbf{E} + \mathbf{v} \times \mathbf{B} = 0$ gives that the poloidal velocity field is parallel to the poloidal magnetic field. Romanova et al. (2002) uses also this boundary condition. Then, we assume that the magnetic field lines rotate at the stellar rotation rate Ω_* i.e. they are frozen at the stellar surface. In the rotating frame of the star, the poloidal electric field is cancelled and we obtain a relation between the angular velocity of the matter and the magnetic surfaces rotation rate from the induction equation in the poloidal plane :

$$\nabla \times (\mathbf{v}_\Phi \times \mathbf{B}_p + \mathbf{v}_p \times \mathbf{B}_\Phi) = 0. \tag{34.85}$$

The discrepancy between these two toroidal velocities is due to the generation of toroidal magnetic field and depends on the mass loading $\kappa = \frac{\rho V_p}{B_p}$ along the magnetic field lines. Finally, we have :
$\mathbf{v}_p \times \mathbf{B}_p = 0$ i.e. $v_p = \frac{\kappa}{\rho}\mathbf{B}_p$ using conservation of mass and magnetic flux, and
$\Omega r = \Omega_* r + \frac{\kappa}{\rho} B_\phi$.

Numerically, to impose correctly boundary conditions on the poloidal velocity, after having copied the components in the ghost cells, we can not use directly the proportionality coefficient $\frac{\kappa}{\rho}$ because of the change of sign of B_z in cylindrical coordinates. We use the scalar product which gives the poloidal velocity component directly parallel to the magnetic field and then project it along the coordinate axis :

$$\begin{cases} v_r = \frac{(v_r B_r + v_z B_z) B_r}{\sqrt{B_r^2 + B_z^2}}, \\ v_z = \frac{(v_r B_r + v_z B_z) B_z}{\sqrt{B_r^2 + B_z^2}}. \end{cases} \tag{34.86}$$

As far as the density and pressure variables are concerned, we use linear extrapolation of their profiles in order to conserve the coronal hydrostatic equilibrium. For instance, we calculate the density slopes inside the domain from the last 3 cells and deduce the density into the ghost cells by linear extrapolation using a minmod TVD limiter for the slopes whereas crude copy of density will destroy the equilibrium. It lacks an important boundary condition on B_ϕ which gives the magnetic torque crucial for our study. In previous works on this topic, we often find zero gradient condition on B_ϕ (Miller & Stone 1997, Romanova et al. 2002, Kuker et al. 2003), which imposes a radial current entering near the star surface thus an artificial force since a dipolar magnetic field line is not radial. Besides, we observe that this kind of boundary condition does not seem to permit to control the star rotation rate which rapidly increases (Long & Romanova 2005). However, we will see in chapter 4 that this boundary condition plays no role in the truncation of discs and in the formation of funnel flows.

Our first simulation attempts with basic boundary condition like $B_\phi = 0$ (only valid for a steady state) did not give good results because it gives a vanishing magnetic torque towards the star. Thus, the stellar magnetic field lines anchored within the disc tends to rotate at this velocity and it is very difficult to connect the star to the disc in order to have a braking of the star.

We take another approach by imposing that the magnetic field lines anchored inside the star tend to match the stellar rotation rate but without forcing it. That is why we prescribe the local azimuthal acceleration to be the discrepancy between the magnetic surfaces rotation rate and the stellar one divided by the propagation time Δt of an Alfvén wave with speed V_a to cross the width between two adjacent rows of cells at the inner edge of the simulation box. This gives in formulae :

$$\rho \frac{\partial}{\partial t}(\Omega r) = \rho \frac{(\Omega_* r - \Omega_B r)}{\Delta t}, \tag{34.87}$$

where $\Omega_B = \Omega - \frac{\kappa}{\rho r} B_\phi$ and $\Delta t = \frac{\Delta R}{V_a}$.
Then, we compute at this location the angular momentum equation to deduce the B_ϕ component. One has to solve a system of two equations with two unknowns B_ϕ and Ω :

$$\begin{cases} \Omega r = \Omega_* r + \frac{\kappa}{\rho} B_\phi, \\ \rho \frac{\partial}{\partial t}(\Omega r) + \rho u_r \frac{\partial}{\partial r}(\Omega r) + \rho u_z \frac{\partial}{\partial r}(\Omega r) - \frac{B_r}{r}\frac{\partial}{\partial r}(r B_\phi) - \frac{B_z}{r}\frac{\partial}{\partial z}(r B_\phi) = 0, \end{cases} \tag{34.88}$$

from the third component of the momentum equation using $\nabla \cdot \mathbf{B} = 0$. In the latter equation, we replace the first term by the expression 34.87. To discretize this equation at the inner edge, we have to express the derivatives in terms of $\frac{\partial}{\partial R}$ and $\frac{\partial}{\partial \alpha}$ as our grid is spherical with $\alpha = \frac{\pi}{2} - \theta$ where θ is the classical angle of the spherical coordinates. The subscript i corresponds to a cell in the first row of ghost cells and the subscript i+1 is the right cell into the computational domain. We thus write in practice :

$$\left(\frac{\partial B_\phi}{\partial R}\right)_{i+1} = \frac{B_{\phi,i+2} - B_{\phi,i+1}}{\Delta R} = \frac{\Delta B_\phi}{\Delta R}, \tag{34.89}$$

$$B_{\phi,i} = B_{\phi,i+1} - \Delta B_\phi, \tag{34.90}$$

$$\left(\frac{\partial B_\phi}{\partial \alpha}\right)_{i+1} = \frac{B_{\phi,i+1,j+1} - B_{\phi,i+1,j-1}}{\Delta \alpha}, \tag{34.91}$$

$$\left(\frac{\partial v_\phi}{\partial \alpha}\right)_{i+1} = \frac{v_{\phi,i+1,j+1} - v_{\phi,i+1,j-1}}{\Delta \alpha}, \tag{34.92}$$

$$\left(\frac{\partial v_\phi}{\partial R}\right)_{i+1} = \frac{v_{\phi,i+1} - v_{\phi,i}}{\Delta R} = \frac{v_{\phi,i+1} - r_i \Omega_*}{\Delta R} - \frac{v_{p,i}}{B_{p,i}\Delta R} B_{\phi,i+1} + \frac{v_{p,i}}{B_{p,i}\Delta R}\Delta B_\phi. \tag{34.93}$$

For each derivatives estimate, we use a minmod limiter using two adjacent cells in order to avoid spurious oscillations.

After some calculations, we obtain for the discretized form :

$$\begin{aligned} \Delta B_\phi = & \left[\frac{\rho v_A}{\Delta R} \left(r_{i+1}\Omega_* + \frac{v_{p,i+1}}{B_{p,i+1}} B_{\phi,i+1} - v_{\phi,i+1} \right) \right. \\ & - B_{r,i+1} \left(\frac{B_{\phi,i+1}}{r_{i+1}} - \left(\frac{z}{R^2}\right)_{i+1} \left(\frac{\partial B_\phi}{\partial \alpha}\right)_{i+1} \right) - B_{z,i+1} \left(\frac{r}{R^2}\right)_{i+1} \left(\frac{\partial B_\phi}{\partial \alpha}\right)_{i+1} \\ & + \rho_{i+1} u_{r,i+1} \left(\left(\frac{r}{R}\right)_{i+1} \left(\frac{v_{\phi,i+1} - r_i\Omega_*}{\Delta R} - \frac{v_{p,i}}{B_{p,i}\Delta R} B_{\phi,i+1} \right) - \left(\frac{z}{R^2}\right)_{i+1} \left(\frac{\partial v_\phi}{\partial \alpha}\right)_{i+1} \right) \\ & + \rho_{i+1} u_{z,i+1} \left(\left(\frac{z}{R}\right)_{i+1} \left(\frac{v_{\phi,i+1} - r_i\Omega_*}{\Delta R} - \frac{v_{p,i}}{B_{p,i}\Delta R} B_{\phi,i+1} \right) + \left(\frac{r}{R^2}\right)_{i+1} \left(\frac{\partial v_\phi}{\partial \alpha}\right)_{i+1} \right) \\ & \left. + \rho_{i+1} \frac{u_{r,i+1}}{r_{i+1}} v_{\phi,i+1} \right. \\ & \left. / \left[B_{z,i+1} \frac{z}{R\Delta R} + B_{r,i+1} \frac{r}{R\Delta R} - \rho_{i+1} u_{r,i+1} \frac{v_{p,i}}{B_{p,i}} \frac{r}{R\Delta R} - \rho_{i+1} u_{z,i+1} \frac{v_{p,i}}{B_{p,i}} \frac{z}{R\Delta R} \right] \right. \end{aligned} \tag{34.94}$$

At each time step, we use this expression to update the B_ϕ value in the ghost cells.

§ 35. Implementation of the splitting method for the magnetic field

The dipolar magnetic field has a particular topology because the magnetic pressure is exactly balanced by the magnetic tension i.e. one has a current-free field i.e. a potential field. Numerically, if we project directly the magnetic field expression onto the grid, we do not generally ensure this characteristic at the machine accuracy because of the discretization of the differential operators and one has numerical forces which would disturb the initial condition because of the strong gradient of the dipole field ($B \sim r^{-3}$). The idea coming from Tanaka (1994) and applied by Powell et al. (1999) in the BATSRUS code is to write the MHD equations by splitting the Lorentz force into dipolar components and deviations from it. By putting 0 subscript for quantities relative to the dipole field and 1 subscript for the deviations, one obtains :

$$J \times B = J_0 \times B_0 + J_0 \times B_1 + J_1 \times (B_0 + B_1). \tag{35.95}$$

The first term is analytically equal to zero for the dipole field, the second one is also equal to zero because $J_0 = 0$ and the third one represents the Lorentz force due to the induced current by the plasma motion. Another assumption is that the dipole field is assumed to be stationary. Thus, we can cancel all the terms including J_0 and $\partial_t B_0$ in the MHD equations. Thus, the numerical error on magnetic stresses initially proportional to $O(B_0^2)$ is reduced to $O(B_0)$ which is important for strong background fields like in our case near the star with low beta regions ($\beta \sim 10^{-2}$). Besides, we introduce a new set of conservative variables in the code $(\rho, m_1, m_2, m_3, e_1, B_{11}, B_{12}, B_{13})$ related to the former one by $B = B_0 + B_1$ and $e = e_0 + e_1$ with $e_1 = \frac{p}{\gamma - 1} + \frac{1}{2}\frac{m^2}{\rho} + \frac{1}{2}B_1^2$.

Excluding the magnetic energy of the dipole field from the computations diminishes the truncation errors when calculating the thermal energy from the total energy within low beta regions ($\beta \sim 10^{-2}$).

Thus, one can split the flux function into two parts, the first one containing the same flux function F_1 for B_1, e_1 as the classical conservative variables and the second one F_2 all the terms including B_0 :

$$F_1 = \begin{pmatrix} \rho \mathbf{v} \\ \rho \mathbf{v}\mathbf{v} + (P + \frac{\mathbf{B}_1^2}{2})\mathbf{I} - \mathbf{B}_1\mathbf{B}_1 \\ \mathbf{v}\mathbf{B}_1 - \mathbf{B}_1\mathbf{v} \\ (e_1 + P + \frac{\mathbf{B}_1^2}{2})\mathbf{v} - \mathbf{B}_1(\mathbf{B}_1 \cdot \mathbf{v}) \end{pmatrix}. \tag{35.96}$$

$$F_2 = \begin{pmatrix} 0 \\ (\mathbf{B}_0 \cdot \mathbf{B}_1)\mathbf{I} - (\mathbf{B}_0\mathbf{B}_1 + \mathbf{B}_1\mathbf{B}_0) \\ \mathbf{v}\mathbf{B}_0 - \mathbf{B}_0\mathbf{v} \\ (\mathbf{B}_0 \cdot \mathbf{B}_1)\mathbf{v} - \mathbf{B}_0(\mathbf{B}_1 \cdot \mathbf{v}) \end{pmatrix}. \tag{35.97}$$

We implement this technique for the Lax Friedrich scheme in VAC. The new conservative variables of the code are $(\rho, m_1, m_2, m_3, e_1, B_{11}, B_{12}, B_{13})$. Instead of reconstructing the background field at the cell edges from the cell centers, we directly calculate in the code these values at the cell edges. Besides, as the fluxes are computed in the local frame linked to the spherical grid, one

uses the analytical expressions in these coordinates to compute the flux F_2:

$$\begin{cases} B_R = \frac{2\mu cos\theta}{R^3} = \frac{2\mu z}{(r^2+z^2)^2}, \\ B_\alpha = -B_\theta = \frac{\mu sin\theta}{R^3} = \frac{2\mu r}{(r^2+z^2)^2}. \end{cases} \tag{35.98}$$

Next, one has to add source terms including the background field in the geometrical source terms due to axisymmetry, resistivity ones and also the Powell ones by well considering the total magnetic field $B_0 + B_1$.

We test our implementation of the splitting method by computing a dipole field within a uniform density and pressure medium. We check that the solution remains force-free during the simulation.

4

The truncation of the disc and funnel flow formation

Chapter content

Since a decade, many numerical works have investigated the star-disc interaction issue (Hayashi et al. 1996; Kuker et al. 2003; Long et al. 2005). However, the formation of accretion curtains seems to be difficult to reproduce. Although Miller & Stone (1997) found such polar accretion in the case of kG dipolar stellar field associated with a disc field in the same direction to this latter, Romanova et al. (2002) were the first to demonstrate magnetospheric accretion along stellar field lines for kG pure dipolar field in axisymmetric simulations and next by performing 3D simulations (Romanova et al. 2003).

In this chapter, we address the issue of the disc truncation radius and its localization as function of the disc (accretion rate) and stellar (dipole field) parameters. In Section 1 we provide analytical constraints for driving steady accretion funnels and derive an estimate of the position of the truncation radius. We then use numerical MHD simulations in Section 2 to verify this prediction. We confirm magnetospheric accretion for a slowly rotating star with an inner disc

hole and weak stellar magnetic field compatible with observations of weak accretors, and study the physical properties of the accretion curtain.

1. The disc truncation radius

For a given accretion disc model, predicting where the truncation by the stellar magnetosphere will occur is an important issue. Different estimates were given in the literature. One considers here a pure dipolar field with a strength at the stellar surface in the equatorial plane equal to B_*.

A first dimensional estimate expresses the truncation radius r_t in the form $r_\mathrm{t} = k r_\mathrm{A}$ where the Alfvén radius

$$r_\mathrm{A} = \left(\frac{B_*^4 R_*^{12}}{2GM_* \dot{M_a}^2} \right)^{1/7} \tag{35.99}$$

is a characteristic length which can be derived by equating the ram pressure of a free-falling spherical envelope with the magnetic pressure of a dipolar field (Elsner & Lamb 1977). Different estimates of the adimensional coefficient k have been given in literature, ranging from 0.5 (Ghosh & Lamb 1979; Königl 1991; Long et al. 2005) to ~ 1 (Arons 1993; Ostriker & Shu 1995; Wang 1996).

A second criterion (Cameron & Campbell 1993; Armitage & Clarke 1996; Matt & Pudritz 2005,and references therein) states that accretion funnels will take place when the magnetic torque due to the stellar field matches the "viscous" or turbulent torque, namely

$$-J_r B_z \simeq \frac{B_\phi^+ B_z}{\mu_o h} = \frac{1}{r^2}\frac{\partial}{\partial r}\eta_v r^3 \frac{\partial \Omega}{\partial r} \simeq -\alpha_v \frac{P}{r} \tag{35.100}$$

where B_ϕ^+ is the toroidal field at the disc surface, h the disc scale height, P the disc pressure and α_v the Shakura & Sunyaev (1973) parameter. This criterion (hereafter A) gives an upper limit for the truncation radius, as it only defines a radius where the star-disc interaction starts to affect accretion. This maximal truncation radius $r_\mathrm{t,max}$ occurs when the plasma beta, defined as $\beta = 2\mu_o P / B_z^2$, becomes $\beta = 2q/(\alpha_v \varepsilon)$ where $q = |B_\phi^+ / B_z|$ is a measure of the magnetic shear and $\varepsilon = h/r$ is the disc aspect ratio. In a thin Keplerian accretion disc, one gets $\beta \gg 1$ at $r_\mathrm{t,max}$ since q is close to unity to avoid opening of the magnetosphere (e.g. Matt & Pudritz 2005).

A third criterion represents a more conservative approach, and gives only a lower limit $r_\mathrm{t,min}$. It states that accretion funnels take place when accretion is no longer possible because of the overwhelming field strength. It is usually written (Koldoba et al. 2002; Romanova et al. 2002)

$$\frac{B^2}{\mu_o} = \rho v^2 + P \tag{35.101}$$

where v is the total speed. However, this criterion is not predictive since the azimuthal velocity v_ϕ is itself an outcome of the star-disc interaction. If one wishes to provide an estimate of the truncation radius, then this criterion becomes $B_z^2/\mu_o = \rho GM/r$, where we used $v_\phi = v_K = \sqrt{GM_*/r}$ and a negligible thermal pressure (both approximations valid in a thin disc). This will be our criterion B. In a thin accretion disc, one has $P = \rho \Omega_K^2 h^2$ and the stationary accretion rate is $\dot{M}_a = \int_0^h 4\pi\rho r u_r dz \sim 4\pi\rho u_0 r h$ where $u_0 = -u_{(z=0)}$, $h = \epsilon r$, $\epsilon \ll 1$. Thus, $\frac{B_z^2}{\mu_o} = \frac{\dot{M}_a}{4\pi r^2 m_s \epsilon^2}\Omega_K r$. This condition translates into $\beta = 2\varepsilon^2 \ll 1$ at $r_\mathrm{t,min}$.

From the previous discussion, it appears quite obviously that $\beta \sim 1$ should be a better approximation for $r_{\rm t}$. This is what we argue next.

The stellar magnetic field, which is bound to become dominant in the magnetosphere, must first favor accretion, i.e. the magnetic torque must be negative. If this is not the case, namely if $r > r_{t,max} > r_{co}$, the disc material is radially expelled. This is the "propeller" regime as studied e.g. by Ustyugova et al. (2006) and references therein. Accretion thus implies $r_{\rm t} < r_{\rm co}$, with stellar magnetic field lines as leading spirals. Below co-rotation, accretion will proceed quite naturally thanks to both the viscous and the stellar torques. There are then two more independent constraints that must be fulfilled in order to produce steady funnel flows. First, the accretion flow must be prevented by the presence of the magnetosphere. The simplest way to express this is to require that the magnetic poloidal pressure balances the accretion ram pressure ρu_r^2. This defines a radius r_{bf} where

$$\beta \simeq m_{\rm s}^{-2} \tag{35.102}$$

where $m_{\rm s} = u_r/C_s$ is the sonic Mach number measured at the disc midplane. Now, at radii $r < r_{t,max}$, accretion is mainly due to the stellar torque and $m_{\rm s} = 4q/\beta \gg \alpha\varepsilon$: material is accreting to the star much faster than in the outer accretion disc. Second, material at the disc midplane must be lifted and loaded onto the stellar field lines. With a dipole field configuration, such a vertical motion can only be due to a vertical thermal plasma pressure gradient. It therefore requires that the magnetic field compression is not too strong. This leads naturally to an equipartition, $\beta \sim 1$ (as already proposed by Pringle & Rees 1972; Aly 1980).

One important point to remark is that once a large scale magnetic field is close to equipartition in an accretion disc, it is able to deviate a large fraction of the disc plasma from its radial motion to a vertical one. This has been shown with the calculations of Magnetized Accretion-Ejection Structures by Ferreira & Pelletier (1995) and confirmed by numerical MHD simulations (Casse & Keppens 2002; Zanni et al. 2007). In some sense, making funnel flows involves the same physics as loading mass in magnetized jets. In fact, almost all of the disc mass can be lifted and loaded onto the field lines when $\beta \sim 1$, it depends mostly on the field bending (see Fig. 3 in Ferreira & Pelletier 1995). This is the reason why we will assume, for finding a simple analytical criterion, that the disc truncation radius r_t is close to the radius where $\beta \sim 1$, namely $r_t \sim r_{bf}$. Using the above estimates, we derive the following two constraints:

$$\beta \sim 1 \quad \text{and} \quad m_s \sim 1. \tag{35.103}$$

that must be fulfilled in order to provide steady state funnel flows. For a dipole field, this right away translates into a theoretical truncation radius

$$\frac{r_{\rm t,th}}{R_*} \simeq 2\, m_s^{2/7} B_*^{4/7} \dot{M}_a^{-2/7} M_*^{-1/7} R_*^{5/7} \tag{35.104}$$

where the stellar field B_* has been normalized to 140 G, disc accretion rate $\dot{M}_a$ to 10^{-8} $\rm M_\odot$ $\rm yr^{-1}$, stellar mass to 0.8 $\rm M_\odot$ and stellar radius to $2\rm R_\odot$. Note that these are all typical values for CTTS while the chosen value of the magnetic stellar field B_* is consistent with observations of dipole fields in such objects (see Valenti & Johns-Krull 2004; Bouvier et al. 2007,and references therein).

It is clear that the conditions given by Eq. (35.103) state that the accretion speed close to the base of the accretion funnel is of the order of the Alfvén speed. As a matter of fact Eq. (35.104) can be rewritten as $r_{\rm t,th} \sim m_s^{2/7} r_{\rm A}$, where the Alfvén radius for spherical accretion $r_{\rm A}$ was defined in Eq. (35.99). Thus, this criterion is really close to the Alfvén radius but

Star	M_* ($M_\odot$)	R_* ($R_\odot$)	$\dot{M} \times 10^8$ ($M_\odot \mathrm{yr}^{-1}$)	P_{rot} (days)	$r_{\rm co}$ (R_*)	${r_t}^d$ (R_*)	$\bar{B}_{obs}$ (kG)	$B_{dip,obs}$ (G)	$r_{\rm t,th}$ (R_*)
AA Tau	0.53	1.74	0.33	8.20	8.0		2.57	< 200	2.6(3.2)
BP Tau	0.49	1.99	2.88	7.60	6.4	3.4(1.3)	2.17	< 250	1.6(2.2)
CY Tau	0.42	1.63	0.75	7.90	7.7	4.2(3.2)			2.0
DE Tau	0.26	2.45	2.64	7.60	4.2		1.35		2.0
DF Tau	0.27	3.37	17.7	8.50	3.4		2.98		1.5
DK Tau	0.43	2.49	3.79	8.40	5.3		2.58		1.7
DN Tau	0.38	2.09	0.35	6.00	4.8		2.14		3.1
GG Tau A	0.44	2.31	1.75	10.30	6.6	1.8(1.)	1.57		2.0
GI Tau	0.67	1.74	0.96	7.20	7.9		2.69		1.9
GK Tau	0.46	2.15	0.64	4.65	4.2	3.8(2.3)	2.13		2.6
GM Aur	0.52	1.78	0.96	12.00	10.0				2.0
IP Tau	0.52	1.44	0.08	3.25	5.2				3.4
TW Hya	0.70	1.00	0.20	2.20	6.3		2.61	150	2.0(2.0)
T Tau	2.11	3.31	4.40	2.80	3.2		2.39	< 120	1.6(1.5)
V2129 Oph	1.35	2.4	1.	6.53	6.8		2.0	350	2.1(3.5)

Figure 38. Main characteristics of some CTTS such as their mass M_*, radius R_*, accretion rate $\dot{M}$, period P_{rot}, corotation radius $r_{\rm co}$, mean magnetic strength $\bar{B}_{obs}$ which includes small-scale field often very different from the large scale field $B_{dip,obs}$ and the resulting theoretical truncation radius $r_{\rm t,th}$ calculated from Eq. (35.104) assuming $m_s \sim 1$ and $B_{*,dip} = 140$G (values into brackets are calculated using maximal observational constraints based on Valenti & Johns-Krull 2004, Daou et al. 2006, Donati & al. 2007, Yang et al. 2007) in comparison with truncation radius r_t^d derived from Najita & al. (2003) (values into brackets are calculated for the stellar mass given in this table).

is derived here on very different physical basis considering magnetically controlled accretion from a rotationally supported Keplerian disc. On the other hand, the co-rotation radius writes $r_{co}/R_* = 7.8\, M_*^{1/3} R_*^{-1} P_*^{2/3}$ for a typical 8 days stellar period P_*, which provides

$$\frac{r_{\rm t,th}}{r_{co}} \simeq 0.25\, m_s^{2/7} B_*^{4/7} \dot{M}_a^{-2/7} M_*^{-10/21} R_*^{12/7} P_*^{-2/3} \tag{35.105}$$

Remarkably, taking typical values for CTTS with a low magnetic dipole field gives a theoretical truncation radius not only smaller than the co-rotation radius but also consistent with observations of inner disc holes (Najita, Carr & Mathieu 2003) (see Fig. 38) . This is in strong contrast with unobserved large scale kG fields usually taken in the literature. This implies right away that the formation of funnel flows should *always* spin up the star unless (i) enough stellar field lines remain connected to the disc beyond r_{co} and/or (ii) ejection of stellar angular momentum is taking place somehow. In the following section, 2.5D numerical MHD simulations are used to show that conditions (35.103) are indeed those prevailing at the disc inner edge. If this is true, then we should recover a truncation radius located at our theoretical estimate (35.104) for a low dipole field of 140 G.

2. Numerical experiments

§ 36. Equations and numerical setup

We use the VAC [11] code (Tóth (1996)) to solve the full set of axisymmetric dimensionless resistive MHD equations (with the magnetic permeability $\mu_0 = 1$) in cylindrical coordinates (r,z):

$$\frac{\partial \rho}{\partial t} + \nabla \cdot (\rho \mathbf{v}_p) = 0, \tag{36.106}$$

$$\frac{\partial \rho \mathbf{v}}{\partial t} + \nabla \cdot (\rho \mathbf{v}\mathbf{v} - \mathbf{B}\mathbf{B}) + \nabla (\frac{B^2}{2} + P) = -\rho \nabla \Phi_G, \tag{36.107}$$

$$\frac{\partial \mathbf{B}}{\partial t} + \nabla \cdot (\mathbf{v}\mathbf{B} - \mathbf{B}\mathbf{v}) = \nabla \times (\eta (\nabla \times \mathbf{B})), \tag{36.108}$$

$$\frac{\partial E}{\partial t} + \nabla \cdot ((E + \frac{B^2}{2} + P)\mathbf{v} - \mathbf{B}(\mathbf{B} \cdot \mathbf{v})) = \eta J^2 - \mathbf{B} \cdot (\nabla \times \eta \mathbf{J}), \tag{36.109}$$

where ρ is the plasma density, $\mathbf{v}_p$ the poloïdal velocity, $\mathbf{v}$ the total velocity, $\mathbf{B}$ the magnetic field, P the thermal pressure, η the magnetic resistivity, $\mathbf{J} = \nabla \times \mathbf{B}$ the current density, $\Phi_G = -\frac{GM_*}{(r^2+z^2)^{1/2}}$ the gravity potential created by the central star and $E = \frac{P}{\gamma - 1} + \rho \frac{\mathbf{v}^2}{2} + \frac{\mathbf{B}^2}{2} + \rho \Phi_G$ the total density energy. The gravity is treated as a source term in the momentum and energy equations of VAC.

Time evolution is done with a conservative second order accurate Total Variation Diminishing Lax Friedrichs scheme with minmod limiters applied on primitive variables, except for density where a van Leer limiter is used instead to better resolve contact discontinuities. Powell source terms are used to ensure the divergence free property of the magnetic field and the code has been modified so as to compute only the deviations from the dipolar component (Tanaka 1994; Powell et al. 1999). The splitting technique has three main advantages. First it is crucial to properly represent an initial force-free configuration numerically. Second, since the total conserved energy contains only the energy associated with the deviation from the dipolar field, this method improves the computation of the thermal energy in low β regions. Third, when used in association with the Powell method, it helps in controlling the divergence of the magnetic field, since only the deviation from the background field is used to calculate the divergence and the Powell source terms. The divergence method used here gives $|\nabla \cdot \mathbf{B}| \Delta R \leq 0.01 |\mathbf{B}|$ but simulations done with PLUTO [12] and a constrained-transport scheme show that our results are not strongly modified by this method (Zanni et al, in prep).

§ 37. Boundary conditions

Boundary conditions take symmetric and asymmetric conditions for the axis and the disc midplane, while continuous (outflow) conditions are used at the outer edge. At the inner edge corresponding to the stellar surface, a linear extrapolation of density and pressure is done. After using free extrapolation for the poloidal velocity, this latter is forced to be parallel to the total poloidal magnetic field. The poloidal field is fixed, contrary to Romanova et al. (2002). We use a

[11] http://www.phys.uu.nl/~toth/

[12] A description of this code can be found in Mignone et al. (2007).

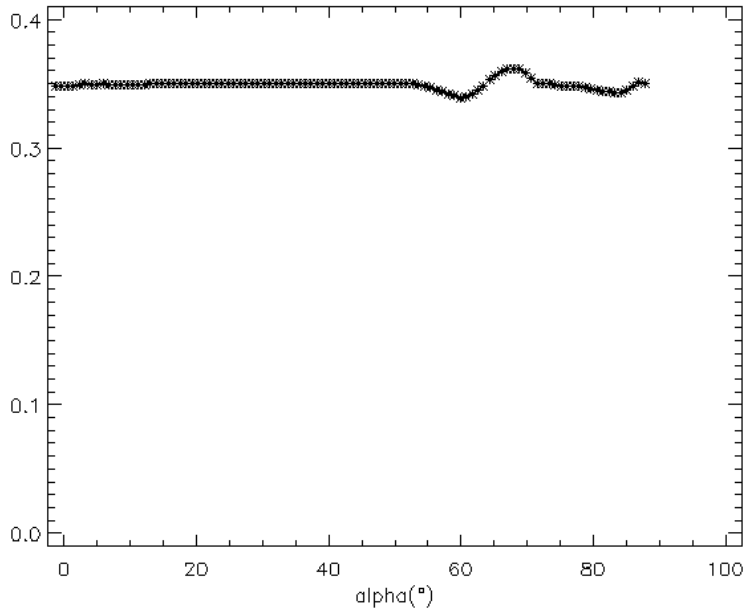

Figure 39. Angular velocity of the magnetic surfaces at the stellar surface after 10 stellar periods. The normalized angular velocity of the star is 0.35. We observe a slightly discrepancy (lower than 4%) localized within the accretion column between 55° and 70°.

boundary condition on the toroidal magnetic field as described in chapter 3. It allows to derive B_ϕ by forcing the magnetic surfaces to locally rotate at the stellar velocity. In practice, the radial derivative of the toroidal field is computed from the angular momentum conservation equation where the temporal derivative giving the local acceleration is replaced by

$$\rho \frac{\partial}{\partial t}(\Omega r) = \rho \frac{(\Omega_* r + v_p B_\phi / B_p - \Omega r)}{\Delta t} \tag{37.110}$$

where the timescale $\Delta t = \Delta R / V_{\rm A}$ is the Alfvén crossing time of one cell ΔR at the inner edge of the simulation box. This allows us to let the system evolve without imposing any arbitrary conditions on B_ϕ, hence on the torques. We check a posteriori that the magnetic surfaces rotate at the stellar velocity with a very good accuracy (see Fig. 39).

§ 38. Initial condition

In the initial conditions we take a Keplerian disc surrounded by an adiabatic corona in hydrostatic (non rotating) equilibrium. The disc is adiabatic with an index $\gamma = 5/3$ and an aspect ratio $\epsilon = h/r = C_s/V_K = 0.1$. The surface of the disc is determined by the pressure equilibrium between the disc and the corona, while the initial truncation radius has been chosen

arbitrarily. The density and pressure expressions for both the disc and the corona are

$$\begin{aligned}
\rho_d &= \rho_{d0}\left[\frac{2}{5\epsilon^2}\left(\frac{R_0}{\sqrt{r^2+z^2}}-\left(1-\frac{5}{2}\epsilon^2\right)\frac{R_0}{r}\right)\right]^{\frac{1}{\gamma-1}},\\
P_d &= \epsilon^2 V_{K0}^2 \rho_{d0}^{1-\gamma}\rho_d^{\gamma},\\
\rho_c &= \rho_{c0}\left(\frac{R_0}{\sqrt{r^2+z^2}}\right)^{\frac{1}{\gamma-1}},\\
P_c &= \frac{2}{5}V_{K0}^2\rho_{c0}^{1-\gamma}\rho_c^{\gamma}.
\end{aligned} \tag{38.111}$$

The density contrast between the disc and the corona is $\rho_{c0}/\rho_{d0} = 0.01$.

One can for instance establish the expression for the coronal density. One writes the hydrostatic equilibrium radially :

$$\frac{1}{\rho_c}\frac{\partial P_c}{\partial R} = -\frac{GM_*}{R^2}. \tag{38.112}$$

Using the polytropic equation of state $P = K\rho^{\gamma}$, we obtain :

$$d\left(\frac{\gamma}{\gamma-1}K\rho_c^{\gamma-1}\right) = d\left(\frac{GM_*}{R}\right) \tag{38.113}$$

Thus, we deduce by integrating this equation :

$$\rho_c = \rho_0\left[\frac{\gamma-1}{\gamma K}\frac{GM_*}{R}\right]^{\frac{1}{\gamma-1}} = \rho_{c0}\left[\frac{GM_*}{R}\right]^{\frac{1}{\gamma-1}} \tag{38.114}$$

A pure dipolar magnetic field is set up in the computational domain in equipartition with the thermal pressure of the disk at $r = R_0$. The rotation period of the star is set in order to place the corotation radius at $r = 2R_0$. The disc has no viscosity but is resistive with an alpha-like magnetic resistivity decreasing on a disc scale height, namely $\nu_{\rm m} = \alpha_{\rm m}\Omega_{\rm k}h^2 exp(-(\frac{z}{h})^4)$. In this chapter, we fix $\alpha_{\rm m} = 0.1$. The initial poloidal flow within the disc is zero and the disc is slightly sub-keplerian with $v_\phi = \sqrt{1-\frac{5}{2}\epsilon^2}\sqrt{\frac{GM_*}{r}}$.

The grid and stellar rotation period were chosen so as to allow a good resolution at the truncation radius R_0 while maintaining the co-rotation radius at $r = 2R_0$ well inside the domain. Our polar grid of $N_R \times N_\theta = 170 \times 100$ is stretched in the spherical R direction (see Fig.40 and Fig. 22 in chapter 2) and goes from $R_{\rm min} = 0.35R_0$ at the stellar surface to $R_{\rm max} = 10.35R_0$.

The results will be presented in adimensional units: lengths will be given in units of R_0, which corresponds to the truncation radius of the reference simulation (see Section § 40); speeds will be expressed in units of the Keplerian speed $V_{K0} = \sqrt{GM_*/R_0}$ and densities in units of ρ_{d0}, which is the initial disc density at $(r = R_0, z = 0)$. Time will be given in units of the Keplerian period at R_0, i.e. $t_0 = 2\pi R_0/V_{K0}$. Mass accretion rates will be given in units of $\dot{M}_0 = \rho_0 V_{K0} R_0^2$ while we will express the torques in units of $\dot{L}_0 = \rho_0 V_{K0}^2 R_0^3$.

§ 39. Reference values

We consider a $M_* = 0.8M_\odot$ young star with a radius of $R_* = 2R_\odot$ and a pure stellar dipole field with $B_* = 141$G. With these assumptions the normalization units will be $R_0 = 2.86R_* = 4\times10^9$m, $V_{K0} = \sqrt{GM_*/R_0} \simeq 1.63\times10^5$m s^{-1} and $\rho_{d0} = \left(B_*^2R_*^6\right)/\left(2\mu_0\epsilon^2V_{K0}^2R_0^6\right) \simeq 5.51\times10^{-10}$kg m^{-3}. Since we place the corotation radius at $2R_0$, the rotation period of the star is $P_* = 2\pi\sqrt{8R_0^3/GM_*} \simeq 5.1$ days while the time will be scaled in units of $t_0 = 2\pi R_0/V_{K0} =$

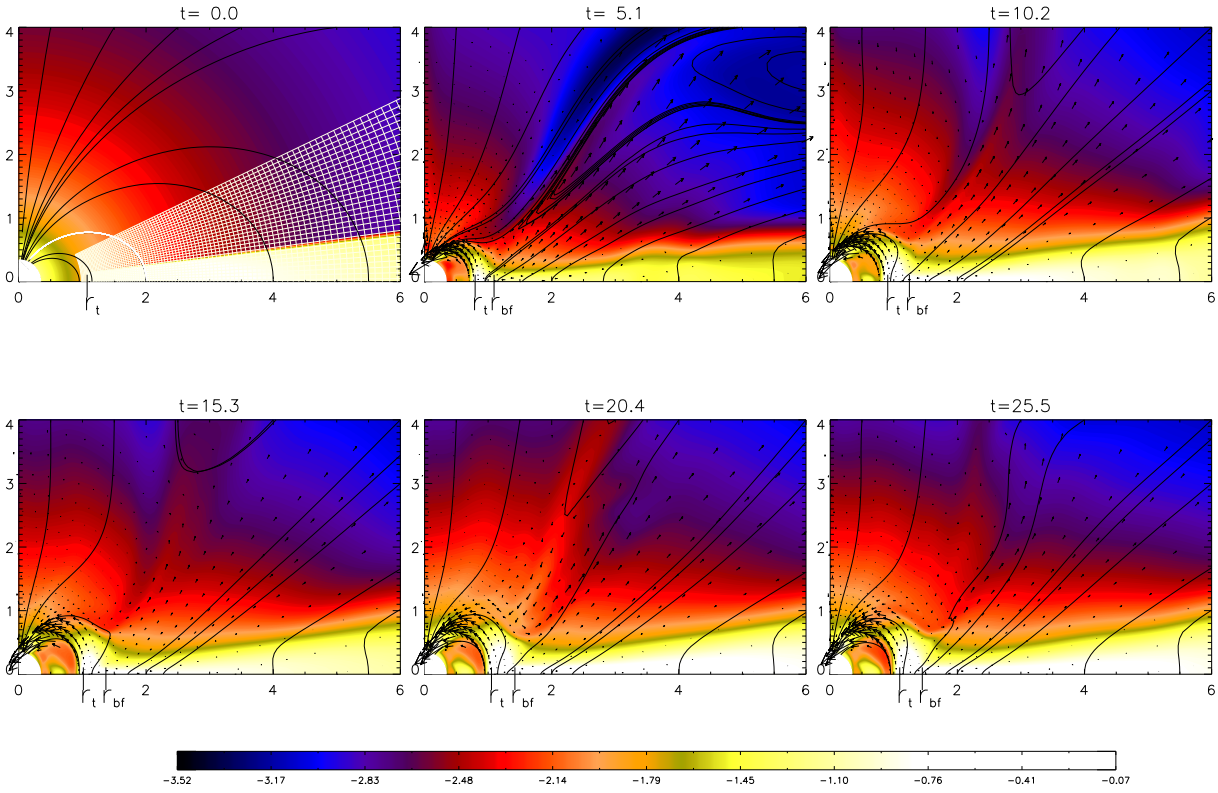

Figure 40. Resistive MHD simulation for a 5 days period CTTS with $B_* = 141\mathrm{G}$ and $\alpha_\mathrm{m} = 0.1$ after t=0,5.1,10.2,15.3,20.4,25.5 Keplerian periods at the disk inner edge corresponding to a physical time of 1.5 months. We show the density distribution in the computational domain using a log scale. The black lines draw the magnetic field lines and the black arrows represent the velocity field. The white line on the first snapshot represents an initial magnetic field line anchored at r_co. We also superimpose a part of the computational grid to show the good resolution we have near the truncation radius. An accretion column is formed between r_t and r_bf (see definitions in text) and one observes the expansion of the poloidal magnetic field and transient disc ejecta. The accretion rate at the stellar surface is equal to $1.9.10^{-9}\mathrm{M}_\odot.\mathrm{yr}^{-1}$ for P=5 and stabilizes towards $0.91.10^{-9}\mathrm{M}_\odot.\mathrm{yr}^{-1}$ at P=15. No X-winds are formed and the star is being spun up.

$1.54 \times 10^5\mathrm{s} \simeq 1.78$ days. The computational domain extends up to 0.3 a.u. Finally the normalization for the accretion rates is given by $\dot{M}_0 = \rho_0 V_{K0} R_0^2 \simeq 2.27 \times 10^{-8}\mathrm{M}_\odot\ \mathrm{yr}^{-1}$.

From these reference values, simulations done here can be scaled for another range of parameters (R_*,M_*,B_*) in the following way:

$$R_0 = 4 \times 10^9 \left(\frac{R_*}{2R_\odot}\right) \mathrm{m},$$

$$V_{K0} = 1.63 \times 10^5 \left(\frac{M_*}{0.8M_\odot}\right)^{1/2} \left(\frac{R_*}{2R_\odot}\right)^{-1/2} \mathrm{m\ s}^{-1},$$

$$\rho_0 = 5.51 \times 10^{-10} \left(\frac{R_*}{2R_\odot}\right) \left(\frac{B_*}{141G}\right)^2 \left(\frac{M_*}{0.8M_\odot}\right)^{-1} \mathrm{kg\ m}^{-3},$$

$$P_* = 5.1 \left(\frac{R_*}{2R_\odot}\right)^{3/2} \left(\frac{M_*}{0.8M_\odot}\right)^{-1/2} \mathrm{days},$$

$$t_0 = 1.54 \times 10^5 \left(\frac{R_*}{2R_\odot}\right)^{3/2} \left(\frac{M_*}{0.8M_\odot}\right)^{-1/2} \text{s},$$
$$\dot{M}_0 = 2.27 \times 10^{-8} \left(\frac{R_*}{2R_\odot}\right)^{5/2} \left(\frac{B_*}{141G}\right)^{2} \left(\frac{M_*}{0.8M_\odot}\right)^{-1/2} \text{M}_\odot \text{ yr}^{-1}.$$

§ 40. Methodology

For these fixed stellar and accretion disc parameters, we make three simulations with different initial truncation radius r_{to}. Our reference simulation (s1) corresponds to an initial truncation radius fulfilling Eq. (35.104), namely $r_{to} = 1$ with $\beta(r_{to}) = 1$. Simulation (s2) is done for $r_{to} = 1.5$ with $\beta(r_{to}) = 10$ and simulation (s3) for $r_{to} = 0.5$ with $\beta(r_{to}) = 0.1$.

We then let the system evolve and observe whether or not the real disc truncation radius r_t converges towards the theoretical radius $r_{t,th}$ as given by Eq. (35.104). With our normalized quantities, the truncation radii in simulations (s2) and (s3) are thus expected to converge towards 1, with $\beta(r_t) \sim 1$. To check this, we identify this radius and then compute the plasma beta. It is however not straightforward to define this radius since the magnetic field is not a solid wall : the radial to vertical deviation of the flow is quite smooth. In practice, we get the truncation radius r_t by detecting a steep decrease in density at the disc midplane (see Fig. 50).

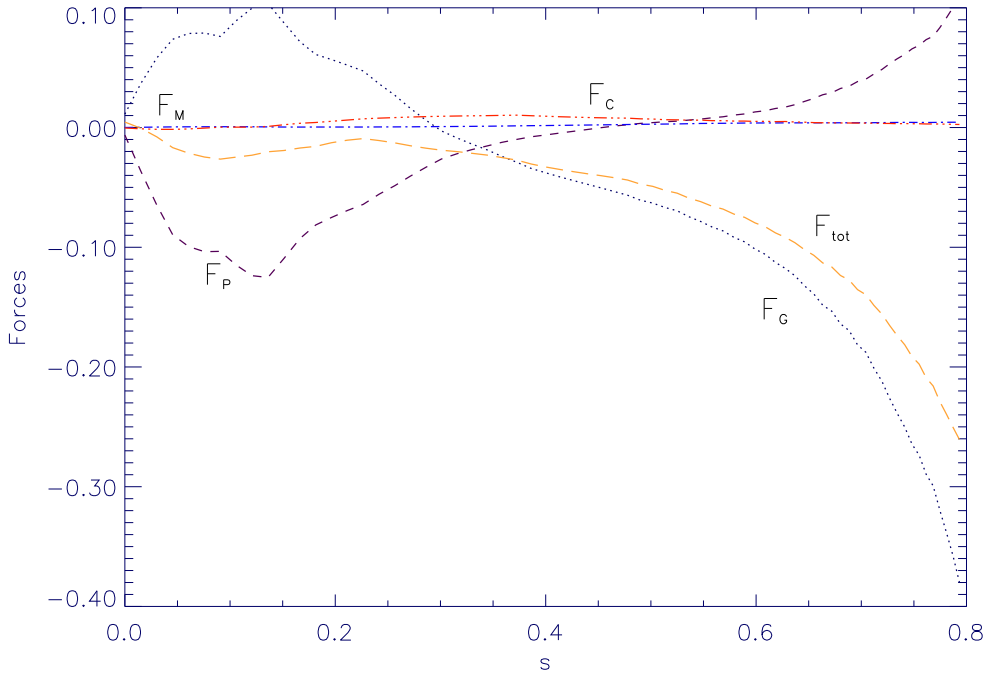

Figure 41. Projection of the forces in normalized units along a magnetic field line in the middle of the accretion column, for run (s1) at $t = 10$. We represent the gravity F_G, the centrifugal force F_C, the thermal pressure gradient F_P, the poloidal magnetic force F_M and the total force F_{tot} as function of the curvilinear coordinate s. The disc midplane is located at $s = 0$ and the disc surface corresponds to $s \sim 0.2$. Gravity begins to dominate the dynamics only at some distance between the disc and the star ($s \sim 1.2$ at the stellar surface).

§ 41. Results

§ 41.1. *The physics of funnel flow*

Figure 40 shows a series of snapshots of our reference simulation (s1). The upper left panel shows the initial condition. We have superimposed a part of the computational grid to show the resolution achieved. We have a resolution of 8 points in the vertical direction within the disc at each radius while the resolution within the accretion column reaches 20 points at the stellar surface. Magnetic field lines are in black while the white line traces an initial magnetic field line connecting the star to the co-rotation radius $r_{\rm co} = 2$. After a rapid transient phase with the opening of stellar field lines, a quasi-steady situation is achieved where quasi-steady accretion columns are formed, even with a low stellar dipole field. The final (equilibrium) truncation radius is $r_{\rm t} \sim 1.1 - 1.2$, thus well below the co-rotation radius.

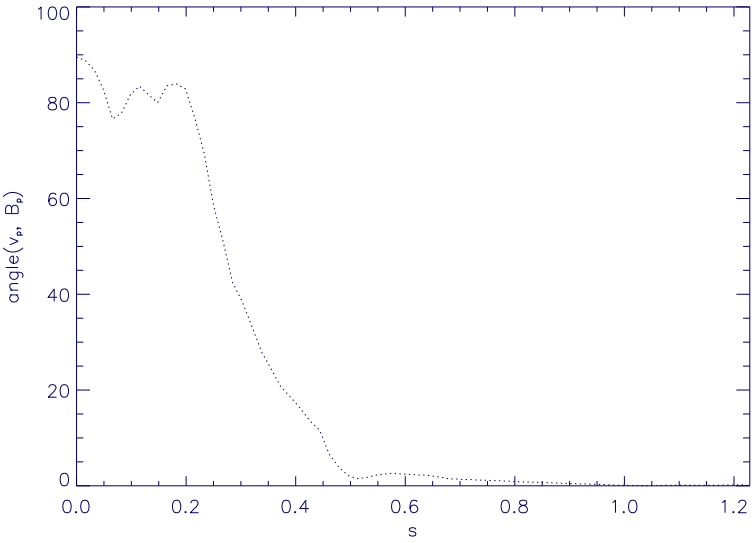

Figure 42. Angle between the poloidal velocity vector and the magnetic field one as function of the curvilinear distance s along a magnetic field line in the middle of the accretion column. One clearly sees the transition between the resistive disc and the ideal MHD funnel flow at $s \sim 0.2$.

Figure 41 shows the projection $F = \vec{B}_p \cdot \vec{F}/|\vec{B}_p|$ of the various forces along a magnetic field line located at the centre of the accretion column at $t = 10$. Since the stellar magnetic moment is directed northwards, a negative force is actually pulling material upwards. Accretion is achieved because of the negative magnetic torque (not shown here) but against the poloidal magnetic force F_M which tends to prevent it. Note however that it remains always negligible with respect to the other forces. What drives the poloidal motion in the accretion column is actually the plasma pressure gradient F_P. It is built in by the accumulation of accreting mass and allows to lift it up and load it onto closed stellar field lines as shown in Fig. 43 corresponding to the zoomed snapshots near the funnel flow drawn in Fig. 44. It acts exactly as in accretion-ejection structures, enabling the necessary transition from the resistive MHD disc to the ideal MHD columns (Ferreira & Pelletier 1995). The plasma pressure gradient remains dominant well above the disc surface, located around the curvilinear coordinate $s = 0.2$. To give a sense to

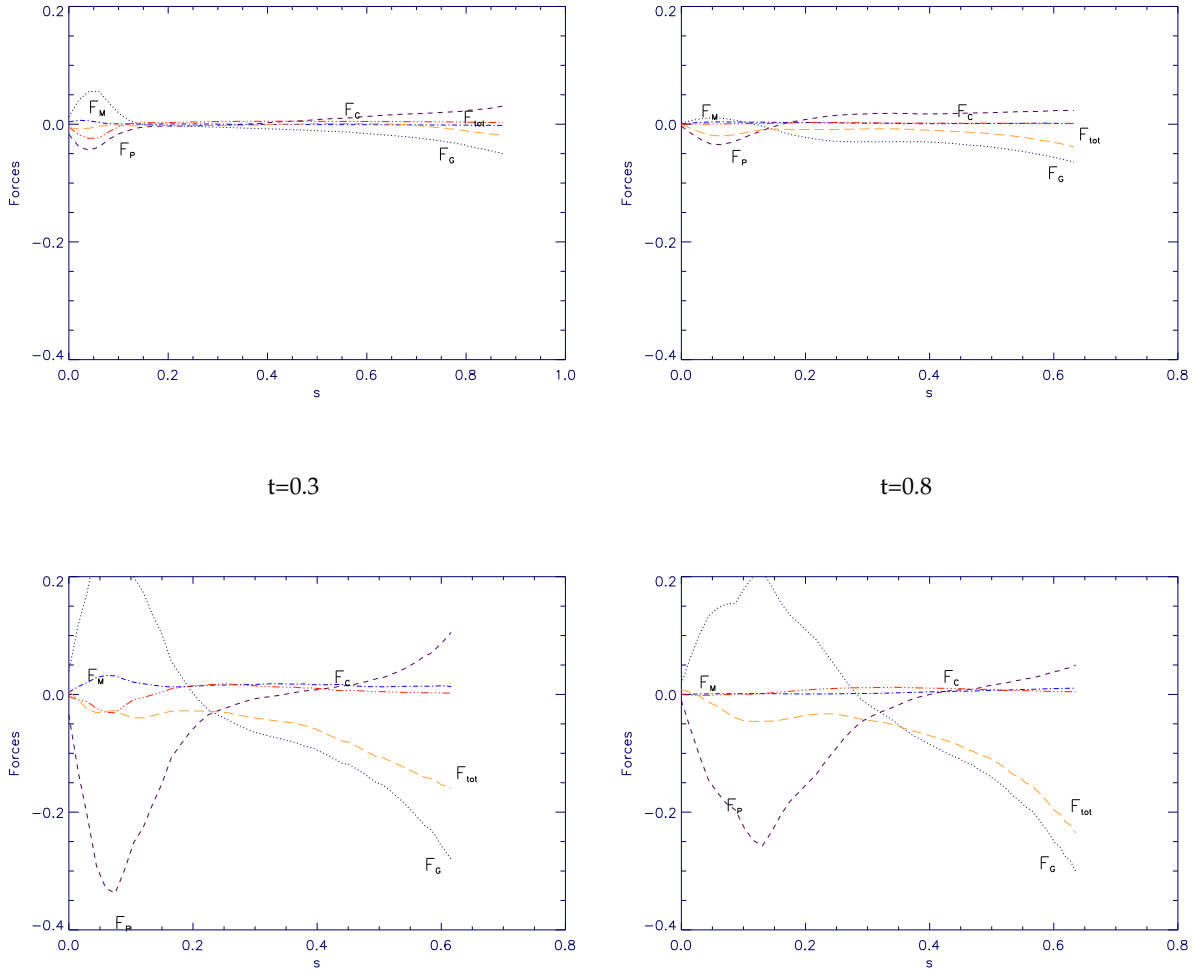

Figure 43. Same caption as Fig. 41 for the series of snapshots presented in Fig. 44. We can remark the build up of the vertical thermal pressure force between t=0.8 and t=1.4 and also the less increase of the gravitation force due to the dipole deformation caused by accretion.

the disc surface at the funnel flow basis, we plot the angle between the poloidal velocity and magnetic field vectors along the central line of the funnel flow and thus one clearly identifies the disc resistive flow with an angle around 90° from the nearly ideal flow constrained to follow the stellar magnetic field lines (see Fig. 42). Given the dipole topology, this is not surprising as material must first be lifted against gravity (F_G is initially positive) by F_P. Then, at some point (that depends mostly on the dipole geometry) gravity overcomes and becomes the leading agent. Again, this is only possible because the centrifugal term F_C plays almost no role due to the efficient azimuthal magnetic braking. Matter then reaches the star in a dynamical time scale with approximately free-fall velocities ($v_{\rm pol} \approx 310 {\rm kms}^{-1}$).

One can take a closer look at some physical quantities across the funnel flow near the stellar surface by plotting these variables versus the angle α defined from the equatorial plane. The

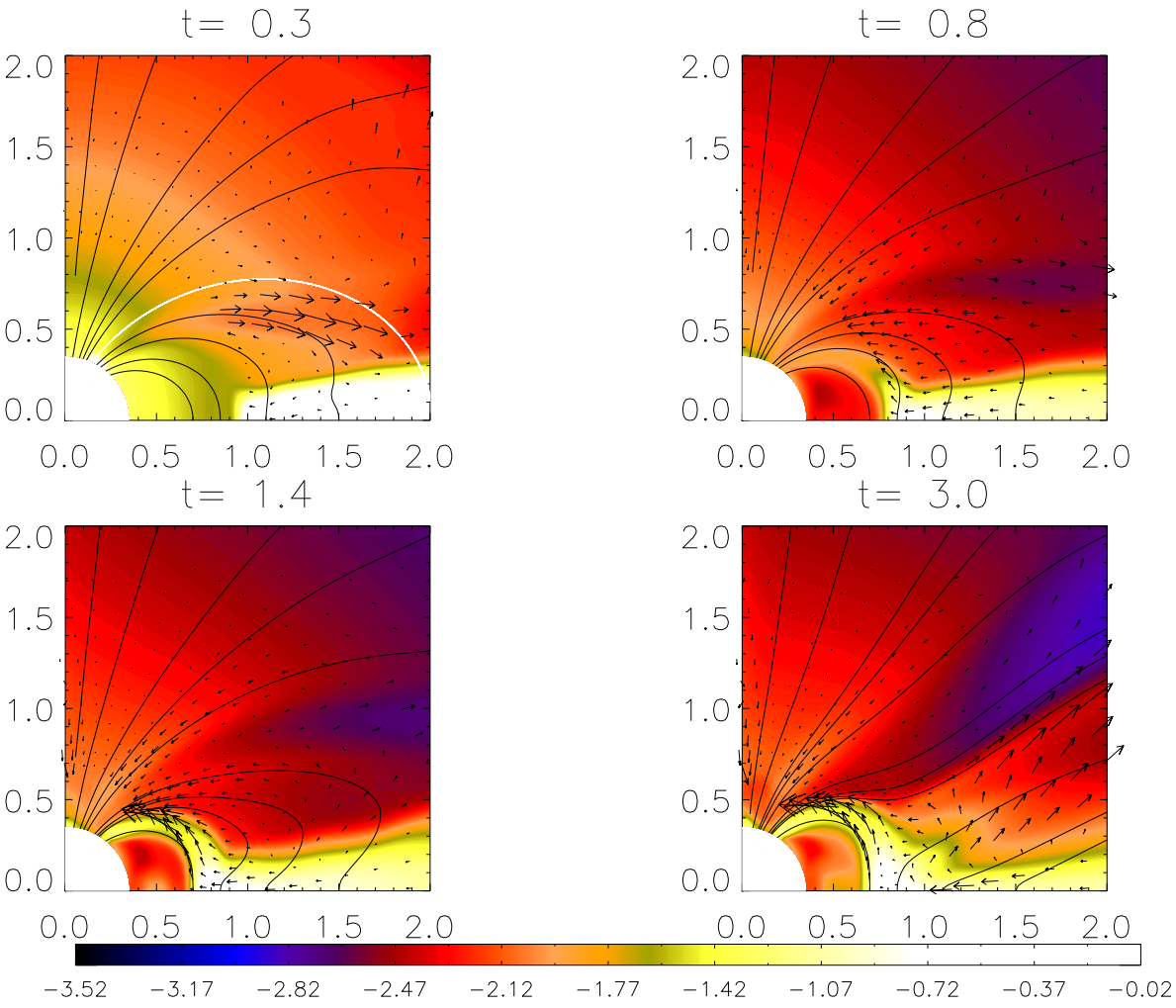

Figure 44. Same caption as in Fig. 40 with a series of snapshots focused on the development of a funnel flow corresponding to the force balance presented in Fig. 43

density plot (see Fig. 45) localizes well the accretion column centered at high latitudes ($\alpha \sim 60°$ with a $FWHM \sim 15°$) initially with a high density contrast of 10 with respect to the corona. The evolution in time shows a shift of the accretion column towards higher latitudes ($\alpha \sim 70°$) with a drop in density contrast till 3 because of not sufficient mass feeding at the disc inner edge. The shift towards higher latitude comes from the fact that the truncation radius is larger when the accretion rate diminishes and thus mass loading is achieved along field lines reaching the star nearer to the pole.

By looking at the magnetic torque via the toroidal component of the magnetic field, one clearly has a braking torque within the funnel flow (see Fig. 46). One confirms it by showing the matter angular velocity (see Fig. 47) which is well lower than the stellar rotation causing matter to collapse onto the stellar surface near free-fall speeds. One also has a negative toroidal field at the polar region where magnetic field lines were opened due to the initial condition (see Fig. 46).

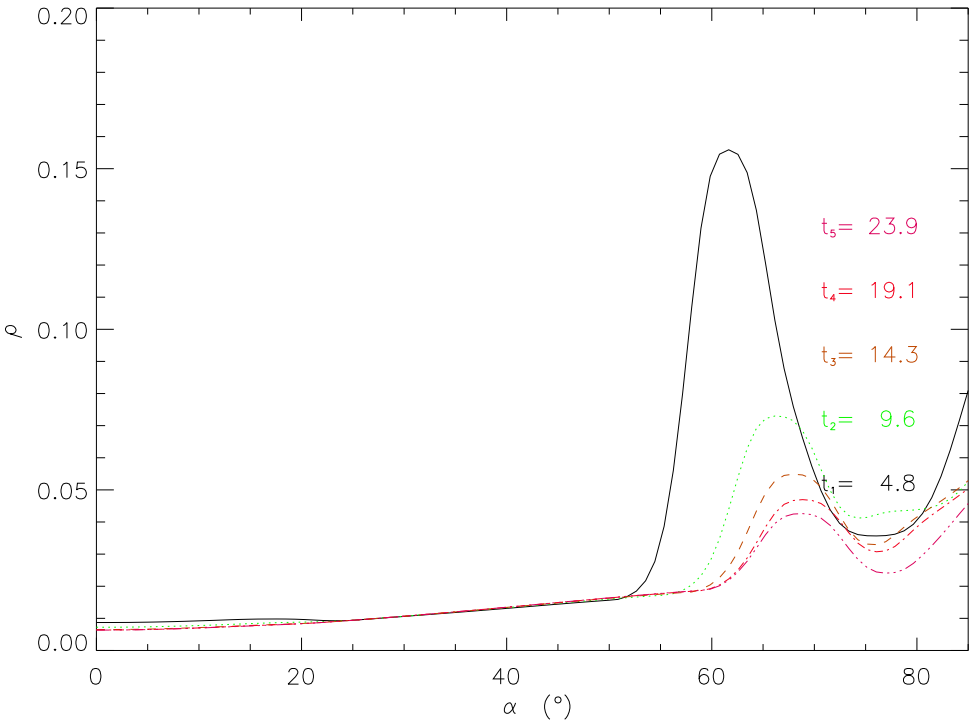

Figure 45. Density distribution at the stellar surface versus the angular distance from the equatorial plane (on the left hand side) as a function of time.

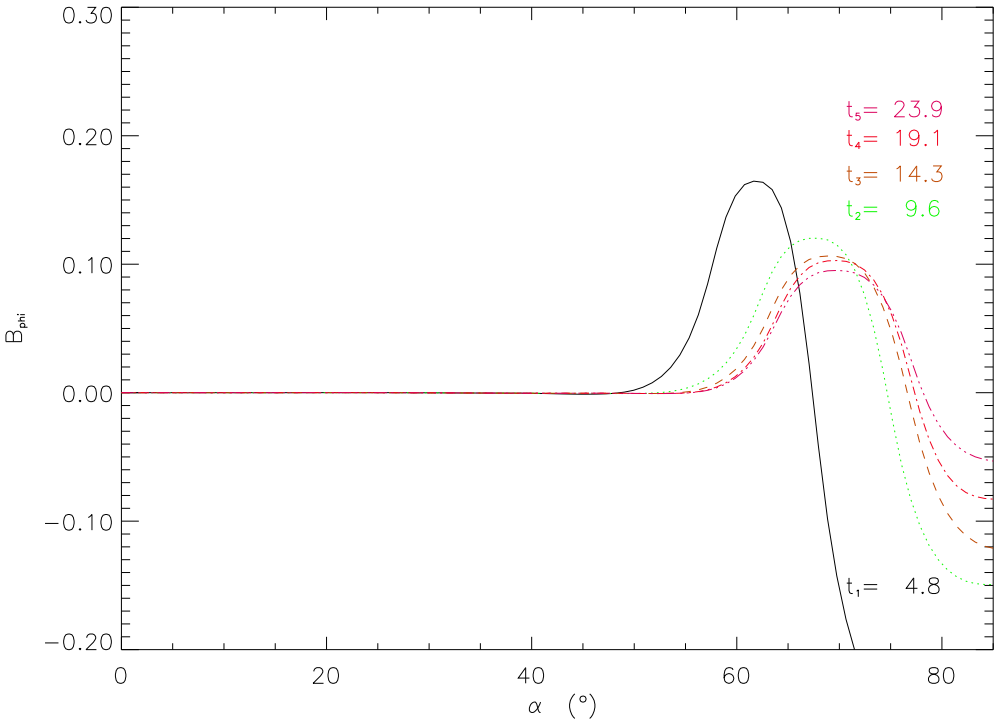

Figure 46. Toroidal magnetic field distribution at the stellar surface versus the angular distance from the equatorial plane.

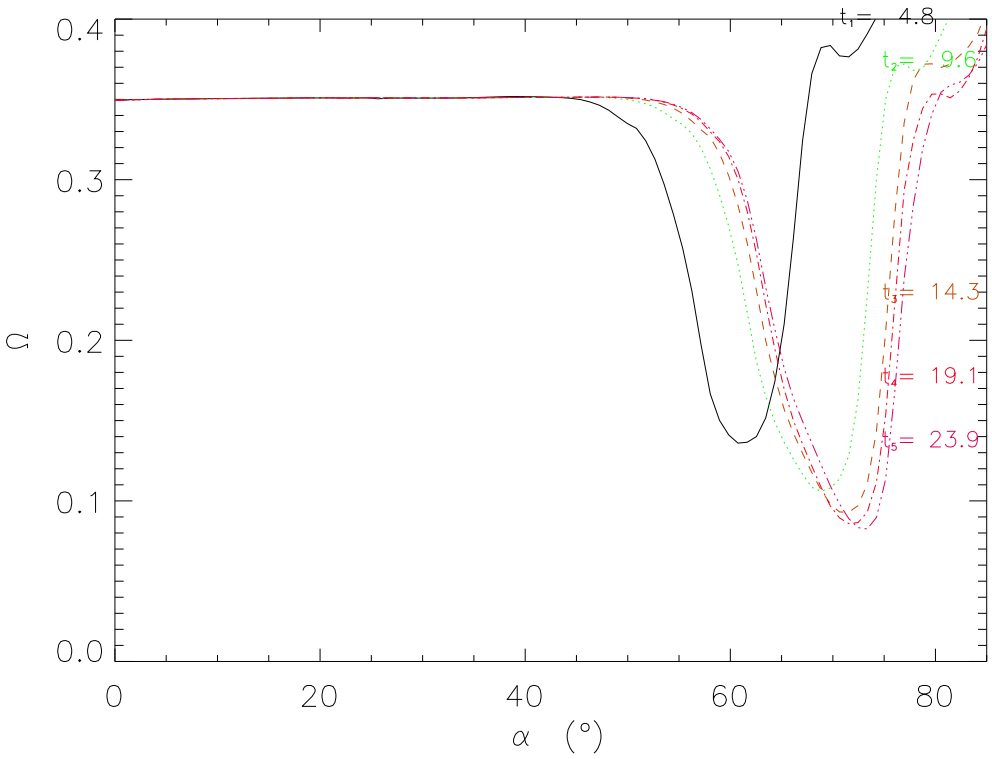

Figure 47. Angular velocity distribution at the stellar surface versus the angular distance from the equatorial plane, for consecutive times during the evolution.

§ 41.2. *Evolution of the magnetic topology*

The strong differential rotation beyond r_t, in a region where $\beta \gg 1$, leads to an expansion of the poloidal magnetic field lines. Such an expansion starts at the inner regions and enforces the outer field lines to inflate as well (but the cause there is not the differential rotation). Once these loops (inflated lines) reach the outer boundary of the computational domain, they open mimicking a reconnection. This opening is actually an effect of the boundary conditions used but, for all practical means, we see no strong bias on the evolution of the system. Anyway, on quite short time scales ($t \sim 3$), most of the stellar magnetic flux not related to the accretion funnels around r_t has been opened (Fig. 40). One might think that a disc wind is driven in this region of the disc as the Blandford & Payne (1982) criterion is fulfilled. Moreover, some mass is indeed leaving the disc along these open field lines. But this is only a breeze and not a proper jet : the ejected material does not reach super-Alfvénic speeds. We note also that no X-winds (Shu et al. 1994) are obtained despite the favorable magnetic configuration [13]. The reason why no disc wind is obtained, neither extended nor X-wind, is that the field threading the disc in these regions is far below equipartition.

The radial distribution of the vertical magnetic field (see Fig. 48) shows that the initial dipole distribution (dashed line) is well modified by the accretion process given the low

[13] This is a direct simulation of the scenario invoked by these authors since the disc magnetic field comes from the opening of the magnetosphere.

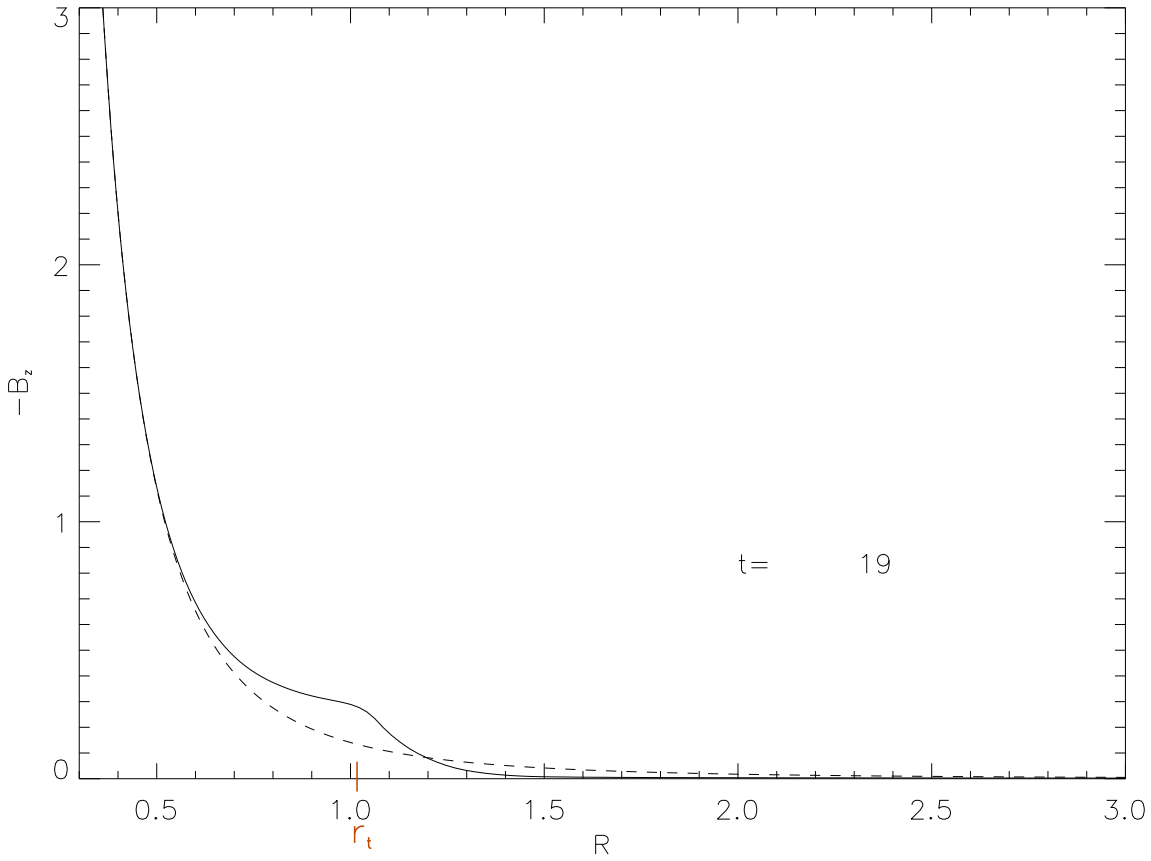

Figure 48. Radial distribution of B_z (solid line) with respect to the initial dipole distribution (dashed line).

resistivity chosen ($\alpha_{\rm m} = 0.1$). One particularly remarks the strong compression of the dipolar magnetosphere near the disc truncation.

§ 41.3. *Truncation radius in simulations*

The results of varying the initial truncation radius (simulations s2 and s3) are summarized in Fig. 49. In both cases, we observe a rapid convergence to $r_{\rm t} \approx 1.1 - 1.2$ on a dynamical time scale. Although some fluctuations in time can be seen in $r_{\rm t}$, it remains strikingly close to unity. Besides, it is really close to the radius of equipartition where $\beta = 1$, r_1, with a relative position lower than 4%. This is another indication of the importance of the plasma pressure gradient in defining the truncation radius and justifies the approximation $\beta(r_t) \sim 1$.

The discrepancies from the mean curves we can see for (s2) and (s3) respectively at t=11 and t=7 is due to some diffusion of matter coming from the accretion column at the stellar surface which next is ejected along opened field lines disturbing a bit the magnetosphere. This is due to the fact that initial conditions for these two simulations depart from equilibrium with equipartition conditions. However, later on, the accreted material reaching the stellar surface is well absorbed by the boundary conditions.

The accretion rate onto the star is the one that is actually observationally determined through, e.g. veiling measurements. It is obtained here by computing the mass flux in the accretion

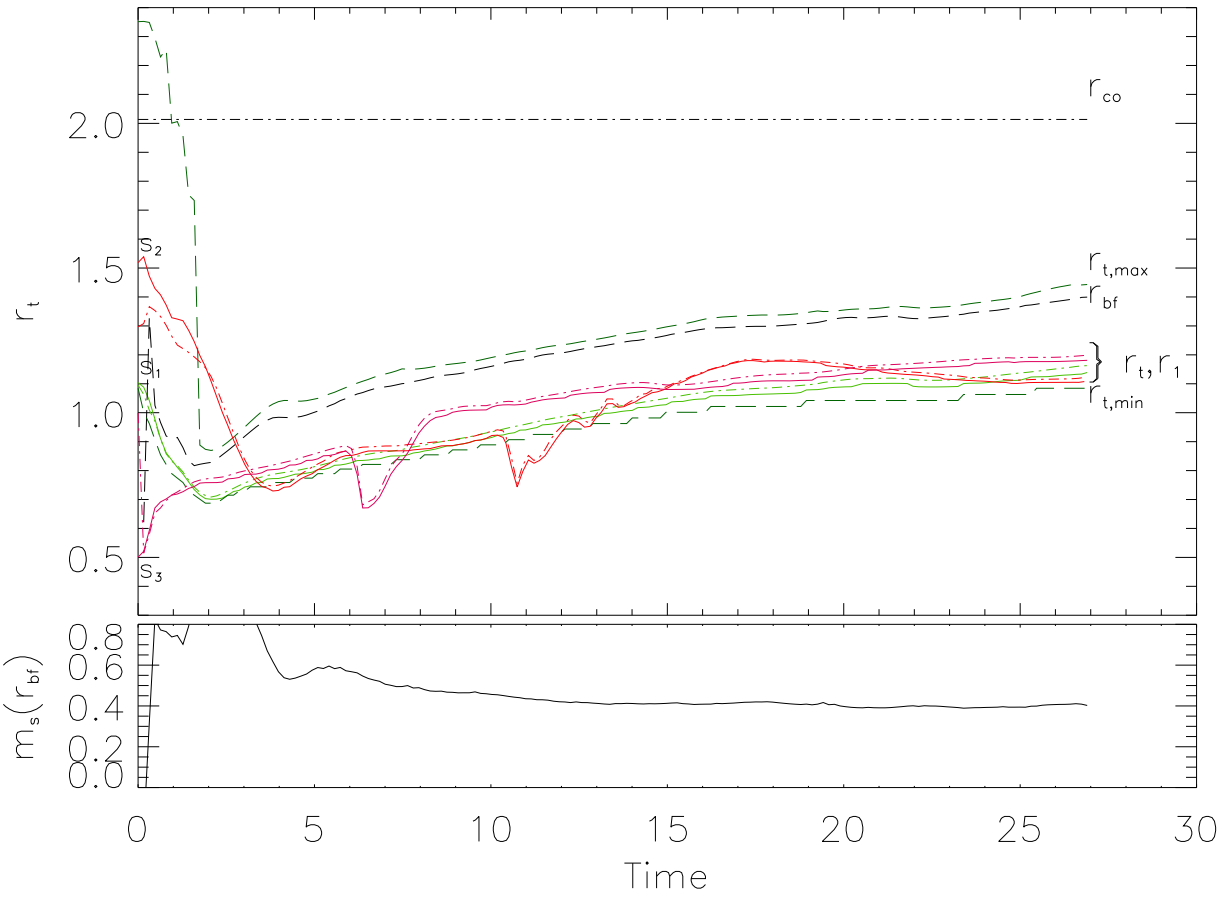

Figure 49. Top - Evolution in time of the position of the truncation radius r_t (solid lines) for a set of resistive MHD simulations with $B_* = 141$G, $P_* = 5.1$days and $\alpha_{\rm m} = 0.1$ and a different initial truncation radius. The time unit is the Keplerian period at r=1. All runs converge towards a truncation radius $r_{\rm t} \sim 1.2$ (solid lines). Dash-dot lines represent, for each simulation, the radius r_1 where $\beta = 1$. We report also the radius $r_{\rm bf}$ (dashed line) which indicates the base of the funnel flow, $r_{\rm t,max}$ (dashed line) and $r_{\rm t,min}$ for our reference run (s1). Bottom - Evolution in time of the sonic Mach number at the base of the funnel, $m_{\rm s}(r_{\rm bf})$, for run (s_1).

column, namely $\dot{M}_a = \int_S \rho \mathbf{v}_p \cdot d\mathbf{S} = -4\pi R_*^2 \int_S \rho v_R \sin\theta d\theta$. Surprisingly, it is found to converge towards 0.91 10^{-9}M$_\odot$.yr^{-1} (see Fig. 52), hence a factor 10 smaller than the mean accretion rate in CTTS. We will come back to this issue later. Now, if we insert this value in Eq. 35.104, we find a theoretical truncation radius $r_{\rm t,th} = 1.38$, using $m_s = 1$. This is off by 20%, which is not bad considering our crude approximations of such a complicated problem.

Since $\beta(r_t) \sim 1$ is well verified, the main source of discrepancy in Eq. 35.104 is due to the assumption of $m_s(r_t) \sim 1$. This is too crude for an obvious reason. Indeed, the disc truncation radius, as measured by the steep drop in density at the equatorial plane, is actually the point where $u_r = 0$, hence $m_s = 0$. Figure 49 shows the evolution of the sonic Mach number m_s computed for run (s1) at $r_{\rm bf}$, which corresponds to the base of the funnel flow where the poloidal magnetic pressure matches the poloidal ram pressure. It can be seen that r_{bf} is larger than r_t by almost 30%. This is not surprising as it is necessary to first brake down efficiently material ($r_{\rm bf}$) before being able to lift it up (r_t). This is also illustrated in Fig. 50 where we plot the radial profile of several quantities at the disc midplane: density ρ, angular velocities (real Ω and Keplerian

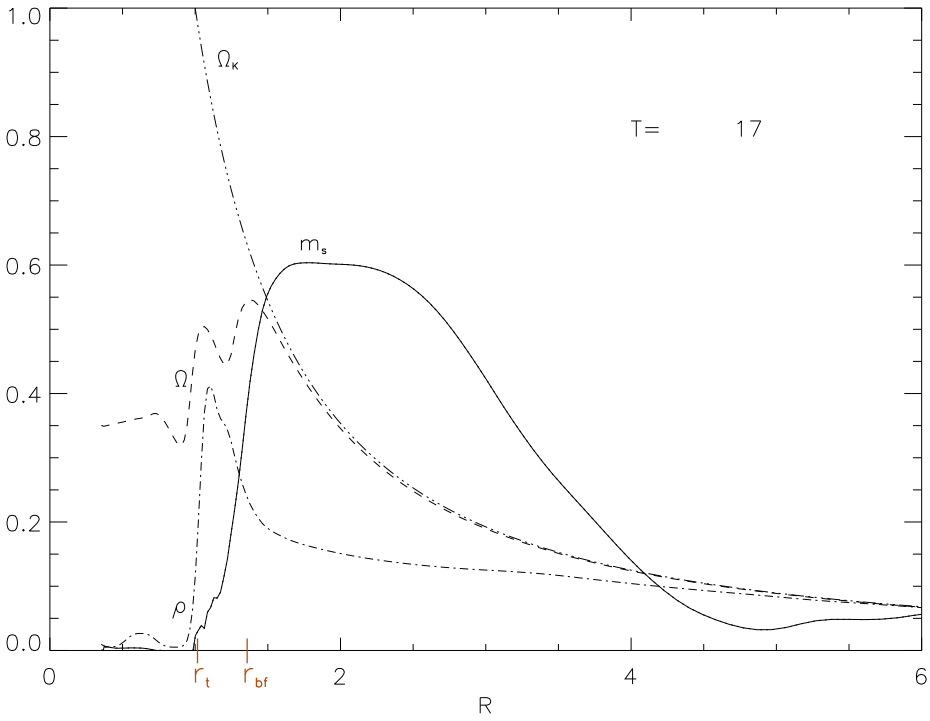

Figure 50. Radial distributions of density ρ, angular velocities Ω (real) and Ω_K (Keplerian) and sonic Mach number $m_s = u_r/C_s$ at the disc midplane, for run (s1) after 17 keplerian rotations. Notice the large accretion velocity in the region of opened stellar field lines.

Ω_K) and m_s. Clearly, taking $m_s = 1$ to derive $r_{t,th}$ is too crude. We find that using a value of $m_s \simeq 0.45$, namely close to the real value $m_s(r_{bf})$ (see Fig. 49), provides a much better estimate with $r_{r,th}$ close to r_t with an accuracy better than 10%.

Although the simulations here do not take into account viscosity, we plotted for completeness in Fig. 49 the evolution of the radius $r_{\rm t,max}$ for run (s1). To do so, we assumed $\alpha_{\rm v} = 1$ (thus overestimating the viscous torque) and measured numerically q (see Sect. 2). As expected, $r_{\rm t,max}$ remains always significantly larger than the real truncation radius $r_{\rm t}$, which implies that criterion A is not good enough. On the other hand, criterion B would give a truncation radius located at $r_t = 0.3$: no accretion column should have been observed at all in our simulations. Our results clearly show that criterion B is not relevant. What about the criterion as expressed in Equation (35.101)? We plotted in Fig. 49 the evolution of the radius $r_{\rm t,min}$ given by this equation and computed for run (s1). It turns out that it gives indeed a nice (though under-) estimate of the real truncation radius r_t as already pointed out by Romanova et al. (2002). This is because the star disc interaction introduces a sharp decrease in both the disc midplane density ρ and azimuthal velocity $v_\phi = \Omega r$ (see Fig. 50). However, as stressed in Sect. 1, while basically correct such a criterion is useless as a predictive tool.

As far as the formation of funnel flows is concerned, we fully confirm the results of Romanova et al. (2002) : these flows are indeed robust features of axisymmetric MHD simulations. Their different boundary conditions on the magnetic field at the stellar surface, namely a fixed normal component and free conditions for B_θ and B_ϕ, do not finally play any

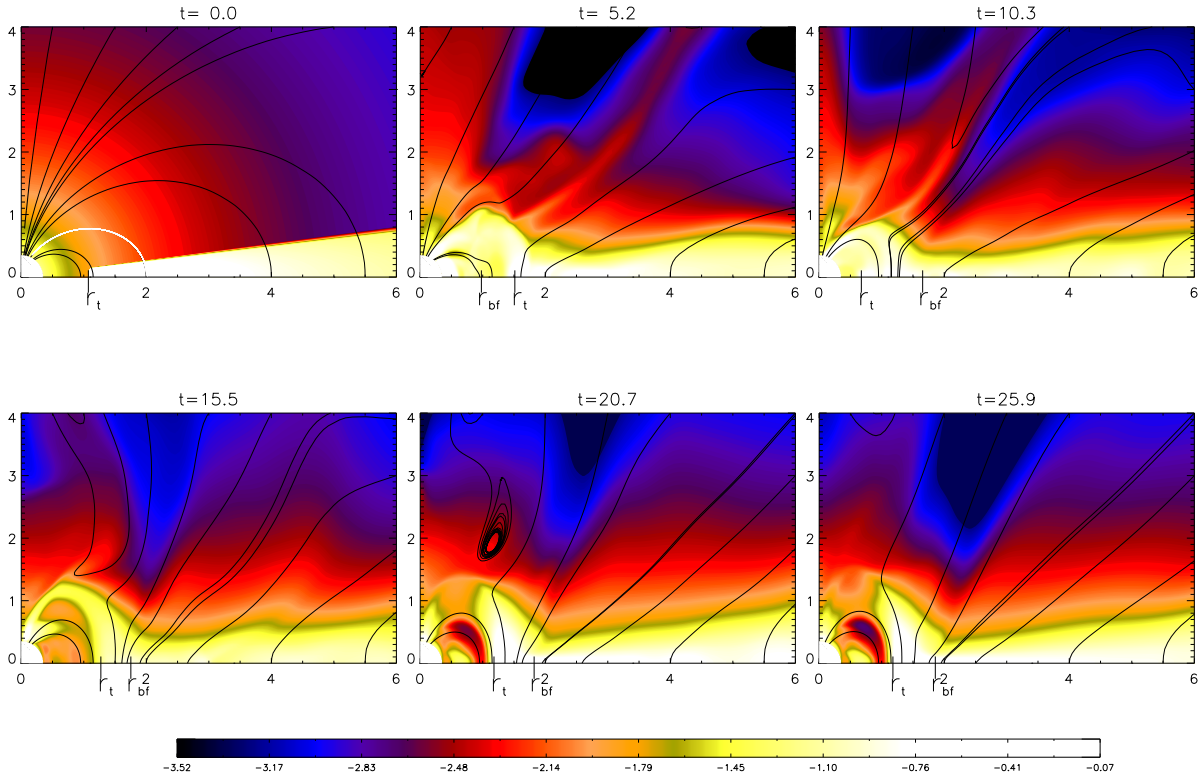

Figure 51. Simulation with the boundary conditions of Romanova et al. (2002) for the inner boundary, i.e. free boundary conditions for B_θ and B_ϕ and fixed B_r component.

significant role for the truncation of the disc and the formation of accretion columns (see Fig. 51). We have also done simulations with other values of the magnetic resistivity parameter α_m with no change in the truncation radius. Note also that Romanova et al. (2002) have included viscosity in their simulations while we did not, with no significant difference in the location of the truncation radius. To be more specific, using Eq. (35.104) with the higher accretion rate of $\dot{M}_a = 9 \times 10^{-8} M_\odot.yr^{-1}$ as measured by Romanova et al. (2002) at t=10, we find $r_{\rm t,th} = 0.9$ for $B_* = 1.1$kG using $m_s = 0.45$, which is consistent with the truncation radius shown Fig. 16 in Romanova et al. (2002) with a good accuracy. The initial condition in Romanova et al. (2002) gives a very high accretion rate around $\dot{M}_a = 1.5 \times 10^{-8} M_\odot.yr^{-1}$ for $\alpha_v = 0.02$ and thus the accretion rate with weaker magnetic field will give an accretion rate a bit greater. By assuming a mean accretion rate of $\dot{M}_a = 6 \times 10^{-8} M_\odot.yr^{-1}$, we would find $r_{\rm t,th} = 0.8$ for $B_* = 630$G, $r_{\rm t,th} = 0.6$ for $B_* = 420$G and $r_{\rm t,th} = 0.4$ for $B_* = 210$G still using $m_s = 0.45$ in good agreement with their Fig. 16.

Furthermore, using Eq. (35.104) with the values provided by Kuker et al. (2003) one gets truncation radii smaller than the inner radial boundary, which explains why these authors did not find accretion columns. We are therefore confident on our main conclusion, that is the validity of our criterion (35.104).

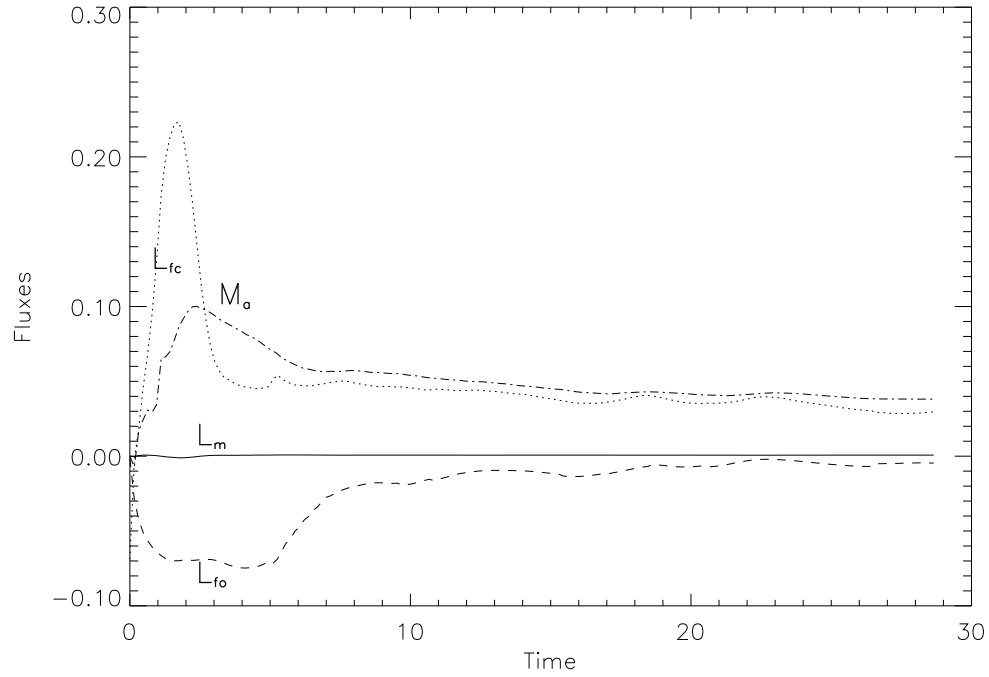

Figure 52. Top - Evolution in time of the accretion rate $\dot{M}_a$ (dash dotted line), angular momentum flux transported by matter $\dot{L}_m$ (solid line) and by the magnetic field, computed for the closed $\dot{L}_{fc}$ (dash line) and open $\dot{L}_{fo}$ (dotted lines) field lines. The units are normalized and the two hemispheres are taken into account.

§ 41.4. *Angular momentum at the stellar surface*

Let us now have a look at the fluxes of angular momentum, namely $\dot{L}_m$ carried in by the infalling material and $\dot{L}_f$ by the magnetic field

$$\begin{aligned} \dot{L}_m &= \int_S \rho\Omega r^2 \mathbf{v}_p \cdot d\mathbf{S} = -4\pi R_*^2 \int_S \rho\Omega r^2 v_R \sin\theta d\theta \\ \dot{L}_f &= -\int_S r B_\phi \mathbf{B}_p \cdot d\mathbf{S} = 4\pi R_*^2 \int_S r B_\phi B_R \sin\theta d\theta \end{aligned} \quad (41.115)$$

To explicitly write these expressions we assumed that the surface element is directed inwards with respect to the surface of the star. The flux carried by the magnetic field is the sum of that carried by closed field lines and open field lines, namely $\dot{L}_f = \dot{L}_{fc} + \dot{L}_{fo}$. It actually corresponds to two possible electric circuits related each to two different electromotive forces. A positive flux describes a positive torque acting on the star and leading to a spin up while a negative flux leads to a spin down. The time evolution of these fluxes is shown in Fig. 52 for our reference run (s1). Without surprise, the incoming angular momentum flux $\dot{L}_m$ due to the accreting material is positive but totally negligible with respect to that carried by the closed magnetic field lines $\dot{L}_{fc}$, which is positive as well: the accreting star is only being spun up.

When looking closer at $\dot{L}_f$, it turns out that there is a negative magnetic contribution to the torque due to the open field lines $\dot{L}_{fo}$. This has been also previously reported in simulations and is a natural outcome of the star-disc interaction (Long et al. 2005). We stress however that the actual torque is not controlled and one should not take it at face value. Indeed, this region of the

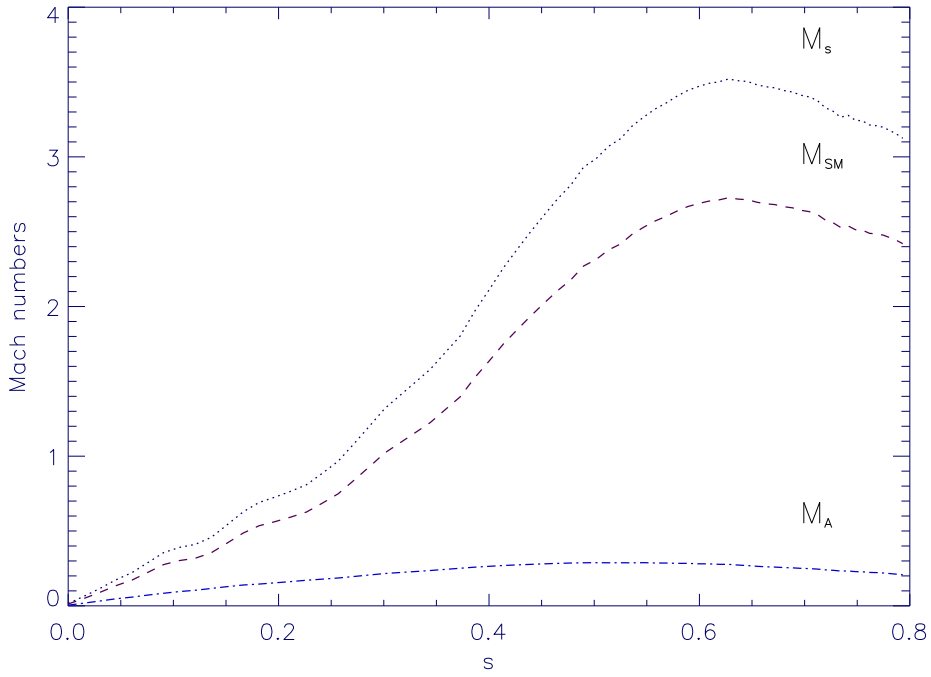

(A)

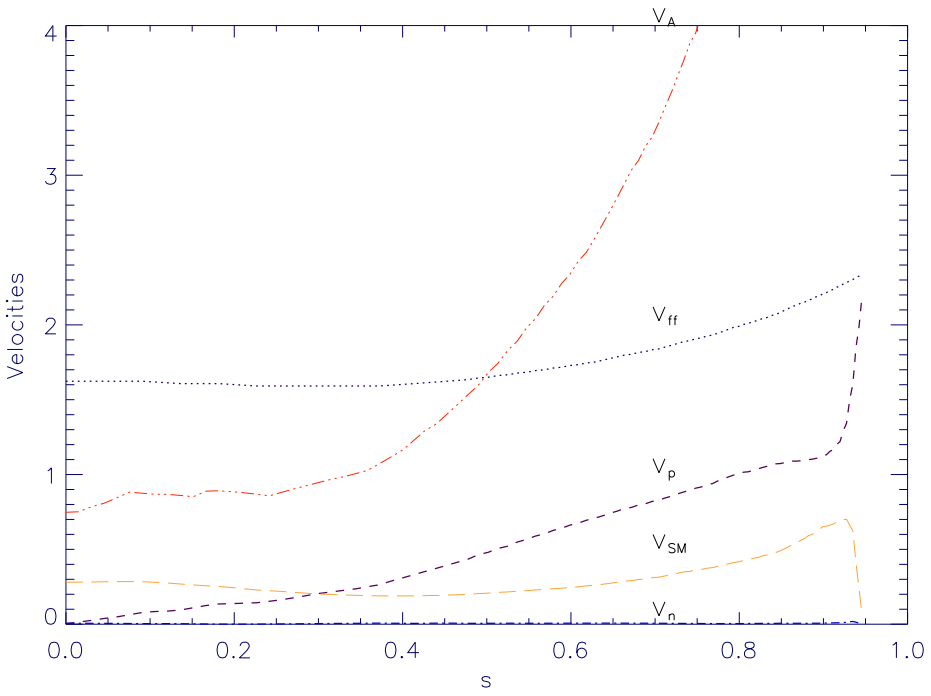

(B)

Figure 53. (A)-Sonic (dotted line), Slow-Magnetosonic (dashed line) and Alfvénic (dash-dotted line) Mach numbers within the funnel flow along the same magnetic field line at t=10 as in Fig. 41. (B)-We represent the free-fall velocity profile v_{ff}, the transverse velocity to the funnel-flow v_n, the Slow-Magnetosonic speed v_{SM}, the poloidal velocity parallel to the magnetic field v_p and the Alfvénic speed v_A.

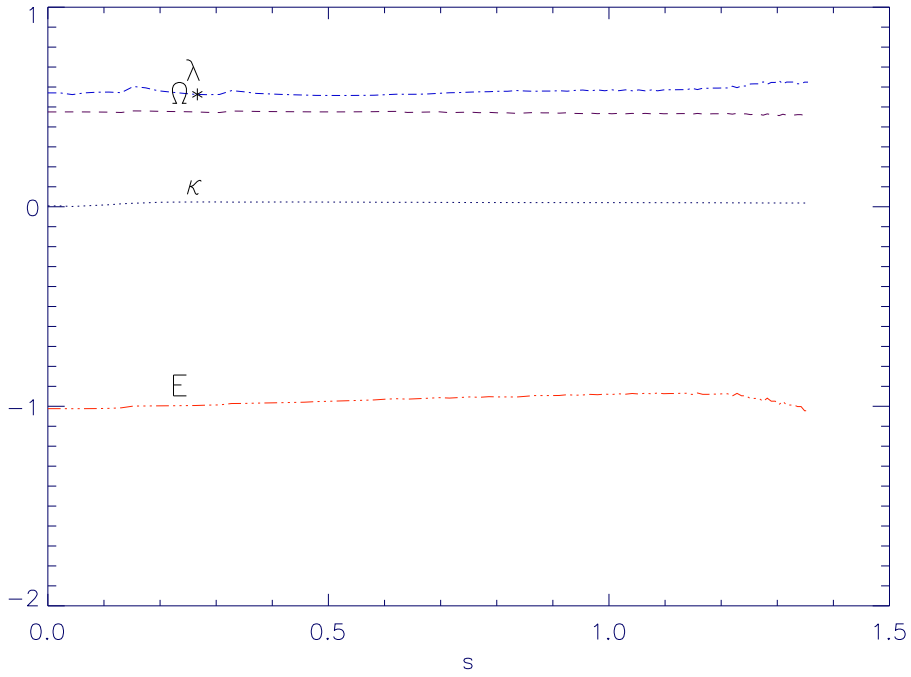

Figure 54. MHD invariants as defined in chapter 1 along a central magnetic field line in the funnel flow at t=17.

magnetosphere should be the locus of a stellar wind but the physics of its launching has never been addressed so far.

§ 41.5. *Relation between accretion rate and magnetic field topology ?*

Finally, let us turn back to our result that the accretion rate $\dot{M}_a$ measured onto the star is about 10 times smaller than expected. In fact, B_* and $\dot{M}_a$ were considered in Eq. 35.104 as independent parameters. However, the mass inflow at the inner edge of the accretion disc is constrained by the magnetic topology. Basically, the magnetosphere acts as a nozzle and the mass flow cannot be arbitrary. In a strict steady-state analysis it would be imposed by the regularity condition at the slow magnetosonic point. In our simulations, the flow reaches the slow point $M_{SM} = 1$ above the disc at $s \sim 0.3$ (see Fig. 53). Then, it remains supersonic with a maximum for the sonic Mach number around $M_s \sim 3.5$ but the funnel flow is always sub-Alfvénic with a maximum Alfvénic Mach number $M_A \sim 0.3$ near the middle path between the stellar surface and the disc inner edge. We show the location of the slow magnetosonic critical surface in Fig. 55 and remark that this point is reached well above the disc and sometimes only in the inner parts of the funnel when the magnetic field lines are too distorted by both the opening of the field and accretion.

In our simulations, we do not observe within the funnel flow an increase of density at the stellar surface with respect to the density at the disc surface (see Fig. 56) and at best a similar density for weak field but this field is really distorted. That is why the slow point is reached well above the disk contrary to predictions of Koldoba et al. 2002. For stronger field ($B_* = 322G$), one has an increase in density by a factor 6 at the stellar surface as shown in Chapter 5. In Romanova et al. (2002), they do not observe such an increase of density even for strong field

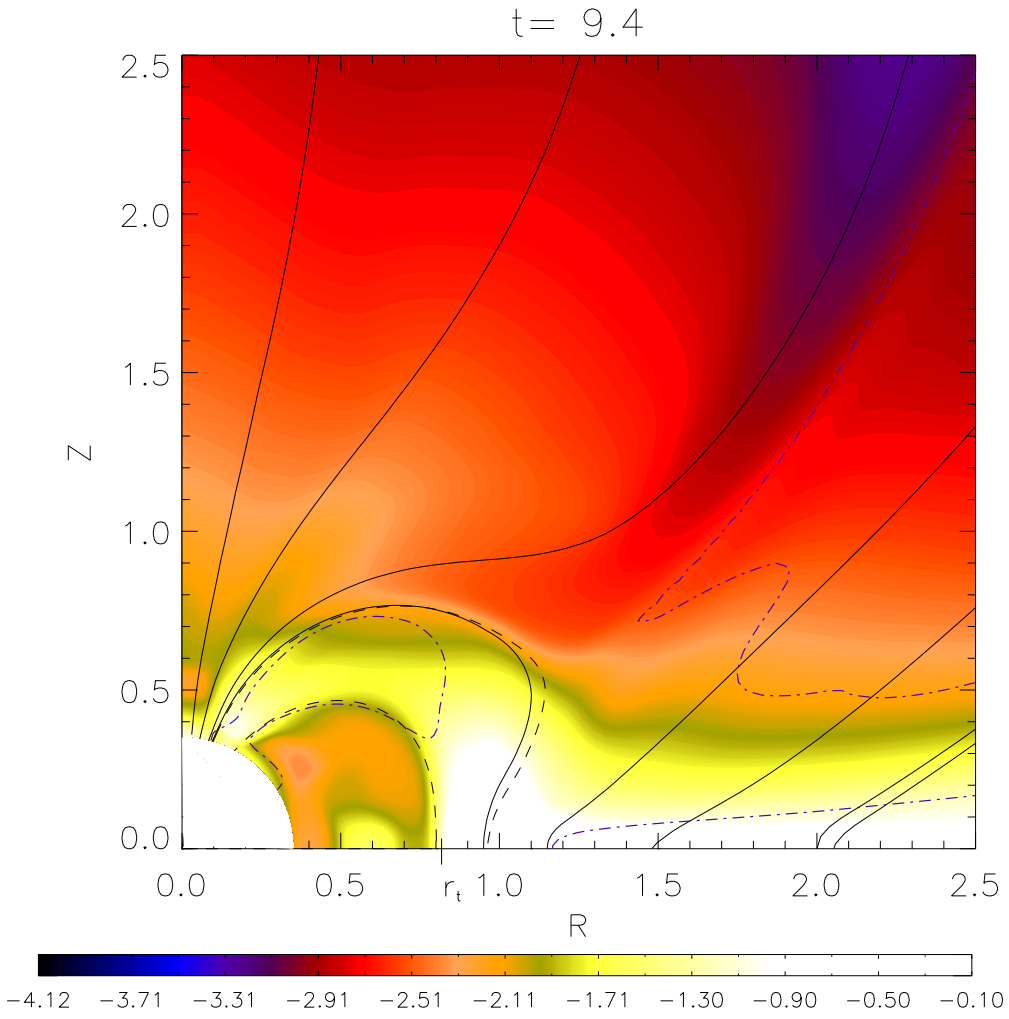

Figure 55. Location of the slow magnetosonic surface within the funnel (blue dashed-dotted line) at t=9.4. We also plot some magnetic field lines (black solid lines) and specially those at the edges of the accretion column (black dashed lines) showing the distorted field. One can remark that the flow within the disc is super-slow and becomes sub-slow at r<1.2 near the truncation radius at r=0.8. Material launching along the opened field lines becomes super-slow above the disc near $z \sim 0.5$.

of kG. In stationary models, ideal MHD conditions imposes conservation of mass and magnetic flux within the accretion column and thus a constant $\kappa = \rho \frac{v_p}{B_p}$ for each field line which gives $\rho \propto r^{-\frac{5}{2}}$ by assuming a free-fall speed near the star. For typically $r_t = 3R_*$, we expect an increase of density around 14. We have in our simulations already constant mass load per magnetic flux unit κ (see fig. 54 with also the other MHD invariants) but the velocity field is far from a free-fall distribution (see fig. 53). This is really important to notice since one would have specific constraints on observations by calculating resulting emission lines for instance. One can also remark the temperature distribution within the funnel flow (Fig. 56) which shows a global increase towards the stellar surface but a small decrease of it just above the disc corresponding to an adiabatic cooling due to the local increase of the cross-section of the deformed funnel-flow.

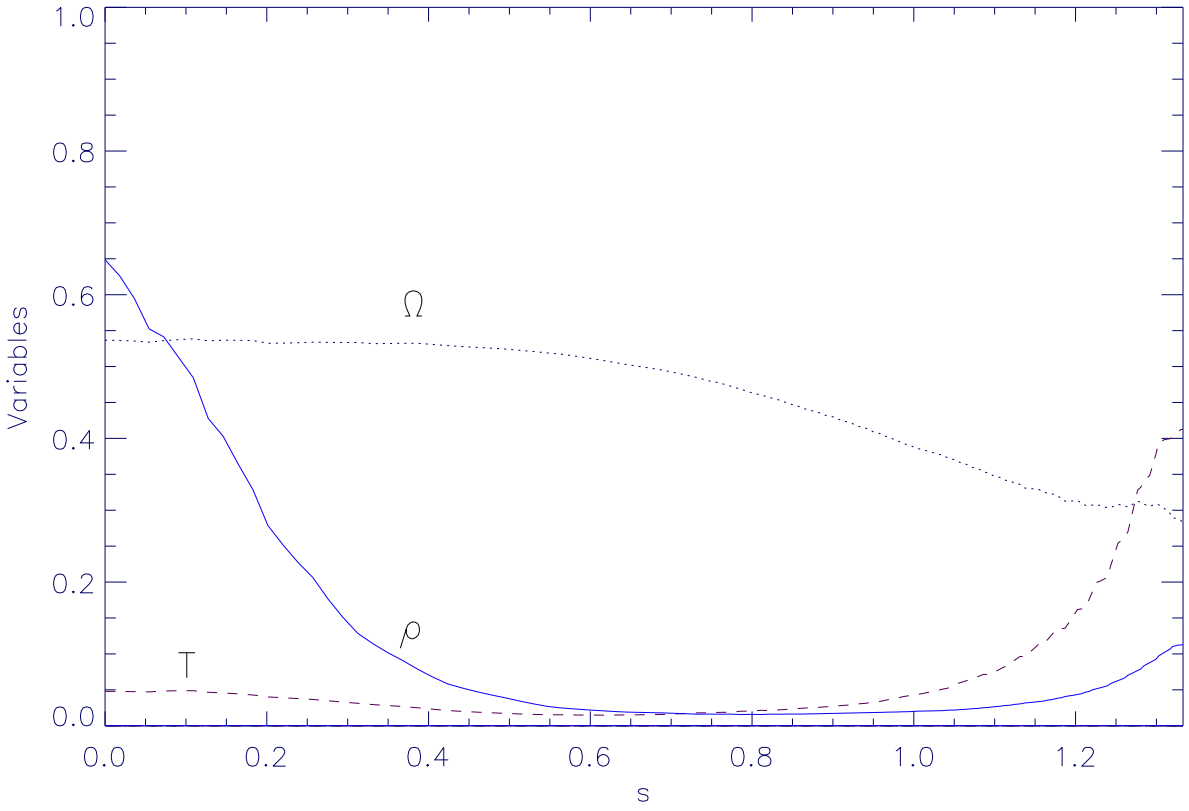

Figure 56. Evolution of density, temperature and angular velocity within the funnel flow along a central magnetic field line

§ 41.6. *Influence of resistivity on the truncation of the disc*

We carried out other simulations with $\alpha_m = 1$ and $\alpha_m = 0.$. We finally obtain the same truncation radius as shown in Fig. 57. This result is not a priori trivial since we can expect that lower disc resistivity will magnify the magnetic torque, braking the accretion flow below the corotation. However, matter has much difficulty to diffuse through the magnetosphere in this case and the truncation radius position results from a fine balance between the toroidal force balance and the less permeability of the magnetosphere.

The magnetic field in the funnel flow in the case $\alpha_m = 1$ is less disturbed by the accretion within the disc with respect to the case $\alpha_m = 0.1$(see Fig. 58) since matter can better diffuse across the magnetic field lines. We compute in this case the force balance along a central magnetic field line inside the accretion column. Both gravity and pressure forces enable matter to reach the stellar surface (Fig. 59) whereas one had a contribution of gravity opposite to the thermal pressure at the funnel flow basis in the lower disc resistivity case. However, this configuration with very high disc diffusivity and no viscosity causes quickly disruption of the disc due to the accelerating magnetic torque which produced excretion of matter within the disc beyond corotation till magnetic reconnection when poloidal field is too radially stretched. Actually, the opening mechanism of the poloidal magnetic field line is reduced in this parameter regime and

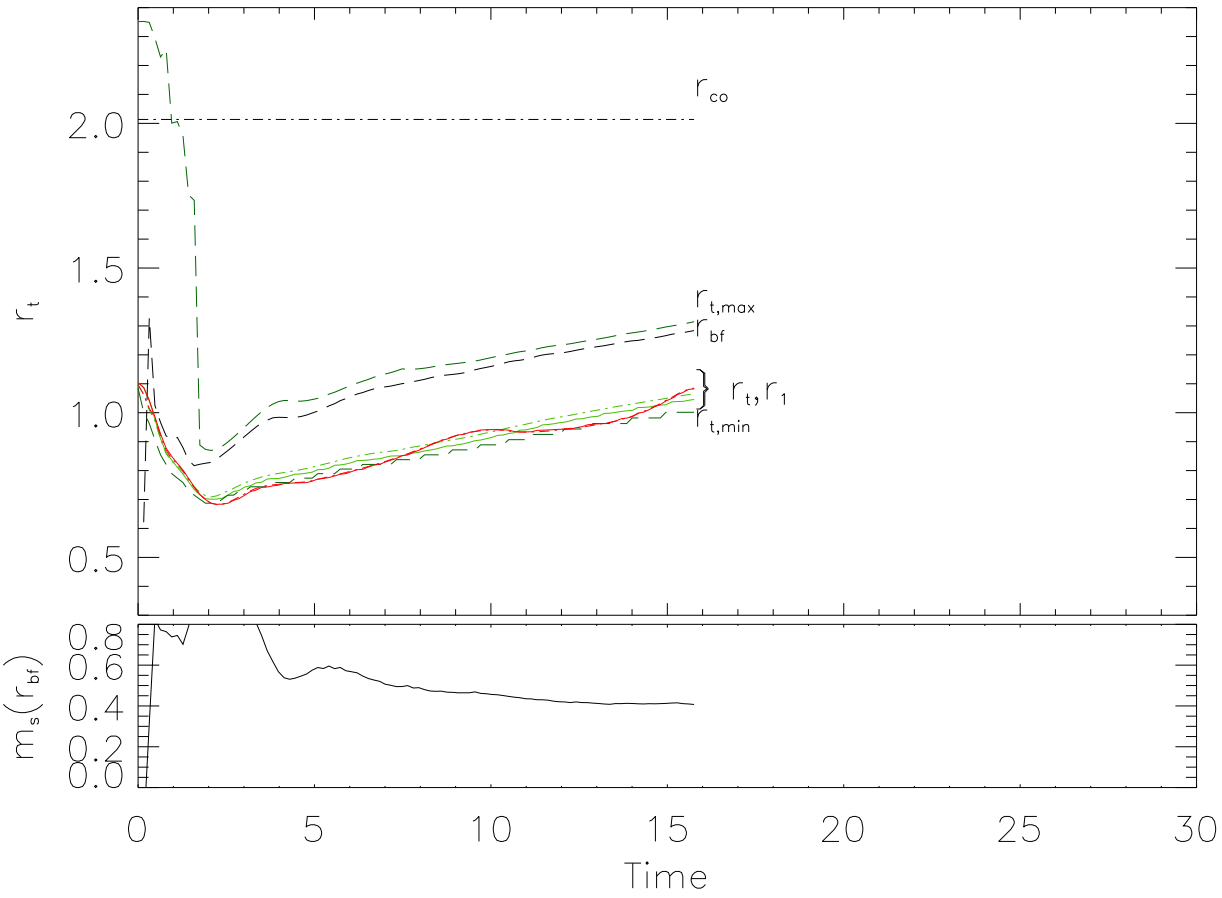

Figure 57. Same caption as in Fig. 49 with $B_* = 141$G, $P_* = 5.1$days and two different disc diffusivities characterized by $\alpha_{\rm m} = 0.1$ (green curve) and $\alpha_{\rm m} = 0.$ (red curve). The two runs converge towards the same truncation radius $r_{\rm t} \sim 1.1$.

thus there is no counterpart to the excretion like previously with low resistivity. Thus, we do not develop a deep analysis of this configuration.

3. Conclusion

We have confirmed that the formation of accretion funnel flows is a robust feature of axisymmetric star-disc interactions. We investigated the physical conditions required to produce steady-state funnel flows onto a dipole and provided an analytic expression of the disc truncation radius. We then used MHD simulations with VAC to show its validity.

Our theoretical expression $r_{t,th}$ relates the disc truncation radius with astrophysical parameters such as stellar dipole field B_*, mass M_*, radius R_* and accretion rate $\dot{M}_a$. Although it resembles the Alfvén radius (Elsner & Lamb 1977) sometimes invoked in similar situations (Bouvier et al. 2007), it has been physically motivated on very different ground. It is shown that it gives an accurate prediction of the real truncation radius as obtained in current 2D MHD simulations of a star-disc interaction.

We report MHD simulations displaying accretion funnels with a weak stellar dipole field $B_* \sim 140$ G from a resistive non viscous disc. In this case, the disc inner edge is found closer to

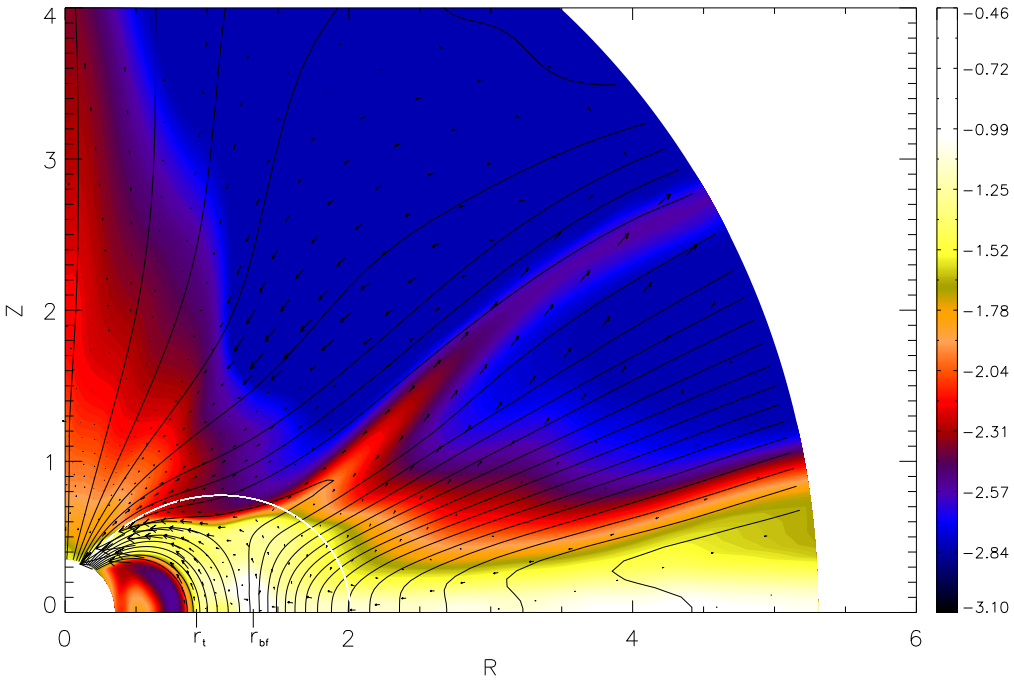

Figure 58. Resistive MHD simulation for a 5 days period CTTS with $B_* = 141\mathrm{G}$ and $\alpha_\mathrm{m} = 1$ after t=10. One shows the density distribution in the computational domain using a log scale as well as flow vectors and magnetic field lines.

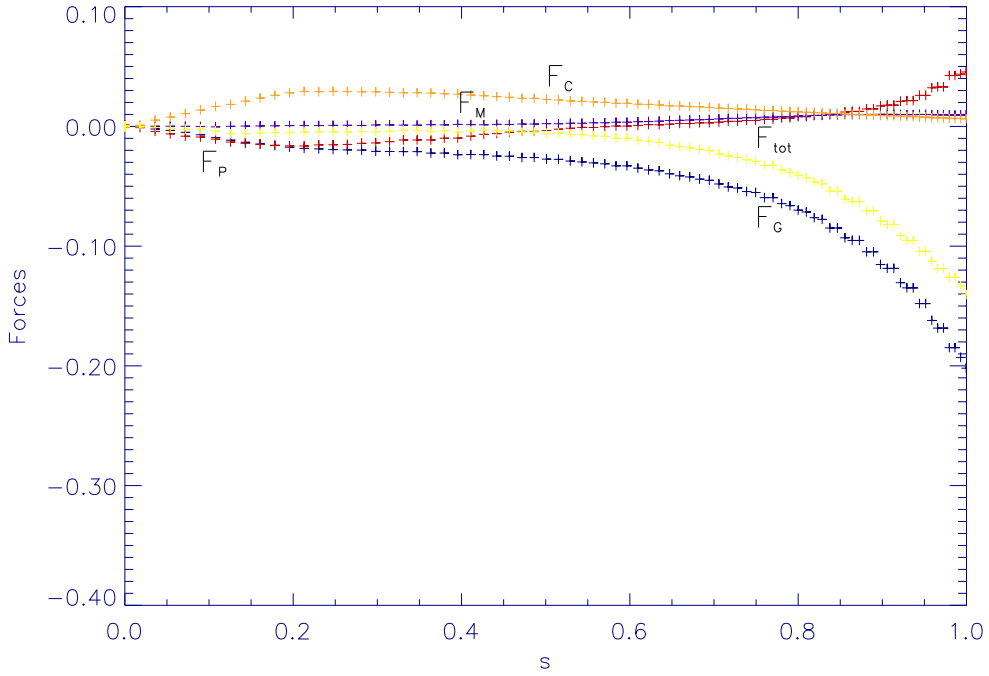

Figure 59. Forces in normalized units within the accretion column near the disc surface in the case $\alpha_\mathrm{m} = 1$. We can remark that the gravity in this case is always negative since the dipole is less distorted by accretion.

the star, below the co-rotation radius, in agreement with the size of inner disc holes. However, the accretion rate onto the star which is imposed by the physics of magnetic accretion is measured to be $\dot{M} \sim 10^{-9} M_{\odot}.yr^{-1}$. Even though this magnitude of accretion rate is found for some T Tauri stars (see Gullbring et al. 1998), this result shows that it is necessary to have stronger fields (by a factor of around 7) to have magnetospheric accretion for typical mean accretion rates of $\dot{M} \sim 10^{-8} M_{\odot}.yr^{-1}$. On the other hand, the few circular polarization measurements available provide an upper limit of 100-200 G for the dipolar component. However, recent spectro-polarimetric observations coupled with magnetic field reconstruction conducted on 2 CTTS V2129 Oph and BP Tau provide higher dipole field component of 350 G and 1.2 kG respectively (Donati et al. 2007,Donati et al. 2008). In any case, if the presence of kG dipole fields around CTTS are indeed ruled out, the requirement of forming quasi-steady accretion funnels imposes that the magnetic topology must be different. This is a firm result based on our dynamical calculations. One then needs to consider other stellar magnetic field topologies such as multipolar components and/or an inclined dipole configuration (Romanova et al. 2003; Long et al. 2007). We can also remark that for FU-Or stars which have huge accretion outbursts with $\dot{M}_a \sim 10^{-4} - 10^{-6}$ M$_{\odot}$ yr^{-1} and assuming similar stellar field strength (Donati et al. 2005), we expect from equation (35.104) direct accretion onto the star.

In this chapter, since there is no viscosity in our resistive accretion disc, we privileged a situation where $r_{\rm t} \ll r_{\rm co}$ in order to reach an open magnetic topology within the main part of the disc. This made possible to have a braking torque feeding the disc even without viscosity. Apart from the localized magnetic flux channeling the accretion funnel, the other stellar magnetic field lines become causally disconnected from the disc. This forbids any disc-locking mechanism and the star is being spun up as a consequence of accretion. We also report the non development of X-winds despite the favorable topology. Both of these aspects deserve however a more detailed analysis as they may depend on the disc resistivity. While the disc truncation radius remained close to its predicted position for about 30 Keplerian periods at the disc inner edge, some variability is obviously taking place. This is a very promising topic as veiling measurements probing accretion onto the star do show variability on different time scales (Alencar & Basri 2000). But making longer simulations requires to assess the role of the turbulent viscosity in order to allow for accretion within the disc beyond corotation for a more extended magnetosphere configuration. Actually, an interesting next step will be to study the possibility of braking a young star by this extended magnetospheric interaction or to find a disc-locking state as Long & al. (2005) claim. We tackle this point in the next chapter, where we mainly concentrate on doing a parameter space study of the star disc interaction by modifying the stellar rotation rate or the stellar magnetic field including in these studies α type viscosity within the disc.

5

Parameter space study of the star-disc interaction

Chapter content

In this chapter, we carry out a series of simulations to study the influence of the different parameters of the star-disc system. The results of the previous chapter showed that for typical T Tauri star parameters, we end up with $r_t < r_{\rm co}$ and a global spin-up of the star with a quasi-stationary magnetospheric accretion. Here, we vary in particular the stellar magnetic field strength B_*, the stellar rotation rate Ω_* and the dissipative properties of the disc described by both diffusivity η and viscosity ν, and determine their influence on the formation of funnel flows and the resulting stellar accretion rate. One includes here the effect of viscosity within the disc, an effect which was omitted in the previous chapter.

We first look at the accretor regime, where the truncation radius is smaller than the corotation one, and show that the inclusion of viscosity introduces an oscillatory shift of the truncation radius position for our accretion disc model. We also run a simulation with the initial condition of Romanova et al. (2002) for sake of comparison with this reference work. Then, we try to find an extended magnetosphere configuration where part of the stellar field remains connected to

the disc beyond $r_{\rm co}$ by increasing the disc resistivity. This would be required in order to obtain a stellar spin-down. We also look closely to the relation between the stellar accretion rate and the magnetic field strength and investigate the influence of other parameters such as the stellar rotation rate which we did not take into account in our analytical criteria for the truncation radius in the last chapter. Finally, we consider the propeller regime where the truncation radius lies beyond the corotation one, and we found transient accretion columns as in Ustyugova et al. (2006) and a global magnetic braking acting onto the star at least for the short timescales explored.

1. Accretor regime ($r_t < r_{co}$)

§ 42. Role of viscosity

§ 42.1. *Simulation with our accretion disc model*

As soon as viscosity is taken into account, it is physically more consistent to alter the initial disc used in chapter 4 in a way which already incorporates a consistent accretion flow. Therefore, one includes in the initial condition the accretion flow due to our chosen viscosity parameter as calculated analytically by Kluzniak & Kita (2000) for an adiabatic disc.

Besides, we use a different internal viscosity and diffusivity profile with a vertical cut-off which follows the adiabatic sound speed of the disc called $f_3(x)$ in Chap. 3 in order to be able to have a wider magnetic connection between the star and the disc. Actually, higher diffusivity at the disc surface diminishes a bit the magnetic torques and we want to keep a magnetic Prandtl number equal to one.

Under these slightly different initial and physical conditions, we perform various runs with varying magnetic field strength. We discuss here a simulation with a 17 day period star, $B_* = 141G$ and compare it with another magnetic field strength case $B_* = 703G$, and always with $\alpha_{\rm m} = \alpha_{\rm v} = 0.1$.

Contrary to the last chapter, we do not reach a stationary state for the magnetic field topology. While we previously found a closed deformed magnetosphere restricted to the disc inner edge and both opened field lines connected either within the star or within the disc, this time one obtains a variable magnetosphere. First, it is compressed by the accretion but then extends again because of the opening of the magnetic field corresponding to the ejection of a plasmoid (see Fig. 60) along the 30° diagonal with respect to the disc midplane at t=15 as already seen in Hayashi et al. (1996). This leads to a cycle of accretion/ejection phenomena on a longer timescale. This phenomenon was already observed in Goodson et al. (1999) also in the case of low disc diffusivity where the radial velocity is greater than the cross-field diffusion velocity of magnetic field lines but here, we are in the accretor regime.

For the weak field case ($B_* = 141G$) and with the timescale of our simulation, one observes two complete cycles which each lasts 7 rotation periods with respect to the disc inner edge (see Fig. 61). Our simulation ends when we see the beginning of a third one, with each time the ejection of a plasmoid. One has only one complete cycle with a longer time of 10 periods for the stronger field case ($B_* = 703G$). We did not continue these simulations because of too big rarefaction of matter within the corona which limits the time step. One can follow the variability

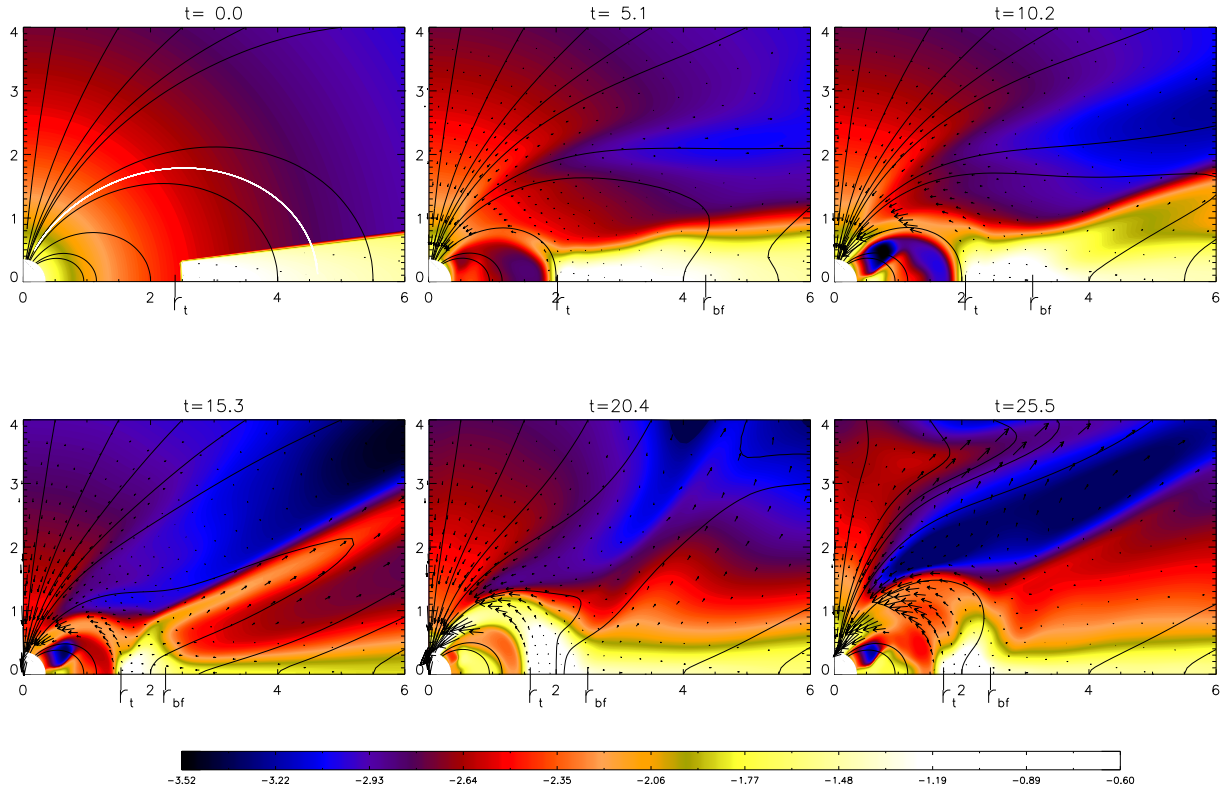

Figure 60. Resistive MHD simulation with $B_* = 703\mathrm{G}$ and $\alpha_\mathrm{m} = \alpha_\mathrm{v} = 0.1$. The density distribution is drawn, the black lines show the magnetic field lines and the black arrows the velocity field. The white line in the initial condition indicates the magnetic field line corotating with the star which has a period of 17 days. After the first dynamical accretion, we observe the formation of a current sheet due to the expansion of the poloidal magnetic field with a strong ejection linked to a strong deformation of the closed magnetosphere and then a new accretion phase with a powerful accretion column. Finally, the magnetosphere is again deformed by both accretion and expansion of the magnetic field due to the differential rotation.

of the disc inner edge by showing the evolution of the truncation position (see Fig. 62) and also the variation of the stellar accretion rate (see Fig. 61).

Let us have a closer view to the evolution of the accretion rate in the inner parts of the disc for the strong field case (see Fig. 63). On the one hand, one has accumulation of matter by a factor 10 with respect to the initial disc density at the disc inner edge caused by accretion which continuously deformed the magnetosphere till the opening of the magnetic field happens in a region where $\beta \gg 1$. On the other hand, magnetospheric accretion happens with a different accretion rate, thanks to the build up of the upward thermal pressure gradient. The opening of the magnetosphere also entails some transient excretion in the disc. We conclude that these cycles can occur periodically, even if one can notice that for the weaker case the period increases, as on the simulated time interval we find decrease of the accretion rate, due to the decrease of the magnetic braking in the outer parts of the disc with time.

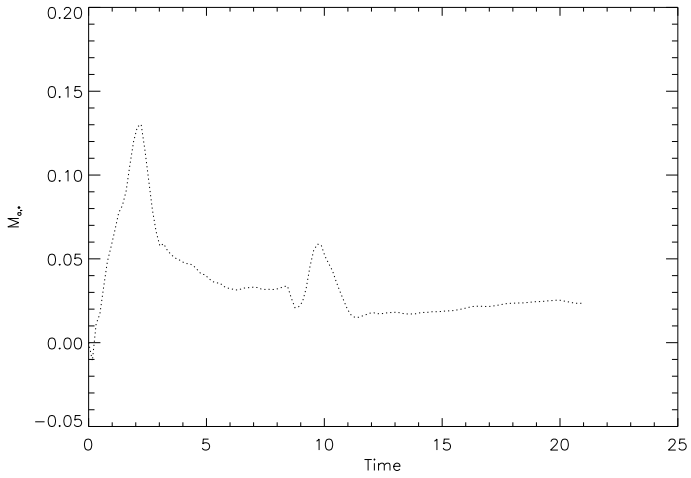

a

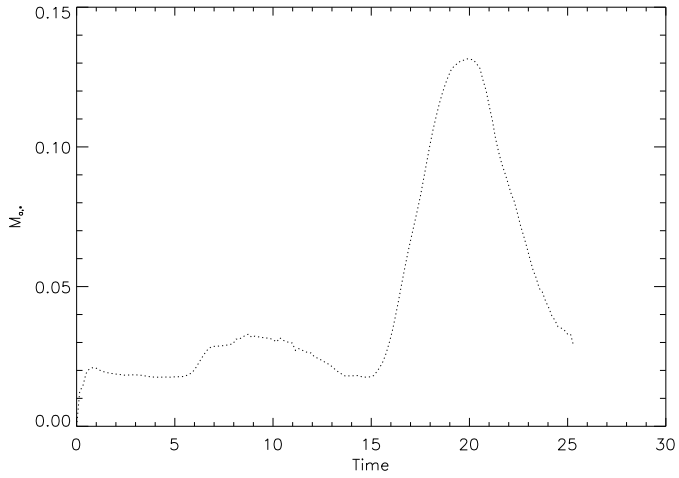

b

Figure 61. Variation of the stellar accretion rate with time for a weak field case (a: $B_* = 141G$) and a strong one (b: $B_* = 703G$). First, one can remark the long term decrease corresponding to the relaxation of the strong magnetic braking for the weak case, whereas one can see a reversed trend for the stronger case because the magnetic braking timescale is longer as the initial truncation radius is further. Then, the period of the magnetospheric cycle is shorter for the weak field case, namely it is around 7 periods with respect to the stronger case, where it is around 10 periods.

§ 42.2. *Simulation with the initial condition of Romanova et al. 2002*

For comparison with the previous and further parametric studies, we reproduce the initial setup of Romanova et al. (2002) done in ideal MHD ($\alpha_m = 0$) and with a viscosity parameter equal to $\alpha_v = 0.02$ for a stellar magnetic field strength equal to $B_* = 141G$, a 10 days period star

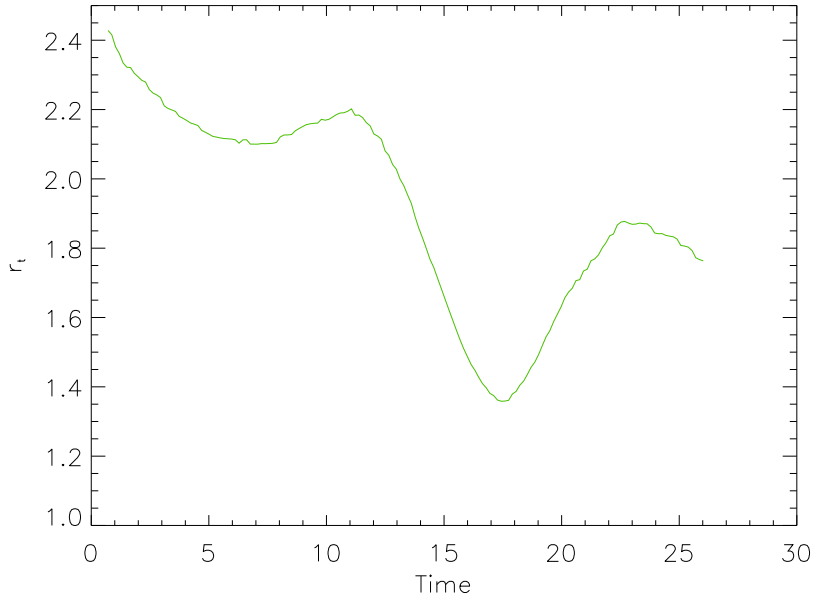

Figure 62. Oscillation of the truncation radius in presence of viscosity for $B_* = 703G$. We clearly see a complete cycle of the magnetosphere after the first dynamical accretion. One also sees a trend to a decreasing of the truncation radius due to the effect of the magnetic braking which increases with the opening of the magnetic field in the disc outer parts.

($\Omega_* = 0.19$) which puts the corotation radius at R=3. The difference with the original work of Romanova is that we use a weaker field and our boundary conditions.

As already remarked in Chap. 3, the accretion rate obtained with this disc structure is higher than our own disc. The viscous disc has varying accretion rate with distance reaching $\dot{M} \sim 0.1$ at the stellar surface and even higher values at the outer edge with $\dot{M} \sim 1$. The normalization for the accretion rate is the same as in chapter 3 i.e. $2.27 \times 10^{-8} \mathrm{M}_{\odot} \mathrm{yr}^{-1}$. One obtains an accretion column after one period at the disc inner edge and this accretion column remains during the simulation (see Fig. 64) as in the original work of Romanova et al. (2002). One can remark the greater accretion rate in the upper parts of the disc which causes advection of the magnetic lines at this location as one has no diffusivity within the disc. As a result, one has a differential rotation along a given field line between the footpoint anchored within the disc which rotates at a slower rate than the part of the field lines advected inwards at the disc surface. Thus, a negative toroidal magnetic field is built near the disc midplane which causes locally an excretion of matter. Then, this leads to magnetic reconnection in the inner parts of the disc, disrupting it into two parts as far as the magnetic field is concerned. The accretion column is feeding in mass by the upper parts of the disc at later times. This phenomenon is well visible in Fig. 5 of the Romanova paper that one shows here for sake of comparison (see Fig. 65) although it is seen at longer timescale for the stronger field case presented there. For the same reason, the opening of the magnetic field with the formation of a plasmoid is well visible at t=10 in our simulation. One can expect that at longer times, the disc structure is rebuilt thanks to the dissipation of magnetic islands seen at t=22.1. Our disc structure seen at the same timescales in chapter 4 or further in this chapter shows a smoother evolution with a much ordered magnetic field within it.

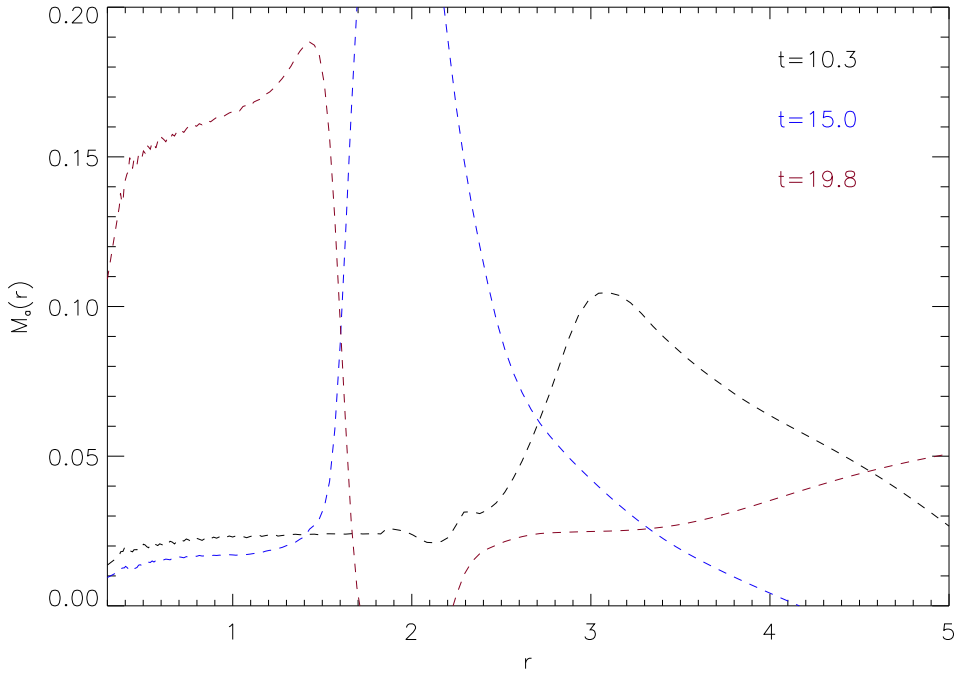

Figure 63. Radial profile of the accretion rate in the disc midplane for three different times showing the time-dependent magnetospheric accretion for the strong field case. t=10 corresponds to the maximum of the first accretion phase, t=15 show the end of this first accretion with accumulation of matter at the disc inner edge and finally one sees the second accretion, which is more powerful due to the greater accumulation of mass.

By looking at the force balance along the central line within the funnel flow when it is well established (Fig. 66), one clearly sees that the thermal pressure force lifts up matter as also found in the results of chapter 4. One can notice the stronger effect with respect to our simulations shown in chapter 4 of both the magnetic and centrifugal forces which prevent matter from being loaded onto magnetospheric lines. This effect is caused by the excretion of matter in the disc midplane which avoids the deformation of the magnetosphere by the accretion, an effect which we clearly observe in our simulations. Besides these important differences, we find the same trend one obtains in our simulation in Chap. 4 with opposite disc properties i.e. a high diffusivity but no viscosity.

§ 43. Influence of resistivity on star-disc connectivity

One of the main trends in observations of YSO is the presence of slow rotators while there are still accretion disc evidences (see Chap. 1). Theoretical models try to understand which physical processes can extract the specific angular momentum to maintain a low rotation rate. In this part, we focus on one possible mechanism which is the magnetic connection between the star and the disc. In previous works, the dipolar magnetosphere connected to the disc was restricted to the inner edge of the disc (Romanova et al. 2002, Long et al. 2005, Bessolaz et al. 2008) and no extended magnetosphere is simulated yet. The goal of this part is to try to find such a configuration.

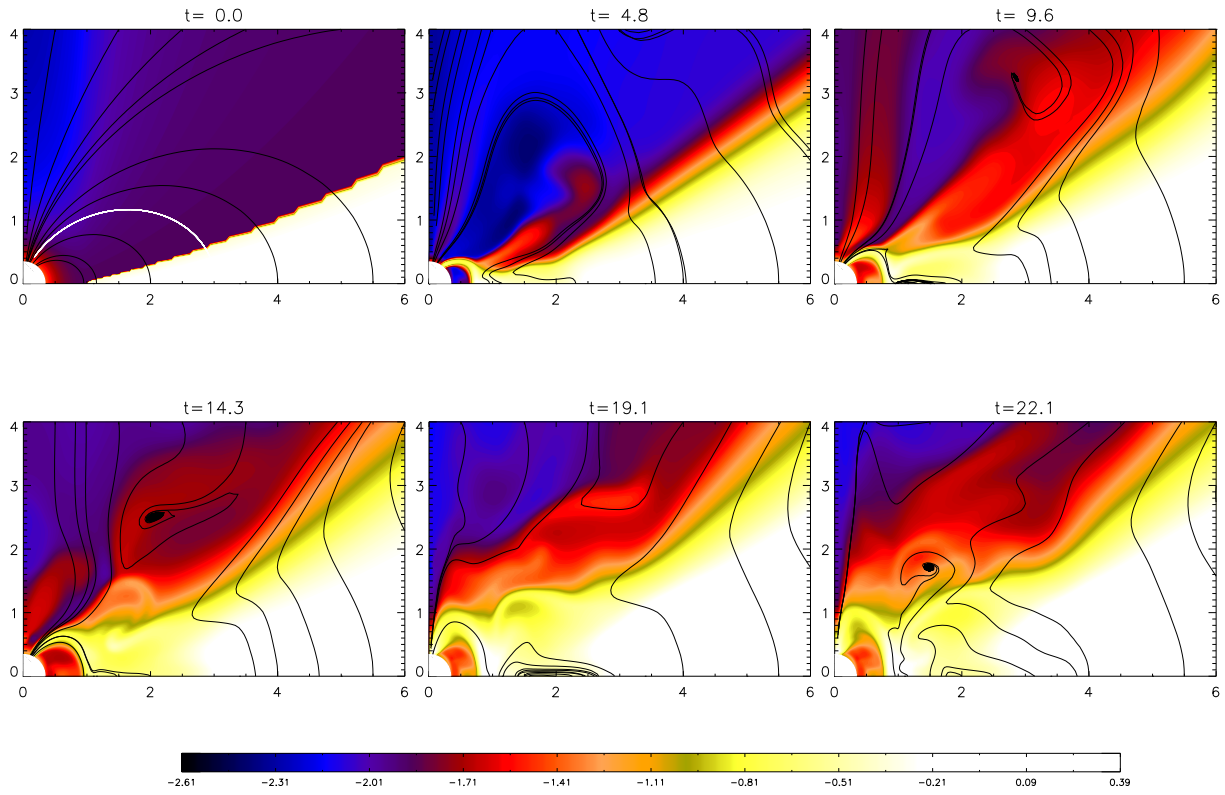

Figure 64. Ideal MHD simulation with the initial condition of Romanova et al. (2002) for a 10 days period CTTS with $B_* = 124\mathrm{G}$ and $\alpha_{\mathrm{v}} = 0.02$. The density distribution is drawn and the black lines show the magnetic field lines. The white line in the initial condition indicates the magnetic field line corotating with the star. One clearly obtains an accretion column after 5 periods. Notice however the excretion in the disc midplane caused by the bending of the magnetic field lines due to greater accretion at the disc surface. This finally produces reconnection in the disc midplane when the field lines are too stretched radially which disrupts the disc into two parts.

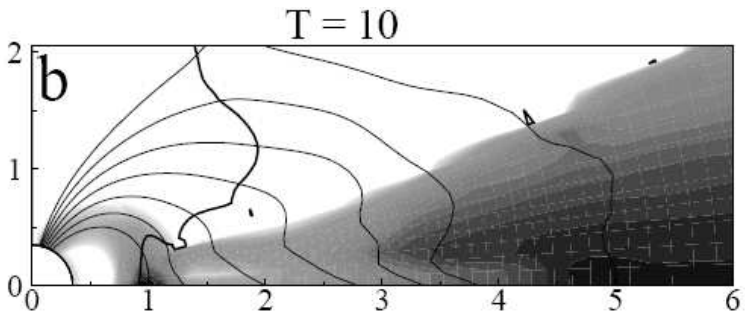

Figure 65. We reproduce here a snapshot from Romanova et al. (2002) with the same parameters as in our simulation except a stronger field strength with $B_* = 1100G$. One can see the excretion in the equatorial plane and accretion in the upper parts which distorts the magnetic field lines in the same way as in our simulation but less quickly as in our weaker field case.

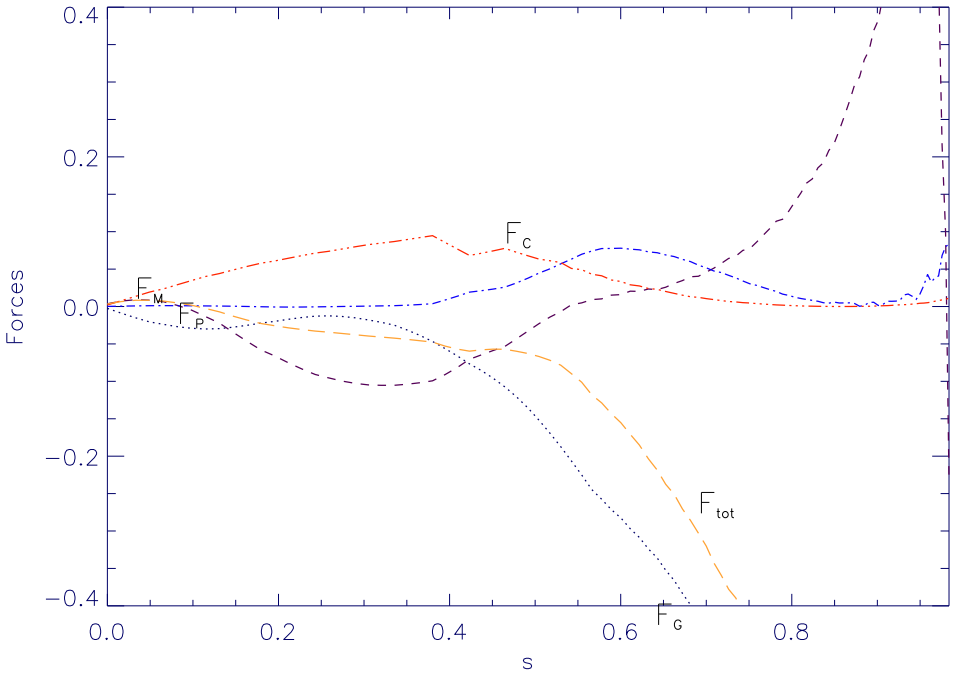

Figure 66. Projection of the forces in normalized units along a magnetic field line in the middle of the accretion column, at $t = 10$ for the simulation shown in Fig. 64. We represent the gravity F_G, the centrifugal force F_C, the thermal pressure gradient F_P, the poloidal magnetic force F_M and the total force F_{tot} as function of the curvilinear coordinate s. The disc midplane is located at $s = 0$.

In the previous chapter, we remark that one really has a restricted star-disc connection for the resistivity parameter $\alpha_m = 0.1$ which always gives a spin up of the star in the accretor regime ($r_t < r_{\rm co}$). In order to connect the star to the disc on a significant spatial range, it is necessary to reduce the differential rotation to avoid the opening of the poloidal magnetic field on dynamical timescales. This can be obtained by considering a greater disc resistivity. Our ultimate goal is to vary the disc resistivity such that a significant part of the stellar field remains connected beyond $r_{\rm co}$. Test simulations show that this also demands a restricted spatial distance between the disc truncation radius and the corotation one contrary to the case used in the last chapter to study the formation of accretion columns. To illustrate that point, we show the changes from our reference simulation done in Chap 4. by using larger dissipative effects within the disc ($\alpha_m = \alpha_v = 1$). Now the accretion rate is greater ($\dot{M} \sim 0.25$) due to higher viscosity and the truncation radius is closer to the star ($r_{\rm t} \sim 0.6$) consistent with our analytical criteria found in Chap. 4. However, one still quickly opens the magnetic field lines just outside the accretion column well below the corotation radius (see Fig. 67). By fine tuning the ratio between the truncation radius and the corotation radius, we find that a connection beyond the corotation radius is possible when $r_{\rm t}/r_{\rm co} \geq 0.75$ in addition to a high disc resistivity . One presents here a simulation with the same parameters as above but with a stronger magnetic field ($B_* = 224$G) which corresponds to a truncation radius at $r_{\rm t} = 1.3$ with respect to the corotation radius at $r_{\rm co} = 1.6$. In this case, we achieve a transient star-disc connection beyond the corotation radius till r=2.5 and a disc wind configuration further

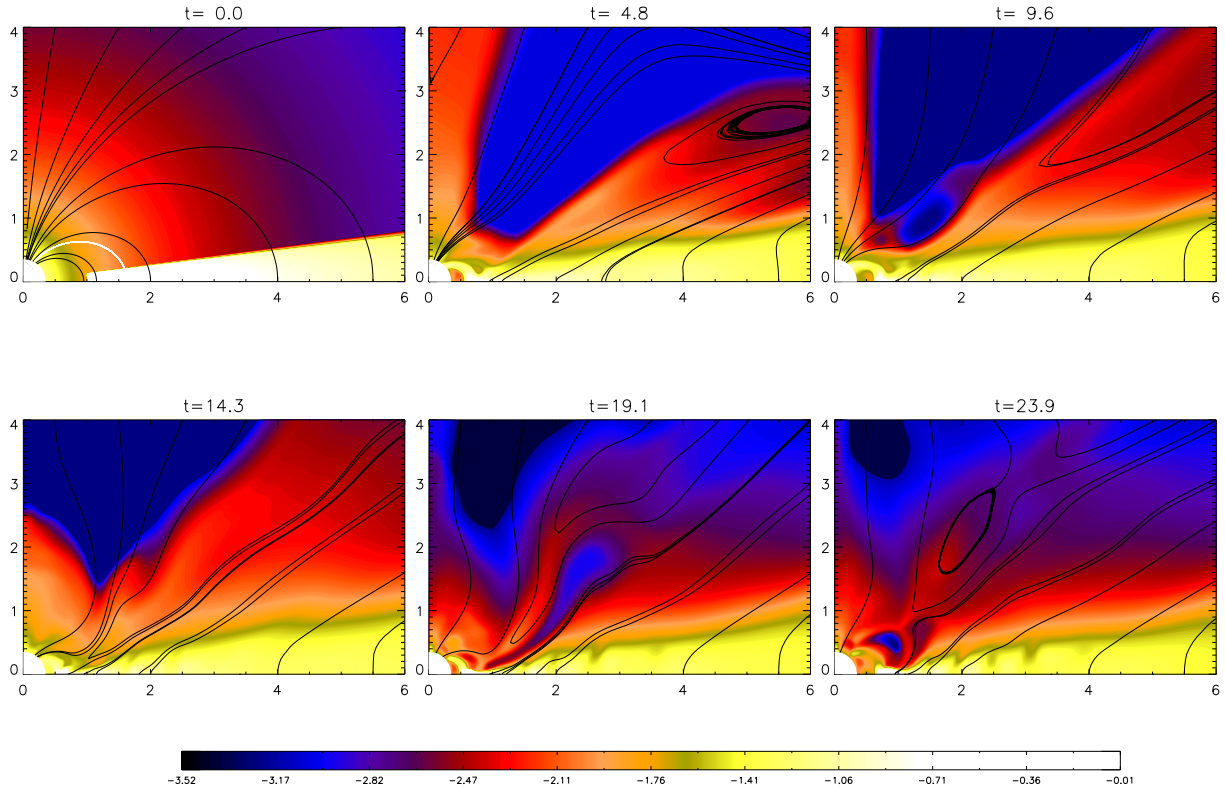

Figure 67. Resistive MHD simulation for a 4 days period CTTS with $B_* = 141$G and $\alpha_{\rm m} = \alpha_{\rm v} = 1$. We achieve a restricted star-disc connection limited to the funnel flow as in our reference simulation in Chap. 4 even though we increase the disc dissipative effects by an order of magnitude. The visco-resistive parameters now reach their upper limit of physically possible values for turbulence.

out (see Fig. 68). However, the disc is quickly expelled by the negative magnetic torque which diffuses inwards till r=1.1, well below the initial corotation radius at r=1.6 (Fig. 69). This might be a numerical artefact already seen in Long et al. (2005) and discussed in chapter 2. It probably comes from the fact that at the stellar surface, field lines anchored at each side of the corotation are really close and numerical diffusion of the toroidal field at this location can easily produce this phenomenon. Future work is needed to convincingly prove the possibility to obtain a global spin down of the star along field lines connected beyond the corotation radius by using greater disc resistivity.

§ 44. Relation between the stellar accretion rate and the star-disc system parameters

§ 44.1. *Effect of the stellar magnetic field strength*

In this part, we want to explore in more detail the relation which links the accretion rate onto the star with the stellar magnetic field strength in the accretor regime as we show in the last chapter that these two parameters are not independent. To do this, we perform different simulations

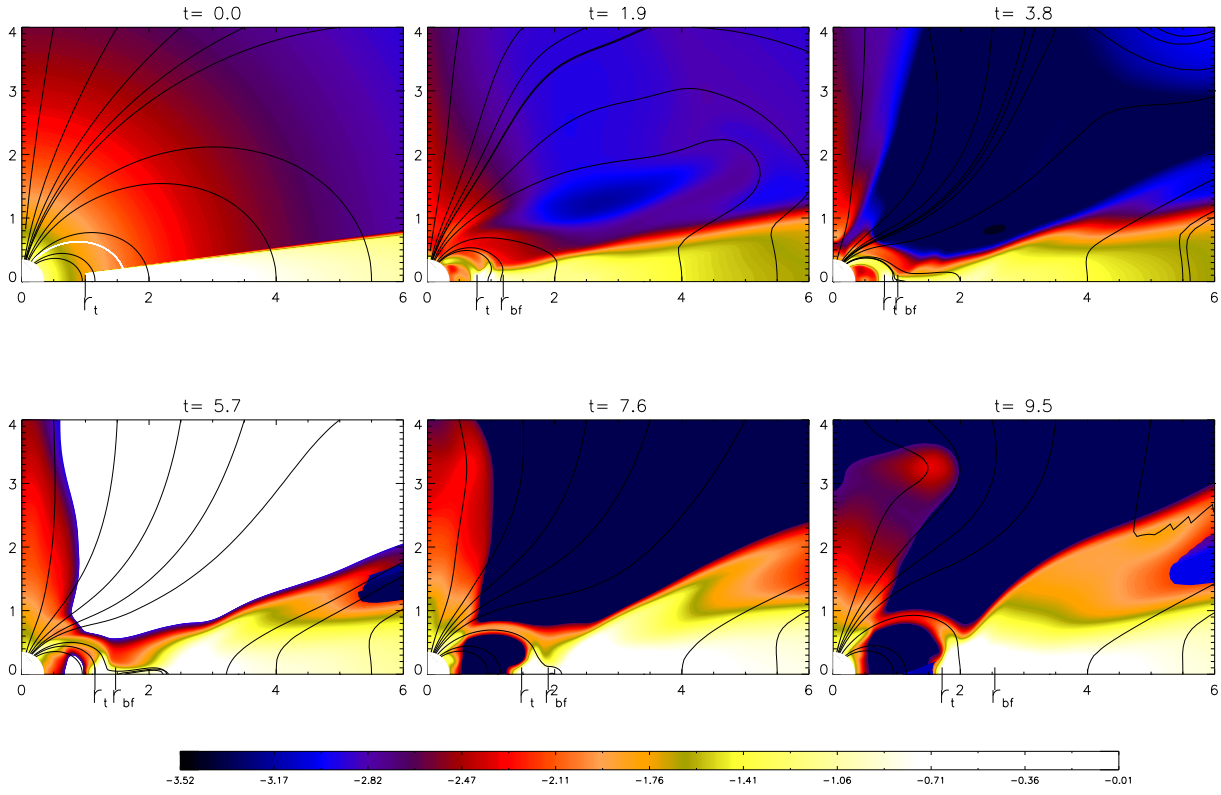

Figure 68. Resistive MHD simulation for a 4 days period CTTS with $B_* = 224$G and $\alpha_{\rm m} = \alpha_{\rm v} = 1$. We achieve a transient star-disc connection beyond the corotation radius till r=2.5 and a disc wind configuration further. On longer times though, the disc is expelled by the negative magnetic torque which diffuses inwards till r=1.1 well below the initial corotation radius at r=1.6.

by varying the magnetic field strength over a decade typically between 100 G and 1000 G, and fixing all the other parameters and particularly keeping low dissipative properties for the disc and a magnetic Prandtl number equal to one ($\alpha_v = \alpha_m = 0.1$). Each magnetic field strength fixes a truncation radius given our initial accretion rate ($\dot{M} \sim 0.01$ i.e. $\dot{M} \sim 3 \times 10^{-10} \mathrm{M}_\odot \mathrm{yr}^{-1}$) and taking into account that the dominating magnetic torque gives a higher accretion rate guessed to be around $10^{-9} \mathrm{M}_\odot \mathrm{yr}^{-1}$ from Chap. 4. In order to maintain an accretor regime even for the stronger field strength, we choose a 17.7 day period star ($\Omega = 0.1$) corresponding to a corotation radius fixed at 4.6. The best choice to study this relation should be with higher disc resistivity where we expect a less dynamical evolution of the star-disc system. In such cases, one could obtain a situation where the disc and stellar accretion rates are similar on a longer timescale without oscillation of the system. However, we do not find such configurations and we rather use more realistic low values for the visco-resistive parameters. Thus, we focus on the first dynamical accretion by measuring the maximum stellar accretion rate. One expects basically that the accretion rate onto the star will increase with the magnetic field strength since the magnetic torque is increased without changing the other parameters considering the same position within

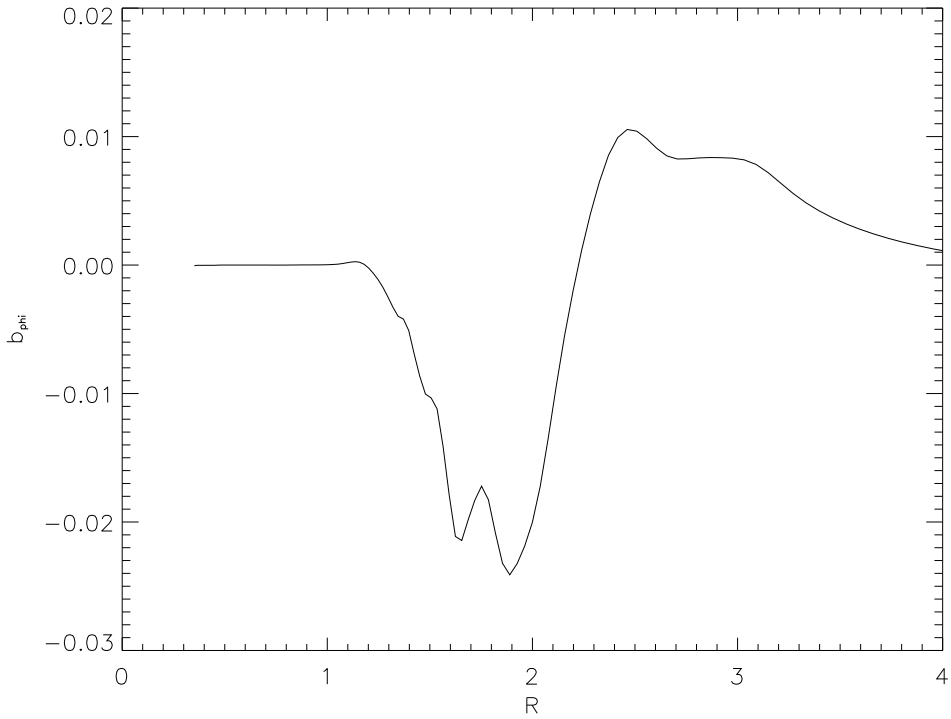

Figure 69. Radial distribution of the toroidal field near the disc surface at t=2. We see the first reversal of sign for the toroidal field at r=1.2 instead of its expected position at the corotation (r=1.6). Then, we have a negative field till the magnetosphere is opening at r=2.2.

the disc. Besides, the normalization between the reference values of the system naturally gives $\dot{M}_* \propto B_*^2$.

To calculate accurately the accretion rate onto the star, one includes only the accretion within the funnel flow by detecting the closed field line anchored at the truncation radius and the first field line which is opened. The latter then locates the adjacent upper closed field line of the accretion column for this weak resistivity parameter range, so that we thereby determine the effective width of the accretion funnel. Actually, we realize that material in the magnetosphere cavity and in the corona above the star can cause a discrepancy for the instantaneous global accretion rate till 50 % when the mass flux is basically computed using the whole stellar surface, as compared to the funnel mass flux only.

We report in Fig. 70 the maximum accretion rate measured for each run. One clearly sees that there is a decrease of the stellar accretion rate when the magnetic field increases. Actually, the stronger the field is, the further the truncation radius is and thus one has a lower magnetic torque which is dominating for this low values of viscosity. Besides, by looking at the force balance along a central field line in the funnel flow, one clearly sees that the thermal pressure is really reduced in the stronger field case since the disc is colder at this position for the same reason. Otherwise, the compression is similar in both cases.

We also measure the position of the truncation radius at this maximum accretion phase for each run and compare it with our analytical criteria. To do that, we use our measurement of the

B_* (G)	$\dot{M}_{*,max}$ (2.27×10^{-8} $M_\odot yr^{-1}$)	$r_{t,min}$ $3R_*$	$r_{t,th}$ $3R_*$	Cycle period 1.78 days	$\dot{M}_{j,max}$ (2.27×10^{-8} $M_\odot yr^{-1}$)	$\dot{M}_{d,min}$ (2.27×10^{-8} $M_\odot yr^{-1}$)
141	0.23 ± 0.02	0.5	0.6	7	0.09	0.07
286	0.15 ± 0.02	1.0	1.1	8	0.01	0.05
703	0.12 ± 0.02	1.6	1.8	10	$< 3 \times 10^{-3}$	0.05

Figure 70. A series of simulations with $\Omega = 0.1$ corresponding to $r_{co} = 4.6$, $\alpha_v = \alpha_m = 0.1$ and varying the magnetic field strength B_*. One reports the maximum stellar accretion rate $\dot{M}_{*,max}$, the disc truncation radius measured at this time $r_{t,min}$ with comparison to the theoretical one $r_{t,th}$, the magnetosphere cycle period observed , the maximum ejection rate $\dot{M}_{j,max}$ and the disc accretion rate at the same time in the inner parts $\dot{M}_{d,min}$.

stellar accretion rate. We find agreement with our analytical criteria better than 20 % (see Fig. 70).

We finally calculate the maximum ejection rate $\dot{M}_{j,max}$ above the disc due to the expansion of the poloidal magnetic field line by computing the mass outflow through the outer edge of the simulation box excluding 20° from the rotation axis. One founds a decrease of the ejection rate when the stellar magnetic field increases. We explain this behaviour by the differential rotation along a magnetic field line connected between the star and the disc which decreases when the distance between the disc inner edge and the corotation decreases. Actually, a stronger field gives a further out truncation radius from the star. Thus, ejection of plasmoids is less efficient for strong magnetic fields going from 40 % for $B_* = 141G$ to lower than 3 % for $B_* = 703G$. To give a scale of comparison, one reports also the minimum accretion rate measured in the inner parts of the disc at the outer edge of the funnel when ejection happens. The plasmoid ejection is also more collimated towards the rotation axis for the weaker field case with a angle of 45° with respect to the equatorial plane whereas the stronger case has an angle of 31°.

Let us now have a look to the ejection happening in the outer region of the disc where the stellar magnetic field has opened (see Fig. 71). In this region, the magnetic field lines are really bent towards the disc verifying the Blandford & Payne criteria (1982). By looking at the velocities along a magnetic field line anchored at r=2 for t=12, the flow reaches the slow and Alfvén point but not the fast point because the field is below equipartition in this region.

§ 44.2. *Effect of the stellar rotation rate*

One can also test if the expression giving the truncation radius found in Chap. 4 depends on the stellar rotation rate. Therefore, we make another simulation with a shorter 5 day period star ($\Omega_* = 0.35$) keeping $B_* = 141G$ and ($\alpha_v = \alpha_m = 0.1$).

Fig. 72 shows a decrease of the stellar accretion rate by a factor 2 for a 3.5 times faster rotating star. As the truncation radius is nearly the same for these two cases mainly imposed by the magnetic field strength, this can be understood by the fact that the differential rotation between the star and the disc inner edge is reduced for the faster rotating star. Actually, one can write the generation of toroidal field using the Ohm's law at the disc surface as :

$$B_\phi^+ = \frac{hrB_z}{\eta}(\Omega - \Omega_*). \tag{44.116}$$

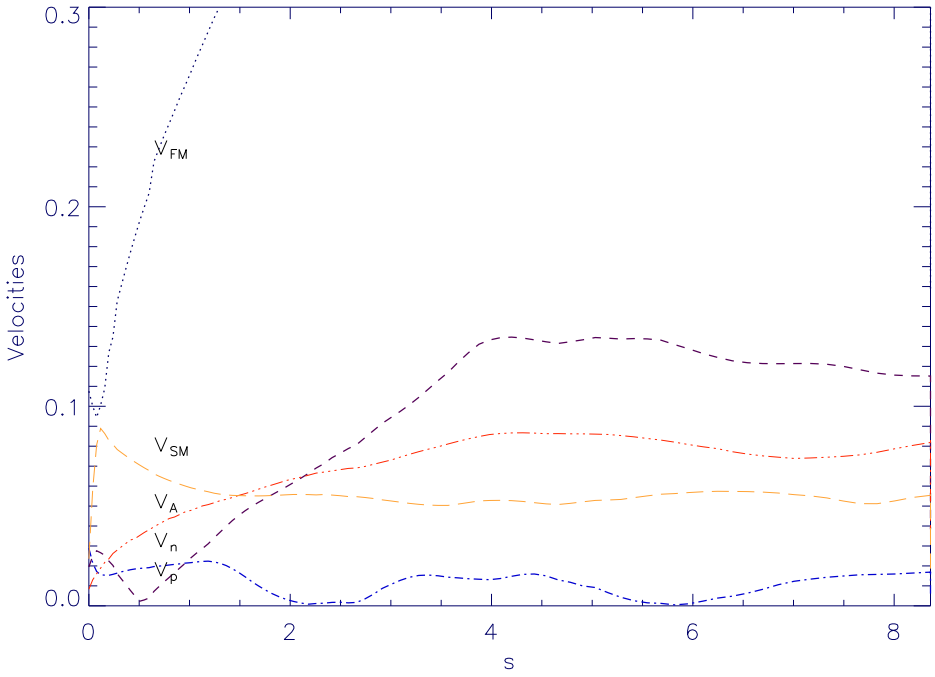

Figure 71. Evolution along an opened magnetic field line anchored within the disc at r=2 (s=0 corresponding to the disc midplane) of the Slow-Magnetosonic speed v_{SM}, the poloidal velocity parallel to the magnetic field v_p, the Alfvénic speed v_A, the Fast-Magnetosonic speed v_{FM} and the transverse speed v_n across the field line. One reaches the Alfvénic point but not the fast one having a breeze-like ejection. The significant transverse velocity shows that one does not have a steady state and that the weak field is distorted by the inner ejection of plasmoids.

Ω_*	$\dot{M}_{*,max}(2.27\times10^{-8}\mathrm{M_\odot yr^{-1}})$	$r_{t,min}$	$r_{\mathrm{t,th}}$	$\dot{M}_{j,max}(2.27\times10^{-8}\mathrm{M_\odot yr^{-1}})$
0.1	0.23	0.55	0.64	0.10
0.35	0.12	0.60	0.77	0.05

Figure 72. A series of simulations with $B_* = 141G$, $\alpha_v = \alpha_m = 0.1$ and varying the stellar rotation rate Ω_*.

This is confirmed by the ejection rate which is also reduced in that case in the same ratio.

By looking at the discrepancy between the measured truncation radius and our analytical criteria, one can see that the stellar rotation rate has a clear contribution, which we did not remark in the last chapter. The main reason is because here we are interested in the first accretion phase with great accretion rate which enhances the differences. However, our analytical criteria still predicts the disc truncation radius at better than 30 % in this critical transient which is acceptable.

§ 44.3. *Effect of the magnetic Prandtl number*

We finally carry out a simulation with a magnetic Prandtl number equal to 10 corresponding to $\alpha_v = 1$ and $\alpha_m = 0.1$ and all other parameters fixed as previously ($B_* = 141G$, $\Omega_* = 0.1$) to see the influence of a highly viscous disc. This is clearly the configuration favoured for the formation of an X wind with small disc diffusivity (Shu et al. 2007) allowing the concentration of

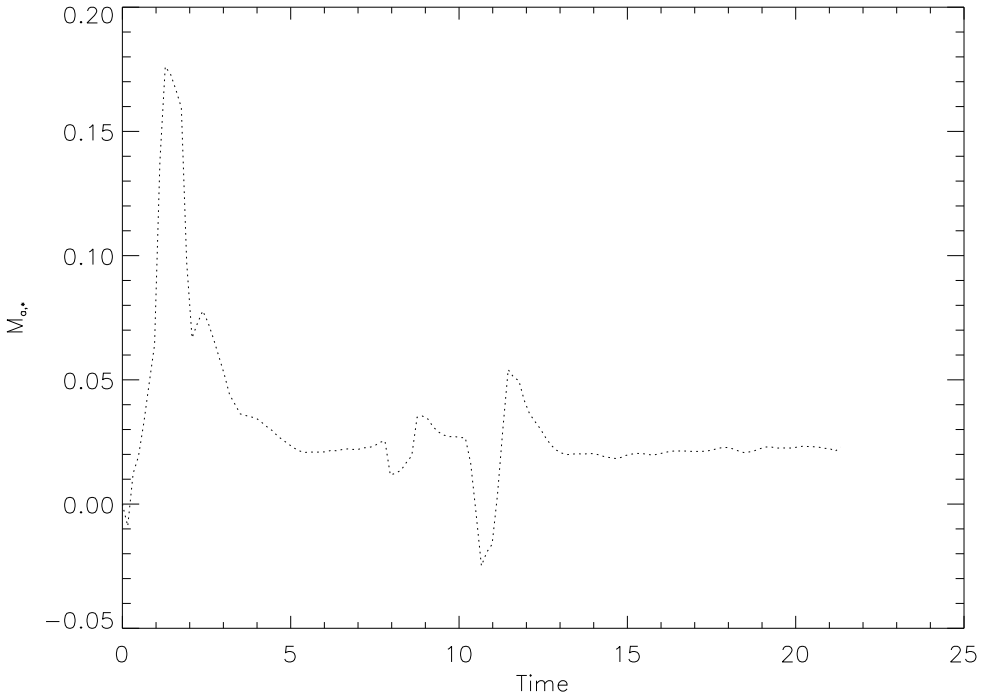

Figure 73. Evolution of the stellar accretion rate with time for the case Pm=10. One obtains a greater accretion rate at the stellar surface than for the Pm=1 case with higher dynamical disturbances in the evolution.

the magnetic flux within the disc at the disc inner edge. One obtains a higher accretion rate onto the star (see Fig. 73) since higher disc viscosity brings more matter at the disc inner edge to feed the accretion column and the stellar accretion rate reaches 0.28 with a truncation radius closer to the star $r_t = 0.4$. Otherwise, the ejection rate is reduced to 0.06 with respect to cases with Pm=1 and we do not have an X wind.

2. Propeller regime ($r_t > r_{co}$)

The propeller regime corresponds to a state where the truncation radius is located beyond the corotation radius $r_{\rm co}$ such that we expect to have only magnetic braking torques acting onto the star. In this situation, we expect not to have accretion columns since the magnetic field lines connected beyond $r_{\rm co}$ rotate quicker than the disc material and thus tend to accelerate matter outwards. However, if the viscosity is sufficient to overpass the magnetic torque, we can wonder if transient accretion is possible as it seems the case in Ustyugova et al. (2006). There are two main ways to have such a situation. Firstly, we can consider a higher rate of rotation for the star nearer the breakup speed which thus corresponds to a younger stage of formation. This is the way explored by Ustyugova et al. (2006) and references therein. Otherwise, one can have a stronger stellar magnetic field which disrupts the disc beyond $r_{\rm co}$ because of the initial conditions of the stellar formation for the system considered. One can also imagine transitions in time between accretors and propellors depending on the variation of the accretion rate. An evolution scenario could be that as the accretion rate tends to diminish during the star formation process, we can

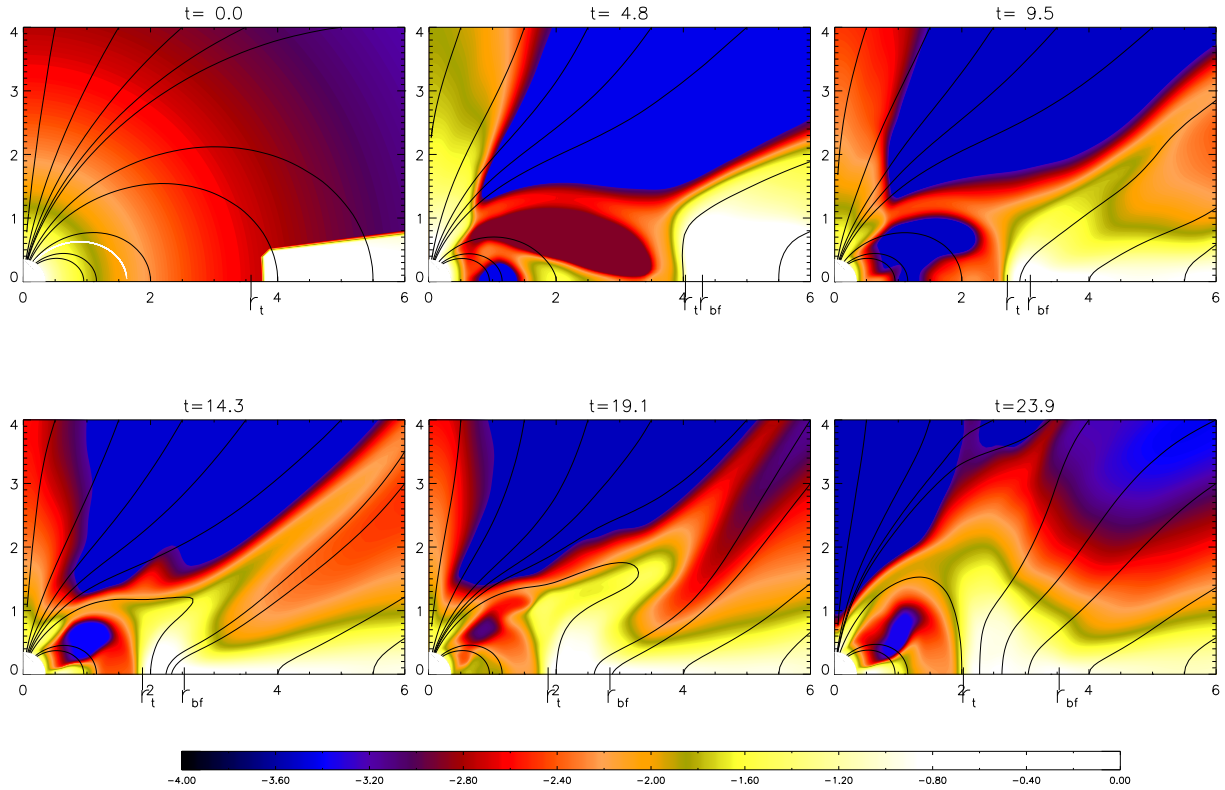

Figure 74. Resistive MHD simulation for a 4 days period CTTS ($r_{\rm co} = 1.6$) with $B_* = 476$G and $\alpha_{\rm m} = \alpha_{\rm v} = 0.1$. We are now in the case where the corotation localized by the white magnetic field line in the initial condition is below the truncation radius ($r_t > r_{\rm co}$) and the disc is initially pushed outwards by the accelerating magnetic torque. Ejection of a plasmoid is seen at t=19.

go from a magnetospheric accretion system like in CTTS to a propeller system where accretion is nearly absent like in WTTS.

§ 45. Dynamical evolution

We choose a star with a 4 day period which corresponds to a corotation at r=1.6 and a magnetic field strength $B_* = 476G$ giving a truncation radius at r=2 assuming an accretion rate around $10^{-9} M_\odot yr^{-1}$. We choose an initial condition where the disc is initially truncated well beyond the corotation radius in order to limit the transients in a region where $\beta \gg 1$ (see Fig. 74). Actually, the magnetic torque accelerates disc matter in this regime and thus if we start with a truncation disc too near the corotation radius, the disc is expelled further and we have to compute for longer time to let the disc go back near the region where $\beta \sim 1$. Thus, one has an initial inflation of the magnetosphere. Then, the disc stabilizes close to r=2. The truncation radius is always located at the equipartition between thermal pressure and magnetic pressure. The transient funnel observed at the end of the simulation beyond the corotation radius does not

reach the slow point and the poloidal velocity of the material at the stellar surface is around 40 % of the free-fall speed. The resulting stellar accretion rate is around 0.005.

§ 46. Ejection properties

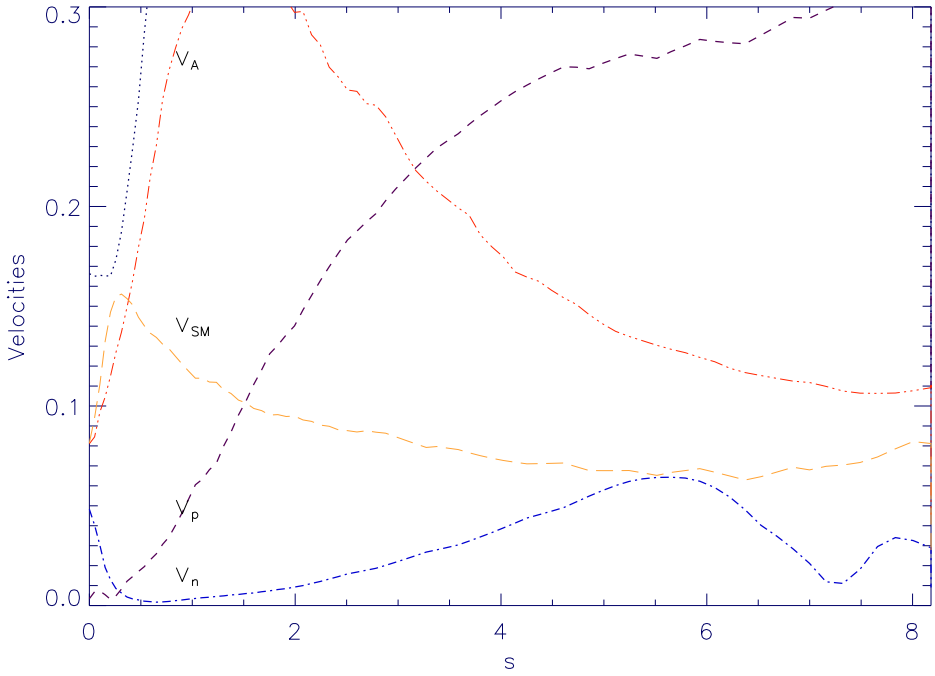

Figure 75. Evolution in the propeller regime along an opened magnetic field line anchored within the disc at r=2.5 (s=0 corresponding to the disc midplane) of the Slow-Magnetosonic speed v_{SM}, the poloidal velocity parallel to the magnetic field v_p, the Alfvénic speed v_A, the Fast-Magnetosonic speed v_{FM} and the transverse speed v_n across the field line. One reaches the Alfvénic point but not the fast one having a breeze-like ejection.

The ejection of material along the opened field lines reaches super-Alfvénic velocities (see Fig. 75) and near keplerian velocities with respect to the footpoint of the considered opened field line. The maximum ejection rate reaches 0.04 similar to the disc accretion rate showing that one can have efficient ejection in this configuration. The ejection is produced with an angle of 30° with respect to the disc midplane.

§ 47. Angular momentum balance

As for the accretor regime in chapter 4, we compute the angular momentum fluxes transported by both matter $\dot{L}_m$ and closed $\dot{L}_{fc}$ or opened $\dot{L}_{fo}$ magnetic field through the stellar surface (see Fig. 76). One obtains a global braking of the star for the timescale reached by the simulation even considering only the closed field lines but one also clearly sees a decreasing of it near the end of the simulation. Particularly, one expects that the accumulation of matter at the disc inner edge brought by viscosity can lead to a shift of the truncation radius below the corotation one

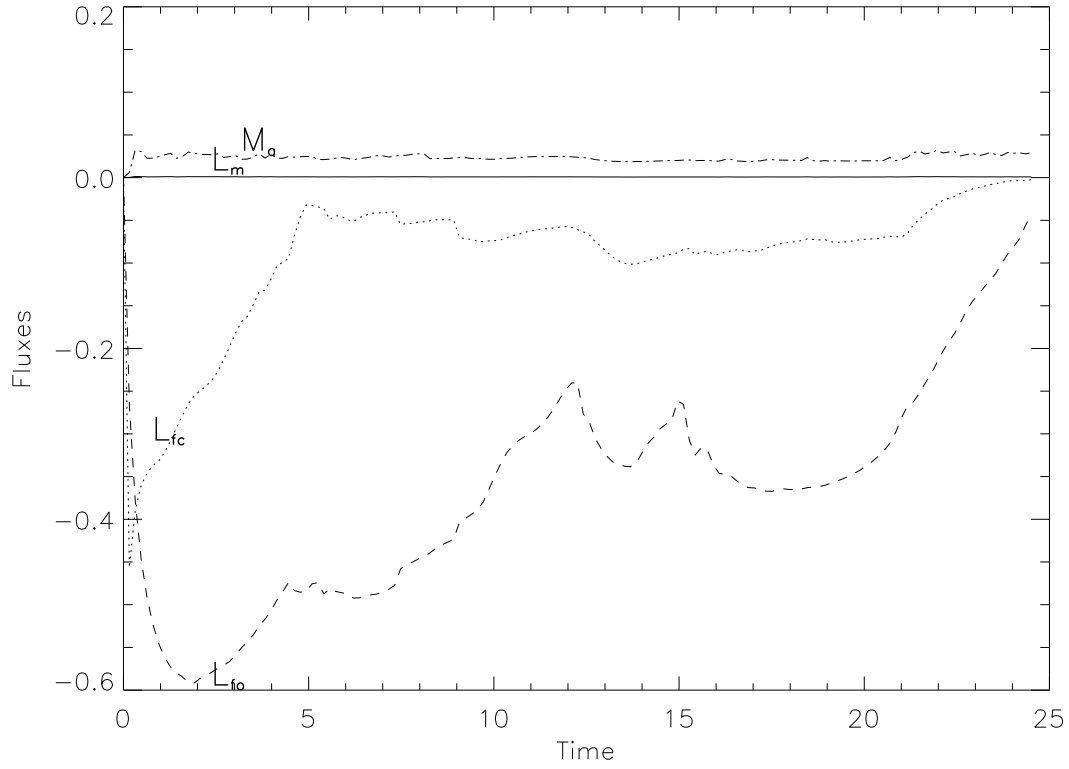

Figure 76. Angular momentum balance at the stellar surface for the simulation shown in Fig. 74. The angular momentum brought by the accretion is always negligible. One observes a global braking of the star by the magnetic torque, even if one excludes the effect of the opened field lines anchored into the star.

producing an accretor phase as discussed previously. However, when the inner part of the disc below the corotation radius will be finished to accrete onto the star, one will have a new phase of propeller with a global braking of the star. To maintain a propeller regime on long timescale, the magnetic torque has to overpass the viscous torque beyond the corotation ($r_{t,max} > r_{\rm co}$).

3. Conclusion

One has shown that viscosity introduces much variability in the star-disc system creating cycles where the magnetosphere can periodically open, reducing the stellar accretion rate while the ejection along a current sheet is enhanced. The increase of the magnetic field strength or the stellar rotation rate lead finally to both reduced stellar accretion rates and ejection rates in the accretor regime, due to a decrease of the differential rotation between the disc and the star. However, we are not able to correctly compute a disc-locking state. Longer term evolution is necessary to have a firm conclusion about the efficiency of the propeller configuration to brake the star.

Conclusion

After having presented the observational context of accreting magnetized protostars such as CTTS belonging to the low mass range, we have discussed some of the main theoretical ideas to understand magnetospheric accretion. We showed to which extent it is possible to have a global braking of a star from an extended magnetosphere anchored within the disc as function of the truncation radius position with respect to the corotation one and the amount of disc dissipative effects. Based on the inefficiency of this magnetic connection found in previous analytical models, one wondered if special configurations including ejection such as X wind (Shu et al. 1994) or ReX wind (Ferreira et al. 2000) can solve this angular momentum issue. Next, we presented an efficient way to compute the star-disc interaction using finite volume methods by explaining their basics and introducing the VAC code used here to carry out simulations. We then went back to previous numerical work to emphasize the recent knowledge acquired from simulations but also their limitations. From this state of the art of the star-disc interaction, we presented the MHD model we used in our simulations. We gave all details of a more realistic accretion disc including both viscosity and resistivity and then which boundary conditions we choose for having a correct description of the stellar magnetosphere, taking into account a splitting strategy for the magnetic field to compute accurately the magnetic stress. The two following chapters presented our results I now emphasize.

The first part of this conclusion focuses on the physical understanding of the truncation of discs and the resulting funnel flows formation. An analytical and predictive criterion for localizing this truncation radius in the accretor regime ($r_t < r_{co}$) was derived by assuming equipartition between magnetic and disc thermal pressure at the disc inner edge and disc sonic Mach number near unity. This criterion is predictive since the knowledge of the stellar accretion rate and dipolar stellar magnetic strength is sufficient to constrain it with a high accuracy level of better than 10 %. This was validated by MHD simulations with the VAC code and indeed in analyzing again previous MHD simulations of the star-disc interaction (Romanova et al. 2002, Kuker et al. 2003). The propeller case shows also the truncation of discs at equipartition. We also observe oscillation of the magnetosphere due to the presence of viscosity in chapter 5 in the accretor regime similar to those described in Goodson et al. (1999). Actually, the stellar accretion rate is controlled by the dominant magnetic field which gives $m_s \sim 1$, whereas viscosity within the disc gives smaller accretion rate with $m_s = \alpha\epsilon$. This triggers a time dependent magnetosphere which can explain some of the variability observed in CTTS (Alencar & Basri 2000).

Accretion funnels are a robust feature of our simulations. Chapter 5 confirms the formation of accretion columns for a variety of stellar magnetic field strengths, stellar rotation rates and magnitude of disc dissipation effects. Only transient funnel flows are obtained in the propeller regime. The formation of such funnel flows is also not too dependent on both boundary

conditions at the stellar surface and the choice of the initial condition defining the disc structure provided that the stellar magnetic field pressure can support the poloidal disc ram pressure. However, an initial disc structure including a suitable accretion flow and diffusivity is essential to have a smooth evolution with no long term transients to study on long timescales the properties of the star-disc interaction. The disc thermal pressure gets enhanced at the disc inner edge by the compression of the magnetic dipole, which lifts up matter into the closed stellar magnetosphere whereas the poloidal magnetic force is always negligible and even pinches the disc material at its basis and opposes the flow within the funnel. The material within the funnel is continuously braked by the magnetic torque. This magnetospheric flow first reaches the sonic point with $M_s \sim 3.5$ and then attains a free-fall speed closer to the stellar surface thanks to gravity. However, the accreted material is always sub-Alfvénic and thus boundary conditions on the stellar surface can influence the accretion flow via magnetic torques. Particularly, in our simulations, we always considered a perfect frozen-in magnetic field at the stellar surface but one can expect that the convective motions can perturb the magnetic field lines. In turn, this can induce Alfvén waves allowing extra heating within the funnel in addition to the dominant adiabatic compression, which is necessary to explain in a consistent way the emission line properties in spectra (Muzerolle et al. 1998).

In our simulations, we found truncation radii consistent with observational constraints from large scale weak dipolar magnetic field ($B_* = 141G$) and disc inner hole measurements ($r_t \sim 3R_*$), but considered only the case of weak accretors ($\dot{M} \sim 10^{-9} M_\odot.yr^{-1}$). The bulk of CCTS have accretion rates an order of magnitude greater, which leads to very small, unobserved disc inner holes (Najita et al. 2007). Thus, this probably points to the necessity to have stronger magnetic fields, implying more complex topology for these higher accretors. Anyway, observations of periodic variability favour an inclined magnetosphere already simulated in 3D by e.g. Romanova et al. (2003) and Long et al. (2007). Moreover, reconstruction from recent spectro-polarimetric observations by Donati et al. (2007) show such multipolar components for the stellar magnetosphere with possibly a strong dipole component.

As far as the stellar angular momentum balance is concerned, we found an anticorrelation between the stellar accretion rate and both stellar magnetic strength and stellar rotation rate in the accretor regime. Actually, for a given rotation rate which fixes the position of the corotation radius, increasing the stellar magnetic field strength gives a truncation radius further out. This latter is thus nearer to the corotation, which limits the differential rotation between the star and the disc and the generation of toroidal magnetic field. Since the magnetic torque controls the accretion at this location, the stellar accretion rate thus diminishes. In the near future, we have to extend the timescale reached by our simulations to confirm these latter trends. Particularly, finding a disc locking state as in Ghosh & Lamb (1978) is still challenging since numerically it is difficult to correctly control the magnetic stress near the stellar surface in the case where the truncation radius is close to the corotation one ($0.77 < r_\mathrm{t}/r_\mathrm{co} < 1$). The use of a lower diffusive scheme as a Roe type one or the AMR version of VAC recently developed in spherical coordinates offer possibilities to investigate this issue and obtain a firm conclusion. The work reported in chapter 4 has lead to the conclusion that the star continuously spins up in the slow rotation range as already shown in Romanova et al. (2002). However, chapter 5 shows that when we consider higher stellar rotation rate for the same magnetic field, the stellar accretion rate is reduced

and one seems to tend towards a disc locking state but with finally a faster rotating star with 1.8 day period. Actually, the closed magnetosphere is restricted at the disc inner edge and thus one can not remove the stellar angular momentum via the magnetic field connected within the disc beyond the corotation as in the Gosh & Lamb (1979) model of an extended magnetosphere. The stellar rotation locking state obtained by Long et al. (2005) with the same restricted magnetosphere is caused by a kind of stellar wind as proposed by Matt & Pudritz (2005) since the stellar braking is caused by the opened field lines connected to the star. Thus powerful stellar winds seem to be the most promising way to explain the braking of young stars as recent observations show evidences for them (Dupree et al. 2005, Kwan et al. 2007), but consistent MHD simulations have to be done, controlling the mass loss rate at the stellar surface. We want to remark that even thought we find powerful ejection events in the propeller regime with a global stellar braking, the accretion phase is only a transient in this regime and can not explain the evolution of CTTS which always present evidences of accretion. Finally, we found that a part of the initial specific angular momentum within the disc is transported by the magnetic field but not totally as argued by Ostriker & Shu (1995) or Li & Wilson (1999). Thus, this acts to increase the stellar angular momentum although with a lower rate with respect to assumptions of Keplerian rotation considered in steady-state analytical models of e.g. Matt & Pudritz (2005).

As far as the ejection is concerned, we obtain breeze-like winds in our simulations and powerful ejection events in the propeller regime. However, all the ejections obtained till now from a pure stellar magnetosphere do not lead to collimated flows (see e.g. Elsner & Fendt 2000, Ustyugova et al. 2006 and the different simulations presented in this thesis) except in Goodson et al. (1999). This is in contradiction with observations of narrow opening angles of a few degrees beyond 50 AU (Burrows et al. 1996, Dougados et al. 2000). Actually, recent observational data measuring both specific angular momentum and poloidal velocities reached within jets are consistent with collimated jets from disc wind configurations (Ferreira et al. 2006). That is why we recently add a disc magnetic field antiparallel to the stellar magnetic moment and in equipartition with the disc thermal pressure to feed continuously the accretion column and have a disc wind. Futhermore, the consistent simulation of such a configuration is really interesting since until now launching of jets from Keplerian discs has always been obtained without taking into account really the inner boundary due to the central object. In that case, our preliminary results show a greater stability of accretion columns with reduced oscillations since now the presence of ejection from the disc imposes higher accretion rate throughout it. Moreover, the expansion of the magnetosphere with the ejection of plasmoids can be collimated by the disc wind in this configuration. Finally, in all the star-disc configurations tested here without including a proper disc magnetic field, we do not find formation of X winds, although the ejection along the current sheet due to the opening of the magnetosphere can sometimes mimic such a wind. This is particularly the case for the most promising scenario according to Shu et al. (2007), namely a small disc diffusivity and high viscosity such that $Pr_m \sim r/h = 10$ which allows the concentration of the magnetic flux at the disc inner edge to be efficient. The inclusion of this extra disc magnetic field in the case of a low disc diffusivity can increase the concentration of magnetic flux at the disc inner edge and could eventually be the support of an X wind. This work is in progress.

Conclusion

Après avoir présenté le contexte observationnel des proto-étoiles magnétisées et accrétantes telles que les CTTS appartenant aux étoiles de faibles masse, j'ai discuté des principaux concepts théoriques permettant de comprendre l'accrétion magnétosphérique. J'ai montré dans quelle mesure il est possible d'obtenir au final un freinage de l'étoile à partir d'une configuration de magnétosphère étendue ancrée dans le disque en fonction de la position relative du rayon de troncation par rapport au rayon de corotation et de l'importance des effets dissipatifs dans le disque. Compte tenu de l'inefficacité de cette connexion magnétique trouvée dans les modèles analytiques antérieurs, on s'est demandé si des configurations particulières prenant en compte les phénomènes d'éjection comme le vent X (Shu et al. 1994) ou le vent ReX (Ferreira et al. 2000) pouvaient résoudre ce problème d'évacuation du moment cinétique. Ensuite, j'ai présenté une manière efficace de calculer numériquement l'interaction entre l'étoile et son disque en utilisant les méthodes de volumes finis en exposant leur fondement théoriques, et en introduisant le code VAC utilisé dans cette thèse pour effectuer des simulations. Je suis revenu enfin sur les travaux numériques antérieurs pour souligner les connaissances récentes apportées par les simulations dans ce domaine mais aussi leurs limitations. A partir de cet état de l'art de l'interaction étoile/disque, j'ai présenté le modèle MHD utilisé dans nos simulations pour traiter à la fois un disque d'accrétion plus réaliste incluant viscosité et resistivité, et des conditions aux limites choisies pour avoir une description correcte de la magnétosphère stellaire, en prenant en compte également une stratégie de séparation du champ magnétique pour mieux calculer les forces magnétiques. Les deux chapitres suivants présentent nos résultats.

La première partie de cette conclusion se concentre sur la compréhension physique de la troncation des disques et de la formation des nappes d'accrétion associées. Un critère analytique et prédictif pour localiser ce rayon de troncation dans le régime accrétant ($r_t < r_{\rm co}$) a été dérivé en supposant une équipartition entre pression magnétique et thermique dans le disque au bord interne de ce dernier ainsi que d'un nombre de Mach sonique dans le disque proche de l'unité. Ce critère est prédictif puisque la connaissance du taux d'accrétion sur l'étoile et de l'intensité de la composante dipolaire du champ magnétique stellaire est suffisante pour le contraindre à une précision meilleure que 10 %. Ceci a été validé par des simulations MHD effectuées avec le code VAC mais aussi en examinant les simulations MHD antérieures de l'interaction étoile/disque (Romanova et al. 2002, Kuker et al. 2003). Le cas du régime "'propeller" ($r_t > r_{\rm co}$) montre aussi la troncation des disques à l'équipartition. On observe aussi une oscillation de la magnétosphère en présence de viscosité dans le chapitre 5 dans le régime accrétant similaire au mécanisme décrit par Goodson et al. (1999). En effet, le taux d'accrétion sur l'étoile est contrôlé par le champ magnétique dominant dans les parties internes du disque qui donne $m_s \sim 1$ alors que la viscosité dans le disque donne des taux d'accrétion beaucoup plus faibles avec $m_s = \alpha\epsilon$. Ceci implique une magnétosphère dépendante du temps qui peut expliquer une partie de la variabilité observée dans les CTTS (Alencar & Basri 2000). La formation de colonnes d'accrétion est une caractéristique robuste de nos simulations. Le chapitre 5 confirme leur apparition pour une variété d'intensité du champ magnétique de l'étoile, de sa vitesse de rotation et des effets dissipatifs du disque. Par contre, dans le domaine "propeller", la formation de ces colonnes n'est qu'un transitoire durant les périodes d'accrétion. La formation de telles colonnes n'est pas aussi

très dépendante des conditions aux limites à la surface de l'étoile ou du choix de la condition initiale définissant la structure du disque à condition que la pression du champ magnétique de l'étoile puisse supporter la pression poloidale dynamique du disque. Pourtant, un modèle de disque incluant initialement un écoulement d'accrétion et de la diffusivité est essentiel pour avoir une évolution continue sans transitoire majeur pour étudier à long terme les propriétés de l'interaction entre l'étoile et son disque. C'est le gradient de pression thermique amplifié au bord interne du disque par la compression du dipôle magnétique qui soulève la matière hors du plan du disque et la charge le long des lignes de champ de la magnétosphère fermée alors que la force magnétique poloïdale est toujours négligeable et même compresse la matière à la base de la colonne et s'oppose à son écoulement. La matière à l'intérieur de la colonne est continuellement freinée par le couple magnétique. Cet écoulement magnétosphérique atteint tout d'abord le point sonique avec au maximum $M_s \sim 3.5$ et puis la vitesse de chute libre à proximité de la surface de l'étoile grâce à la gravité. Cependant, la matière accrétée l'est toujours à une vitesse sub-Alfvénique et ainsi les conditions aux limites à la surface de l'étoile peuvent influencer l'écoulement d'accrétion en amont par l'intermédiaire des couples magnétiques. En particulier, dans nos simulations, on a toujours considéré un champ magnétique parfaitement gelé à la surface de l'étoile mais on peut s'attendre que les mouvements de convection perturbent les lignes de champ magnétique ce qui peut induire des ondes d'Alfvén pouvant fournir une source de chaleur supplémentaire dans les colonnes d'accrétion en plus de la compression adiabatique. Ceci est nécessaire pour expliquer de façon consistante les propriétés des raies d'émission dans les spectres (Muzerolle et al. 1998).

Dans nos simulations, on trouve des rayons de troncation consistants avec les contraintes observationnelles qui sont les faibles valeurs pour la composante dipolaire du champ magnétique ($B_* = 141G$) et les mesures de rayons internes des disques ($r_t \sim 3R_*$), mais en considérant seulement le cas d'étoiles faiblement accrétantes ($\dot{M} \sim 10^{-9} M_\odot.yr^{-1}$). La majorité des CTTS ont des taux d'accrétion un ordre de grandeur supérieur ce qui conduirait à de très faibles rayons internes de disques non observés (Najita et al. 2007). Ainsi, cela montre probablement la nécessité d'avoir des champs magnétiques plus forts impliquant une topologie du champ plus complexe pour ces étoiles accrétant davantage de masse. De toute façon, l'observation de variabilité régulière favorise les configurations avec magnétosphère inclinée comme simulée déjà en 3D par exemple par Romanova et al. (2003) et Long et al. (2007). De plus, la reconstruction du champ magnétique à partir d'observations en spectro-polarimétrie par Donati et al. (2007) montre de telles composantes multipolaires pour la magnétosphère avec la possibilité d'avoir aussi une forte composante dipolaire.

En ce qui concerne le bilan de moment cinétique pour l'étoile, on a trouvé une anticorrélation entre le taux d'accrétion sur l'étoile et à la fois l'intensité du champ magnétique stellaire ou sa vitesse de rotation dans le régime accrétant. En effet, pour une vitesse de rotation donnée qui fixe la position du rayon de corotation, augmenter le champ magnétique stellaire éloigne le rayon de troncation du disque. Ce dernier est donc plus proche de la corotation ce qui limite la rotation différentielle entre l'étoile et le disque et donc la génération de champ magnétique toroïdal. Puisque le couple magnétique contrôle l'accrétion dans cette région, le taux d'accrétion à la surface de l'étoile diminue. Très prochainement, on doit étendre les échelles de temps atteintes par nos simulations pour confirmer les tendances précédentes. En particulier, trouver un état

de "disc locking" comme décrit par Ghosh & Lamb (1978) est toujours un défi du point de vue numérique puisque il est difficile de contrôler correctement les couples magnétiques à la surface de l'étoile dans le cas où le rayon de troncation est proche de la corotation ($0.77 < r_t/r_{co} < 1$). L'utilisation d'un schéma numérique moins diffusif comme celui de Roe ou de la version AMR de VAC récemment développée en coordonnées sphériques sont différentes possibilités pour étudier ce problème et obtenir une conclusion définitive. Le travail présenté dans le chapitre 4 a mené à la conclusion que l'étoile est continûment accélérée dans le cas d'un rotateur lent comme déjà montré dans Romanova et al. (2002). Pourtant, le chapitre 5 montre que quand on considère une plus grande vitesse de rotation pour le même champ magnétique, le taux d'accrétion sur l'étoile est réduit et on semble tendre vers un état de "disc-locking" mais au final avec une grande vitesse de rotation pour l'étoile avec une période de rotation autour de 1,8 jours. En effet, la magnétosphère fermée est restreinte à proximité du rayon interne du disque et ainsi on ne peut pas retirer du moment cinétique de l'étoile par l'intermédiaire des lignes de champ connectées au disque au delà de la corotation comme dans le modèle de Ghosh & Lamb (1979) de magnétosphère étendue. Le maintien d'une vitesse de rotation de l'étoile constante obtenue par Long et al. (2005) avec le même type de magnétosphère restreinte est permis par un genre de vent stellaire comme proposé par Matt & Pudritz (2005) puisque le freinage de l'étoile est provoqué par les lignes de champ magnétique ouvertes connectées à l'étoile. Ce mécanisme de vent stellaire puissant semble la manière la plus prometteuse pour expliquer le freinage des étoiles jeunes puisque de récentes observations montrent des preuves de leur existence (Dupree et al. 2005, Kwan et al. 2007), mais des simulations MHD consistantes doivent être effectuées en contrôlant le taux de perte de masse à la surface de l'étoile. Je veux faire remarquer que même si on trouve dans nos simulations des épisodes d'éjection puissants dans le régime "propeller" avec un freinage global de l'étoile, la phase d'accrétion n'est pas permanente dans ce régime et ne peut pas expliquer l'évolution des CTTS qui présentent toujours des preuves d'accrétion sur l'étoile. Par contre, ce régime peut expliquer l'évolution des étoiles plus jeunes de classe I. Finalement, nous avons trouvé qu'une partie du moment cinétique spécifique initial à l'intérieur du disque est stocké dans le champ magnétique mais pas totalement comme supposé par Ostriker & Shu (1995) ou Li & Wilson (1999). Ainsi, cela participe à augmenter le moment cinétique de l'étoile bien qu'à de plus faibles taux en comparaison des hypothèses de rotations Képlériennes faites dans la plupart des modèles analytiques stationnaires comme par exemple celui de Matt & Pudritz (2005).

En ce qui concerne maintenant les mécanismes d'éjection, nous n'avons obtenu que des vents non permanents qualifiés de brises par opposition aux vents de disque, et des épisodes d'éjection massives dans le cas du regime "propeller". Pourtant, tous les phénomènes d'éjection obtenus jusqu'à présent en considérant seulement une magnétosphère stellaire ne conduisent pas à des écoulements collimatés (voir par exemple Elsner & Fendt 2000, Ustyugova et al. 2006 et les différentes simulations présentées dans cette thèse) à l'exception de Goodson et al. (1999), ce qui est en contradiction avec les observations de jets de matière avec des faibles angles d'ouverture de quelques degrés au delà de 50 u.a. (Burrows et al. 1996, Dougados et al. 2000). En effet, de récentes données d'observation mesurant à la fois le moment cinétique spécifique de la matière et les vitesses poloïdales atteintes à l'intérieur des jets sont consistantes avec des jets collimatés provenant de configurations de vents de disques étendue (Ferreira et al. 2006). C'est pourquoi

récemment nous avons inclu un champ magnétique propre dans le disque dont la direction est antiparallèle au moment magnétique de l'étoile et qui est en équipartition avec la pression thermique du disque dans le but d'avoir une alimentation en masse continue pour la colonne d'accrétion et de former un vent de disque. En outre, la simulation consistante d'une telle configuration est très intéressante puisque jusqu'à présent le lancement de jets à partir de disques d'accrétion Képlériens a toujours été obtenu sans prendre en compte les conditions aux limites imposées par l'objet central. Dans ce cas là, nos résultats préliminaires montrent une plus grande stabilité des colonnes d'accrétion avec des oscillations réduites puisque maintenant la présence d'éjection provenant du disque implique de plus grand taux d'accrétion dans le disque. De plus, l'expansion de la magnétosphère avec l'éjection de plasmoïdes peut être collimatée par le vent de disque dans cette configuration. Finalement, dans toutes les configurations étoile/disque testées ici, on ne trouve pas de formation de vents X (Shu et al. 1994) bien que l'éjection le long de la nappe de courant causée par l'expansion de la magnétosphère peut dans certains cas évoquer un tel vent. Cette absence de vent X est particulièrement frappante dans le scénario le plus favorable d'après Shu et al. (2007) où une faible diffusivité dans le disque associée à une forte viscosité telle que $Pr_m \sim r/h = 10$ permet une concentration efficace du flux magnétique au bord interne du disque. L'inclusion d'un champ magnétique propre au disque dans le cas d'une faible diffusivité présente dans ce dernier peut accroître encore davantage le flux magnétique au bord interne du disque et finalement pourrait être le moyen d'avoir un vent X puisqu'on n'en a pas trouvé la trace dans les modèles prenant en compte uniquement la magnétosphère stellaire. Ce travail est en cours.

Contributions

Referred Publications

Accretion funnels onto weakly magnetized young stars Bessolaz, N.; Zanni, C.; Ferreira, J.; Keppens, R.; Bouvier, J.; 2008 ; Astronomy and Astrophysics ; 478 ; 155

Proceedings, Talks and Posters

MHD simulations of the magnetic coupling between a young star and its accretion disk Bessolaz, N.; Ferreira, J.; Keppens, R.; Bouvier, J.; 2006 ; SF2A-2006: Proceedings of the Annual meeting of the French Society of Astronomy and Astrophysics Eds.: D. Barret, F. Casoli, G. Lagache, A. Lecavelier, L. Pagani, p.447 ; 447

Contributed talk "MHD simulations of the magnetic coupling between a young star and its accretion disk" at the 2nd European School on Jets from Young Stars: High Angular Resolution Observations in Elba Island - Italy, September 4-8, 2006

Contributed talk "MHD simulations of star-disk interaction in young stars" at the 3rd JETSET School and Workshop : Numerical MHD and Instabilities in Sauze d'Oulx, Torino - Italy, January 8-13, 2007

Poster "MHD simulations of star-disk interaction in young stars with the VAC code" at IAU Symposium 243 : Star-disk interaction in young stars in Grenoble, 21-25 May, 2007

Large scale magnetic fields in discs: jets and reconnection X-winds Ferreira, Jonathan; Bessolaz, Nicolas; Zanni, Claudio; & Combet, Céline; 2007 ; IAU Symposium ; 243 ; 307

Contributed talk "MHD simulations of the interaction between a magnetized young star and its accretion disc" at the 8th Dutch Astrophysics Days in K.U.Leuven, Belgium, March 25-26, 2008

Bibliography

- Adams, F. C., Lada, C. J., & Shu, F. H., 1987, Astrophysical Journal, 312, 788
- Adams, F. C., Shu, F. H., & Lada, C. J. 1988, Astrophysical Journal, 326, 865
- Akeson, R. L., et al. 2005, Astrophysical Journal, 622, 440
- Alencar, S. H. P., & Basri, G., 2000, Astronomical Journal, 119, 119, 1881
- Alencar, S. H. P., & Batalha, C. 2002, Astrophysical Journal, 571, 378
- Aly, J. J., 1980, Astron. & Astrophys., 86, 192
- Aly, J. J. 1984, Astrophysical Journal, 283, 349
- Aly, J. J., & Kuijpers, J., 1990, Astron. & Astrophys., 227, 473
- Andre, P., Ward-Thompson, D., & Barsony, M., 1993, Astrophysical Journal, 406, 122
- Appenzeller, I., Oestreicher, R., & Jankovics, I. 1984, Astron. & Astrophys., 141, 108
- Armitage, P. J., Clarke, C. J., 1996, Mon. Not. of the Royal Astron. Soc., 280, 458
- Arons, J., 1993, Astrophysical Journal, 408, 160
- Baan, W. A. 1977, Astrophysical Journal, 214, 245
- Baan, W. A. 1979, Astrophysical Journal, 227, 987
- Balbus, S. A., & Hawley, J. F. 1991, Astrophysical Journal, 376, 214
- Bardou, A., & Heyvaerts, J. 1996, Astron. & Astrophys., 307, 1009
- Basri, G. 1990, Memorie della Societa Astronomica Italiana, 61, 707
- Basri, G., Marcy, G. W., & Valenti, J. A. 1992, Astrophysical Journal, 390, 622
- Beristain, G., Edwards, S., & Kwan, J. 1998, Astrophysical Journal, 499, 828
- Bertout, C., Basri, G., & Bouvier, J. 1988, Astrophysical Journal, 330, 350
- Bertout, C. 1989, Annual Review of Astron and Astrophys, 27, 351
- Bessolaz, N., Ferreira, J., Keppens, R., & Bouvier, J. 2006, SF2A-2006: Semaine de l'Astrophysique Francaise, 447
- Bessolaz, N., Zanni, C., Ferreira, J., Keppens, R., & Bouvier, J. 2008, Astron. & Astrophys., 478, 155
- Blandford, R. D., & Payne, D. G. 1982, Mon. Not. of the Royal Astron. Soc., 199, 883
- Blokland, J. W. S., van der Swaluw, E., Keppens, R., & Goedbloed, J. P. 2005, Astron. & Astrophys., 444, 337
- Bodenheimer, P. 1995, Annual Review of Astron and Astrophys, 33, 199
- Bouvier, J., Bertout, C., Benz, W., & Mayor, M. 1986, Astron. & Astrophys., 165, 110
- Bouvier, J. 1987, Circumstellar Matter, 122, 369
- Bouvier J., Covino E., Kovo O., Martín E. L., Matthews J. M., et al., 1995, å, 299, 89-107.

- Bouvier, J., Forestini, M., & Allain, S. 1997, Astron. & Astrophys., 326, 1023
- Bouvier J., Chelli A., Allain S., Carrasco L., Costero R., et al., 1999, Astron. & Astrophys., 349, 619-635.
- Bouvier J., Grankin K. N., Alencar S. H. P., Dougados C., Fernàndez M., et al., 2003, Astron. & Astrophys., 409, 169-192.
- Bouvier, J., Alencar, S. H. P., Harries, T. J., Johns-Krull, C. M. & Romanova, M. M., 2007 in Protostars and Planets V, Reipurth, B., Jewitt, D. & Keil, K. (Eds), pp 479-494
- Bouvier, J. 2007, IAU Symposium, 243, 231
- Brio, M. & Wu., C. C., 1988, J. Comput. Phys., 75, 400
- Burrows, C. J., et al. 1996, Astrophysical Journal, 473, 437
- Cabrit, S., Edwards, S., Strom, S. E., & Strom, K. M. 1990, Astrophysical Journal, 354, 687
- Calvet, N., & Gullbring, E. 1998, Astrophysical Journal, 509, 802
- Cameron, A. C. & Campbell, C. G., 1993, Astron. & Astrophys., 274, 309
- Cargo, P. & Gallice, G., 1997, J. Comp. Phys., 136, 446
- Casse, F., & Ferreira, J. 2000, Astron. & Astrophys., 361, 1178
- Casse, F., & Keppens, R. 2002, Astrophysical Journal, 581, 988
- Chiang, E. I., & Goldreich, P., 1997, Astrophysical Journal, 490, 368
- Cieza, L., & Baliber, N. 2007, Astrophysical Journal, 671, 605
- Corcoran, M., & Ray, T. P. 1998, Astron. & Astrophys., 331, 147
- Dai, H.-L., & Li, X.-D. 2006, Astron. & Astrophys., 451, 581
- D'Alessio, P., 2003, Revista Mexicana de Astronomia y Astrofisica Conference Series, 18, 14
- Damiani, F., Micela, G., Sciortino, S., & Harnden, F. R., Jr., 1995, Astrophysical Journal, 446, 331
- Donati, J.-F., Paletou, F., Bouvier, J., & Ferreira, J., 2005, Nature, 438, 466
- Donati, J.-F., et al., 2007, Mon. Not. of the Royal Astron. Soc., 380, 1297
- Donati, J. F., et al. 2008, ArXiv e-prints, 802, arXiv:0802.2052
- Dougados, C., Cabrit, S., Lavalley, C., & Ménard, F. 2000, Astron. & Astrophys., 357, L61
- Dullemond, C. P., van Zadelhoff, G. J., & Natta, A. 2002, Astron. & Astrophys., 389, 464
- Dupree, A. K., Brickhouse, N. S., Smith, G. H., & Strader, J. 2005, Astrophysical Journal, Letters, 625, L131
- Dutrey, A., Guilloteau, S., Duvert, G., Prato, L., Simon, M., Schuster, K., & Menard, F., 1996, Astron. & Astrophys., 309, 493
- Edwards, S., Cabrit, S., Strom, S. E., Heyer, I., Strom, K. M., & Anderson, E. 1987, Astrophysical Journal, 321, 473
- Edwards, S., Hartigan, P., Ghandour, L., & Andrulis, C. 1994, Astronomical Journal, 108, 1056
- Edwards, S., Fischer, W., Hillenbrand, L., & Kwan, J. 2006, Astrophysical Journal, 646, 319
- Einfeldt, B., Munz, C.D., Roe, P.L. & Sjogreen, B., 1991, J. Comp. Phys., 92, 273
- Eisner, J. A., Hillenbrand, L. A., White, R. J., Akeson, R. L., & Sargent, A. I. 2005, Astrophysical Journal, 623, 952

- Elsner, R. F., & Lamb, F. K. 1977, Astrophysical Journal, 215, 897
- Fendt, C., & Camenzind, M. 1996, Astron. & Astrophys., 313, 591
- Fendt, C., & Elstner, D. 2000, Astron. & Astrophys., 363, 208
- Ferreira, J., & Pelletier, G. 1995, Astron. & Astrophys., 295, 807
- Ferreira, J. 1997, Astron. & Astrophys., 319, 340
- Ferreira J., Pelletier G., Appl S., 2000, Mon. Not. of the Royal Astron. Soc., 312, 387
- Ferreira, J., Dougados, C., & Cabrit, S. 2006, Astron. & Astrophys., 453, 785
- Feigelson, E. D., & Montmerle, T., 1999, Annual Review of Astron and Astrophys, 37, 363
- Gardiner, T. A. & Stone, J. M., 2005, J. Comp. Phys., 205, 509
- Ghosh, P., & Lamb, F. K. 1978, Astrophysical Journal, Letters, 223, L83
- Ghosh P. & Lamb F. K., 1979, Astrophysical Journal, 232, 259-276.
- Goodson, A. P., Winglee, R. M., & Boehm, K.-H. 1997, Astrophysical Journal, 489, 199
- Goodson, A. P., Böhm, K.-H., & Winglee, R. M. 1999, Astrophysical Journal, 524, 142
- Gregory, S. G., Jardine, M., Simpson, I., & Donati, J.-F., 2006, Mon. Not. of the Royal Astron. Soc., 371, 999
- Gullbring, E., Hartmann, L., Briceno, C., & Calvet, N., 1998, Astrophysical Journal, 492, 323
- Guenther, E. W., Lehmann, H., Emerson, J. P., & Staude, J. 1999, Astron. & Astrophys., 341, 768
- Günther, H. M., Schmitt, J. H. M. M., Robrade, J., & Liefke, C., 2007, Astron. & Astrophys., 466, 1111
- Harten, A., Lax, P.D., & Van Leer, B., 1983, SIAM Rev., 25, 35
- Hartigan, P., Hartmann, L., Kenyon, S. J., Strom, S. E., & Skrutskie, M. F. 1990, Astrophysical Journal, Letters, 354, L25
- Hartigan, P., Edwards, S., & Ghandour, L. 1995, Astrophysical Journal, 452, 736
- Hartmann, L., Hewett, R., & Calvet, N. 1994, Astrophysical Journal, 426, 669
- Hayashi, C., 1966, Annual Review of Astron and Astrophys, 4, 171
- Hayashi M. R., Shibata K., & Matsumoto R., 1996, Astrophysical Journal, 468, L37-L40.
- Herbst W., Bailer-Jones C. A. L., Mundt R., Meisenheimer K., and Wackermann R.,2002, å, 396, 513-532.
- Herbst, W., Eislöffel, J., Mundt, R., & Scholz, A. 2007, Protostars and Planets V, 297
- Hirose, S., Uchida, Y., Shibata, K., & Matsumoto, R. 1997, Publications of the ASJ, 49, 193
- Johns, C. M., & Basri, G. 1995, Astrophysical Journal, 449, 341
- Johns-Krull C. M., Valenti J. A., Hatzes A. P., & Kanaan A.,1999, Astrophysical Journal, 510, L41-L44.
- Johns-Krull, C. M., & Valenti, J. A. 2000, Stellar Clusters and Associations: Convection, Rotation, and Dynamos, 198, 371
- Johns-Krull, C. M., Valenti, J. A., Piskunov, N. E., Saar, S. H., & Hatzes, A. P. 2001, Magnetic Fields Across the Hertzsprung-Russell Diagram, 248, 527
- Kenyon, S. J., & Hartmann, L. 1987, Astrophysical Journal, 323, 714
- Kenyon, S. J., Yi, I., & Hartmann, L. 1996, Astrophysical Journal, 462, 439

- Keppens, R., MacGregor, K. B., & Charbonneau, P. 1995, Astron. & Astrophys., 294, 469
- King, A. R., Pringle, J. E., & Livio, M. 2007, Mon. Not. of the Royal Astron. Soc., 376, 1740
- Kley, W., & Lin, D. N. C. 1992, Astrophysical Journal, 397, 600
- Kluzniak, W., & Kita, D. 2000, ArXiv Astrophysics e-prints, arXiv:astro-ph/0006266
- Kluźniak, W., & Rappaport, S. 2007, Astrophysical Journal, 671, 1990
- Koldoba, A. V., Lovelace, R. V. E., Ustyugova, G. V., & Romanova, M. M., 2002, Astronomical Journal, 123, 2019
- Königl. A., 1991, Astrophysical Journal, 370, L39-L43.
- Küker M., Henning T., Rüdiger G., 2003, Astrophysical Journal, 589 , 397
- Kulkarni, A. K., & Romanova, M. M. 2007, IAU Symposium, 243, 291
- Kundurthy, P., Meyer, M. R., Robberto, M., Beckwith, S. V. W., & Herbst, T. 2006, Astronomical Journal, 132, 2469
- Kurosawa, R., Harries, T. J., & Symington, N. H. 2006, Mon. Not. of the Royal Astron. Soc., 370, 580
- Kurosawa, R., Romanova, M. M., & Harries, T. J. 2008, ArXiv e-prints, 802, arXiv:0802.0201
- Kwan, J., Edwards, S., & Fischer, W. 2007, Astrophysical Journal, 657, 897
- Lamm, M. H., Mundt, R., Bailer-Jones, C. A. L., & Herbst, W. 2005, Astron. & Astrophys., 430, 1005
- Lamzin, S. A., Vittone, A. A., & Errico, L. 2001, Astronomy Letters, 27, 313
- Landau L. & Lifchitz E., Hydrodynamics, Ed. Mir, 1971
- Lesur, G., & Longaretti, P.-Y. 2005, Astron. & Astrophys., 444, 25
- Lesur, G., & Longaretti, P.-Y. 2007, Mon. Not. of the Royal Astron. Soc., 378, 1471
- LeVeque, R. J., Finite volume Methods for Hyperbolic Problems, CUP, 2003
- Li, J., & Wilson, G. 1999, Astrophysical Journal, 527, 910
- Littlefair, S. P., Naylor, T., Burningham, B., & Jeffries, R. D. 2005, Mon. Not. of the Royal Astron. Soc., 358, 341
- Long M., Romanova M. M., & Lovelace R. V. E., 2005, Astrophysical Journal, 634, 1214-1222.
- Long M., Romanova M. M., & Lovelace R. V. E., 2007, Mon. Not. of the Royal Astron. Soc., 374, 436.
- Lovelace, R. V. E., Romanova, M. M., & Bisnovatyi-Kogan, G. S., 1995, Mon. Not. of the Royal Astron. Soc., 275, 244
- Low, B. C. 2001, J. Geophys. Res., 106, 25141
- Lynden-Bell, D., & Pringle, J. E. 1974, Mon. Not. of the Royal Astron. Soc., 168, 603
- McCaughrean, M. J., & O'dell, C. R. 1996, Astronomical Journal, 111, 1977
- Martin, S. 1996, Bulletin of the American Astronomical Society, 28, 886
- Matt, S., & Pudritz, R. E. 2004, Astrophysical Journal, Letters, 607, L43
- Matt, S., & Pudritz, R. E., 2005, Mon. Not. of the Royal Astron. Soc., 356, 167
- Matt, S., & Pudritz, R. E. 2007, IAU Symposium, 243, 299
- Menard, F., & Bastien, P., 1992, Astronomical Journal, 103, 564

- Meyer, M. R., Calvet, N., & Hillenbrand, L. A. 1997, Astronomical Journal, 114, 288
- Mignone, A., Plewa, T., & Bodo, G. 2005, Astrophysical Journal, Supplement, 160, 199
- Mignone, A., Bodo, G., Massaglia, S., Matsakos, T., Tesileanu, O., Zanni, C., & Ferrari, A., 2007, Astrophysical Journal, Supplement, 170, 228
- Miller K. A. & Stone J. M., 1997, Astrophysical Journal, 489, 890-902
- Montmerle, T., Feigelson, E. D., Bouvier, J., & Andre, P. 1993, Protostars and Planets III, 689
- Montmerle, T., & Grosso, N. 1999, Star Formation 1999, Proceedings of Star Formation 1999, held in Nagoya, Japan, June 21 - 25, 1999, Editor: T. Nakamoto, Nobeyama Radio Observatory, p. 273-279, 273
- Muzerolle, J., Hartmann, L., & Calvet, N. 1998, Astronomical Journal, 116, 455
- Najita, J., Carr, J. S., & Mathieu, R. D., 2003, Astrophysical Journal, 589, 931
- Najita, J. R., Carr, J. S., Glassgold, A. E., & Valenti, J. A., 2007, Protostars and Planets V, 507
- O'dell, C. R., & Wen, Z. 1994, Astrophysical Journal, 436, 194
- Ostriker, E. C., & Shu, F. H., 1995, Astrophysical Journal, 447, 813
- Powell K. G., Roe P. L., Linde T. J., Gombosi T. I., de Zeeuw D. L., 1999, J. Comp. Phys., 154, 284
- Pringle, J. E., & Rees, M. J. 1972, Astron. & Astrophys., 21, 1
- Rebull, L. M. 2001, Astronomical Journal, 121, 1676
- Reipurth, B., Bally, J., & Devine, D. 1997, Astronomical Journal, 114, 2708
- Roe, P. L., 1981, J. Comp. Phys., 43, 357
- Romanova M. M., Ustyugova G. V., Koldoba A. V., & Lovelace R. V. E., 2002, Astrophysical Journal, 578, 420-438.
- Romanova, M. M., Ustyugova, G. V., Koldoba, A. V., Wick, J. V., & Lovelace, R. V. E., 2003, Astrophysical Journal, 595, 1009
- Romanova, M. M., Kulkarni, A., Lovelace, R. V. E., Ustyugova, G. V., & Koldoba, A. V. 2004a, Astrophysical Journal, 616, 151
- Romanova, M. M., Ustyugova, G. V., Koldoba, A. V., & Lovelace, R. V. E. 2004b, Astrophysical Journal, 610, 920
- Romanova, M. M., Ustyugova, G. V., Koldoba, A. V., & Lovelace, R. V. E. 2005, Astrophysical Journal, 635, 165
- Romanova, M. M., Kulkarni, A., Long, M., Lovelace, R. V. E., Wick, J. V., Ustyugova, G. V., & Koldoba, A. V. 2006, Advances in Space Research, 38, 2887
- Rozyczka, M., Bodenheimer, P., & Bell, K. R. 1994, Astrophysical Journal, 423, 736
- Rusanov V. V., 1961, J. Comp. Math. Phys. USSR, 1, 267
- Ryu, D., Jones, T. W., & Frank, A., 1995, Astrophysical Journal, 452, 785
- Safier, P. N. 1998, Astrophysical Journal, 494, 336
- Sargent, A. I., & Beckwith, S. 1987, Astrophysical Journal, 323, 294
- Scharlemann, E. T. 1978, Astrophysical Journal, 219, 617
- Shakura, N. I., & Sunyaev, R. A., 1973, Astron. & Astrophys., 24, 337
- Shay, M. A., Drake, J. F., Rogers, B. N., & Denton, R. E., 2001, J. Geophys. Res., 106, 3759

- Shu F., Najita J., Ostriker E., Wilkin F., Ruden S., Lizano S., 1994, Astrophysical Journal, 429, 781
- Shu, F. H., Galli, D., Lizano, S., & Cai, M. J. 2007, IAU Symposium, 243, 249
- Smirnov, D. A., Fabrika, S. N., Lamzin, S. A., & Valyavin, G. G. 2003, Astron. & Astrophys., 401, 1057
- Smirnov, D. A., Lamzin, S. A., Fabrika, S. N., & Chuntonov, G. A. 2004, Astronomy Letters, 30, 456
- Smirnov, D. A., Romanova, M. M., & Lamzin, S.Ã. 005, Astronomy Letters, 31, 335
- Smith, N., Bally, J., Licht, D., & Walawender, J. 2005, Astronomical Journal, 129, 382
- Spruit, H. C., & Taam, R. E. 1990, Astron. & Astrophys., 229, 475
- Spruit, H. C., & Taam, R. E. 1993, Astrophysical Journal, 402, 593
- Stassun, K. G., Mathieu, R. D., Mazeh, T., & Vrba, F. J. 1999, Bulletin of the American Astronomical Society, 31, 932
- Stassun, K. G., Mathieu, R. D., Vrba, F. J., Mazeh, T., & Henden, A. 2001, Astronomical Journal, 121, 1003
- Stelzer, B., & Neuhäuser, R., 2001, Astron. & Astrophys., 377, 538
- Stempels, H. C., & Piskunov, N. 2002, Astron. & Astrophys., 391, 595
- Stone, J. M., & Balbus, S. A. 1996, Astrophysical Journal, 464, 364
- Stone, J. M., & Norman, M. L., 1992, Astrophysical Journal, Supplement, 80, 791
- Strafella, F., Pezzuto, S., Corciulo, G. G., Bianchini, A., & Vittone, A. A. 1998, Astrophysical Journal, 505, 299
- Strassmeier, K. G., Rice, J. B., Ritter, A., Küker, M., Hussain, G. A. J., Hubrig, S., & Shobbrook, R. 2005, Astron. & Astrophys., 440, 1105
- Tanaka T., 1994, J. Comp. Phys., 111, 381
- Toro, E. F., Spruce, M. & Spears, W., 1994, Shock waves, 4, 25
- Toro, E.F., 1999, Riemann Solvers and Numerical Methods for Fluid Dynamics, Springer, 2nd edition
- Tóth G., 1996, Astrophys. Letters & Communications, 34, 245
- Tóth G., 1997, J. Comp. Phys., 138, 981
- Tóth G., 2000, J. Comp. Phys., 161, 605
- Tóth G., Odstrčil D., 1996, J. Comp. Phys., 128, 82
- Tóth, G., Kovacs, D., Hansen, K. C., & Gombosi, T. I., 2003, AGU Fall Meeting Abstracts, 1130
- Urpin, V. A. 1984, Soviet Astronomy, 28, 50
- Ustyugova, G. V., Koldoba, A. V., Romanova, M. M., & Lovelace, R. V. E. 2006, Astrophysical Journal, 646, 304
- Uzdensky, D. A., Königl, A., & Litwin, C. 2002, Astrophysical Journal, 565, 1191
- Uzdensky, D. A., Königl, A., & Litwin, C. 2002, Astrophysical Journal, 565, 1205
- Uzdensky, D. A. 2004, Astrophysics and Space Science, 292, 573
- Valenti J. A. & Johns-Krull C. M. , 2004, Astrophysics and Space Science, 292, 619-629.

- van Ballegooijen, A. A. 1994, Space Science Reviews, 68, 299
- van der Holst B., Keppens R., 2007, J. Comp. Phys., 226, 925
- Velikhov E.P., 1959, Soviet JETP,35,1398
- Vogel, S. N., & Kuhi, L. V. 1981, Astrophysical Journal, 245, 960
- von Rekowski, B., & Brandenburg, A. 2004, Astron. & Astrophys., 420, 17
- von Rekowski, B., & Brandenburg, A. 2006, Astronomische Nachrichten, 327, 53
- Wang, Y. M., 1996, Astrophysical Journal, 465, 111
- Yang, H., Johns-Krull, C. M., & Valenti, J. A., 2007, Astronomical Journal, 133, 73
- Yelenina, T. G., Ustyugova, G. V., & Koldoba, A. V. 2006, Astron. & Astrophys., 458, 679
- Zanni, C., Ferrari, A., Rosner, R., Bodo, G., & Massaglia, S., 2007, Astron. & Astrophys., 469, 811